



HAL
open science

Multifunctional platforms for cancer theranosis

Vivek Thakare Sudam

► **To cite this version:**

Vivek Thakare Sudam. Multifunctional platforms for cancer theranosis. Radiochemistry. Université Bourgogne Franche-Comté, 2018. English. NNT : 2018UBFCK022 . tel-02079405

HAL Id: tel-02079405

<https://theses.hal.science/tel-02079405>

Submitted on 26 Mar 2019

HAL is a multi-disciplinary open access archive for the deposit and dissemination of scientific research documents, whether they are published or not. The documents may come from teaching and research institutions in France or abroad, or from public or private research centers.

L'archive ouverte pluridisciplinaire **HAL**, est destinée au dépôt et à la diffusion de documents scientifiques de niveau recherche, publiés ou non, émanant des établissements d'enseignement et de recherche français ou étrangers, des laboratoires publics ou privés.



Thesis

Presented to

THE UNIVERSITY OF BOURGOGNE FRANCHE-COMTE

to obtain the title of

**DOCTOR OF
THE UNIVERSITY OF BOURGOGNE-FRANCHE-COMTE**

Discipline: Chemical Sciences

by

VIVEK SUDAM THAKARE

M. S (Pharm.)

Multifunctional platforms for cancer theranosis

Defended on July, 19th 2018 in front of the committee

Éva JAKAB TÓTH	Directrice de Recherche, Centre de Biophysique Moléculaire, CNRS, Orléans	Rapporteur
Fabienne GAUFFRE	Directrice de Recherche, Université de Rennes 1, CNRS, Rennes	Rapporteur
Stéphane ROUX	Professeur à l'Université de Bourgogne Franche-Comte	Examineur
François LUX	Maître de Conférences, Université Lyon1	Examineur
Frédéric BOSCHETTI	Chief Executive Officer, Chematech	Encadrant de thèse
Franck DENAT	Professeur à Université de Bourgogne-Franche-Comte	Director



Acknowledgements

This thesis work was carried out within the company CheMatech and also at the Institute of Molecular Chemistry of the University of Burgundy (ICMUB) in the team Polyamines, Porphyrins Developments and Applications (P2DA).

I express my gratitude to Dr. Frédéric BOSCHETTI, (PhD, University of Bourgogne) and CEO of the company CheMatech for having given me the opportunity to perform my doctoral research work at Chematech. My sincere thanks to him for guiding me in my research and for providing constant support throughout my doctoral training.

I would especially like to thank Professor Franck DENAT, Director of ICMUB, for welcoming me and having me in his excellent team at ICMUB. I thank him for having offered me his valuable supervision and timely motivation. I also acknowledge his pleasant nature and attention for details.

A big thank you to my colleague and friend, Mr. Guillaume PAULIN, Manager of the GMP laboratory at CheMatech, for always being available for interesting discussion and his precious help and advice in the chemical synthesis. The great thing was, all our communications were in French, which was fun and learning experience.

I would also like to thank my colleague Mr. Stéphane MARTEL, Manager of the R & D and Analysis laboratory at CheMatech, for providing me guidance in addressing routine chemistry and technical problems. I also thank him for his work in the laboratory as well as for the maintenance of many devices.

I would also like to express my gratitude to Dr. Mathieu MOREAU and Dr. Claire BERNHARD for interesting scientific discussions and their valuable advice, particularly while planning radiolabelling and animal studies at CGFL. This thesis work would not have been possible without their timely support, encouragement and friendship.

I equally thank all wonderful colleagues from CGFL, Dijon who I got chance to interact with and have directly or indirectly contributed to my knowledge.

I would like to thank Prof. Olivier TILLEMENT, Dr. Lux FRANÇOIS and Vulong TRAN for their collaboration while working on AGuIX nanoparticles and welcoming me to work in their laboratory during the secondment.

I would like to extend my sincere gratitude to Dr. Victor GONÇALVES and Coline CANOVAS, for collaborating in the development of PSMA based theranostics.

I thank Prof. Anthony ROMIEU for his valuable time, support and scientific advice on many interesting topics including fluorescent dyes and their characterization.

I also extend my gratitude to Prof. Stephané ROUX and his team in Besançon for excellent collaboration in developing multifunctional gold nanoparticles. I hope this collaboration will go a long way in developing diverse theranostics in future.

I express my sincere gratitude to Prof. Kevin PRISE and Dr. Karl BUTTERWORTH for welcoming me at their laboratory in Centre for Cancer Research and Cell Biology, Queens University Belfast, Belfast, UK during the secondment.

I would like to thank Professor Sandrine LACOMBE, Co-ordinator of ARGENT, Prof. Nigel MASON, The Open University, Milton Keynes, UK and all other supervisors/members of the ARGENT project consortium who have timely trained, motivated me whilst assessing my progress throughout the project.

I also thank Marie-José PENOUILH, Fanny CHAUX and Myriam HEYDEL for their help and advice on mass spectrometry, NMR and other analyses. I also thank Marcel SOUSTELLE for the elementary analysis

I would also like to thank the IT team consisting of Dr. Alain TABARD (deceased), Dr. Christine STERN, Anne COMBET and Thierry BELLOIR of P2DA group whose constant support has been crucial in realising and facilitating my work and stay in Chematech and ICMUB.

I do not forget to extend my thanks to all the permanent and non-permanent members of the P2DA team and ICMUB, who have been great and accommodating. All these people have added a great deal of value to my experience, learning and stay in ICMUB.

Lastly, I would like to warmly thank my colleagues and friends met during these three years of thesis, with whom I spent very good moments; Adrien DUBOIS, Sophie POTY, Mylène BONNAUD, Coline CANOVAS, Jacques PLIQUETT, Léo BUCHER, Clement MICHELIN, Yann BERNHARD, Damien LHENRY, Bertrand BRIZET, Valentine QUESNEAU, Sylvain DEBIEU, Vivian LIORET, Ibai VALVERDE, Marc PIRROTTA, Victor GONCALVES and Richard DECREAU.

Finally, I dedicate this work to my parents who have always been there for me with their unconditional support and to my wife Debarati for her unwavering support and love, without whom nothing would have been possible.

Table of Contents:

Chapter I . Introduction	11
I-1 Preface.....	12
I-1.1 Overview of ARGENT project:.....	13
I-2 Cancer theranosis: Approaches and avenues	15
I-2.1 Cancer therapy:.....	16
I-2.2 Cancer Diagnosis:.....	22
I-3 Monomolecular Multimodal Platform in cancer theranosis:.....	30
I-3.1 Chelators used in multimodal platforms:.....	31
I-3.2 Fluorescent probes for NIR based optical imaging:	35
I-3.3 Targeting ligands for cancer:	38
I-3.4 Conjugation Site and Chemistry:.....	43
I-4 Objectives of the research thesis:	48
Chapter II . Multifunctional polysiloxane (AGuIX) nanoparticles for cancer theranosis.....	51
II-1 AGuIX Nanoparticles in cancer theranosis:	52
II-1.1 Synthesis and structure of AGuIX:	53
II-2 Functionalization of AGuIX:	56
II-2.1 Nanoparticle synthesis and functionalization with silane chelators:.....	57
II-2.2 Physico-chemical properties of functionalized nanoparticles:	62
II-2.3 Radiolabelling and study of the stability of radiolabelled nanoparticles:	68
II-3 Animal imaging in TSA tumor model:	70
II-4 Conclusions:	72
Chapter III . Multifunctional gold nanoparticles for cancer theranosis	73
III-1 Gold Nanoparticles for cancer theranosis:	74
III-2 Development of DOTAGA based amine functionalized gold nanoparticle:.....	77
III-2.1 Synthesis of DOTAGA-Lys-TA-NH ₂	77
III-2.2 Amine functionalized DOTAGA gold nanoparticle (Au@DOTAGA-Lys-TA-NH ₂):.....	79
III-3 Development of gold nanoparticles for PET-MRI:	80
III-3.1 Synthesis of DOTAGA-Lys-TA-NODAGA ligand	80
III-3.2 Gold nanoparticles based on DOTAGA-Lys-TA-NODAGA for PET-MRI:	84
III-4 Radiolabelling and stability of the radiolabelled nanoparticles for PET-MRI:.....	86
III-5 Animal imaging and biodistribution studies in TSA tumor model:	88
III-6 Development of PSMA targeted gold nanoparticles:.....	90
III-6.1 Synthesis of the DOTAGA-Lys-TA-Glu-PSMA.....	90
III-6.2 Determination of the PSMA binding activity using the enzymatic assay:.....	92
III-6.3 Gold nanoparticle based on DOTAGA-Lys-TA-Glu-PSMA:	93
III-7 Radiolabelling and stability study of the PSMA targeted nanoparticles:	94

III-8 Development of a PET-Optical ligand for gold nanoparticles:	95
III-8.1 Synthesis of a PET-Optical ligand for gold nanoparticles	95
III-8.2 Photo-physical characterization of the PET-Optical probe (24):	99
III-9 Development of amine functionalized NODAGA ligands for gold nanoparticle synthesis: ...	100
III-10 Conclusions:	101
Chapter IV PSMA targeted multimodal imaging	103
IV-1 Introduction:	104
IV-1.1 PSMA as a biomarker in prostate cancer:	105
IV-2 PSMA inhibitors in prostate cancer theranosis:	106
IV-2.1 Anti-PSMA monoclonal antibodies in prostate cancer theranosis:	106
IV-2.2 Small molecule based PSMA inhibitors in prostate cancer theranosis:	107
IV-3 Synthesis of PSMA targeted monomolecular PET-Optical imaging probe:	114
IV-3.1 Synthesis of chelator-linker moiety:	114
IV-3.2 Synthesis of PSMA ligand and its derivative:	115
IV-3.3 Synthesis of chelator-linker-PSMA ligand:	116
IV-3.4 Synthesis of bioconjugatable IR-783:	119
IV-3.5 Synthesis of chelator-linker-PSMA ligand-IR783:	121
IV-4 Characterization of the PET-Optical probe	123
IV-4.1 Photophysical characterization of the PET-Optical probe:	123
IV-4.2 Radiolabelling and stability of the PET-Optical probe:	125
IV-4.3 Binding affinity measurements using NAALDase assay:	127
IV-5 Conclusions:	129
Chapter V . Bimodal imaging probes for bioconjugation to antibody fragments and nanoparticle functionalization	131
V-1 Multimodal imaging probes for bioconjugation:	132
V-2 Synthesis of trifunctional probe for PET-Optical imaging:	134
V-2.1 Synthesis of bifunctional chelating agent:	134
V-2.2 Synthesis of the linker system bearing chelator and conjugation site:	134
V-2.3 Synthesis of a trifunctional probe using bioconjugatable IR-783:	136
V-3 Photo-physical characterization of the trifunctional probe:	139
V-4 Chemical biology of the antibody drug conjugates:	141
V-4.1 Non-specific Conjugation through Native Residues	141
V-4.2 Conjugation through genetically engineered sites	143
V-4.3 Enzymatic Bioconjugation:	143
V-4.4 Labelling strategies in antibody conjugation:	145
V-4.5 Difference between conjugates of mAb fragments and full scale mAb?	146
V-5 Activatable fluorescent molecular imaging probes based on antibody/antibody fragments: ...	149

V-6 Development of HER-2 targeted bimodal probe based on antibody fragment:	151
V-6.1 Synthesis of F(ab') ₂ of trastuzumab:	152
V-6.2 Reduction of F(ab') ₂ fragments:	153
V-6.3 Conjugation of the bimodal probe to Fab' fragment:	154
V-6.4 Characterization of the bimodal conjugate:	154
V-7 Animal imaging in breast cancer model:	157
V-8 Development of the multifunctional nanoparticles:	159
V-9 Chemical functionalization of AGuIX using bimodal probe:	160
V-9.1 Thiolation of the AGuIX:	160
V-9.2 Conjugation of the bimodal probe to AGuIX:	161
V-10 Characterization of the functionalized nanoparticles:	162
V-10.1 Physico-chemical characterization of nanoparticle properties:	162
V-10.2 Photophysical characteristics of the functionalized nanoparticles:	164
V-11 Radiolabelling and stability of the functionalized nanoparticles:	165
V-12 Animal imaging in breast cancer model:	167
V-13 Conclusions:	169
Chapter VI . Experimental Section.....	171
Chapter VII . References	219
Chapter VIII . Publications	233

Glossary of abbreviations

ADC	Antibody drug conjugates
AGuIX	Activation et Guidage de l'Irradiation X
ARGENT	Advanced Radiotherapy Generated by Exploiting Nanoprocesses and Technologies
APTES	(3-Aminopropyl) triethoxysilane
BFC	Bifunctional chelator
Boc	tertiary butyloxycarbonyl
BODIPY	4,4-difluoro-4-borata-3a-azonia-4a-aza-s-indacene
cGMP	current Good Manufacturing Practices
CT	Computed tomography
DIPEA	N,N-diisopropyl ethyl amine 4-dimethylaminopyridine
DLS	Dynamic light scattering
DMF	Dimethyl formamide
DOTA	1,4,7,10-tetraazacyclododecane-1,4,7,10-tetraacetic acid
DOTAGA	1,4,7,10-tetraazacyclododecan-1-glutaric acid-4,7,10-triacetic acid
DTPA	Diethylene triamine penta acetic acid
EDC	1-ethyl-3-(3-dimethylaminopropyl) carbodiimide
EDTA	Ethylene diamine tetraacetic acid
FDG	fluorodeoxyglucose
Gln	Glutamine
Glu	Glutamic acid
HBED	N, N'-bis-(2-HydroxyBenzyl)ethylenediamine-N, N'-diacetic acid
HBTU	2-(1H-benzotriazol-1-yl) -1,1,3,3-tetramethyluronium hexafluorophosphate
HEPES	4-(2-HydroxyEthyl)-1-piperazineethane sulfonic acid
HER-2	Human epidermal growth factor receptor 2
HOBt	4-hydroxybenzotriazole
HPLC	High-Performance Liquid Chromatography

HRMS	High resolution mass spectrometry
IC₅₀	Inhibitory Concentration at 50%
ITLC	Instant thin layer chromatography
Lys	lysine
mAb	monoclonal Antibody
MALDI-TOF	Matrix Assisted Laser Desorption Ionisation- Time of Flight
MRI	Magnetic Resonance Imaging
NCS:	Isothiocyanate
NHS	N-Hydroxy-Succinimidyl
NIR	Near infrared
NMR	Nuclear Magnetic Resonance
NOTA	1,4,7-triazacyclononane-1,4,7-triacetic acid
NODAGA	1,4,7-triazacyclononane-1-glutaric acid-4,7-diacetic acid
PBS	Phosphate Buffer Saline
PEG	Polyethylene glycol
PET	Positron Emission Tomography
PSMA	Prostate-Specific Membrane Antigen
SDS	Sodium dodecyl sulphate
SPECT	Single Photon Emission Computed Tomography
TACN	1,4,7-Triazacyclononane
t-Bu	tert butyl
TCEP	tris(2-carboxyethyl)phosphine
TFA	Trifluoroacetic acid
TSTU	N, N, N',N'-Tetramethyl-O-(N-succinimidyl)uranium tetrafluoroborate

Chapter I. Introduction

I-1 Preface

Cancer is one the deadliest maladies afflicting mankind amounting to 1 in 6 of all global death totalling to about 8.8 million deaths in 2015, as estimated by WHO. Cancer is the second leading cause of death globally, and the number of new cases is expected to rise by about 70% over the next 2 decades. Approximately 70% of deaths from cancer occur in low and middle-income countries. The financial burden of cancer management has been tremendous, with the estimated total annual economic cost of cancer in 2010 to be around US\$ 1.16 trillion (www.who.int). A significant quantum of resources has been invested to address this medical need at the academic as well as industry level that has led to improvements in our understanding of the disease.

However, this comprehension of the cancer biology has not been proportionately translated into corresponding improvements in cancer care. One of the important reasons that precluded this is the lack of selective delivery of anti-cancer compounds to cancerous tissue. Owing to lack of selectivity, a high systemic exposure to anti-cancer agents more often leads to a dose-limiting toxicity. As a result, many efforts are being directed towards selectively delivering the toxic payloads to cancer, making targeted delivery an important approach in overcoming the current limitations of cancer therapy. Recent developments in immunology, gene/cell therapy and nanotechnology are expected to significantly improve the therapy and diagnosis of cancer, thereby increasing efficacy with which the disease is being treated currently.

Nanotechnology has been one of the major breakthroughs in research that has found its value in life sciences amongst several other applications and cancer is no exception to this. Several nanotechnology driven approaches have borne fruits as evident from the growing list of the nanomedicines approved by health authorities across the globe. In 2011, the European Commission published a recommendation on the definition of nanomaterial predisposing size as the critical factor (1-100 nm) with the acknowledgment that the upper limit of 100nm not justified across whole range of nanomaterials. Several research programs have been funded by European Union (EU) focussing on leveraging the science at nanoscale and ARGENT has been one of them. The FP7 European Multi-ITN (Marie Curie Actions Initial Training Network) project “Advanced Radiotherapy, Generated by Exploiting Nanoprocesses and Technologies (ITN ARGENT)” started in March 2014. The prime objective of this inter-sectorial and multidisciplinary ITN is to create a new generation of researchers and experts able to develop and propose to the society new tools and concepts for the improvement of cancer therapy and diagnosis.

I-1.1 Overview of ARGENT project:

50% of the patients receive radiotherapy as part of their cancer treatment. The main limitation of this treatment is the lack of tumor selectivity, which causes severe side effects, and radioresistance. The most promising developments to improve the performances of radiation-based therapies is the use of fast ion beam radiation (carbon therapy and proton therapy) and nanoparticles-enhanced therapies. ARGENT brings together world-leading researchers of different disciplines, physicists and medical physicists, chemists, biologists, medical doctors and SMEs with the aim of understanding and exploiting the nanoscale processes that drive these phenomena (<http://itn-argent.eu/>). This European effort should lead to the development and optimization of new nanodrugs together with advanced radiation protocols. This will open a new era for radiotherapy with subsequent economic and ‘quality of life’ benefits for the EU population. In order for Europe to fully exploit its world-lead, a new generation of supra-disciplinary researchers familiar with following domains must work in an orchestrated manner: i) Physics and medical physics: explaining the physical interactions of radiation; ii) Chemistry: describing the chemical processes and methodologies for tailoring nano-agents; iii) Biology: elucidating the effects in vitro and in vivo.



Figure I-1: The partners within the ARGENT consortium spearheading the collaborative interdisciplinary research on cancer.

This project is strongly supported by the medical community. As an end point, this inter-sectoral and multi-disciplinary programme will form young researchers and experts able to

create a platform on which next generation cancer therapy will be built. The consortium aims to train a cohort of 13 PhDs (Early Stage Researchers – ESRs) to subsequently act as leaders and ambassadors in the field. The ITN ARGENT strategy relies on i) improving our understanding of the processes and mechanisms underlying radiation damage on a nanoscopic level, ii) applying the improved know-how in the production and development of functionalised nanodrugs to amplify the effects of medical beams and iii) developing of concepts and codes for clinical applications, taking into account the new information.

The ITN-ARGENT consortium is represented by 6 academic, 3 industrial and 6 associated partners that complement and leverage the competencies and expertise developed since their establishment (Figure I-1). The ARGENT research program is based on three work packages; nanodosimetry, theranostic nanoagents and preclinical evaluation. Each work package is with group of ESRs based on their respective projects and scientific/technical competencies.

The Preclinical Evaluation team combines their efforts to understand better how nanoscale processes initiated by the interaction of radiation with living matter affects biological responses, establishing a link between nanoscale interaction and clinical effects. Combining advanced experimental, theoretical, and modelling tools, the team investigates nanoscale interactions for preclinical testing in cell-based models and exploring their clinical applicability. The major goal of this team in ARGENT is to evaluate the use of the new methods and tools developed in the project for better patient outcome. The scientific work package on theranostic nanoagents is comprised of experimentalists from chemistry, biology, and medical physics. The goal of this work package is to design, synthesize, and characterize the next generation of technologies as radiosensitizers and diagnostic tools. The group also studies their fate inside the cellular environment and the cell damage caused by the combination of nanoparticles and different radiation beams. The Nanodosimetry team combines experiments and simulations to answer the most fundamental questions regarding the mechanisms present in radiation induced damage in cells. They study the interactions between biomolecules, nanoagents, and ion and photon radiation with both experiment and simulation. Being a part of the ARGENT team as one of the ESRs gave me an opportunity to perform my doctoral research at Chematech, one of the industrial partners in the consortium along with its affiliate Institute of Molecular Chemistry (UMR CNRS 6302), Université de Bourgogne-Franche Comté, Dijon.

Chematech is one the leading European research based enterprise developing chemical tools based on chelation chemistry. These chemistries find applications in antibody conjugation, nanoparticle development and other technologies useful in therapy and diagnosis of diseases. Chematech is led by its CEO, Dr. Frédéric Boschetti and represents one of the pillars of the

ARGENT team owing to its unique capability in the development of the macrocyclic compounds used in imaging and nuclear medicine. This is further strengthened by the scientific and advisory support received from Institute of Molecular Chemistry, Université de Bourgogne-Franche Comté, Dijon which is spearheaded by Prof. Franck Denat. Apparently, this thesis has received the unique mentorship of both Dr. Boschetti and Prof. Denat who are experts in the field of macrocyclic and conjugation chemistry from industry and academia. In the context of the aforementioned objectives, the work package designated towards ‘Nanoagents for cancer theranosis’ forms the important aspect of the current thesis and steers in the direction that aims to develop novel tools for cancer theranosis.

I-2 Cancer theranosis: Approaches and avenues

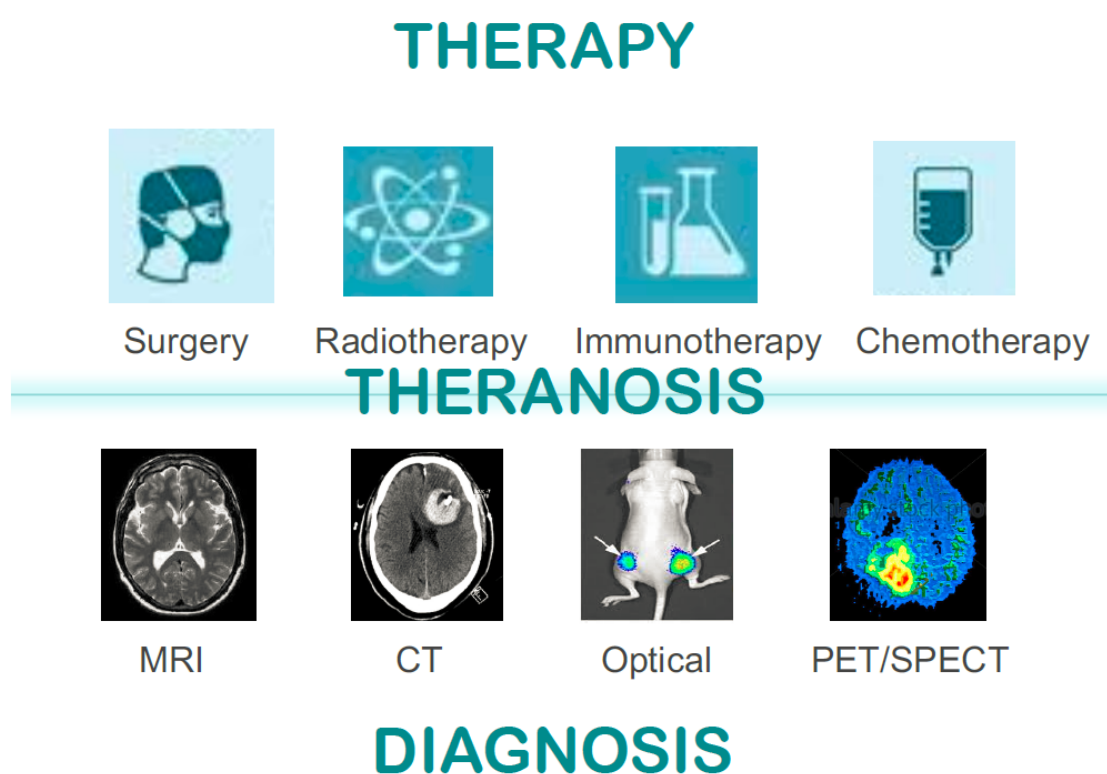


Figure I-2: Key drivers of cancer therapy, diagnosis and theranosis.

The term “theranostics” signifies any material that permits the combined diagnosis and treatment along with the potential to follow up of a disease and has been coined by the US consultant John Funkhouser, in August 1998 [1]. Theranostics implies the development of the two modalities in an integrated manner that serves the function of a diagnostic test and a therapeutic agent in an interdependent and concerted manner so as to cater towards comprehensive care of a specific disease. The ultimate aim of developing a theranostic is to simultaneously image and monitor the diseased tissue, drug pharmacokinetics, and pharmacodynamics with the long-term objective of fine tuning the therapy and dose with a control unattainable hitherto.

I-2.1 Cancer therapy:

As implied in the Figure I-2, the cancer therapy relies on four major treatment modalities namely; surgery, radiotherapy, chemotherapy and immunotherapy. These approaches could be used as standalone or in combination with each other depending on the tumor type and its stage. Majority of the benign cancers can be treated by surgical resection, whereas the malignant ones need a concomitant approach. Radiotherapy involves exposing the tumor lesions to high energy ionising radiations (e.g: X-rays) as an external beam radiotherapy. On the other hand, ‘brachytherapy’ or internal radiation therapy involves locally exposing the cancerous tissue to radiation by implanting the seeds of radioactive substance at the affected site. Alternatively, the radiotherapy can also be provided by delivering the sequestered radioisotope (e.g: ^{177}Lu , ^{90}Y) at the cancerous lesions in conjunction with a targeting ligand. This typically involves conjugating the chelator molecule to the targeting ligand that targets specific receptors on the cancer cells. The chelator molecule serves the purpose of sequestering the radioisotope which otherwise would be difficult to target. The ligand can be a peptide as in the case of recently (January 2018) FDA approved Lutathera®(Lutetium dotatate) which is referred to as Peptide Receptor Radionuclide Therapy (PRRT) or it can be a monoclonal antibody where it is referred to as ‘Radioimmunotherapy’. Zevalin®(^{90}Y ibritumomab tiuxetan) and Bexxar ®(^{131}I - tositumomab) are the approved products in this category (www.fda.gov). Chemotherapy represents one of the most traditional approaches in the cancer therapy that involves administration of a chemotherapeutic (synthetic or semi-synthetic drugs) to the cancer patients. These drugs are cytotoxic as they usually interfere with the key metabolic processes that are important for the cell survival or cell growth. Since the action of the cytotoxic drugs is not selective to cancer cells they also affect the normal healthy cells resulting in serious side effects. Many research efforts are being directed to address this issue by modifying the existing drugs or developing the new drugs that are more selective to cancerous cells. Much of the nanoparticle based research focussing on drug delivery encompasses the delivery of such anti-cancer drugs so as to target them only to the tumor site minimising the deleterious effects on the healthy tissue [2]. Immunotherapy represents the most recent and advanced therapeutic modalities for cancer therapy based on sound understanding of the molecular immune mechanisms underlying the pathophysiology. Monoclonal antibodies (mAbs) form the mainstay of the immunotherapy and were first produced by Milstein and Köhler (Cambridge University), who were awarded the Nobel Prize in Physiology or Medicine in 1984. mAbs possesses exquisite specificity owing to their greater surface area binding, which results in decreased ‘off-target’ effects/toxic effects as

compared with most small molecule drugs. With the advancement and the synergy of immunology, molecular biology and protein engineering, it has been possible to develop engineered proteins including monoclonal antibodies that are highly efficacious, stable and cater to different types of diseases/cancers. Various mechanisms have been thought to play roles in mediating the tumoricidal effects of mAb. These include signalling promoted by cross-linking of surface antigen that leads to cell death, blockade of an activation signal that is essential for continued cell growth, antibody-dependent cellular cytotoxicity (ADCC), complement mediated cytotoxicity (CMC) and the ability of mAb to alter the cytokine milieu or augment development of an active anti-tumor immune response. Of the various monoclonal antibodies approved for diverse disease categories 27 have been only approved for cancer highlighting the importance these magic bullets in cancer therapy [3, 4]. Bolstering the concept of the magic bullets, monoclonal antibodies have also been utilized as a cancer targeting cargo to deliver the highly potent cytotoxic molecules giving rise to new class of drugs; antibody drug conjugates referred to as ADCs. With only four approved ADCs currently in market, this is a very recent addition to the armamentarium against cancer, yet with lot of promise as witnessed by the prolific pipeline (> 50) that is at moment under clinical investigation (www.adcreview.com).

I-2.1.1 Nanoparticles in cancer therapy:

One of the hallmarks of the cancerous lesion is its altered physiological and anatomical state that makes it more vulnerable to the action of nanoparticles by virtue of an effect termed as 'Enhanced Permeability and Retention effect'. The EPR effect is a combined result of complex biological processes viz; angiogenesis, vascular permeability, lymph-angiogenesis, heterogeneous tumor genetic profile and microenvironment and poor lymphatic clearance. Any macromolecular system including nanoparticle that is injected into the biological subject, has propensity to get lodged in the milieu of the cancerous tissue owing to its leaky vasculature and poor lymphatic drainage. This enables the dislodged cargo to exert its action locally at the site endogenously (drug release from nanoparticle) or under the influence of an external stimuli (radiosensitization by nanoparticles upon radiation). Many approaches based on the macromolecular/nanoparticulate delivery have been developed for the cancer therapy and diagnosis as exemplified in the Figure I-3. Categorically, they have been classified as lipid based carriers, polymeric carriers, inorganic nanoparticles, conjugates and viral nanoparticles.

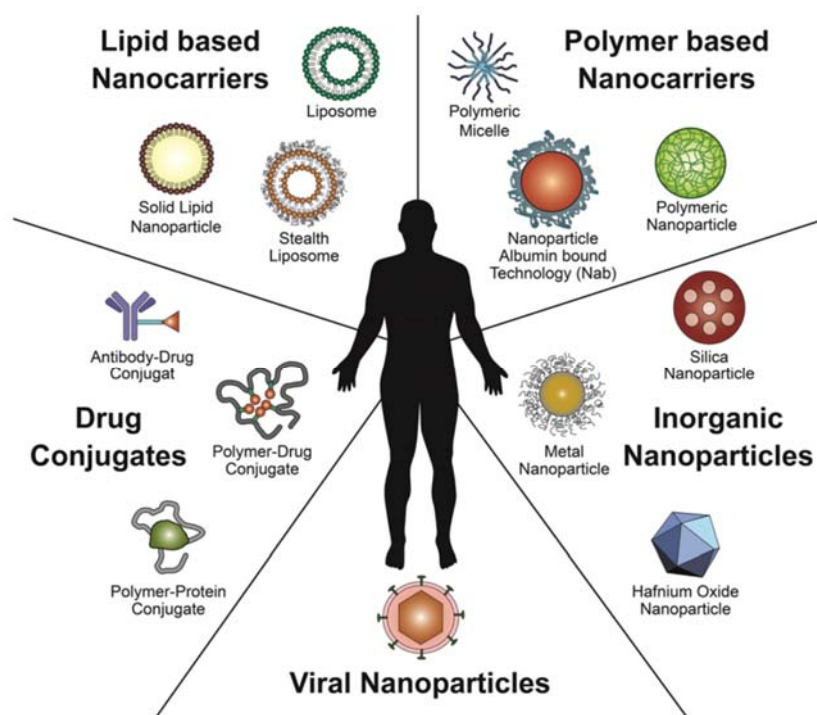


Figure I-3: Schematic illustration of different nanotherapeutic platforms. Adapted from [5]. Lipid nanocarriers include liposomes, solid lipid nanoparticles, SMEDDS etc. that are made from fatty acid derivatives. Several liposomal formulations like Doxil, Myocet, Mepact, Marqibo, DaunoXome etc. have been approved in US/EU/Asia for cancer therapy. Polymeric nanoparticles are composed of the matrix based nanoparticles fabricated using chemically synthesized polymers (e.g: PLGA), polymeric micelles which are made up of amphiphilic copolymers (e.g: Polycaprolactone-polyglutamic acid) and polymer encapsulated/coated systems (e.g: Abraxane – Albumin bound paclitaxel nanoparticles). Conjugates include more often covalently conjugated polymer drug systems or antibody drug conjugates which have been one of the hot topics in the targeted drug delivery with the clinical pipeline abuzz with several lead candidates. Virus like particles (VLP) are viruses devoid of genetic materials making them non-infectious. VLP are made up of the viral surface proteins/capsids that can house drug/tracer/gene/protein which acts as a cargo and can be useful in therapeutic, imaging and vaccine applications. Inorganic nanoparticles typically encompass silica nanoparticles, gold nanoparticles, iron oxide nanoparticles and other metallic nanoparticles (e.g: quantum dots etc). Inorganic nanoparticles are usually non-biodegradable and can pose toxicity issues and hence need a due consideration with respect to their physico-chemical characteristics so as to address any potential biocompatibility/bio persistence issues. Nonetheless, despite these challenges several inorganic nanoparticles have made it to clinic (ferumoxtran, ferucarbotran etc.) and many are on their way to do so (e.g: AGuIX – Phase I and Hafnium oxide NPs – Phase I/II) as can be seen from the clinical trial database (www.clinicaltrials.gov).

I-2.1.1.1 What is the difference between passive and active targeting of nanoparticles?

By virtue of the anatomic and physiological peculiarities of the cancerous lesions, the nanotechnology based research has been able to drive the results in its strides and is one of the main reasons that justify the application of nanomedicines in oncology compared to other disease areas. Passive targeting of the nanoparticles harnesses the EPR effect and involves use of the nanoparticles without any specific surface chemistry manipulations but within a certain size range. Active targeting involves modification of the nanoparticle surface with the ligands that have higher affinity to the receptors expressed mainly on the surface of the cancerous cells.

Although the approved nanomedicines justify the promise offered by the nanoparticles, there are multitude of factors that pathophysiologically differentiate patients from each other depending on the tumor type and its extent. Moreover, the distribution and accumulation of NPs in tumors could be highly variable and is likely influenced by the biological and physicochemical properties of each material. As a result of this, an EPR effect alone might not be effective in eliciting the adequate response giving rise to molecularly specific approaches in the context of personalized medicine. Active targeting of the nanoparticles with small molecule ligands/peptides/antibody or its fragments that target the specific receptors on the cancer cells presents one such avenue to bolster the performance of nanoparticles [6].

I-2.1.2 Nanoparticles in radiotherapy:

The line of treatment for the cancer has improved in recent years owing to development of the drugs with targeted mechanism of actions. However, the elements associated with diet, environment, lifestyle and the ageing population still increase the likelihood of cancer incidence. Amongst the population benefitted by the increase in the survival post treatment, it has been observed that 49% are cured by surgery, 40% by radiotherapy alone or combined with other modalities, and 11% by chemotherapy alone or combined with other modalities. Radiotherapy represents a very cost-effective component (5% of total) of cancer care particularly for palliation and symptom control in patients with advanced-stage or recurrent cancer [7].

Radiotherapy has witnessed significant advances resulting in sophisticated modalities such as image-guided radiotherapy, stereotactic radiotherapy, intensity-modulated radio-therapy, and proton therapy. These techniques have enabled the application of the higher doses to cancerous tissue with higher accuracy and precision whilst sparing or minimising the radiation exposure to the surrounding healthy tissue making radiation therapy more effective. Recently, the nanoparticles based on heavy atoms ($Z > 50$) have shown the promise in improving the radiotherapeutic outcomes by acting as radiosensitizers. Continued research in

this field; understanding the biological matter and radiation interactions, developing new chemistries for nanoparticles and preclinical and clinical studies of the promising nanoparticulate candidates is helping understand their potential to address and explore this avenue.

I-2.1.2.1 How do nanoparticles enhance the radiotherapy?

Upon exposure to the ionising radiations, elements with high atomic number like; gadolinium (Gd, $Z = 64$), gold (Au, $Z = 79$), iodine (I, $Z = 53$) and platinum (Pt, $Z = 78$), exhibit elevated photoelectric absorption of IR energy in comparison to surrounding soft tissue eliciting a radiosensitizing effect. The effect of ionizing radiations on biological systems can be broadly classified into physical, chemical, and biological phases. The phase in which high energy particles (photons, electrons, protons, or heavy ions) travel through their biological medium and bring about ionization and/or excitation of the molecules is referred to as physical phase, which leads to breakage of chemical bonds and generation of free radicals [8].

The physical phase is followed by the chemical phase that entails; scavenging and fixation reactions involving highly reactive free radicals that interact rapidly with molecules. Scavenging indicates the inactivation of free radicals by reducing agents such as thiol containing molecules (e.g: glutathione), whereas fixation causes an irreparable damage to biological components by molecules with high electron affinity, such as oxygen. Damage to the key components of the cellular machinery causes impairment of the cell function [9].

In the context of radiobiology, the biological (molecular, cellular and tissue) phase/effect is exhibited as the 5 Rs: repair, reoxygenation, redistribution, repopulation, and intrinsic radiosensitivity. Radiosensitizers enhance the effects of radiotherapy via multiple mechanisms through a cascade of events entailing three phases that ultimately results in the amplification of damage caused to the targeted tissue [10].

The inorganic nanoparticles have a key role in augmenting the radiation therapy as most of these nanoparticles are composed of the elements with high atomic mass number making them ideal for radiosensitizing applications. Within the purview of the ARGENT program, gadolinium based silica nanoparticles and gold nanoparticles have been identified as key theranostics considering several years of research experience of consortium members dedicated to the development of these systems.

Gold nanoparticles represent one of the widely researched inorganic nanoparticles for their radiosensitizing potential. The chelate functionalized gold nanoparticles is one of the main areas of research within the frame of collaboration between Chematech and ICMUB, Université de Bourgogne-Franche Comté (from Dijon) and UTINAM, Université de Bourgogne-Franche Comté (Besançon). The group in Besançon is led by Prof. Stephane Roux

who has been spearheading the activities relevant to development of these nanoparticles since last few years. The nanoparticles developed by the team of Prof. Roux have also been extensively studied by researchers within the consortium of ARGENT.

AGuIX nanoparticles are a novel class of Gadolinium based nanoparticles that have shown promise as radiotherapeutic sensitizers and MR contrast agents. With the proof of concept demonstrated at the pre-clinical stages, these nanoparticles are under clinical development (Phase I) for indications relevant to brain metastases. These nanoparticles are being developed under the concerted efforts of Nano-H and Theraguix (co-founded by Prof. Olivier Tillement) along with other academic partners.

These nanoparticles will be exploited in this thesis by developing advanced synthetic ligands that will be used as building blocks for the fabrication of the next generation of multifunctional nanoparticles.

I-2.2 Cancer Diagnosis:

Cancer diagnosis forms one of the integral part of the cancer management even before the commencement of the therapy. It entails understanding the spatial and temporal distribution of the cancer lesions and also involves identifying the molecular signatures associated with cancer form. Imaging plays a crucial role in cancer diagnosis with different modalities offering different levels of information and can be broadly categorized as nuclear and non-nuclear; nuclear imaging typically involves use of a radioisotope/ionising radiation whereas a non-nuclear imaging involves use of electromagnetic radiation or energy forms least likely to cause any radiation induced damage (Figure I-4 and

Table I-1). Although, diagnosis based on imaging is crucial in terms of the body level assessment of the malignancy, this has to be supported by the histopathological and immunochemical examination of the cancerous tissue to identify and get molecular insights into nature of the cancerous lesions. This can also help and subsequently refine the selection of the tracer and imaging tools to keep track on the disease prognosis.

I-2.2.1 Imaging in cancer diagnosis:

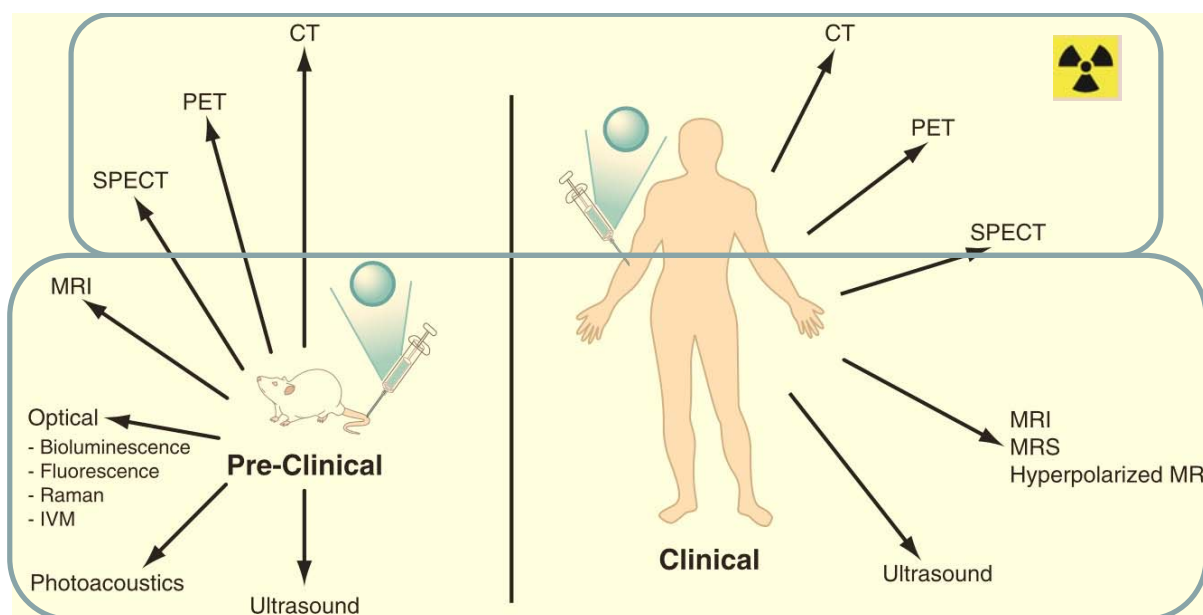


Figure I-4: Key nuclear and non-nuclear molecular imaging tools used in pre-clinical and clinical set ups. Adapted from [11].

I-2.2.1.1 PET and SPECT imaging:

PET and SPECT are nuclear/radioactivity based molecular imaging tools that can ascertain the biochemical changes and extent of molecular targets with a seamless depth of penetration and high sensitivity. Imaging of the molecular target using PET/SPECT entails identification and synthesis of a radiolabelled imaging agent that is specific and selective for the target of

interest.

Table I-1: Molecular imaging tools and their features. Adapted from [12].

Imaging Technique	Source of energy	Spatial Resolution (mm)		Acquisition Time (time units)	Amount of tracer (ng)	Detection Sensitivity (mol/L)	Depth of penetration (mm)	Safety Profile
		Animal	Clinical					
SPECT	Gamma rays	5-12	1-4	min-h	1-1000	10^{-10} - 10^{-11}	limitless	Ionising Radiation
PET	Photon annihilation	3-8	1-3	min-h	1-100	10^{-11} - 10^{-12}	limitless	Ionising Radiation
MRI	Radiofrequency	0.01-0.1	0.5-1.5	min-h	10^3 - 10^6	10^{-5} - 10^{-6}	limitless	Non-Ionising Radiation
CT	X-rays	50 μ m	1-2mm	min	-	10^{-3}	limitless	Ionising Radiation
Optical	Visible to infrared waves	1-5	<5	s-min	10^3 - 10^6	10^{-9} - 10^{-12}	1-20	Non-Ionising Radiation, safety linked probe dose

The small quantity of this radiolabelled agent in the magnitude of nanomolar quantities is administered intravenously to the subject following which, the radioactivity is then traced through the body and its distribution determined from scans obtained with a PET/SPECT camera or detector.

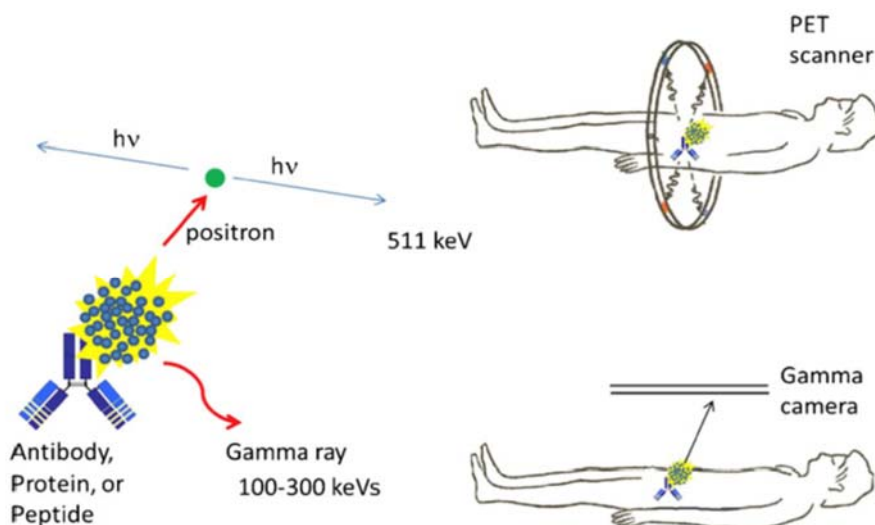


Figure I-5: Scheme illustrating the principles imaging based on PET and SPECT[13].

In SPECT imaging, the radioisotope emits γ -rays that is detected by a 360° rotating gamma camera consisting of photon detector array. The detection of gamma rays enables reconstruction of an image that identifies the location of the radioisotopes which in turns helps in diagnosis. On the other hand, PET is based on positron emission decay, where the injected radioisotope emits a positron that traverses through the tissue ($\sim <2$ mm) and gets decelerated by loss of its kinetic energy till it ensues collision with an electron. The emission

of a positron and its annihilation with electron results in an emission of two 511 keV photons at 180° to each other; these photons are detected as a coincident event, making it possible to localize more precisely their source and reconstruct an image (Figure I-5).

I-2.2.1.2 Radioisotopes used in nuclear medicine:

Radioactive isotopes have been widely used in diagnosis as well as for therapy in oncology in addition to their use in drug development research. These isotopes can be used after integration into a pertinent chemical structure (e.g: ¹⁸F, ¹¹C) or they can be sequestered/chelated using chelators (ligands) to have them in a form that is stable under physiological conditions. A vast number of radiometals are being routinely produced, with a broad variety of half-lives and emission profiles. A wide range of radioisotopes at disposal makes it feasible to select specific nuclear properties that are necessary for requisite applications. Table I-2 summarizes the list of the radioisotopes with their properties and applications that are currently in use in nuclear medicine and research.

Table I-2: Different radioisotopes used in imaging and therapy [14, 15].

Radioisotopes	Atomic Number	Half-Life	Decay Mode (%)	Production	Application
¹¹ C	6	20.4 min	β ⁺ (100)	Cyclotron	PET Imaging
¹³ N	7	9.96 min	β ⁺ (100)	Cyclotron	PET Imaging
¹⁵ O	8	2.03 min	β ⁺ (100)	Cyclotron	PET Imaging
¹⁸ F	9	109.8 min	β ⁺ (97)	Cyclotron	PET Imaging
⁶² Cu	29	9.76min	β ⁺ (100), EC (3)	Cyclotron	PET Imaging
⁶⁴ Cu	29	12.8 h	β ⁺ or β ⁻ , EC	Cyclotron	PET Imaging
⁶⁷ Ga	31	3.3 days	EC (100)	Cyclotron	SPECT Imaging
⁶⁸ Ga	31	68 min	β ⁺ (89), EC (11)	Generator	PET Imaging
⁸² Rb	37	1.25 min	β ⁺ (95), EC (5)	Generator	PET Imaging
^{94m} Tc	43	52 min	β ⁺ (72), EC (28)	Cyclotron	PET Imaging
^{99m} Tc	43	6 hr	IT (100)	Generator	SPECT Imaging
¹¹¹ In	49	2.8 days	EC (100)	Cyclotron	SPECT Imaging
¹²³ I	53	13.2 hr	EC (100)	Cyclotron	PET Imaging
¹²⁴ I	53	4.2 days	β ⁺ (23), EC (77)	Cyclotron	PET Imaging
¹²⁵ I	53	60 days	EC (100)	Reactor	SPECT Imaging, Brachytherapy
⁴⁴ Sc	21	3.9 hr	β ⁺ (94), EC (6)	Generator	PET Imaging
⁴⁷ Sc	21	80.2 hr	β ⁻ (100)	Generator	Radiotherapy
⁹⁰ Y	39	64.1 hr	β ⁻ (100)	⁹⁰ Zr (n, p) ⁹⁰ Y	Radiotherapy
⁸⁹ Zr	40	78.5 hr	β ⁺ (23), EC (77)	Cyclotron	PET Imaging
¹⁷⁷ Lu	71	159.4 hr	β ⁻ (100)	¹⁷⁶ Lu(n,γ) ¹⁷⁷ Lu	Radiotherapy

*EC- Electron Capture; IT-Isomeric Transition.

I-2.2.1.3 Magnetic Resonance Imaging:

MRI is a widely used imaging modality that is analogous to nuclear magnetic resonance (NMR) in principle and allows imaging of atomic nuclei within the body. MRI involves using

high power magnet and radiofrequency (RF) energy so as to visualize the internal structure and soft tissue morphology of the body.

MRI involves use of a strong magnetic field that aligns the magnetic moments of protons in a sample producing an equilibrium magnetization along the z-axis (M_z) with a magnitude of M_0 . When a radio frequency (RF) pulse is applied to the sample, at a resonance frequency capable of transferring energy to protons, magnetic moments of the protons rotate away from the z-axis by an angle called the flip angle. The flip angle depends on the imaging sequence applied, but it is generally the transverse plane (xy-plane), resulting in a net magnetization of M_{xy} . When the RF is removed, the magnetic moments of the protons relax to equilibrium. The time needed for the magnetic moments to relax to its equilibrium state is termed as the relaxation time and is dependent on the tissue under investigation [16, 17]. By varying the parameters of the pulse sequence, different contrasts may be generated between tissues based on the relaxation properties of the hydrogen atoms therein. In principle, MRI is based on the study of Nuclear Magnetic Resonance (NMR) of protons (water) present in the tissues and the contrast of an MRI image depends in particular on the density of the water and the relaxation times of the proton spins, which vary according to the physiological properties of tissue/site [18, 19].

The contrast in soft tissue with MRI arises due to differences in the proton density, spin-lattice or longitudinal relaxation time (T_1) and spin-spin or transverse relaxation time (T_2) of the protons. T_1 is the time constant of the exponential recovery process of M_0 along the z-axis after an RF pulse. Protons that relax quickly (short T_1) are able to recover full magnetization along the z-axis and can produce high signal intensities. For protons that relax more slowly (long T_1), full magnetization is not recovered before subsequent RF pulses, as a result they produce less signal and result in saturation effect. T_1 weighted images illustrate anatomical information and are envisaged when a clear image of the structure is necessary. On the other hand, T_2 is the time constant of the exponential decay of the transverse magnetization (M_{xy}) after an RF pulse. T_2 reflects the amount of time taken by the magnetic moments of protons to become randomly aligned in the xy-plane after an RF pulse, resulting in a net magnetic moment of zero in the xy-plane. T_2 weighted images are generated by eliminating the dephasing effects caused by extrinsic magnetic field inhomogeneities and taking into account only the molecular interactions. Thus, T_2 weighted images can generate good pathological information wherein accumulation of the abnormal fluid appears bright against the normal tissue background [16, 20].

Although, water in the biological milieu acts as an endogenous contrast for the MRI the intrinsic variations of T_1 and T_2 are small. As a result, it has become obvious that in many

clinical situations an exogenous contrast agent is administered which can greatly improve the diagnostic value of MR, just as the case for X-ray and CT [21]. Ideally, a MR contrast agent must induce a strong local effect on the T1 or T2 relaxation times of water, have suitable pharmacokinetic properties and be nontoxic at the administered doses. One of the common approaches to altering the relaxivity of water is to introduce a high spin paramagnetic metal such as Fe or Gd into its vicinity. Water molecules bound to the high-spin metals relax in orders of magnitude faster than free water, leading to a dramatic change in T1 that can be observed by MR. As the paramagnetic ions cannot be administered directly, owing to their inherent toxicity resulting from the interference of the physiological process, it is imperative to administer these ions in a form that is innocuous to cellular machinery. This can be typically achieved by sequestering the metal using an organic chelate or administering the metal in non-ionisable atomic form [22, 23].

At present, there are two main classes of MRI contrast agents: the first is gadolinium-containing small molecule complexes (with chelate) and the second is superparamagnetic iron oxide nanoparticles (SPIONs). Whereas, gadolinium shortens the T1 relaxation time of protons inside tissues, the iron present in SPIONs possesses a large magnetic moment that reduces the MRI signal intensities resulting in a negative contrast enhancement in T2 weighted images. In the context of the targeted MRI agents, the nanoparticles based on gadolinium and iron oxide have been widely studied and reported [23, 24].

MRI has a number of important advantages compared with other imaging modalities including 1) no need for ionizing radiation. 2) unlimited depth of penetration. 3) high spatial resolution (

Table I-1).4) concurrent collection of physiological or metabolic data with high-resolution anatomical images. 5) High soft tissue contrast superior to that attainable with CT.6) molecular information/imaging when used in conjunction with targeted MRI compatible imaging agents; and 7) Excellent clinical utility and value. Although MRI is an extremely useful imaging technique, it suffers from few drawbacks like; poor sensitivity compared to other imaging modalities, high cost and use of contrast agents (potential dose limiting toxicity concerns). Nonetheless, the high spatial resolution of MRI has hugely benefitted medical diagnostics and basic research [11].

I-2.2.1.4 Optical imaging:

Optical imaging is advantageous compared to radiological imaging as it is rapid, inexpensive and sensitive. Optical imaging obviates the need for exposure to harmful radiation by employing non-ionizing radiation like visible, ultraviolet, and/or infrared light. This electromagnetic radiation spectrum generates images by exciting electrons which upon

relaxation to ground state release energy that is transduced into signals revealing the information associated with the tissue, cell or organelles in the form of an image. Unlike the whole-body imaging techniques such as MRI and PET, optical imaging can offer real-time images with high resolution. As, the subcellular processes can be captured by optical microscopy, optical imaging has been used to understand the behaviour of various nanomaterials at the cellular levels in living subjects [25]. Currently, numerous fluorescent dyes are being widely used as optical imaging probes (discussed in detail in following sections). However, in vivo optical imaging suffers from a major drawback of limited penetration depth in tissue and background signals caused by light scattering. As result, many efforts in advancing optical imaging techniques and probes are being made to maximize penetration depth and minimize background signals. Advanced techniques stemming from optical imaging include; Optical Coherence Tomography, Photoacoustic Imaging, and Raman Spectroscopy to list few. Employing NIR radiation and NIR based fluorophores have been proven to overcome the tissue auto-fluorescence. On the other hand, the photo-bleaching and the limited absorption coefficient of fluorescent dyes can be to certain extent overcome by developing nanoparticle-based optical probes [26].

I-2.2.2 Multimodal Imaging:

Despite development of various imaging techniques, no single imaging modality offers a comprehensive functional or anatomic information. Every technique has its own unique shortcomings on spatial or temporal resolution, depth of tissue penetration detection sensitivity and cost [27]. MRI and CT can provide high resolution images with detailed information of anatomy but lacks target sensitivity (mM to μ M range). In contrast, PET is high sensitivity imaging modality, but is limited by the range of positron in tissue, resulting in low spatial resolution (4–6 mm for human whole-body PET scanners, 1 mm in small animal imaging and preclinical PET scanners). This causes partial volume effects and the anatomic information offered is inconclusive [28]. On the other hand, optical imaging techniques suffer from low tissue penetration, despite the high detection sensitivity; while ultrasound offers good spatial resolution, but is limited by its poor penetration and sensitivity. Thus, the above nuclear and non-nuclear imaging techniques represent the strengths of molecular imaging each with their own share of advantages and disadvantages. Synergistic combination of the above modalities offers hope to overcome clinical diagnostic challenges by offering complementary and comprehensive information. Multimodality aims to combine the techniques that provide structural/anatomical information (MRI, CT or US) and the one that offers high sensitivity with functional or molecular information (PET, SPECT or optical). This has resulted in different dual modal technologies like PET/CT, PET/MRI, SPECT/MRI, and MRI/optical [27, 29]. Combination of PET or SPECT with optical imaging also holds potential as a technology that helps combine whole body imaging with image guided surgery giving rise to PET/optical and SPECT/optical imaging [30].

Although multimodality offers potential to improve diagnostic capabilities at clinic, it has several challenges at different levels. Hybrid imaging necessitates development of the multimodal scanners that present design and engineering complexities. This has to be supported by the image processing advancements to combine the results obtained from the two measurements without any loss/masking of the information [31]. Multimodal imaging also poses the significant challenge to chemists to develop the multimodal probes or contrast agents that can help maximise and refine the hybrid imaging outcomes. Administering a single agent that combines two modalities is a desirable feature in terms of the patient convenience and compliance. Emergence of the targeted or personalized therapy based on molecular signatures of the cancer has further added a new dimension to this area of hybrid imaging. Small molecule/peptide, antibody and nanoparticles based multimodal contrast agents play a very crucial role in multimodal imaging. Research outlined in this thesis aims to address this concern and contribute to the new strides taken in this direction.

I-2.2.2.1 Nanoparticles in multimodal imaging:

Although there are lot of preclinical studies reported in literature [32], very limited number of nanoparticles are used in the clinic [24]. Amongst the ones used in clinic, majority of them are for the cancer therapy as most of them cater to the drug delivery challenges of the anti-cancer drugs. Nanoparticles for imaging or theranosis is relatively a new concept and present challenges and opportunities different from the nanoparticles for drug delivery. As an unmet clinical need, the detection of early tumor development at primary and metastatic sites can be improved by use of nanoparticles owing to their potential of targeting accuracy to tumors. The design of imaging methodologies based on nanoprocesses and technologies that could detect tumors earlier would significantly improve patient outcomes. The properties of the nanoparticles that are desirable from the viewpoint of imaging are slightly different from those expected for drug delivery and this difference stems mainly from the pharmacokinetic requirements. A nanoparticle for imaging is expected to quickly reach the tumor environment and get cleared from the system as early as possible whereas the one for drug delivery needs to remain in the circulation for relatively longer time so as to deliver adequate dose at the site of cancerous lesion. As a result of this, nanoparticles in the size range of 5-10nm are generally favourable for imaging application. Size in this range also ensures that the nanoparticles are quickly cleared from the circulation mostly via renal clearance [33]. Other factors that can influence the biological behaviour of nanoparticles is the surface chemistry, surface potential/charge and particle shape. Nanoparticles present a versatile platform to combine different modalities in order to be used as bi/multimodal tracer in imaging and/or theranosis. Presence of the high specific surface area (surface area per unit weight or volume) enables appending of the high sensitivity probes to the nanoparticles surface whereas the bulk/core of the nanoparticles can possess the properties needed for other imaging tracers/therapy.

I-3 Monomolecular Multimodal Platform in cancer theranosis:

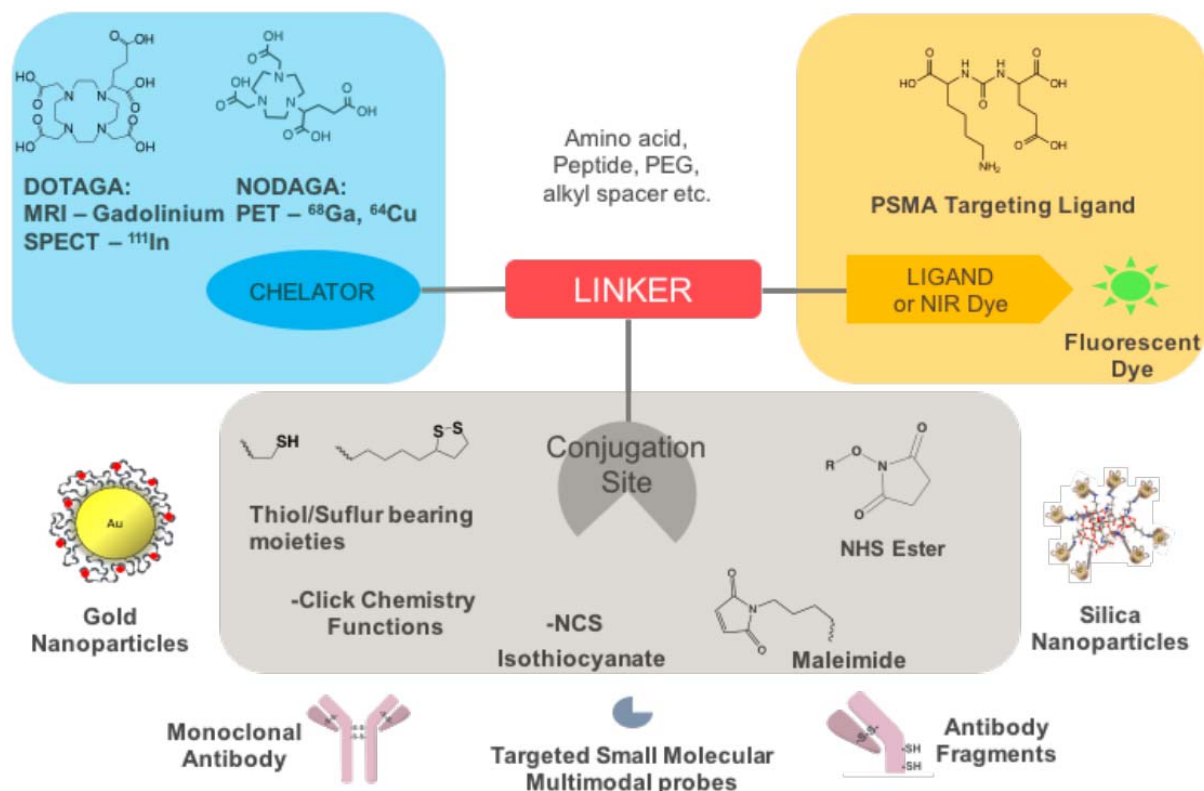


Figure I-6: Multimodal platform for the development of diverse theranostics.

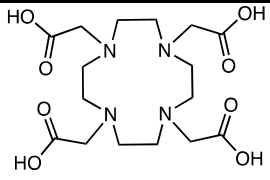


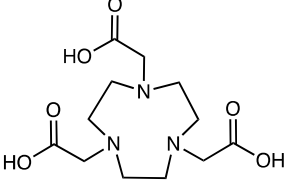


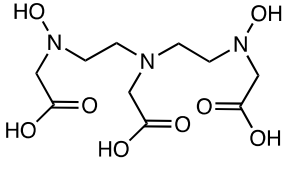


Broadly, imaging contrast agents include small molecules, peptides, proteins, and nanoparticles. Majority of the scans use small molecules based tracers that are below 2,000 kDa and measure approximately 1 nm (e.g: ^{18}F -FDG for PET, iodinated small molecules for CT, and chelated gadolinium for MRI). Peptide based imaging agents are gaining momentum owing to their specificity and ease of synthesis relative to larger proteins. This has led to the approval of such agents towards specific class of cancer (e.g: NETSPOTTM/ ^{68}Ga -DOTATATE for neuroendocrine tumors)(www.adacap.com). Protein imaging agents, such as radiolabelled monoclonal antibodies, are less common but offer precise molecular information and are a growing area of research. Nanoparticles offer an exciting class of imaging agents that can be used for both anatomic and molecular imaging. Developing a platform that caters to multiple such avenues forms the basis of the current thesis. Monomolecular multimodal platforms have been one of the thrust areas of research at Chematech and ICMUB. Monomolecular multimodal platform (MOMIP) aims to develop the systems (conjugates/nanoparticles) that are easy to develop and characterize and yet retain their multimodality. For instance, modification of an antibody for PET-Optical probe development using independent stepwise approach i.e conjugation first with PET probe and then optical probe appears very complex in terms of the developing optimal process of conjugation as well as the precise characterization of the probe conjugated in this manner.

Whereas, conjugation with MOMIP is one step process along with precise characterization of the resulting bioconjugate. This is furthermore important and valuable in development/functionalization of the nanoparticles where these systems are inherently complex to characterize. Thus, the purpose of this platform is to provide researchers and the clinicians, the tools that encompass diverse modalities in a single integrated system towards improved cancer/disease management. In this context, the current thesis aims to harness this approach in diverse possible manner and generate multimodal tools for cancer therapy. This platform can be applied for the development of the small molecule based multimodal imaging ligands or for the ligands that can be in turn used for nanoparticle synthesis or antibody bioconjugation that can have substantial theranostic value. Figure I-6 highlights this approach in a pictorial/infographic format representing the general and versatile nature of the multimodal platform that can be easily customized or adapted based on the product and the feasibility of the chemistry desired.

I-3.1 Chelators used in multimodal platforms:

The increasing number of radioisotopes in nuclear medicine has necessitated the corresponding increase in the development of the novel chelators to suit the requirement of the complex's stability in terms of thermodynamic stability and kinetic inertness. Each radiometal ion has different physical and chemical properties like; ligand donor atom preferences (e.g. N, O, S), size, oxidation state, coordination number and coordination geometry. As result of this, a correct choice of the chelator suiting the attributes of the chosen radioisotope has to be made so that the resulting complex exhibits optimal characteristics suitable for the *in vivo* stability. Broadly, the chelators have been classified as linear or acyclic and macrocyclic. In the context of this doctoral thesis, the key radiometals/metals that are of interest for theranostic applications include Gadolinium/Gd (for MRI and radiosensitization), Copper $64/^{64}\text{Cu}$ (for PET) and Indium-111/ ^{111}In (for SPECT). As a result, only those chelators useful for the complexation of above radiometals will be discussed. A detailed account of the chelators used in radiochemistry has been outlined in an excellent review by Price and Orvig [14].

Table I-3: Properties of the chelators used in this thesis for theranostic applications.

Chelator	Radiometal/ metal	Labelling/ radiolabelling conditions	logK _{ML}
 <p>DOTA (1,4,7,10-tetraazacyclododecane-1,4,7,10-tetraacetic acid)</p> <p>Coordination Number: maximum 8</p> <p>Donor Site: N₄O₄</p> <p>Bifunctional Derivative used in this thesis: DOTAGA</p>	⁶⁴ Cu ⁺²  ¹¹¹ In ⁺³ 	25–90°C, 30–60 min, pH 5.5–6.5 37–100°C, 15–60 min, pH 4.0–6.0 37–100°C, 15min– 6 h, pH 5.0–6.0	22.2, 22.7 23.9 (pM 17.8–18.8) 24.7
 <p>NOTA (1,4,7-triazacyclononane-1,4,7-triacetic acid)</p> <p>Coordination Number = 6</p> <p>Donor Site: N₃O₃</p> <p>Bifunctional Derivative used in this thesis: NODAGA</p>	⁶⁴ Cu ⁺²  ¹¹¹ In ⁺³ 	25 °C, 30–60 min, pH 5.5–6.5 60–95 °C, 20–30 min, pH 4.0–5.0	21.6 26.2 (pM 21.6)
 <p>DTPA, diethylenetriaminepentaacetic acid</p> <p>Coordination Number = 8</p> <p>Donor Site: N₃O₅</p> <p>Bifunctional Derivative: DTDTPA</p>	⁶⁴ Cu ⁺²  ¹¹¹ In ⁺³ 	40 °C, 60 min, pH 6.5 25 °C, 5–10 min, pH 4.5–5.5	21.4 29.0 (pM 24.9)

The table has been adapted from [14, 34, 35]. Green-Best match; Orange-moderate match; Red-poor match.

DTPA is one of the oldest and most widely used acyclic chelator in radiochemistry and can be radiolabelled with many radiometal ions at room temperature within few minutes. However, the complexes of DTPA suffer from potential stability issues in vivo and are not as stable as

the ones formed with macrocyclic chelators. As a result of this, there is a decrease in its use which is gradually being replaced by chelators like DOTA and NOTA derivatives [36].

Nonetheless, DTPA has been successfully used in the FDA approved SPECT agent OctreoScan™(¹¹¹In-DTPA-octreotide), a somatostatin-targeting peptide-conjugate used for imaging neuroendocrine tumors [37]. DTPA (Gd complexed) based contrast agents for MRI have been approved and marketed under different brand names (Table I-4). Also, the first-generation gold nanoparticles from our group were based on the bifunctional chelator (BFC); DTDTPA (thiolated DTDTPA) and are currently being upgraded to the advanced form by use of the BFC based on DOTA and NOTA.

Table I-4: Gadolinium based contrast agents marketed in US and Europe [34].

Chemical Name	Generic Name	Trade/Product Name
Acyclic Chelators		
Gd-DTPA	Gadopentetate Dimeglumine	Magnevist®
Gd-DTPA-BMA	Gadodiamide	Omniscan®
Gd-DTPA-BMEA	Gadoversetamide	Optimark®
Gd-BOPTA	Gadobenate Disodium	Multihance®
Gd-EOB-DTPA	Gadoxetate Disodium	Primovist®
MS-325	Gadofosveset Trisodium	Vasovist®
Macrocyclic Chelators		
Gd-DOTA	Gadoterate Meglumine	Dotarem®
Gd-HP-DO3A	Gadoteridol	Prohance®
Gd-DO3A-Butrol	Gadobutrol	Gadovist®

DOTA is the most versatile and widely used chelator and is of significant value for MRI as several marketed products are based on the gadolinium complex of the DOTA in its different forms as can be seen from the Table I-4. Due to relatively lower stability, the DTPA based contrast agents are more likely to release the Gd⁺³ in vivo. This can have implications in potential kidney toxicity that can result in Nephrogenic Systemic Fibrosis (NSF) and hence are being widely replaced by DOTA based complexes [38]. DOTA has been gold standard for some of the radioisotopes and forms stable complexes with ¹¹¹In, ¹⁷⁷Lu, ^{86/90}Y, ²²⁵Ac, and ^{44/47}Sc. Owing to the lack of geometric fit, DOTA does not form very stable complexes with PET isotopes like ⁶⁴Cu and ⁶⁸Ga, which can be addressed by deployment of NOTA. NOTA is a hexadentate N₃O₃chelator and has been successfully used as chelator of choice for ^{67/68}Ga and ⁶⁴Cu. NOTA is now considered to be the “gold standard” for ⁶⁴Cu⁺² and Ga³⁺ chelation, with facile and favourable radiolabelling conditions (RT, 30–60 minutes) and excellent in

vivo stability [39, 40].

Table I-1 summarizes the properties of the key chelators that are relevant to the research work described in this thesis.

I-3.1.1 Influence of the chelator on the properties and stability of the theranostics:

Selection of the correct combination of the chelator and metal is key to the successful development of theranostics. *In vivo* kinetic inertness of the metal–chelate complex is of utmost consideration in identifying the right match between the chelator and metal. Although, thermodynamic stability constants ($K_{ML} = [ML]/[M][L]$) can be a useful gauge for the initial level comparisons, but they do not necessarily predict the *in vivo* stability. Experiments like acid dissociation and competitive radiolabelling have been proposed but they are not representative and do not reflect the environment encountered at physiological conditions. Challenge studies can be performed by incubating the chelate-metal complex with ions like Na^+ , K^+ , Ca^{2+} , Mg^{2+} , Cu^{2+} or Fe^{3+} to identify the trans-chelation mediated instabilities. Alternatively, the complex can be subjected to EDTA challenge assays to mimic the potential endogenous chelators. Ultimately, the correct match can only be justified by performing the *in vitro* stability assessment in serum and performing *in vivo* studies focussing on biodistribution and pharmacokinetics.

Despite the stability and inertness with a given radiometal (e.g. NOTA vs. DOTA for ^{68}Ga), it may not be the optimal match for a certain application (e.g. a specific peptide vector). For instance, NOTA forms a more stable complex with ^{68}Ga than does DOTA, but owing to differences in charge and physical properties (e.g. neutral vs. charged complex), DOTA may provide superior *in vivo* properties with certain vectors [41]. This exemplifies the complex set of variables that need due consideration when constructing radiometal-based radiopharmaceuticals. Another interesting feature related to the influence of chelator, is that they can modulate the binding affinity of the peptide based radiopharmaceuticals. Findings by Maecke et al., claim that ‘The chelate makes difference’ in the context of peptide based imaging agents. It has been demonstrated that the combination of the chelate and metal can have a substantial effect on the binding affinity as well as the tumor localization in animal models [42].

In the view of the multimodality, it is necessary to use the right form of the bifunctional chelators so as to conjugate it to the multimodal assembly. This necessitates the use of the bifunctional chelator so that properties of the base chelators are unaffected. One of the strategies in offering the bifunctionality to the chelator (e.g: DOTA and NOTA) is to append a side arm containing two carboxylate groups on the macrocyclic ring. This can be done for instance, by employing the glutaric arm during the macrocycle synthesis so that the original

coordination sphere of the chelator remains intact yet offering a site for conjugation (e.g: DOTAGA and NODAGA) [42-44]. Thus, chelator remains an integral and important component in development of a multimodal theranostics.

I-3.2 Fluorescent probes for NIR based optical imaging:

Optical imaging based on NIR light for fluorescence possesses several merits in comparison to visible light. NIR range light does not cause any potential damage to the biological tissue unlike the ionising radiations. Majority of the biomolecules are transparent to NIR due to very low absorption coefficients. As a result, the auto-fluorescence signals arising from the background tissue are very low resulting in increased signal-to-noise ratio and high sensitivity of detection. Moreover, the NIR light can penetrate deeper in the tissue owing to reduced light scattering and the low absorption from the background [12]. Although many biological windows have been proposed for defining the diagnostic range of wavelength for NIR imaging the one comprising between 650 and 1450 nm holds and appears reasonable for most of the studies (Figure I-7) [45].

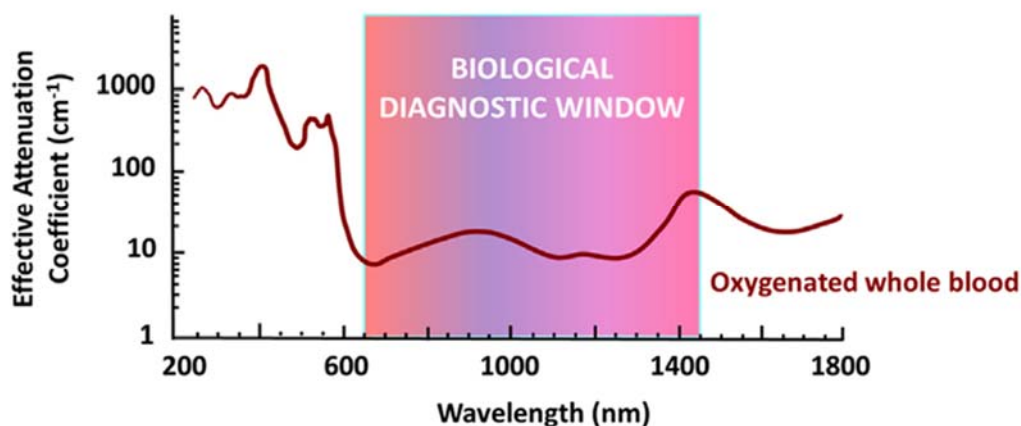


Figure I-7: Absorption spectrum of the oxygenated whole blood and the biological diagnostic window defined from 650–1450 nm. Adapted from [46].

An ideal fluorescent probe should cater to below requirements:

- Good photo stability,
- High quantum yields,
- High molar extinction coefficients,
- Large Stokes shifts (energy difference between maxima of absorption and emission spectra) to prevent the reabsorption effects,
- Chemical stability and adequate solubility in physiological media,
- Low toxicity and minimal tendency to aggregation.

NIR imaging can be realised by the probes with different physico-chemical characteristics and

can be broadly classified into four families; 1. Organic fluorophores, 2. Fluorescent proteins, 3. Quantum dots (QDs) 4. Lanthanide(III)-based complexes and nanomaterials [46]. The interest of the thesis lies in particularly using the organic fluorophores for the development of the multimodal platform. Organic fluorophores offer significant advantage over the counterparts owing to their customizable nature and possibility to integrate them with other systems to offer multimodality. Based on their widespread use in the biology, organic NIR-emitting probes, can be considered belonging to three general classes: BODIPYs, squaraines and cyanines.

BODIPY fluorescent probes belong to a family of probes based on borondipyrromethane characterized by high quantum yields and distinctively sharp absorption and emission spectra. Moreover, they possess very high photostability and chemical stability under physiological conditions. Some of the disadvantages that preclude their practical applications include low water solubility, small Stokes shifts and comparatively low molar extinction coefficients ($10^4 \text{ M}^{-1} \cdot \text{cm}^{-1}$). Furthermore, most of the BODIPY-based probes emit in the visible/deep red ranges making it difficult for their use in NIR based imaging [47].

Table I-5: Photophysical properties of the representative fluorophores. Adapted from [46, 48].

Fluorescent Probe	λ_{abs} (nm)	λ_{em} (nm)	ϵ ($10^5 \cdot \text{M}^{-1} \cdot \text{cm}^{-1}$)	Φ (%)
Cy5-NHS	646	662	2.5	20
Cy5.5-NHS	673	707	2.09	20
Cy7-NHS	750	773	1.99	30
Cy7.5-NHS	788	803	2.23	-
BODIPY NIR	557	723	-	3
ICG	785	807	-	0.3
IR820	818	867	-	4.2
IR783	777	812	1.3	2
IRDye [®] 800CW	774	789	2.4	-
KSQ-4	786	817	-	8

Squaraines are zwitterionic fluorophores bearing a oxocyclobutenolate core that is substituted with heterocyclic/aromatic groups located on the opposite ends of the molecule. Due to its peculiar structure, the photophysical properties of the squaraine dyes are very sensitive to the surrounding medium and hence can be explored for development of the responsive fluorescent probes. Squaraines have high molar extinction coefficients (in order of $10^5 \text{ M}^{-1} \cdot \text{cm}^{-1}$) in NIR regions with moderate quantum yields and photostability. Squaraines suffer

from drawbacks related to smaller Stokes shift and solubility. The vulnerability to the nucleophilic attack and the aggregation induced fluorescence quenching are the other factors that can limit their use [49].

Cyanine fluorophores are composed of two heteroaromatic rings that are linked together by a polymethine bridge (Figure I-8). The excitation and emission wavelengths of the probes are strongly influenced by the length of the polymethine bridge: the longer the bridge, the higher the values of absorption and emission wavelengths. These properties can also be tuned by extending the aromaticity as be seen based on change from Cy5 to Cy5.5 or from Cy7 to Cy7.5 (Figure I-8) [50]. Cyanine probes demonstrate large molar extinction coefficients, in the order of $10^5 \text{ M}^{-1}\text{cm}^{-1}$, and considerably high fluorescence quantum yields including in the NIR range with values up to 30% (Table I-5). The dyes that have been chosen for development of the multimodal platform include Cy5 and IR-783, which represent two distinct regions of the spectrum in terms of the absorption/emission properties. The current experience of our group in applying Cy5 in the development of antibody bioconjugatable probes has been considerable (unpublished data) and hence has been envisioned to be extended to ligands for multifunctional gold nanoparticles. Nevertheless, it is of crucial importance to select the correct form of the dye for development of the theranostics. Different properties of the fluorescent dyes like lipophilicity, solubility, polarity/charge, etc. can have profound influence on the affinity of the ligand towards its target or properties of the multimodal platform that contains it. As a result, a prior understanding of these variables during the development can be of considerable importance. Highlighting this feature, Bunschoten et al., performed systematic assessment of the influence of the chemical modifications of the fluorescent dye on integrin targeted bimodal probes. They developed a matrix-based scoring system to demonstrate a large influence of relatively small changes in the chemical design of fluorescent labels. This approach not only resulted in an optimized $\alpha_v\beta_3$ -integrin targeted hybrid tracer but also provides a systematic approach to the optimisation of such tracers [51].

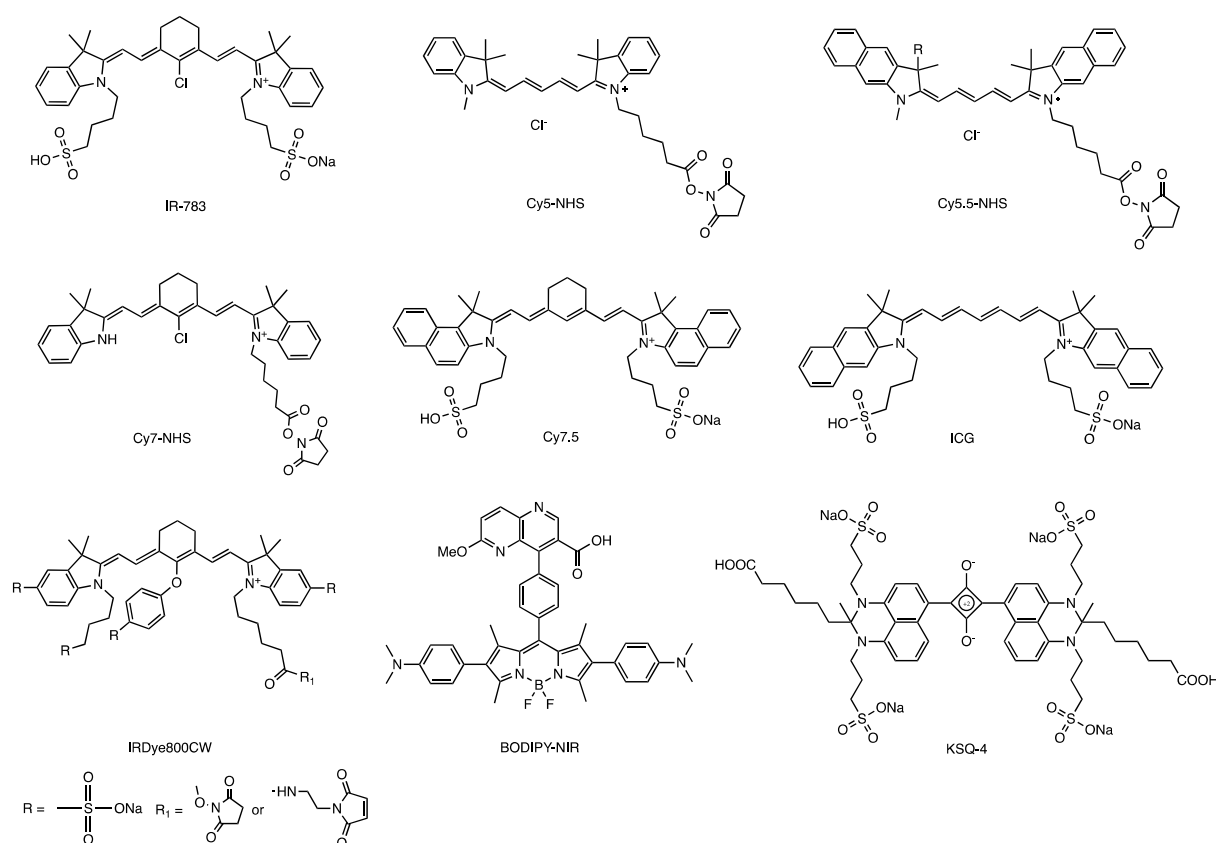


Figure I-8: Chemical structures of some NIR-emitting organic dyes and their derivatives.

Compared to the widely used Cy5, studies with IR-783 has been limited in the applications pertaining to multimodality. Nonetheless, the versatile nature of the IR-783 and its implications in wide range of biological responses has been noteworthy ranging from imaging to photothermal therapy [52, 53]. IR-783 is a commercially available fluorescent NIR dye. This dye is peculiar not just in terms of physico-chemical properties but also its biological properties as it can be used as dual imaging and targeting agents. IR-783 and its derivative show preferential uptake in tumor cells but not normal cells as has been demonstrated in a variety of cancer cell lines, tumor xenografts, spontaneous mouse tumors in transgenic animals and human tumor samples and this is proven to be mediated by tumor hypoxia and organic anion-transporting polypeptides (OATPs) [54, 55]. These diverse properties make IR-783 a probe of choice for the development of multimodal platforms.

I-3.3 Targeting ligands for cancer:

Cancerous cells express wide range of receptors on their surface which are different or expressed to a significantly greater extent compared to normal healthy cells. This difference mainly stems from the requirement of meeting the high growth and metabolic rate of the fast-growing cancerous cells. This provides the possibility to differentiate the cancer cells from the normal ones and presents the opportunity to selectively target the cancer cells for the purpose

of diagnosis and/or therapy and forms the basis of active targeting. Typically, these receptors on the cancer cells can be targeted by ligands that could be a small molecule (<500Da), peptide or protein/monoclonal antibody.

I-3.3.1 Small molecular/Peptidic ligands:

Small molecule based ligands present a viable and versatile option for the vectorization of the different kinds of tracers based on small chemicals, macromolecules and nanoparticles. Targeted tracers for theranosis based on such ligands has been one of the key areas of interest of our group in Dijon. Various chelators and fluorescent dyes have been linked alone or in combination to different targeting ligands like PSMA ligand, cRGDfk, folic acid, bombesin [56] and CXCR4 ligand [57] to name few. The most widely used ones therefore deserve a brief mention in this context (Figure I-9).

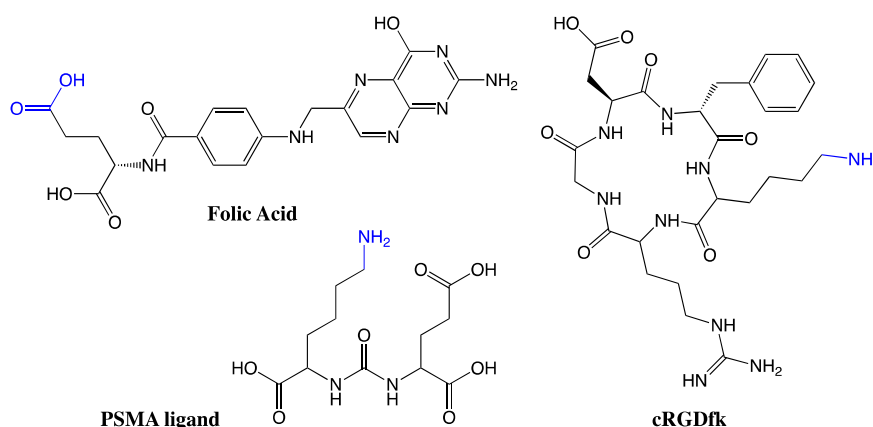


Figure I-9: Commonly used targeting ligands in targeted cancer therapeutics and diagnostics (Blue is the site of conjugation).

I-3.3.1.1 Folic Acid:

Folic acid (FA) has been famously utilized as a ligand for the selective targeting and delivery of macromolecular drugs into tumor cells via membrane-bound tumor associated folate receptors. Folate receptor is glycosylphosphatidylinositol-linked membrane protein that binds to its ligands from the extracellular fluid and transposes them inside the cell via a non-destructive, recycling endosomal pathway [58]. The overexpression of folate receptor (FR) on wide range of cancer cells qualifies it as a potential target for different types of ligand and antibody directed cancer theranostics. Folate receptors exist in three major forms; FR- α , FR- β , and FR- γ , of which FR- α is overexpressed by many types of tumor cells including those of the ovary, brain, kidney, breast, myeloid cells and lung. The density of the folate receptor appears to increase as cancer stage/grade progresses [59, 60]. Owing to the internalization of

the ligand, folic acid is particularly suitable for targeted drug delivery of anti-cancer compounds. The importance of FA as a targeting ligand for cancer research is evident from the fact that, five FA-based small molecule drug conjugates have been evaluated in clinical trials. European Medicines agency had approved 'vintafolide' and 'etarfolide' for women with platinum-resistant ovarian cancer, however its sponsor (Endocyte) later withdrew its application owing to inability to perform additional clinical investigation. Vintafolide is folate conjugated vinblastine, whereas etarfolide is a companion diagnostic based on SPECT imaging for assessment of the folate expression in patients (www.ema.europa.eu). Despite the setback, there is continued interest in the development of folate targeted therapeutics and diagnostics and approval of folate based tools in near future is very likely [61].

1-3.3.1.2 RGD peptide:

Once tumors have surpassed the size of $>1 \text{ mm}^3$, diffusion alone is no longer enough to provide the tumors cells with sufficient amounts of oxygen and nutrients. To cater to this deficit, tumor develops additional new blood vessels (Angiogenesis). This process is a hallmark of tumor growth process and represents an interesting target, not only for imaging but also for therapy. Targets like Integrin ($\alpha_v\beta_3$) and vascular endothelial growth factor (VEGF) have implications in the angiogenesis and have been exploited for cancer therapy and diagnosis. Cilengitide inhibits the integrin receptors $\alpha_v\beta_3$ and $\alpha_v\beta_5$ and has been approved for targeted antiangiogenic therapy whereas antibody bevacizumab (Avastin), targets and blocks the vascular endothelial growth factor (VEGF) [62, 63].

Integrin ($\alpha_v\beta_3$) is a cell adhesion receptor that is highly expressed on most of the tumor vasculature including the tumor cells in some cases. This receptor has high affinity with proteins and peptides containing the arginine-glycine-aspartate (RGD) sequence making it an important tumor marker. This has particular relevance in molecular imaging as the RGD conjugates can serve as tracers owing to their receptor mediated binding that results in preferential accumulation in tumor vasculature. Both linear and cyclic RGD peptides can be employed as targeting vectors to develop $\alpha_v\beta_3$ -targeted imaging tracers. However, linear RGD peptides suffer from low binding affinity ($IC_{50} > 100 \text{ nM}$), lack of specificity towards $\alpha_v\beta_3$ and are vulnerable to rapid degradation by proteases in serum in comparison to cyclic RGD peptides. Moreover, it has been shown that cyclization of RGD peptides via linkers, such as S-S disulfide, thioether, and aromatic rings, leads to increased integrin binding affinity [64, 65]. This has led to increasing use of peptides like c(RGDfk) in developing RGD targeted tracers or nanoparticles for cancer theranosis [62, 66].

I-3.3.1.3 PSMA ligand:

Human prostate cancer cell line LNCaP for first time revealed the presence of the type II integral membrane glycoprotein called prostate-specific membrane antigen (PSMA) [6]. Majority of the prostate cancers exhibit significantly elevated expression of PSMA compared to benign prostatic tissue and low expression in non-target tissues. As a result, PSMA is considered to be an ideal target for both therapy and diagnosis [67]. Research efforts to develop the ligands based on monoclonal antibody led to approval of capromab pendetide (ProstaScint®) for SPECT imaging [68]. However, the inherent disadvantages of the full-scale antibody and the quest for better and improved probes for imaging has generated substantial and continued interest in development of small molecule based ligands [69]. Current body of research indicates different chemical families of PSMA ligands; phosphorous-based (including phosphonate, phosphate and phosphoramidate), thiol-based, carbamate-based and urea-based ligands. Although phosphorous based PSMA ligands exhibited nanomolar inhibitory potency, these compounds are highly polar and manifested poor pharmacokinetic profile limiting the clinical translation. Thiol-based and carbamate agents were considered a good alternative, owing to their enhanced membrane permeability and oral bioavailability. These agents however suffered from poor metabolic stability and selectivity receding their advancements [70]. Addressing these concerns, a series of novel urea-based PSMA ligands has been developed. Of these, the Glu-urea-Lys containing binding motif has been of particular interest and led to lead candidates based on optimal combination of radiolabel bearing moiety/chelator and linker [71]. The favourable properties of the Glu-urea-Lys and the extensive experience of our group in developing Glu-urea-Lys based imaging agents makes it a compelling case to be used as targeting ligand for the building of multimodal theranostics for prostate cancer (Chapter III & IV).

I-3.3.2 Monoclonal Antibody:

Contributing to the major immunotherapeutic advances, monoclonal antibodies (mAbs) have been able to bring about a paradigm shift in the cancer treatment and care. mAbs target the specific receptors on the cancer cells and induce a cascade of events (e.g: antibody dependent cytotoxicity/ADCC) leading to cancer cell death. In addition to being used as a standalone medicine, monoclonal antibodies have also been used as a vehicle for delivery of highly potent anticancer molecules (e.g: maytansinoids) [72], radioisotopes (e.g: ¹⁷⁷Lu for brachytherapy) and imaging tracers [73]. Use of the mAbs for the targeted delivery of cargos, necessitates the use of chemical biology based approaches to conjugate the molecule of interest to the mAbs (as described in detail in Chapter 5). The interest of our group in Dijon mainly lies in using monoclonal antibodies for imaging [43, 74]. The choice of the target is

critical to the selection of the monoclonal antibody. mAbs target several different receptors on the cancer cells like HER-2, EGFR, CD20, CD30 etc. to name few. Table I-6 enlists the mAbs that have been approved in oncology.

Table I-6: Tumor-associated antigens targeted by monoclonal antibodies [75].

Antibody	Target	FDA-Approved indication	Mechanism of action
Trastuzumab (Herceptin [®]) humanized IgG1	HER2 (ErbB2)	HER2-positive breast cancer, as single agent or in combination with chemotherapy for (i) adjuvant or (ii) palliative treatment; HER2-positive gastric or gastroesophageal junction carcinoma, as first-line treatment in combination with cisplatin and capecitabine/5-FU	Inhibition of HER2 signaling; ADCC
Bevacizumab (Avastin [®]) humanized IgG1	VEGF	For the palliative treatment of colorectal cancer, non-squamous non-small cell lung cancer, glioblastoma, or renal cell carcinoma	Inhibition of VEGF signaling
Cetuximab (Erbix [®]) chimeric human/murine IgG1	EGFR (ErbB1)	In combination with radiation therapy for the initial treatment of locally or regionally advanced squamous cell cancer of the head and neck (SCCHN); As a single agent for SCCHN patients with whom prior platinum-based therapy has failed; Palliative treatment of pre-treated metastatic EGFR-positive colorectal cancer	Inhibition of EGFR signaling; ADCC
Panitumumab (Vectibix [®]) human IgG2	EGFR (ErbB1)	As a single agent for the treatment of pre-treated EGFR-expressing, metastatic colorectal carcinoma	Inhibition of EGFR signaling
Ipilimumab (Yervoy [®]) IgG1	CTLA-4	For the treatment of unresectable or metastatic melanoma	Inhibition of CTLA-4 signaling
Rituximab (Rituxan [®] and Mabthera [®]) chimeric human/murine IgG1	CD20	For the treatment of CD20-positive B cell non-Hodgkin lymphoma (NHL) and chronic lymphocytic leukemia (CLL), and for maintenance therapy for untreated follicular CD20-positive NHL	ADCC; direct induction of apoptosis; CDC
Alemtuzumab (Campath [®]) humanized IgG1	CD52	As a single agent for the treatment of B cell CLL	Direct induction of apoptosis; CDC
Ofatumumab (Arzerra [®]) human IgG1	CD20	Treatment of patients with CLL refractory to fludarabine and alemtuzumab	ADCC; CDC
Gemtuzumab ozogamicin (Mylotarg [®]) humanized IgG4	CD33	For the treatment of patients with CD33-positive acute myeloid leukemia in first relapse who are 60 years of age or older and who are not considered candidates for other cytotoxic chemotherapy (withdrawn from use in June 2010)	Delivery of toxic payload, calicheamicin toxin
Brentuximab vedotin (Adcetris [®]) chimeric IgG1	CD30	For the treatment of relapsed or refractory Hodgkin lymphoma and systemic anaplastic lymphoma	Delivery of toxic payload, auristatin toxin
⁹⁰ Y-Ibritumomab Tiuxetan (Zevalin [®]) murine IgG1	CD20	Treatment of relapsed or refractory, low-grade, or follicular B cell NHL; Previously untreated follicular NHL in patients who achieve a partial or complete response to first-line chemotherapy	Delivery of the radio-isotope yttrium-90
¹³¹ I-Tositumomab (Bexxar [®]) murine IgG2	CD20	Treatment of patients with CD20 antigen-expressing relapsed or refractory low-grade, follicular, or transformed NHL	Delivery of the radio-isotope iodine-131; ADCC; direct induction of apoptosis

I-3.3.3 How does the targeting using small ligand differ from the antibody based targeting?

Use of targeting moieties is the basic premise on which the principles of active targeting is based. One of the basic questions that a chemist is confronted with is whether to use a small molecule based ligand or an antibody given the varied choice of molecules at disposal. Obviously, this choice is greatly influenced by the disease in question and its intended target. However, it is necessary to understand the differences between these two classes while employing them in theranosis. Most of the monoclonal antibodies are highly specific to a receptor expressed on the cancer cells and hence might be the only choice for the targeting. On the other hand, the number of small molecule based ligands specific to certain receptors is relatively limited. The principle difference between antibody and small molecules stems from their pharmacokinetic properties. The circulation half-life of monoclonal antibodies is quite high compared to the small molecules (3-4 days vs hours) [76]. This is due to the fact that the small molecules are excreted rapidly from the system due to their small size unlike macromolecular antibodies (except when the chemical ligand shows high protein binding). Since the penetrative power of the ligand depends upon its ability to diffuse rapidly across the

milieu of the cancerous tissue, this favours the chemical ligand over antibody. In the context of developing targeted nanoparticles, it is important to pay attention to the effect on the nanoparticle properties upon conjugation with antibody or a chemical ligand which can have drastic effect of the pharmacokinetics of the probe [77]. Limitations on the use of the organic solvent during targeted nanoparticle synthesis further narrows the choice of antibody for such applications. Besides this, use of antibodies can entail higher costs relative to chemical based ligands which are relatively much less expensive to synthesize. Thus, above considerations make chemical ligands more apt for the applications in imaging and theranosis. Nonetheless, the novel formats of the antibodies which are less bulky can overcome the hurdles associated with full scale antibody while realising such developments. Also, it might become imperative to use antibody or antibody fragments where corresponding chemical ligand for the receptor (disease) might not be available or yet developed.

I-3.4 Conjugation Site and Chemistry:

A conjugation site enables the multimodal platform to be grafted onto the protein (monoclonal antibody or its fragment) or the nanoparticle. Majority of the bioconjugation reactions that are used for this application have been summarized in Figure I-10. Typically, the nucleophilic site is present on the substrate/protein/nanoparticles. Lysine residues are present in abundance whereas cysteine residues can be generated via reduction of the endogenous disulfide bonds or can be engineered into the monoclonal antibodies. Likewise, the amino groups can be present on the nanoparticles (e.g: AGuIX) and thiol groups can be generated on its surface via thiolation reactions using Traut's reagent. Chemical conjugation is an important step in appending the multimodal platform onto the antibody/fragment/protein and is expected to take place within short period of time under mild aqueous conditions. In order to graft the optimal amount of the platform the probe to protein/nanoparticle ratio needs to be optimized to obtain the desired stoichiometry.

The chemistry that has been widely exploited for development of diverse set of gold nanoparticles includes the sulfur-Au chemistry. Irrespective of the aliphatic or aromatic character and surface structures, sulfur bearing molecules are chemisorbed on Au by a strong thiol-Au bond ($40\text{-}50 \text{ kcal.mol}^{-1}$)[78]. This gives an opportunity to synthesize the multifunctional ligands bearing the sulfur atoms that can be grafted onto the gold surface. The strategy for development of the multifunctional gold nanoparticles described in Chapter III relies primarily on the use of lipoic acid as grafting moiety.

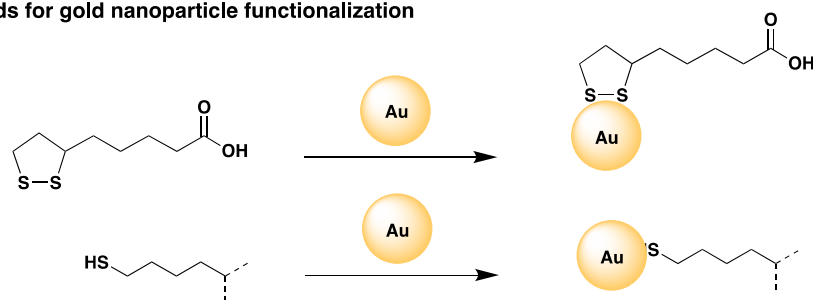
Amide based conjugation reactions involve peptide coupling mechanisms. To realize the conjugation reaction based on peptide coupling, NHS esters have been hitherto used as a workhorse that entails conversion of the carboxylate group with a relevant coupling agent

(e.g: TSTU, carbodiimide plus NHS, etc.). NHS ester based compounds react with primary amines (nucleophilic substitution) under slightly alkaline conditions (pH 7.2 to 9) to yield stable amide bonds whilst releasing N-hydroxysuccinimide (NHS) as by-product. Alternatively, the NHS esters can be generated in-situ and coupling can be carried out in the same reaction mixture. Numerous fluorescent dyes, linkers, and chelating agents are commercially available as their NHS esters.

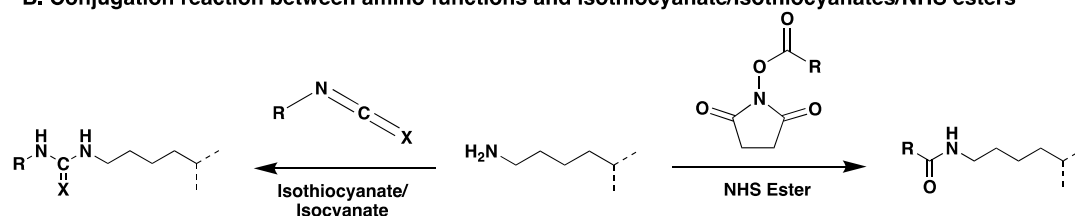
Other conjugation chemistry harnessing the nucleophilicity of the amino group involves chemical functionalities like isocyanate or isothiocyanate. Isocyanates are mostly used in polymer chemistry reactions taking place in organic solvents. Their application in aqueous conjugation reactions is very limited owing to water sensitive nature of isocyanate. On the other hand, isothiocyanates (NCS) are quite stable under aqueous conditions even compared to NHS esters and hence find application in acting as conjugation handles. NCS containing compounds normally undergo conjugation reaction at pH of 9 (or above) and hence might need due consideration when dealing with proteins/nanoparticles prone to degradation in alkaline conditions. On the similar lines, hydrazine/aminoxy group undergoes reductive amination reactions like oxime ligation and hydrazone formation based on its reaction with carbonyl compounds and these reactions have implication in bioconjugation [79].

Second to amino group, thiols have been widely explored for the bioconjugation applications. The unique nucleophilicity of thiols, particularly in its deprotonated thiolate form ($-S^-$) enables it to undergo wide variety of reactions. The dissociation energy of sulfhydryl is substantially lower relative to the corresponding alcohols which provides it much higher acidity. The conjugation reactions involving thiols usually involve either a nucleophilic addition or displacement reaction with the thiolate anion acting as the nucleophile. Thiols undergo reactions with α -halocarbonyl compounds, perfluoroaromatic molecules, Michael acceptors (maleimide and vinyl moiety), 2-cyanobenzothiazole, phenyloxadiazole sulfone etc. [80].

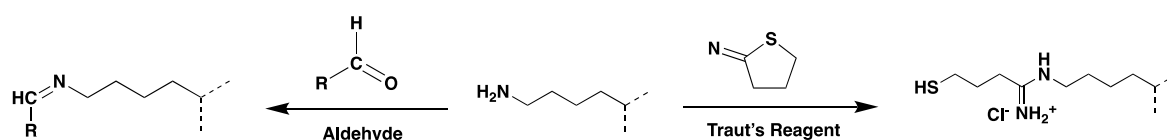
A. Ligands for gold nanoparticle functionalization



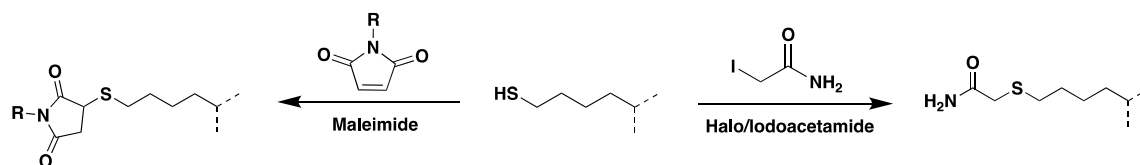
B. Conjugation reaction between amino functions and isothiocyanate/isothiocyanates/NHS esters



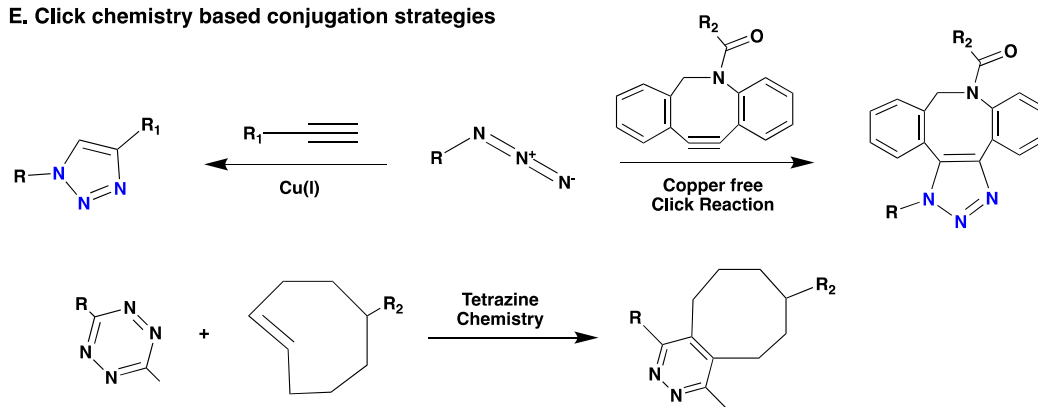
C. Amine mediated schiff's base formation and thiolation reactions



D. Thiol mediated michael addition and nucleophilic substitution reactions



E. Click chemistry based conjugation strategies



F. Silane mediated functionalization of silica nanoparticles

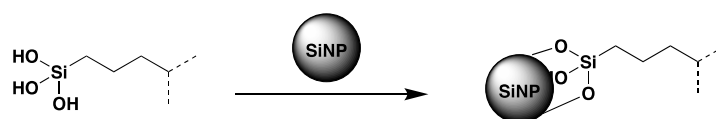


Figure I-10: Chemical strategies for bioconjugation & nanoparticles functionalization [81].

Ever since their first introduction by Friedmann, maleimide-mediated reactions (with thiols) represent as of today the most frequently used functional groups for bioconjugation and is one of the key Michael addition reactions. The optimal reaction conditions for maleimide-mediated conjugation, are near neutral conditions (pH 6.5–7.5), to avoid the reaction of maleimide with amines, which usually need a relatively higher pH. Maleimides are prone to hydrolysis beyond pH 8 resulting in a mixture of isomeric non-strained maleamic acids unreactive toward sulfhydryls and can thus compete with thiol modification [82, 83]. The halo substitution and the Michael addition (involving maleimide) will be exploited in the current research work in realizing and applying the multimodal platform to theranosis.

Owing to its versatile nature, click chemistry has influenced wide range of chemical fields like; drug development, and polymer chemistry, chemical biology and nanoscience. Click chemistry is quite relevant to the applications where the time is a limiting factor like bioconjugation reactions or radiochemistry owing to the sensitive nature of the protein or the limited half-life of the radioisotope. Click ligations are rapid and efficient that enables to maximize yield while being selective and clean obviating the post reaction work-up. Click reactions are mainly of three types; the Cu-catalyzed azide-alkyne cycloaddition (CuAAC), the strain- promoted azide-alkyne cycloaddition (SPAAC) and the inverse electron demand Diels-Alder reaction (iEDDA) [84]. CuAAC leads to formation of a 1,2,3-triazole ring which can be considered as a small and a rigid stereoisomer of an amide linkage causing least perturbation of the vector activity. On the other hand, despite its wide utility, SPAAC ligations can impregnate the probe structure with a hydrophobic and bulky benzocyclooctatriazole footprint which can lead to dramatic changes in the pharmacokinetics of the tracer and significantly impaired its uptake [85]. Nonetheless, click chemistry based cycloaddition reactions (CuAAC, SPAAC) are rapid and modular with higher yields and release nontoxic by-products, remain stable in physiological conditions and utilize benign solvents [86, 87]. Inverse Electron-Demand Diels–Alder (iEDDA) cycloaddition entails reaction between 1,2,4,5-tetrazines and trans-cyclooctene (TCO) was introduced in 2008 providing a marked improvement over the sluggish SPAAC ligation. iEDDA is currently being explored for varied applications owing to its extremely fast kinetics ($k > 800 \text{ M}^{-1} \cdot \text{s}^{-1}$, fastest biorthogonal reaction). However, it still leaves the tracer with a bulky bicyclic [6.4.0] ring system. One of the drawbacks associated with click reactions for bioconjugation is, solubility of the reagents like alkynes, DBCO and tetrazines in aqueous conditions, which can be to certain extent addressed by including hydrophilic moieties (e.g: PEG spacers) in the structure. Nevertheless, the commercial availability of a wide range of click chemistry tools; derivatives of azides, alkynes, DBCOs, tetrazine and TCO reagents has made these reactions a popular

choice for bioconjugation applications [88, 89].

Silanization/silylation is one the widely used processes in functionalization or modification of the silicon surfaces in materials chemistry. The 3-aminopropyltriethoxysilane (APTES) is the most frequently used organosilane coupling agent in such treatments to generate amine functionalized surfaces [90]. Silanization is a condensation reaction taking place at the surface of the silica leading to formation of Si-O-Si bond. The silylation process is very complex and does not involve a single mechanism. Thus, many different intermediates are possible [91]. This chemistry has been also explored to alter the surface chemistry of the inorganic nanoparticles like iron oxide nanoparticles (SPIONs) or silica nanoparticles [92]. Developing organosilanes based on chelators represent an interesting avenue to functionalize the silica nanoparticles with the chelator of choice. It is using this organosilane based conjugation chemistry, we envisioned functionalization of AGuIX nanoparticles for multifunctionality (Chapter II).

I-4 Objectives of the research thesis:

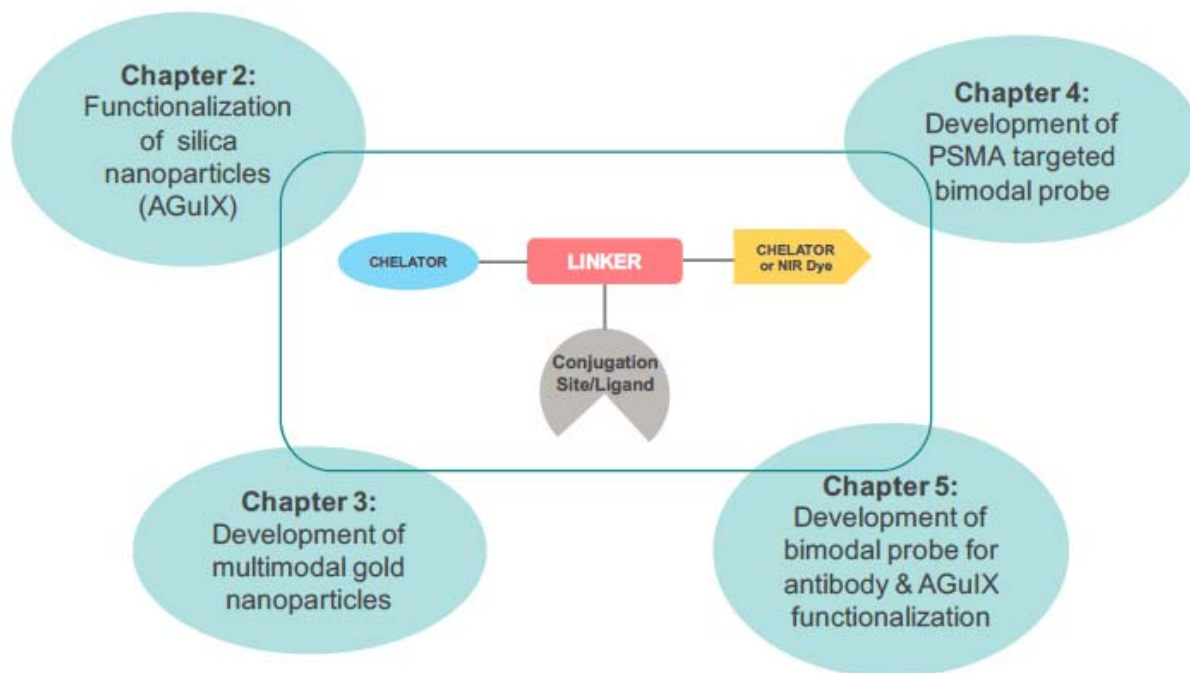


Figure I-11: Application of the monomolecular multimodal platform towards development of theranostics.

In the current thesis, the multimodal platform has been exploited to synthesize the customized chemical moieties that can be applied across broad spectrum of systems as depicted in the Figure I-11. Chapter II entails development of the silane derivatives of the chelators that can be used for the synthesis and functionalization of the silica nanoparticles (AGuIX). It demonstrates the efficient use of precursors used for functionalization of AGuIX. It also sheds light on its physico-chemical and radiochemical properties along with investigation in TSA tumor model to underscore its importance in theranostics. Chapter III deals with development of the multifunctional ligands that can be used for fabrication of gold nanoparticles with varied properties and aspects. These include ligands for PET, PET-MRI and PET-Optical imaging as well as PSMA targeted ligands for SPECT imaging. Since gold is a high Z atom, the nanoparticles manufactured using these ligands can obviously be used for radio-sensitizing applications giving rise to a sophisticated set of theranostic tools. Focussing on the tools useful for the prostate cancer management, Chapter IV highlights the state of the art in the PSMA targeted multimodal imaging agents. It focusses on the development of small molecule based PSMA targeted bimodal (PET-Optical) imaging agent. Along with the synthesis, it also delves into the suitability of this probe in terms of its photophysical, binding and radiochemical properties. In the last chapter, the focus has been to apply the multimodal platform in developing a versatile bimodal imaging probe that can be applied to the bioconjugation of monoclonal antibody fragments as well as functionalization of silica

nanoparticles. This has been supported by the characterization as well as examination of these systems in relevant animal model. The above objectives fit well in the context of the expertise available and research focus at Chematech/ICMUB as well as the goals of the ARGENT program that aims to focus on developing the processes and technologies catering to the improvement of breast, prostate and brain cancer management.

*Chapter II. Multifunctional polysiloxane (AGuIX)
nanoparticles for cancer theranosis*

II-1 AGuIX Nanoparticles in cancer theranosis:

Of the diverse inorganic components present in the nature, silicon or Si (IV) is one of the essential trace inorganic species having a biological significance. Although, it's not clear what form of metabolism does silica undergo, under ordinary physiological conditions, Si(IV) is present as silica, hydrated silica, or hydrated silicate ions, and is taken into the cells for promoting the growth of the connective tissue like bone and cartilage. In-vitro experiments have revealed that silica/orthosilicic acid has influence on the differentiation and gene expression levels the osteoblasts. Cells have the innate ability to engulf particles with size less than a few micrometers through their cell membrane with a lipid-bilayer structure through a process called endocytosis. Silica or hydrated silica particles in the size range of nanometer to micrometer can not only get inside the cells but can also exert biological influence depending on its nature and can be harnessed to deliver a drug or an imaging tracer [93].

Stöber demonstrated the sol-gel synthesis method for the preparation of monodispersed spherical silica particles. This was performed by hydrolysis and condensation of tetraethylorthosilicate (TEOS) in ethanolic medium with ammonia as a base [94, 95]. Since then, Stöber method has been deployed in different ways for the synthesis of silica nanoparticles for various applications. The aqueous sol-gel process can be defined in simple terms as the conversion of a precursor solution into an inorganic solid via inorganic polymerization reactions induced by water. Typically, a sol-gel process consists of the following steps: i) Compounding of a homogeneous solution through dissolution of metal organic precursors in an organic solvent (miscible with water), or via dissolution of inorganic salts in water; ii) transformation of the homogeneous solution into a sol by treatment with a suitable reagent (in most cases, water with or without any acid/base); iii) Subsequent steps involve aging and thermal treatment (sintering)[96]. The primary step in a sol-gel reaction is the formation of an inorganic polymer induced by hydrolysis and condensation reactions, which results in the conversion of the molecular precursors into a crosslinked solid structure. Under the optimal conditions of the precursor concentration, solvent, pH and agitation, nanoparticles of desired particle size can be synthesized.

AGuIX nanoparticles have been synthesized on same principle, wherein TEOS condensation in the presence of APTES gives rise to amino group bearing nanoparticles. The AGuIX is a hybrid nanoparticle based on a polysiloxane core and complexed gadolinium situated at the periphery. The concerted efforts of the team led by Prof. Tillement at Claude Bernard University, Lyon over a decade has led to the development of this platform. This platform represents a unique combination of silica and chelation chemistry making it one of its kind amongst myriad of nanoparticles currently explored in theranosis. These nanoparticles are

multimodal in that they can be used both as a positive contrast agent in MRI and as a radiosensitizing agent in cancer theranosis. This chapter will focus on the thesis work carried out in the context of these nanoparticles after a brief introduction of this platform technology.

II-1.1 Synthesis and structure of AGuIX:

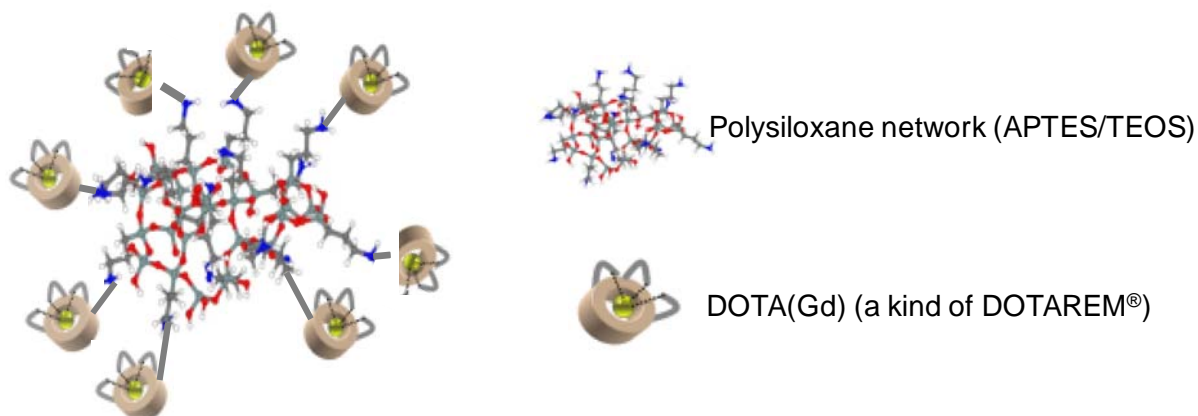


Figure II-1. Structure of AGuIX nanoparticle.

As can be seen from the Figure II-1, classical AGuIX nanoparticles are composed of a polysiloxane backbone surrounded by around ten DOTAGA ligands. 98-99% of these ligands are complexed with Gd^{3+} ions. A typical tetraazamacrocyclic (DOTA/DOTAGA) provides 8 coordination sites for the chelation of the Gd^{3+} ion. Conventional DOTA (1,4,7,10-tetraazacyclododecane-1,4,7,10-tetraacetic acid) has four carboxylate arms, whereas DOTAGA provides an additional carboxylate group available from the glutaric arm that serves as an anchoring point for synthesis of multimodal agents. This macrocyclic chelator has a very high complexing constant for the Gd^{3+} ion ($\log K = 25.6$) and slow dissociation kinetics [97]. As a result, any release of Gd^{3+} ions into the body after injection of the particles is precluded, which otherwise would cause a toxic effect. The particles also have about fifteen primary amine functions at the surface that can be used for subsequent functionalization. On the other hand, these particles have an average hydrodynamic diameter of about 3-5 nm and a mass of about 10 kDa, making them amenable to renal elimination.

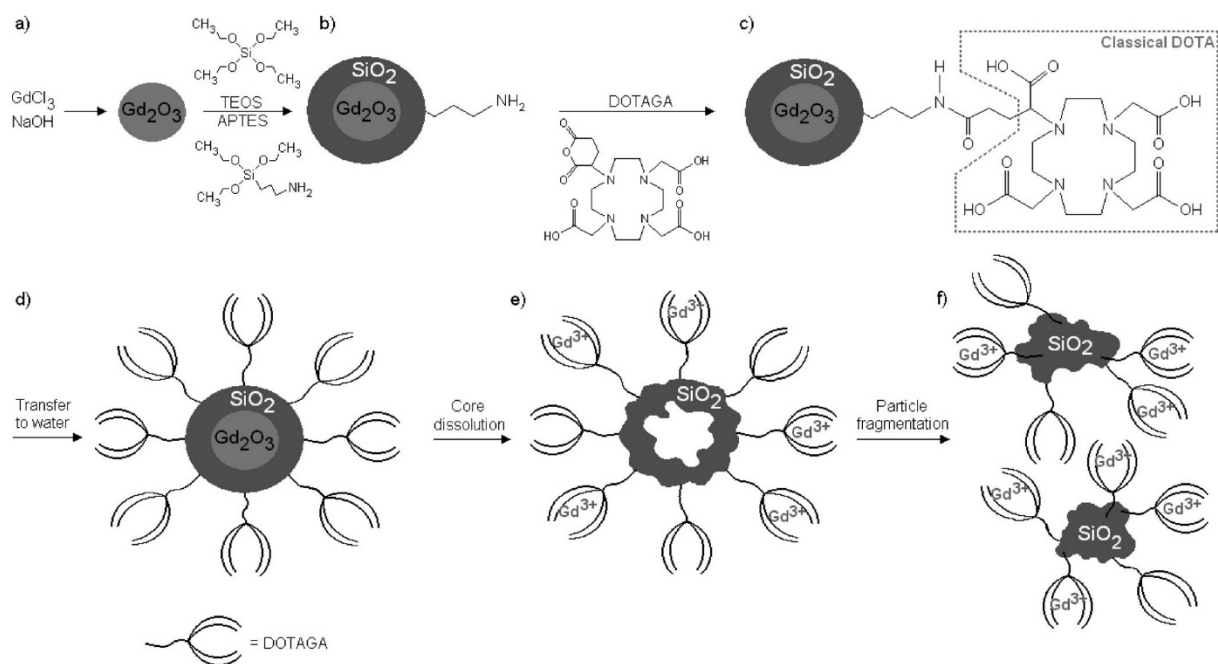


Figure II-2. Classical synthesis of AGuIX nanoparticles. a) core synthesis, b) polysiloxane shell synthesis, c) DOTAGA grafting, d) transfer to water, e) core dissolution, f) polysiloxane fragmentation. Figure adapted from [98].

The AGuIX nanoparticle synthesis involves a mixed bottom-up and top-down approach as explicated in the Figure II-2. The synthesis starts with the preparation of a core of gadolinium oxide via alkaline treatment of the $GdCl_3$ salt, which is then encapsulated in a polysiloxane layer. This is obtained by hydrolysis-condensation of tetraethoxysilane (TEOS) and 3-aminopropyltriethoxysilane (APTES) on the surface of the Gd core. TEOS has been a chemical of choice to crosslink and densify the polysiloxane network as reported in majority of the silica nanoparticle based schemes whereas APTES enables to have the amine groups integrated with the siloxane core that remains at the surface of the particle and which can be used as appendage point for subsequent functionalization chemistry. Following the shell synthesis, DOTAGA is coupled to the surface amino groups via an amide bond. Presence of the DOTAGA groups on the surface increases the water dispersibility/solubility and the colloidal stability of the nanoparticles. Finally, the nanoparticles are transferred to water, during which the dissolution of the gadolinium oxide core causes the fragmentation of the polysiloxane layer, giving rise to ultrafine nanoparticles: AGuIX® nanoparticles. The released Gd^{3+} is subsequently chelated by the free DOTAGA causing it to be lodged at the periphery of nanoparticles [99]. The ultrasmall nanoparticles are then purified to remove the extraneous components using the ultrafiltration device. After purification, the AGuIX® nanoparticles are lyophilized to get a powder that can be stored at room temperature for more than one year. The AGuIX nanoparticles can be produced on a large scale in a reproducible

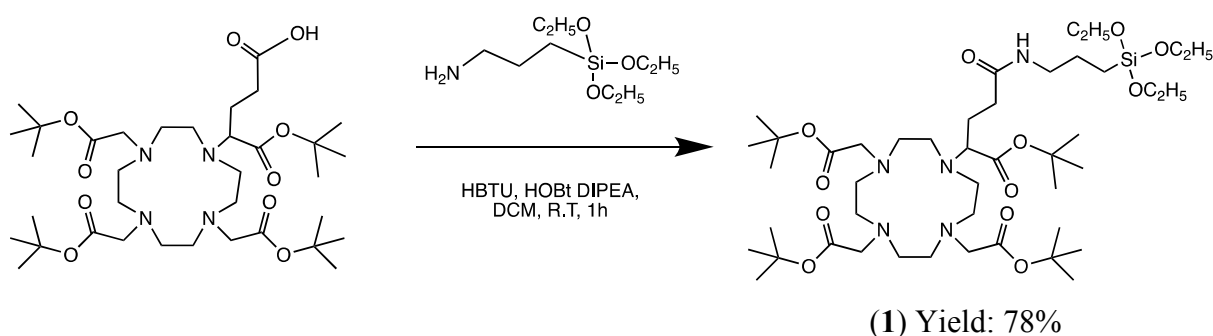
manner at the laboratory scale (~ 50 g of particles corresponding to ~ 50 mmol of Gd³⁺). A lot has been also produced under conditions of Good Manufacturing Practices (GMP) in partnership with Carbogen AMCIS (600 g) for the investigations pertaining to the human clinical trial.

II-2 Functionalization of AGuIX:

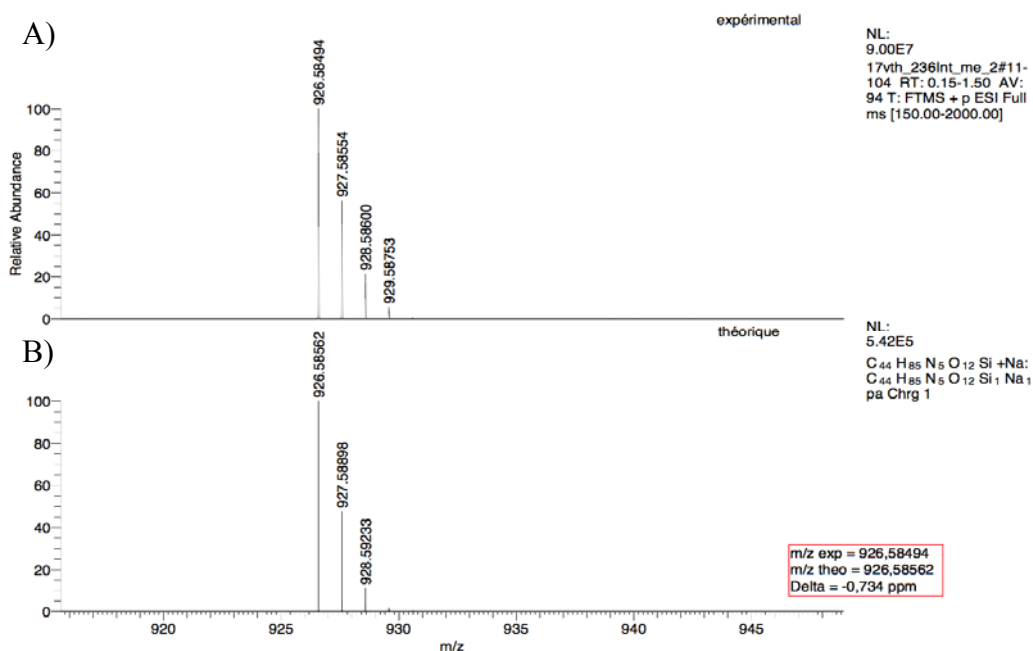
Surface chemistry of the nanoparticles defines its ability to remain stable at physiological conditions and also its amenability to undergo surface alteration or functionalization. AGuIX nanoparticles are rich in surface composition in that they possess abundant silanol (from hydrolysed and uncondensed TEOS) and amino (from hydrolysed APTES) groups. Since, the silanol and amino groups have different acid–base properties, the surface amino groups also control the repulsive forces amongst the adjacent particles, and hence contribute to the stability. Some of the amino groups are also then used to attach a chelate (DOTAGA) that will ultimately form complex with gadolinium. Moreover, AGuIX nanoparticles offer further scope for its functionalization via availability of the active surface moieties like -NH_2 (from APTES), -COOH (from the free uncomplexed carboxylate groups of DOTAGA) or -OH (silanols). In the previous work, Morlieras et al. demonstrated use of -COOH and -NH_2 groups for the functionalization of the nanoparticles with peptide ligand and fluorescent dye[35]. Truillet et al. exemplified synthesis of NODAGA functionalized AGuIX based on amide coupling employing the -NH_2 of nanoparticle and the NHS ester of NODAGA[100]. However, this approach is not so lucrative as reaction conditions are not amenable to the stability and yield of the final product. In this chapter, we demonstrate for first time the functionalization of AGuIX with NODAGA employing the surface silane chemistry. Part of this work was performed during my secondment at Prof. Tillement's group in Lyon and was result of the close collaboration with his team involving Dr. Lux François and Vulong Tran. The first step toward realization of this approach was to synthesize silane bearing chelates and then perform functionalization of AGuIX using the silane bearing chelators.

II-2.1 Nanoparticle synthesis and functionalization with silane chelators:

II-2.1.1 Synthesis of the DOTAGA-Silane:

Figure II-3. Synthesis scheme of DOTAGA(tBu)₄-APTES (1).

DOTAGA-(tBu)₄ was used as a starting point for the synthesis of DOTAGA-silane compounds. DOTAGA-(tBu)₄ was first activated to form an ester using HBTU and HOBT, which was then peptide coupled with APTES ((3-aminopropyl)triethoxysilane) (Figure II-3). To get rid of the excess of the reagents and side products the product containing organic phase (dichloromethane) was successively washed with weakly acidic, basic and neutral aqueous solution. The product was obtained as a light brown viscous residue (1). The formation of the product was confirmed by HRMS (Figure II-4). The product was detected as [M+Na]⁺ species at $m/z = 926.5$.

Figure II-4. Mass spectrum of DOTAGA(tBu)₄-APTES (1): A) Experimental spectrum, B) Simulated/Theoretical spectrum.

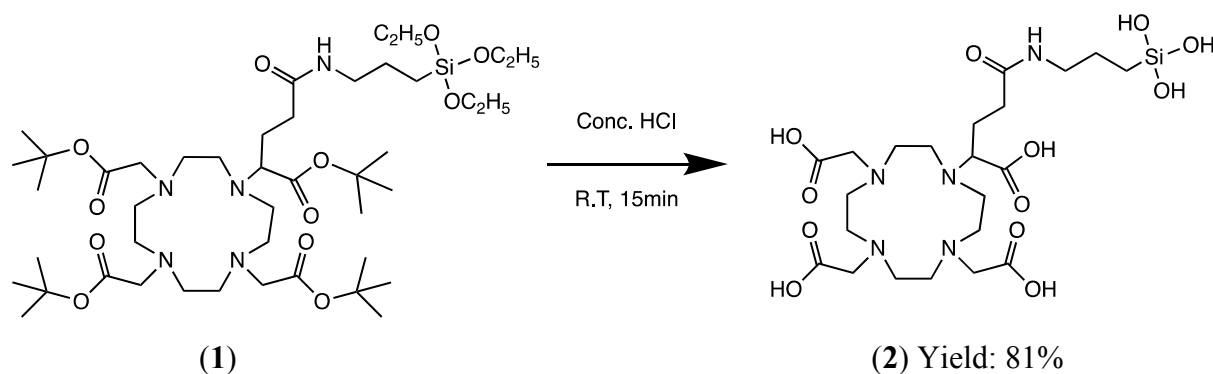
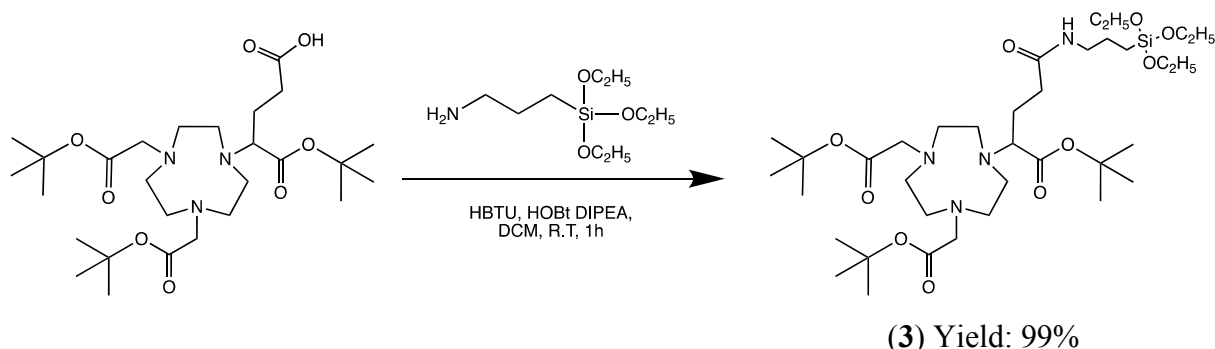


Figure II-5. Synthesis scheme of the DOTAGA-Silane (2).

Typically, deprotection of the t-butyl group can be brought about by treatment with TFA, however, the experience with simple macrocyclic compounds suggests that conc. HCl acts as an effective and fast deprotecting agent. As a result, deprotection of the compound (1) could be easily effected by a brief treatment with conc. HCl (36% HCl) (Figure II-5). Compound (2) was obtained with a yield of 81% as a light brownish brittle compound as a salt of chloride and HPF₆ that tended to be hygroscopic when left at room temperature.

II-2.1.2 Synthesis of the NODAGA-Silane:

Figure II-6. Synthesis scheme of NODAGA-(tBu)₃-APTES (3).

On the similar lines as followed for DOTAGA, synthesis of a silane derivative of NODAGA was attempted as NODAGA is a more efficient chelator for the PET based radioisotopes like ⁶⁴Cu and ⁶⁸Ga and hence could be of significant value in development of variants of AGuIX with multimodal imaging capability. NODAGA-(tBu)₃-APTES was synthesized in a manner analogous to the compound (1), where in the t-butyl protected NODAGA (NODAGA-(tBu)₃) was coupled to APTES using HBTU based coupling chemistry (Figure II-6). This intermediate protected compound (3) was obtained in good yield (99%) and could be detected as [M+H]⁺ species at m/z = 663.4 when analysed by HRMS (Figure II-8). Alternatively, the compound could also be characterized by proton and carbon NMR.

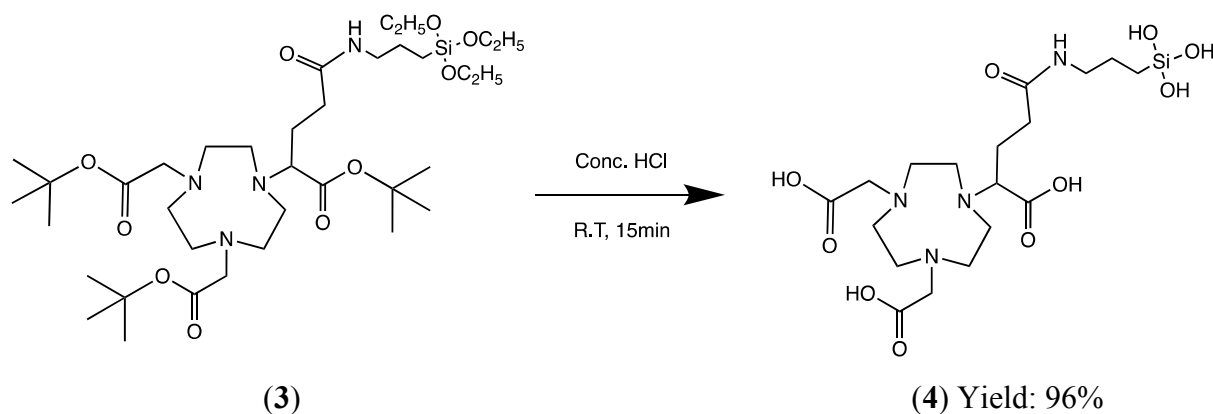


Figure II-7. Synthesis scheme of the NODAGA-Silane (4).

Deprotection of the compound (3) proceeded quickly in conc. HCl as expected (Figure II-7). The excess HCl was immediately evaporated off. The residue obtained was easily solubilized in water which upon lyophilisation afforded a light brown compound obtained as a salt of HCl and HPF₆.

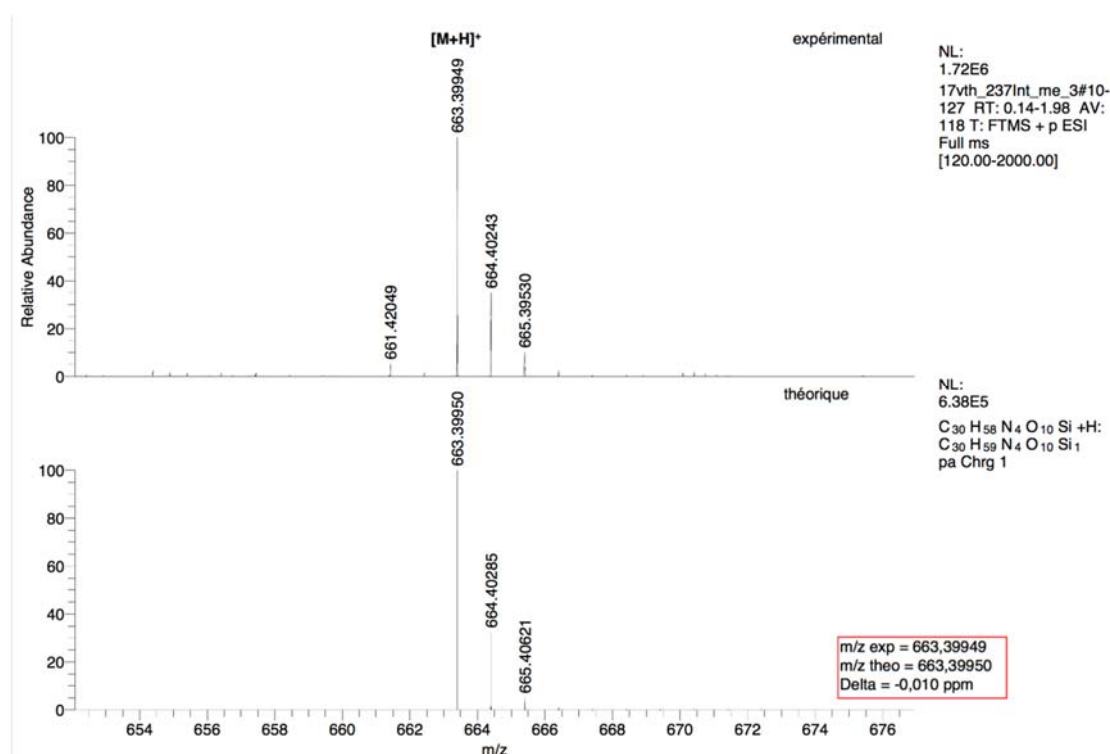


Figure II-8. Mass spectrum of NODAGA-(tBu)₃-APTES(3): A) Experimental spectrum, B) Simulated/Theoretical spectrum.

Organic silanes in general are labile compounds as they have propensity to undergo inter- and intra-molecular condensation reactions, hence, the silanes depicted above can form and exist in dimeric or oligomeric form. As a result, an accurate characterization attributable to monomolecular species might not be always feasible. Nonetheless, the complementary characterization tools enable to ascertain the analysis of the compounds synthesized here.

Moreover, adapting the process of the nanoparticles synthesis/functionalization to completely harness the utility of these silanes has delivered successful results and has been discussed in following sections. The silanes synthesized hereof have not just been used for functionalization of nanoparticles but also explored for the one pot synthesis of the silica nanoparticles (AGuIX).

The one pot synthesis of the nanoparticles based on these silanes forms the part of research thesis of Vulong Tran, one of the ESRs within the consortium of ARGENT project at Université Claude-Bernard, Lyon. This highlights the collaborative and multidimensional value of the work described here.

II-2.1.3 Nanoparticle functionalization with silane bearing chelators:

Silica surfaces can be treated with silane derivatives so as to have the materials with desired surface chemistry. For instance, treatment of the glass surface/silicon wafers with APTES can result in the formation of amine functionalized surfaces that can be used for varied application like enzyme immobilization or building antibody coated surfaces. Based on similar principle, we condensed the surface silanols present on the AGuIX surface with silane bearing chelators.

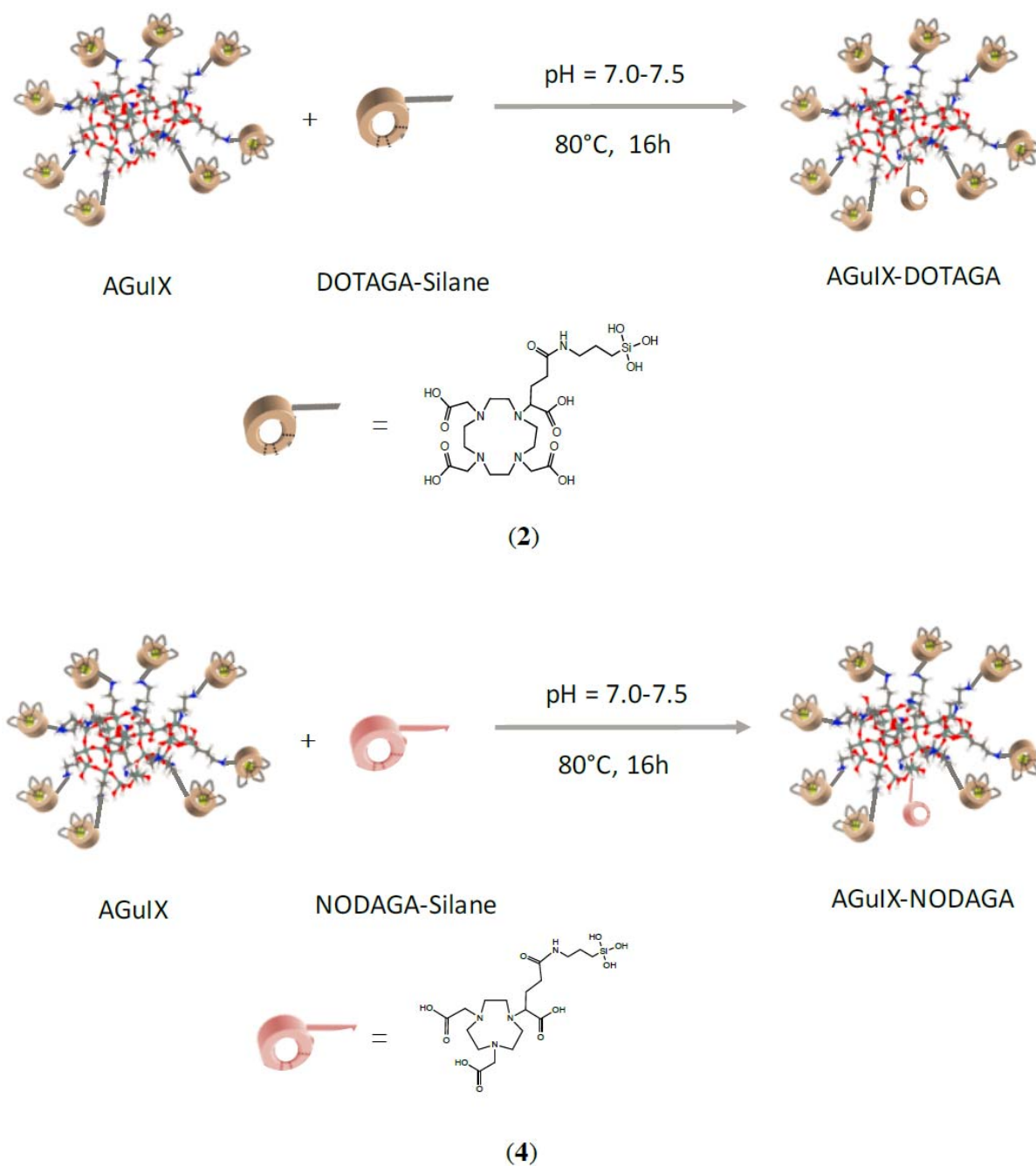


Figure II-9. Functionalization of the AGuIX nanoparticles with the silane derivatives of DOTAGA and NODAGA.

The silane derivatives were briefly dissolved in alkaline aqueous solution so as to have the monomeric species present in the solution. Each type of chelator silane was mixed with AGuIX in molar ratio of Gd: silane-chelator = 10: 1.5 with the pH adjustment, if needed. The nanoparticle solution was stirred in light protected environment for overnight (16h) at the pH of 7.0-7.5 (Figure II-9). Furthermore, this process is currently undergoing optimization with respect to various process parameters and concentrations, so as to have optimally developed process yielding defined nanoparticle characteristics.

The pH of the solution was adjusted to 2 by adding HCl solution before the purification to quench any further reactions/degradation. Then each solution was purified with tangential filtration through Vivaspin membranes (MWCO = 5 kDa) employing 9 cycles. Following this, pH of the solution was readjusted to 7.4 and solution was filtered through 0.2 μm membrane to remove dust and large impurities/microbes. Finally, the solution was lyophilized in vials to obtain the powder that could be stored for long time at room temperature.

II-2.2 Physico-chemical properties of functionalized nanoparticles:

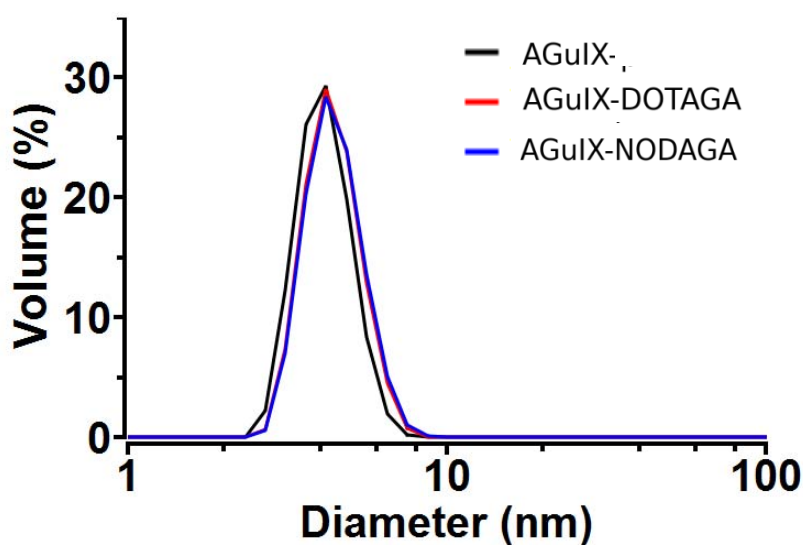


Figure II-10. Dynamic light scattering measurement of AGuIX nanoparticles.

Table II-1. Physico-chemical properties of the functionalized nanoparticles.

Sample	AGuIX	AGuIX-DOTAGA	AGuIX-NODAGA
Hydrodynamic Diameter (nm)	4.2 ± 0.8	4.5 ± 0.9	4.5 ± 0.9
Zeta Potential (mV at pH 7.4)	+8.15	-8.43	-13.7

DLS measurements were performed on the native and the functionalized nanoparticles using Zetasizer Nano-S (633 nm He-Ne laser) from Malvern Instruments. Measurements was made

using 1 mL of the solution at around 5 – 10 g/L with a single use PMMA cuvette (Carl Roth GmbH, Germany) at 20 °C. For the Zeta potential, the lyophilized powder was re-dispersed in water to achieve 100 mg/mL solution and diluted to 10 mg/mL in an aqueous solution containing 5 mM NaCl and adjusted to the desired pH (7.4) just before each measurement. Zeta potential measurements were recorded at 20 °C within a DTS 1061 folded capillary cell (Malvern Instruments Ltd, USA). The zeta potential (ζ) was automatically calculated from electrophoretic mobility based on the Smoluchowski equation, $v = (\epsilon\epsilon_0\zeta / \eta)\zeta$, where v is the measured electrophoretic mobility, η is the viscosity, ϵ is the dielectric constant of the electrolytic solution, $\epsilon_0 \approx 8.854 \times 10^{-12} \text{ C}^2\text{N}^{-1}\text{m}^{-2}$ is the vacuum permittivity.

As has been routinely observed, AGuIX nanoparticles exhibited a hydrodynamic diameter (D_h) of 4.2nm, whereas functionalized nanoparticles displayed a slight increase amounting to the size of 4.5nm for both AGuIX-DOTAGA and AGuIX-NODAGA. This small increase in the size could be attributed to the appendage of the chelators on to the nanoparticles. This inference was compounded from the zeta potential measurement results, wherein the surface potential of the nanoparticles changed from positive to negative after grafting of the chelators on nanoparticles. In its native form, AGuIX has a slight positive charge owing to the presence of surface amino groups (+8.15mV). Upon functionalization, the surface charge turned negative with the value of -8.43mV and -13.7mV for AGuIX-DOTAGA and AGuIX-NODAGA (Table II-1). Moreover, a monomodal symmetric peak/correlogram obtained after the DLS analysis (Figure II-10) suggests that the nanoparticles are monodisperse, despite the small particle size range.

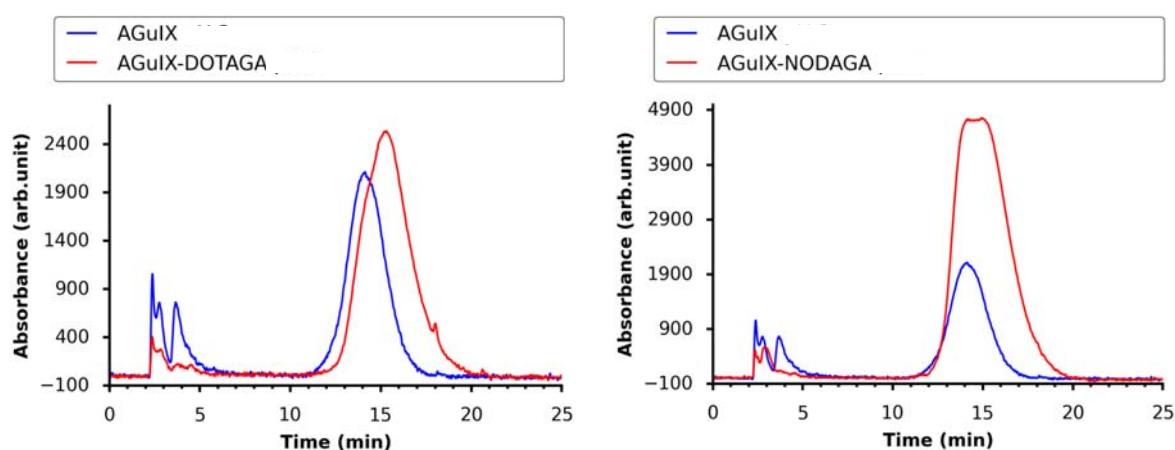


Figure II-11. Chromatographic analysis of the functionalized nanoparticles using HPLC at 285nm.

Although AGuIX are a class of nanoparticles, their unusual small size permits their analysis by reverse phase HPLC, which otherwise is not so common. As can be seen from the Figure

II-11, AGuIX exhibit a retention time of about 14min. The retention time of AGuIX-DOTAGA was slightly shifted to right with retention time of 15.5min. Similar observations were made for AGuIX-NODAGA. In addition, a relative peak broadening was also observed which could be due to different size and charge characteristics of the functionalized nanoparticles in comparison to AGuIX.

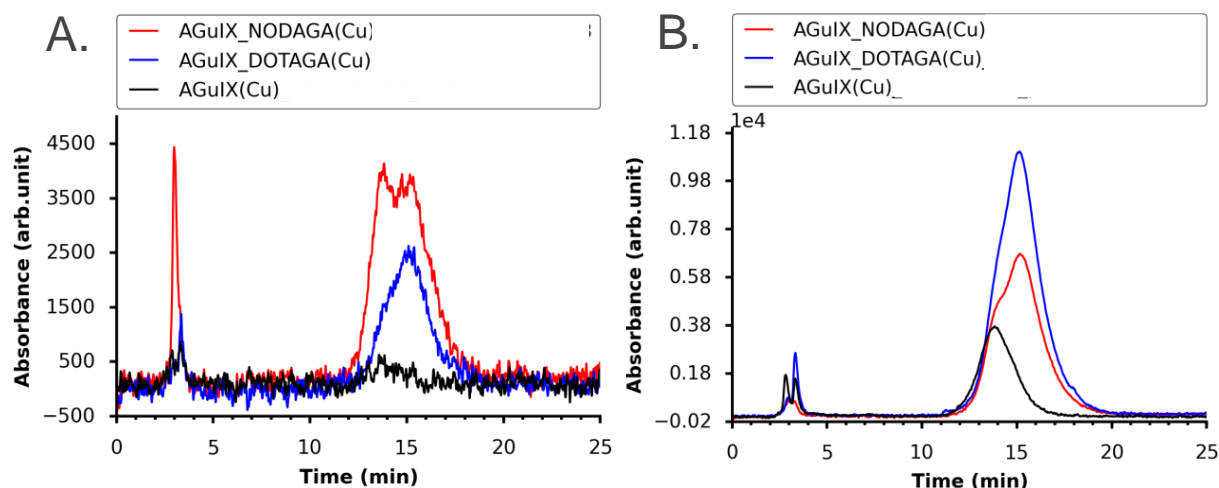


Figure II-12. Chromatographic analysis (RP-HPLC) of the Cu^{2+} complexed functionalized nanoparticles at A) 700nm and B) 375nm.

To further verify that indeed the chelators have been grafted on the nanoparticles, AGuIX-DOTAGA and AGuIX-NODAGA were complexed with Cu^{2+} (using molar excess of CuCl_2) by incubating at pH 3 and 80°C for 2h. The Cu^{2+} labelled nanoparticles were analysed by HPLC with detection at 700nm as the copper chelate complex is blue coloured and exhibits λ_{max} in this region. As can be seen from Figure II-12, pristine AGuIX exhibits almost a flat profile with a small spike at around 15min as the amount of free/uncomplexed DOTAGA present on AGuIX to chelate Cu^{2+} is only 1% of the total DOTAGA present on AGuIX. However, with the functionalised nanoparticles; AGuIX-DOTAGA and AGuIX-NODAGA there is distinct peak at 15min (at the same position as observed at 375nm) which indicates grafting of the free chelators which afford the nanoparticles the ability to complex Cu^{2+} .

Relaxometric studies were also performed on the nanoparticles to evaluate the effect on contrast properties by the measurements of the longitudinal and the transversal relaxivity (respectively r_1 and r_2). One of the common approaches to increase relaxivity is to decrease the molecular tumbling by attaching/integrating gadolinium complexes to a macromolecular structure through rigid linkages [101].

The longitudinal relaxivity (r_1) increased from 13.70 to 17.97 or 18.17 $\text{mM}^{-1} \cdot \text{s}^{-1}$, (whereas, r_2 increased from, 19.15 to 25.44 and 25.84) indicating an increase in rotational correlation time

resulting from the grafting of a ligand. On the end, the ratio r_2/r_1 slightly increased but stayed around 1.4 indicating that the efficiency of the NPs as positive contrast agents was still maintained (Table II-2).

Table II-2. Relaxometric properties of AGuIX, AGuIX-DOTAGA and AGuIX-NODAGA at 37 °C (1.4 T & 60 MHz).

Sample	Concentration (mM)	T ₁	r ₁	T ₂	r ₂	r ₂ /r ₁
AGuIX	100	0.73	13.70	0.52	19.15	1.40
AGuIX-DOTAGA	76.3	0.729	17.97	0.515	25.44	1.42
AGuIX-NODAGA	76.3	0.721	18.17	0.507	25.84	1.42

Fourier Transform Infra-Red (FTIR) spectroscopy is an excellent tool for the qualitative assessment of the materials based on the functional groups present on it. The FTIR analysis of a compound or material generates a spectrum which acts as a signature of its structural information. This is due to the fact that different types of bonds, and thus different functional groups, absorb infrared radiation of different wavelengths. Although the analysis takes into account the absorbance by the materials, it is typically converted to transmittance and represented as plot of % transmittance against the wavenumber as has been depicted in Figure II-13.

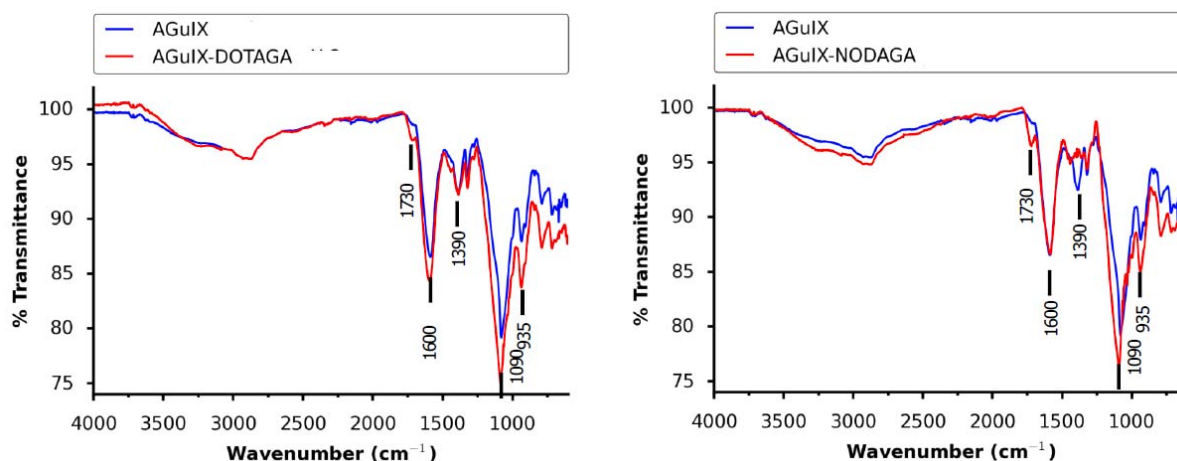


Figure II-13. FTIR Spectroscopy of the functionalized nanoparticles performed on lyophilized powder (at pre-lyophilisation pH of 2).

There has been a slight increase in intensity of peak at 1730 cm^{-1} and 935 cm^{-1} that proves the appearance of free COOH groups. Strangely, in the case of AGuIX-NODAGA, peak at 1390 cm^{-1} reduces. Probably, this peak is a combination of signals from COOH and NH_2 . This could be possibly due to the fact that NODAGA contains one COOH and one NH_2 group less

than DOTAGA, the contribution of those peaks in the total spectrum is less than in the case of AGuIX-DOTAGA. Nonetheless, complementing other tools of characterization, FTIR data supports the successful grafting of the chelators onto the AGuIX.

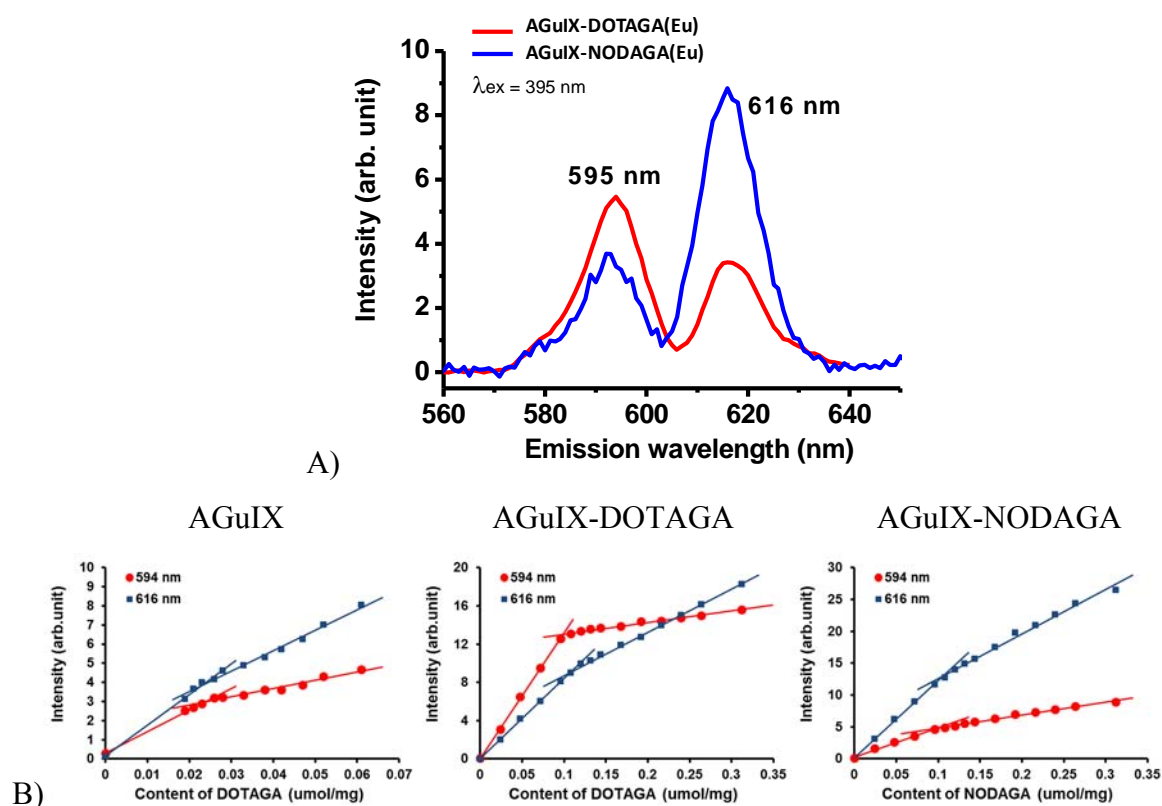


Figure II-14. Eu³⁺ Phosphorescence based titration of the grafted macrocycle on the nanoparticles: A) Emission spectrum of Eu³⁺ chelate of AGuIX-DOTAGA/NODAGA. B) Titrimetric determination of free chelator content based on inflection point employing phosphorescence.

Estimation of the number of the free chelators is of utmost importance to ascertain the number of chelators grafted onto nanoparticles and for the overall characterization of nanoparticles as a tracer. Assay to quantify the number of free chelators present in the solution based on the spectrophotometric/colometric and luminescent analysis have been developed for the chelate functionalized nanoparticles [100, 102]. The colorimetric assay is based on the use of xylenol orange as an indicator which has the ability to form a coloured complex with Gd³⁺. Xylenol orange is a weaker ligand than chelator like DOTAGA. An aqueous solution of GdCl₃ is gradually added to a colloidal solution of nanoparticle containing free chelators. When there is no more accessible chelator, Gd³⁺ ions are chelated by xylenol, thus modifying the UV-vis absorption spectrum of xylenol. At pH values between 2 and 4, the absorption spectrum of xylenol orange is characterized by a strong absorption band at 443 nm in the absence of Gd³⁺. When xylenol orange is coordinated to Gd³⁺, two main absorption bands are observed at 479

and 569 nm. The amount of the free chelators can then be retrospectively computed based on the amount of the Gd^{3+} added to the nanoparticle solution, until there is change in the color of the solution or change in the spectrum. On the other hand, luminescence assay is based on the principle of phosphorescence observed with the complex of europium with chelator. Luminescence titrations are more sensitive and accurate compared to the colorimetric assays and hence can be employed when the colorimetric assays fall short of providing necessary information. The concept of this innovative tool for accurate chelate quantification arises from (i) the finger print of lanthanide luminescent centres with the chelating agent, (ii) the high sensitivity at relatively low sample concentrations and (iii) the exclusion of the parasitic signals coming from the background. Europium has several advantages that makes it the lanthanide of choice for this assay; (i) Close chemical reactivity to gadolinium ions (ii) Similarity of the stability constants for chelation (DOTAGA, NODAGA) to that of gadolinium (iii) Sensitivity of the luminescence spectrum to the ion environment enabling separation of each component and (iv) The fluorescence background of residual organic impurities can be overcome due to long lifetime allowing time-resolved assays. In the case of functionalized AGuIX described in this chapter, the free chelator content was determined by luminescence assay. As can be seen from Figure II-14, the excitation of the europium chelate complex at 395nm results in an emission spectrum with two peaks at 595nm and 616nm. Varying concentration of Europium was incubated with fixed amount of functionalized nanoparticles at 80°C for 48h at pH 5 (acetate buffer) following which phosphorescence measurements were done. The estimate of the free chelators grafted on AGuIX could be made based on the inflection point observed in the titration curves. Based on these titration curves, it was observed that the amount of the free chelators appended on the AGuIX were around 10% in comparison to the pristine AGuIX (1-2% free chelators). This roughly translates to one free chelator on each nanoparticle that possesses approximately 10 DOTAGA-Gd chelates/complexes.

II-2.3 Radiolabelling and study of the stability of radiolabelled nanoparticles:

AGuIX nanoparticles have the potential to act as multimodal imaging agents in addition to their radiosensitising potential. The presence of the residual free chelators like DOTAGA can be labelled with a suitable isotope like ^{111}In for SPECT-MRI imaging [103]. With the advent of the commercial FDA approved PET-MRI systems for clinical diagnosis, it has become possible to obtain the functional and the anatomical information necessary for the detailed and accurate diagnosis in single sitting. Despite the commonly used radionuclide for PET is ^{18}F (half-life 110 min), ^{68}Ga (half-life 68 minutes) is gaining popularity owing to its ease of availability from a commercially available $^{68}\text{Ge}/^{68}\text{Ga}$ generator system that can deliver the ^{68}Ga nuclide reliably for up to a year, without the need of a cyclotron. NODAGA functionalized AGuIX have been used for PET-MRI imaging and have been shown to be radio-labelled with ^{68}Ga [100, 104]. Using the current novel scheme of functionalization, the NODAGA functionalized AGuIX have been demonstrated for first time to be radiolabelled with ^{64}Cu . Unlike ^{68}Ga , the 12.7-hours half-life of ^{64}Cu provides enough flexibility to image both smaller molecules and larger slowly clearing proteins and nanoparticles making it an isotope of choice for the proposed application.

The AGuIX-NODAGA nanoparticles could be easily radiolabelled with a facile protocol. Nanoparticles were incubated with ^{64}Cu in AcONH_4 buffer (pH: 5.8) for 45min at 37°C . Post the incubation, the radiolabelled nanoparticles were analysed with SA-ITLC using 0.1M EDTA as a mobile phase. The radiochemical purity of the nanoparticles was found to be satisfactory (>95%).

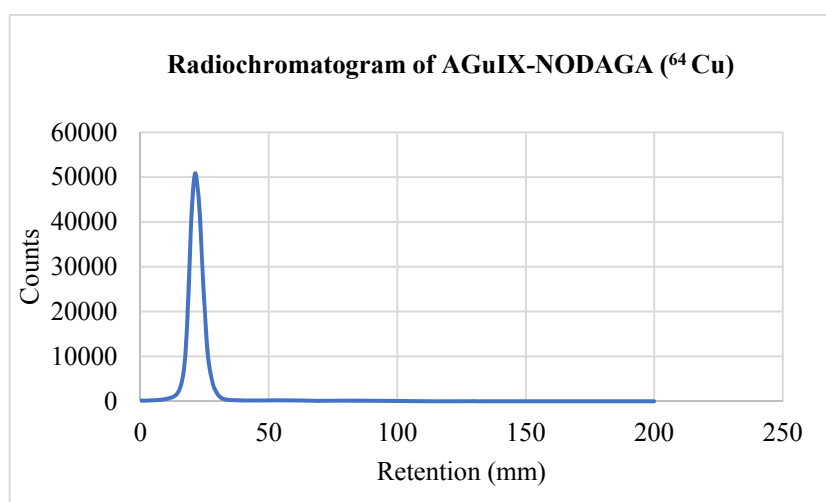


Figure II-15. Radio-chromatogram of the AGuIX-NODAGA(^{64}Cu) performed by ITLC using 0.1M EDTA as mobile phase.

With the good radiochemical purity, it becomes necessary to assess the integrity of the radiolabelled nanoparticles under physiological conditions, wherein the radiolabelled

nanoparticles might potentially undergo any alteration owing to nanoparticle degradation or trans-chelation of ^{64}Cu under the influence of endogenously present bivalent cations or chelating moiety. The radiolabelled nanoparticles were incubated with human plasma at 37°C for up to 48h. Moreover, EDTA challenge assay was performed at pH 7 in HEPES buffer to ascertain the resistance of the nanoparticle to trans-chelation by commonly employed chelating agent EDTA.

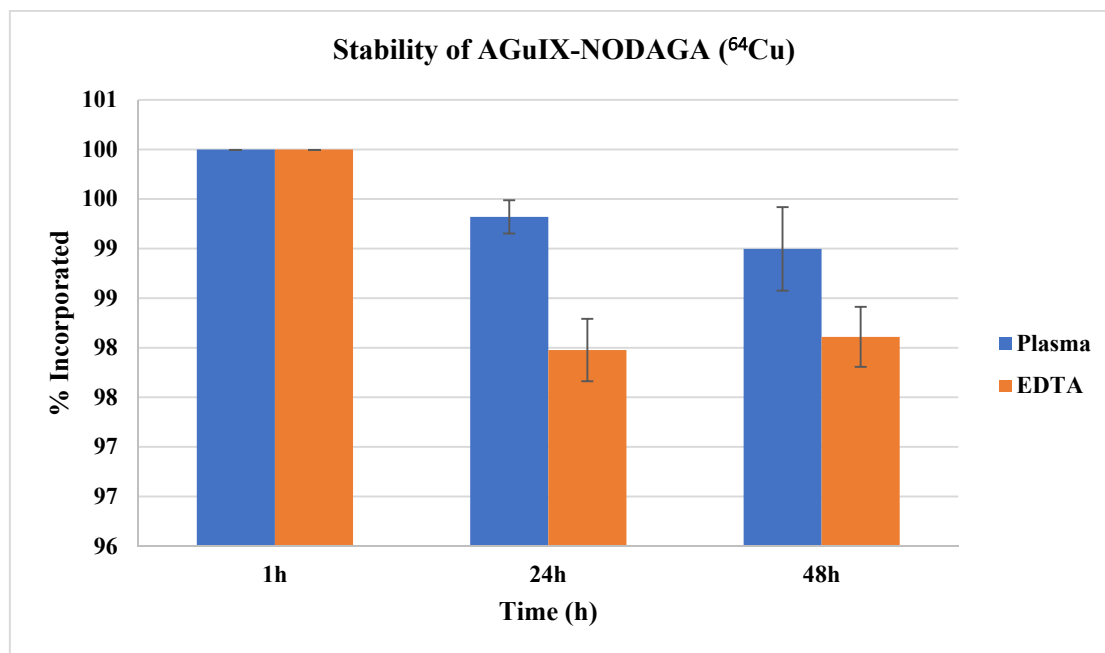


Figure II-16. Stability of the radiolabelled nanoparticles in human plasma and EDTA.

As can be seen from the above Figure II-16, the ^{64}Cu complexed AGuIX-NODAGA were found to be stable over much longer duration. More than 98% of the ^{64}Cu remained incorporated in the nanoparticles at end of 48h. The anticipated time spent by the nanoparticles inside the biological system (*in vivo-mice*) would be much shorter than 48h. EDTA challenge test revealed that more than 95% of the ^{64}Cu remained incorporated in the AGuIX-NODAGA at end of 48h. The large excess of EDTA experienced by the nanoparticles as in the above experiments may not be relevant to conditions *in vivo* but still generates the confidence in stability of radiolabelled AGuIX-NODAGA.

II-3 Animal imaging in TSA tumor model:

To evaluate the targeting potential and understand the pharmacokinetics of the nanoparticles the radiolabelled nanoparticles were intravenously injected into mice bearing TSA tumor (mammary adenocarcinoma). The dose of the nanoparticles was calibrated taking into consideration the amount of the nanoparticles needed for the radiosensitization during the radiotherapy based on the previous experience with these nanoparticles. The nanoparticles are currently under Phase I clinical trial in France for their radiosensitizing application. The nanoparticles were radiolabelled as explained earlier. 10mg of AGuIX-NODAGA(^{64}Cu) nanoparticles in PBS corresponding to activity of 10 MBq was injected via tail vein in each mouse (n=3). The PET-MR dual imaging was performed at 1 and 24 hours after the injection of the radiolabelled nanoparticles using a LabPET scanner (Trifoil Imaging) coupled in line with a small animal 3T MR small animal imaging system (MR Solutions) after anaesthetizing the mice with isoflurane (1.5-3% in air) [105]. After the last image acquisition, animals were sacrificed by isoflurane anaesthesia followed by pentobarbital overdose. Blood, tumour and organs were collected, weighed and radioactivity in these samples was measured with a gamma-well counter. The counter was cross-calibrated to the dose calibrator used to measure the injected dose and the linearity range was determined for all the geometries used in *ex-vivo* counting. Data were then converted to percentage of injected dose and to percentage of injected dose per gram of tissue.

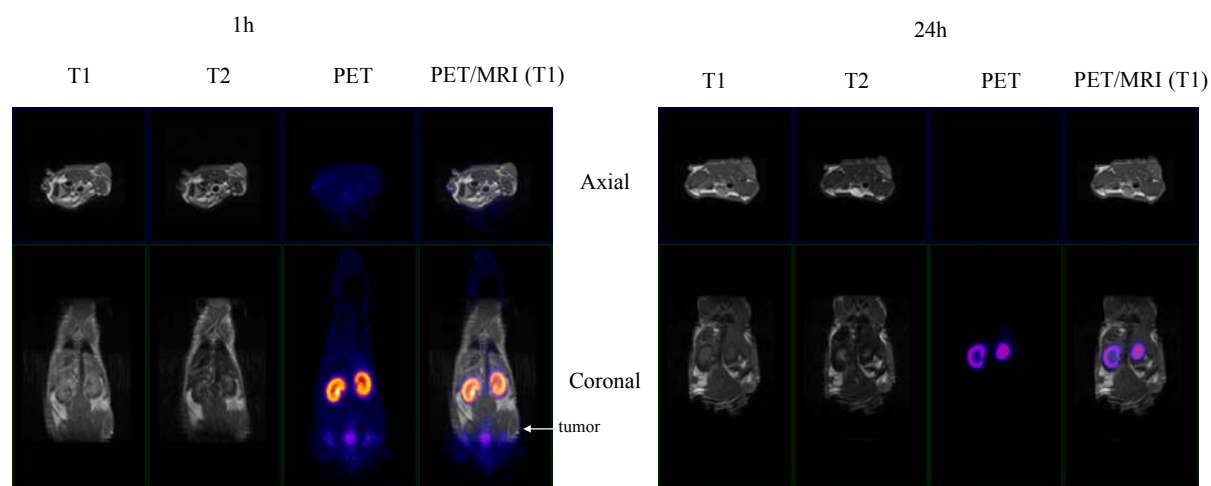


Figure II-17. PET-MRI imaging in TSA tumor models at 1h and 24h after injection of AGuIX-NODAGA(^{64}Cu).

As can be seen from the axial and the coronal images (Figure II-17), the nanoparticles provided enhanced PET-MRI images with modest accumulation at the tumor site and major accumulation in kidneys and bladder at end of 1h. At 24h, the decrease in the intensity of the signals was evident indicating excretion of the nanoparticle preferentially via renal route. This

was further compounded by the biodistribution analysis based on the gamma counting the signals received from the recovered organs (Figure II-18).

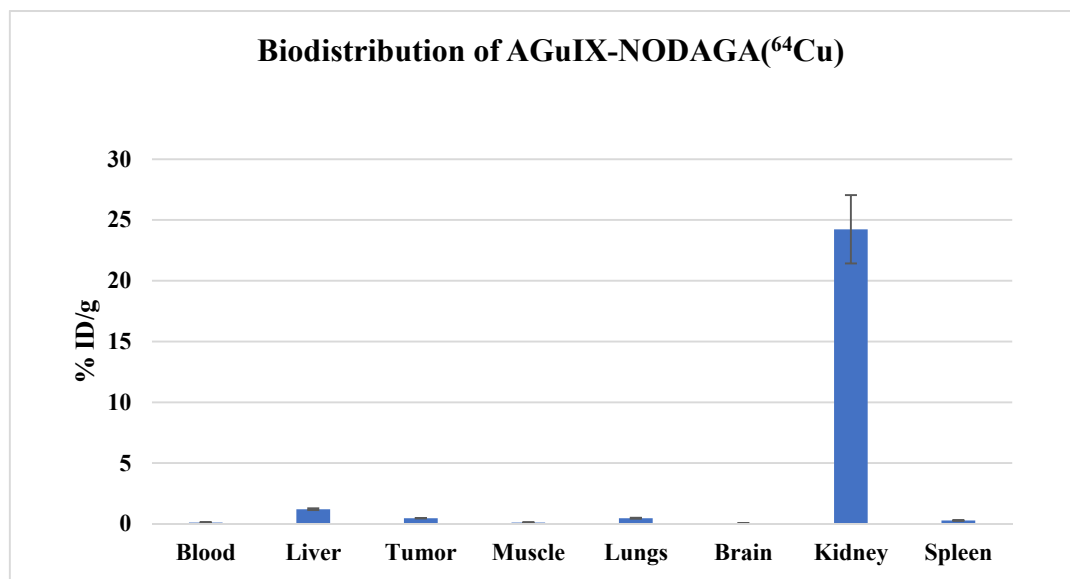


Figure II-18. Biodistribution of AGuIX-NODAGA(⁶⁴Cu) at the end of 24h.

At the end of 24h, the nanoparticles were observed to be distributed into liver, tumor, lungs and spleen. However, these signals were relatively quite weak compared to the signals from the kidneys which could possibly indicate that the nanoparticles are in process of getting excreted.

Moreover, at the end of 24h the nanoparticles are significantly cleared from the circulation with signals from blood almost nil. The accumulation in the tumor was not very high and several factors could be attributed to this including the tumor model/physiology and hence it could be interesting to evaluate this multifunctional system in other tumor models. Nonetheless, the studies highlight the fact that the nanoparticles can be cleared from the body via renal excretion and do not suffer from the problem of biopersistence in major organs as is observed with many other inorganic nanoparticles. This clearly demonstrates the value of this multifunctional nanoparticles in cancer theranosis.

II-4 Conclusions:

AGuIX are a novel and unique class of nanoparticles amongst several types of silica based nanoparticles reported in literature. These nanoparticles have exhibited an excellent theranostic value through their rigorous assessment in different pre-clinical models. Currently, these nanoparticles are undergoing clinical trials (Phase I) for their radiosensitizing application. The existing method of nanoparticle synthesis and functionalization is cumbersome and hence warranted new approaches for facile development. The works demonstrated in this chapter addresses this aspect as can be seen from below conclusions:

1. Silanes based on DOTAGA and NODAGA have been synthesized based on the prior knowledge and experience with these chelators and have been characterized using NMR, elementary analysis and mass spectrometry.
2. The chelator based silanes have been successfully demonstrated to be used for the functionalization of the AGuIX nanoparticles and these nanoparticles have been characterized qualitatively and quantitatively using various techniques.
3. The NODAGA functionalized nanoparticles have been radiolabelled with ^{64}Cu and the stability of the AGuIX- NODAGA (^{64}Cu) assessed in human plasma and EDTA has been shown to be favourable until 48h.
4. The NODAGA functionalized nanoparticles/ AGuIX- NODAGA (^{64}Cu) have been investigated in TSA tumor model in mice for the PET-MRI application. Pharmacokinetic and biodistribution studies demonstrated moderate tumor accumulation and renal clearance of the nanoparticles at the end of 24h, highlighting the theranostic potential of these nanoparticles.

The work performed in this chapter holds considerable value in terms of the applicability of the tools/approaches developed. The outcomes also highlight the strengths of the collaborative efforts between the teams in Dijon and Lyon. Further work encompasses, the optimization of the synthesis/functionalization processes in employing silanes to afford customized and well-defined materials as well as biological investigation in additional *in-vitro/in-vivo* tumor models to better ascertain their theranostic value.

*Chapter III. Multifunctional gold nanoparticles for cancer
theranosis*

III-1 Gold Nanoparticles for cancer theranosis:

Inorganic nanoparticles possess unique physico-chemical, optical and/or electronic properties compared to nanoparticles made of organic materials. These attributes are particularly useful for the development of imaging agents or theranostics. Amongst this class, gold nanoparticles are widely investigated nanoparticles for diverse set of applications including computed tomography, radiotherapy, MRI/PET/SPECT, drug delivery, etc. Gold nanoparticles have a high X-ray absorption coefficient (at 100 keV Au=5.16 and I=1.94), amenability to surface functionalization, good tissue compatibility, special surface plasmon resonance properties and ability to passively target tumor. The ease of functionalization of these nanoparticles make them unique as multifunctional nanoagents.

Chematech and ICMUB have been able to develop unique ligands based on linear or macrocyclic chelator compounds particularly for nanomedicine. These ligands have been successfully used for functionalization of gold nanoparticles. This has been achieved by harnessing the nanoparticle synthesis expertise of scientists led by Prof. Stephane Roux from UTINAM, Besançon. This collaboration is significant not just in terms of the institutional partnership but also within the framework of ARGENT as these gold nanoparticles will be/are being used and explored biologically for diverse cancer applications by the partners within this consortium.

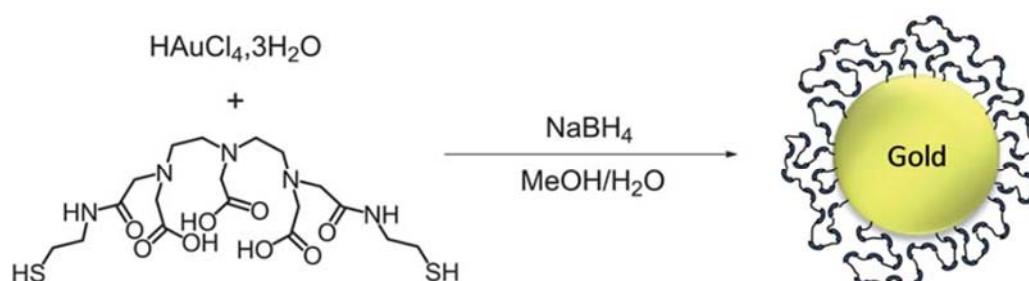


Figure III-1: Synthesis of gold nanoparticles based on DTDTPA. Adapted from [106].

The first-generation gold nanoparticles based on DTDTPA have been reported in 2008, DTDTPA was synthesized from diethylenetriaminepentacetic acid bis-anhydride and aminoethanethiol (Figure III-1)[107]. These nanoparticle ($\text{Au}@$ DTDTPA-Gd) were found to be promising for MRI imaging. Moreover, these nanoparticles have also been implicated in SPECT imaging and have been shown to be cleared from the body via renal excretion [106]. Owing to the presence of high atomic number atoms like Au and Gd, these nanoparticles have exhibited radiosensitizing properties in preclinical models of gliosarcoma and prostate cancer [108, 109]. These studies clearly stand the testimony to the multifunctionality of this class of gold nanoparticles.

Recently, gold nanoparticles based on macrocyclic chelators have been synthesized as an advancement over the DTDTPA based nanoparticles. Macrocyclic chelators have excellent chelating ability in terms of stability of the complexes with the heavy atom or radioisotope compared to the linear chelators like DTPA. In a recently published paper, gold nanoparticles based on macrocyclic ligands (Au@DTDOTA, Au@TA-DOTA and Au@TA-DOTAGA) have been shown to increase the lifespan of rats bearing 9L gliosarcoma owing to radiophysical effects after intravenous administration. It can also be noted that there were differences in the efficiency of radiosensitization amongst this class of nanoparticles which could be attributed to the structural changes associated with the macrocyclic ligands [110].

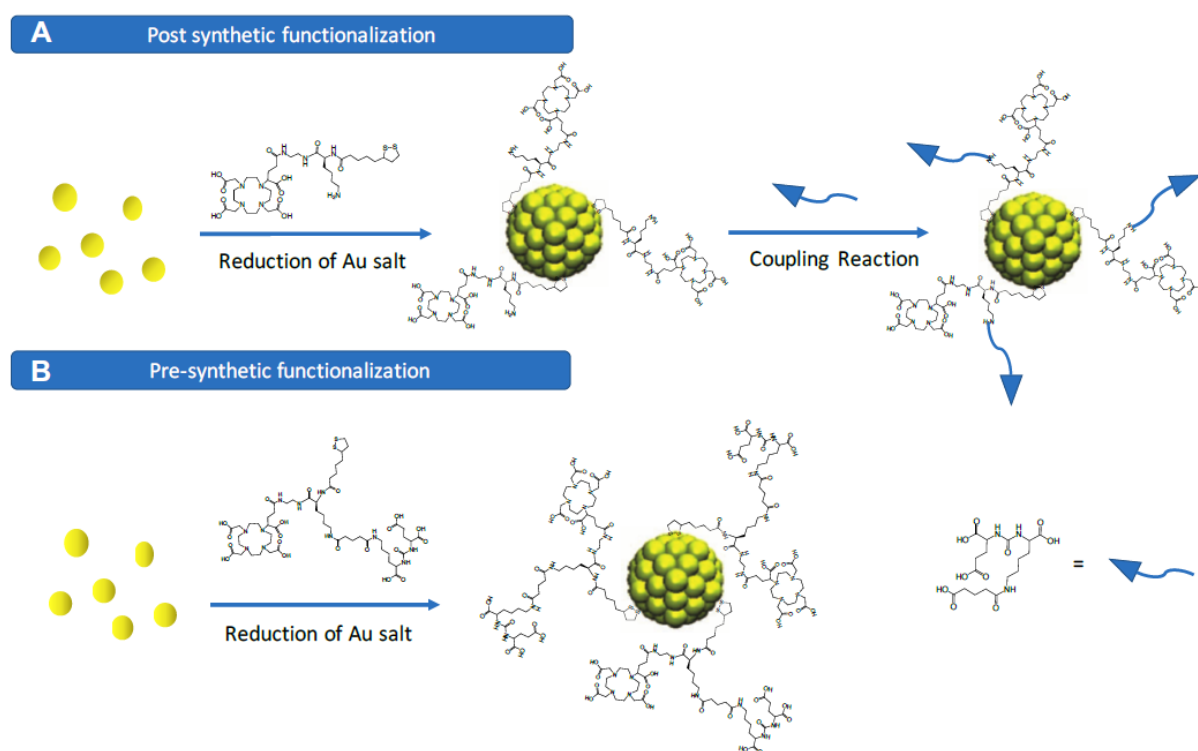
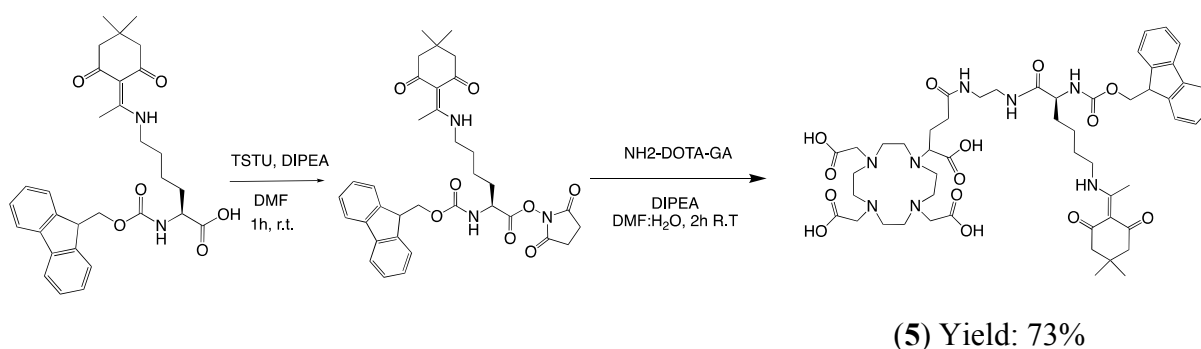


Figure III-2: Functionalization strategies for gold nanoparticles.

The nanoparticles mentioned above are limited in terms of further functionalization, for the purpose of imparting multimodality in the context of imaging or for active targeting. This stems from the absence of functional group that is easily amenable to grafting of a targeting ligand or an alternate chelating/contrast agent. This necessitates the availability of site on the ligand that can be easily conjugated to agents mentioned above. Development of ligand bearing an amino function presents a rational approach in developing the gold nanoparticles that can be functionalized later in a post-functionalization approach (Figure II-2_A). Alternatively, the amino bearing ligand can be derivatized with desired agent (targeting ligand) and then can be employed for gold nanoparticle synthesis depicting a pre-

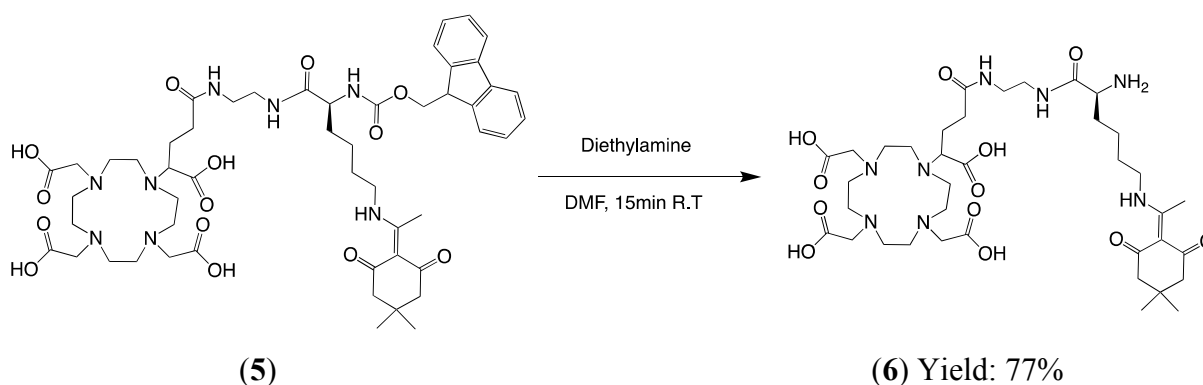
functionalization approach (Figure III-2_B). Generation of an amino group containing ligand was based on developing a linker system that is capable of integrating the chelating moiety, gold binding moiety and an amino group. Following sections describe the approaches and the ligands that were synthesized towards achieving this objective, so as to develop diverse set of gold nanoparticles with a high value in cancer theranosis.

III-2 Development of DOTAGA based amine functionalized gold nanoparticle:

III-2.1 Synthesis of DOTAGA-Lys-TA-NH₂Figure III-3: Synthesis scheme of DOTAGA-Lys-Fmoc-Dde (**5**).

The development of an amine functionalized gold nanoparticle began with synthesis of DOTAGA-Lys-Fmoc-Dde. Synthesis of DOTAGA-Lys-Fmoc-Dde (Figure III-10) could be realized by coupling of DOTAGA-NH₂ with activated NHS ester of Lysine-Fmoc-Dde. Since, the deprotected DOTAGA-NH₂ was used, the reaction was carried in aqueous DMF solution, as DOTAGA-NH₂ is only soluble in water. The NHS ester of Lys-Fmoc-Dde could be obtained in DMF solution and was verified by LC-MS following which DOTAGA-NH₂ was added to the reaction mixture to perform an amide coupling. The resulting compound (**5**) was purified by flash chromatography with the yield of 73% and HPLC purity of 98%.

Compound (**5**) was a crucial intermediate in terms of the orthogonality offered by the differentially protected lysine which can be explored in sequential manner to get the desired topology of the subsequent compounds.

Figure III-4: Synthesis of DOTAGA-Lys-Dde-NH₂ (**6**).

DOTAGA-Lys-Dde-NH₂ was obtained by deprotection of the Fmoc group present in compound (**5**) by treating with diethylamine (Figure III-4). The reaction proceeds very

quickly and does not alter the stability of the dde group present on the epsilon amino group. The purified compound (**6**) was characterized by HR-MS that revealed the molecular peak at 811.456 [M+H]⁺ and a purity of over 99%.

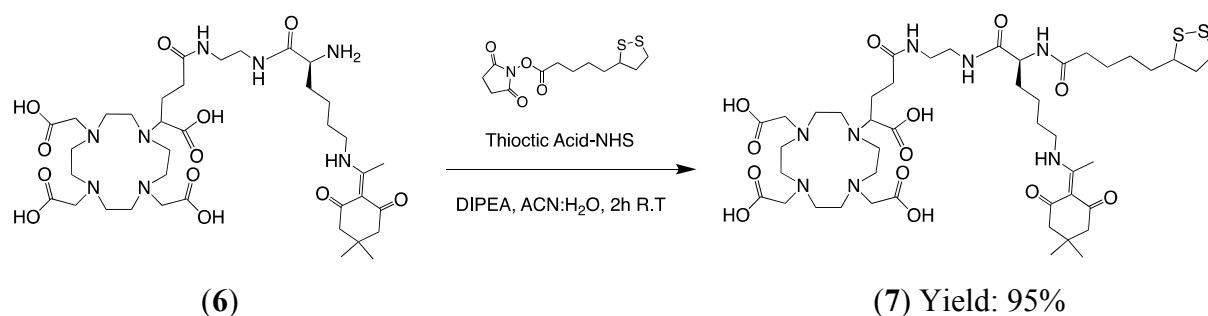


Figure III-5: Synthesis of DOTAGA-Lys-TA-Dde (**7**).

In order to impart the ability to compound to be employed for the synthesis of gold nanoparticles, it is necessary to possess the functionality that will bind over the surface of the gold surface. A thiol bearing moiety is a function of choice in developing gold nanoparticles. DTDTPA is a chelator bearing two thiol groups that has been demonstrated previously to be useful in the development of first generation gold nanoparticles. However, the replacement of linear chelators by macrocyclic chelators appears to be a better alternative as the latter forms more stable and inert complexes with gadolinium ions. Thioctic acid represents a preferable handle for the attachment of the chelator to the gold surface as it possesses two sulfur atoms that can enforce stronger, monomolecular and uniform bond formation between gold and the chelator and prevent any potential inter-molecular polymer formation unlike DTDTPA. This was achieved by treating compound (**6**) with pre-synthesized thioctic acid-NHS ester in the presence of base (Figure III-5). Amide coupling resulted in compound (**7**) that was purified by flash chromatography and obtained in good yield (95%) and purity.

The last step of the scheme entailed deprotection of the Dde group on the lysine side chain to obtain the anticipated compound containing the desired features. This was realized by adopting the deprotection strategy proposed by Bradley et al. [111].

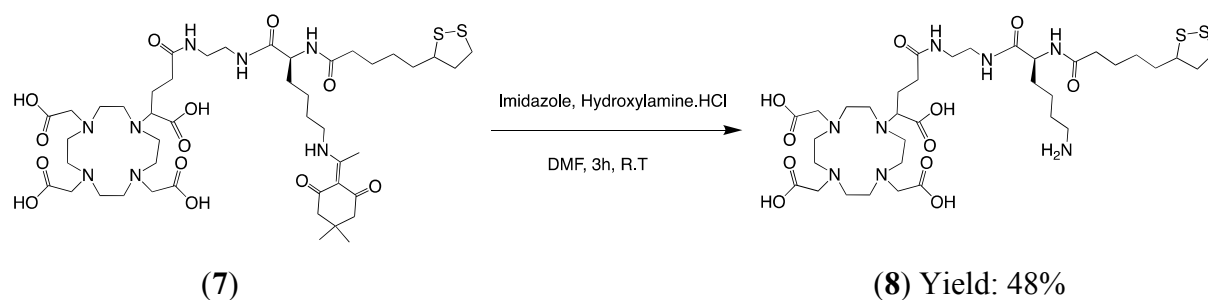


Figure III-6: Synthesis of DOTAGA-Lys-TA-NH₂ (**8**)

Treatment of compound (7) with imidazole and hydroxylamine hydrochloride in DMF resulted in clipping off of the Dde resulting in the expected compound (8) (Figure III-6). The compound was readily soluble in water and was hence considered good candidate for synthesis of gold nanoparticles. It was purified as a white creamish powder using C18 chromatography with a moderate yield of 48% and HPLC purity of 93%.

III-2.2 Amine functionalized DOTAGA gold nanoparticle (Au@DOTAGA-Lys-TA-NH₂):

Gold nanoparticles were developed employing the bifunctional ligand (8) that was synthesized for the theranostic application as described in preceding section. Typically, the gold salts were reduced using NaBH₄ in the presence of equimolar amount of the ligand (8). This experiment was performed at the lab of Prof. Stephane Roux in Besançon. The gold nanoparticles thus developed were stable in terms of the colloidal stability of the dispersion. The hydrodynamic diameter of these nanoparticles was around 5 nm as measured by DLS (performed in Besançon). This was in alignment with the previous observations made for the DTDTPA functionalized gold nanoparticles. Moreover, stability assessment of these nanoparticles was performed using UV-visible spectroscopy and the zeta potential measurements.

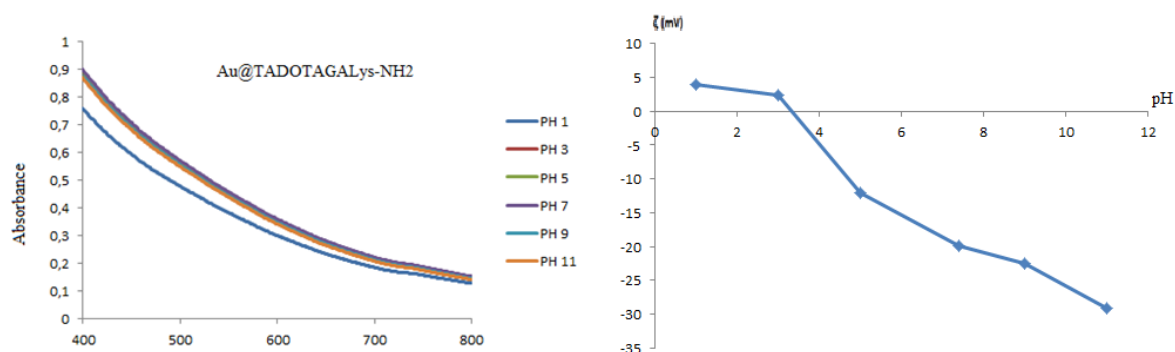


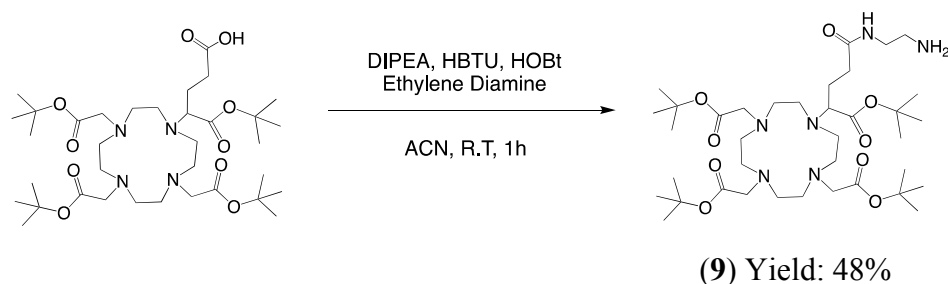
Figure III-7: UV-visible spectra of the Au@DOTAGA-Lys-TA-NH₂ nanoparticle solution and the zeta potential at different pH.

As can be seen from the above Figure III-7, the dilute nanoparticle solution exhibited a unique spectrum in the range of 400-750nm, that remained unchanged for a pH ranging from 1 to 12. Moreover, the zeta potential values over same pH range revealed a net negative surface charge at the physiological conditions (-20mV at pH 7.4). This can be expected owing to the presence of surface carboxylate groups from the chelate moieties. The DOTAGA moiety can be partially complexed with Gd (for MRI) or any other radioisotope for nuclear imaging and this is not expected to alter the stability of nanoparticles. Above observations clearly demonstrate the ability of the ligands to yield stable gold nanoparticles that can be of value in theranosis (radiotherapy and imaging).

III-3 Development of gold nanoparticles for PET-MRI:

III-3.1 Synthesis of DOTAGA-Lys-TA-NODAGA ligand

With a proof of concept demonstrated, pertaining to the development of the amine functionalized DOTAGA containing gold nanoparticles, attempts were made to develop and harness the amine function for developing more advanced gold nanoparticles. In the following section, we describe the approach adopted in this direction towards development of nanoparticles for PET-MRI application.

Figure III-8: Synthesis of DOTAGA(tBu)₄-NH₂ (9).

In order to develop the intermediates that be later used in a versatile manner for further addition of a functionality (e.g: chelator/targeting ligand), the protected form of the chelator was used, which otherwise would not be feasible with the unprotected chelator. The synthesis begins with DOTAGA(tBu)₄ which has been a key starting compound in majority of the tetraazacyclododecane based imaging probes in our group. DOTAGA(tBu)₄ is converted into its amine bearing form DOTAGA(tBu)₄-NH₂ through classical coupling chemistry using HBTU and HOBt as coupling agents (Figure III-8). Possibility of the covalent dimers formation necessitates the use of the ethylene diamine in excess (eq. 50). Post reaction work-up was necessary to get rid of the excess of the reagents. This involved washing of the organic phase (dichloromethane) successively with acidic, basic and neutral aqueous solutions followed by drying over MgSO₄. The compound was finally purified by flash chromatography using C18 column using water (0.1%) and acetonitrile (0.1%) as eluents. The compound (9) was obtained in good yield of 48% as a TFA salt.

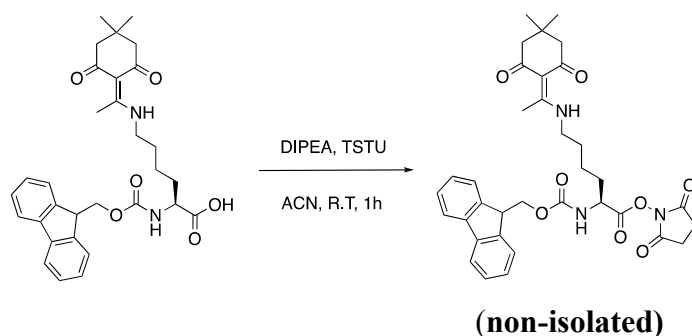
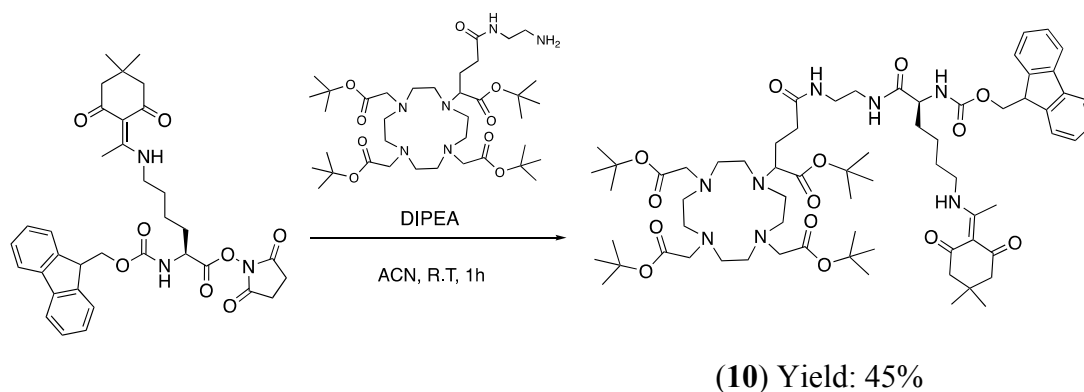
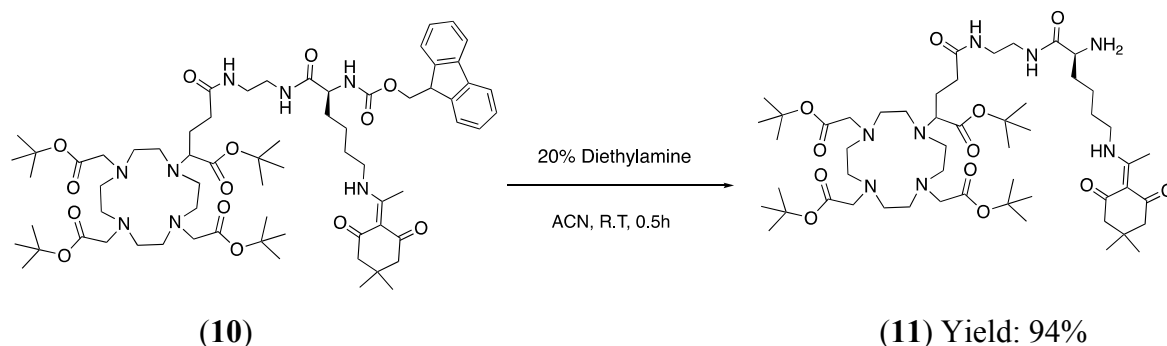


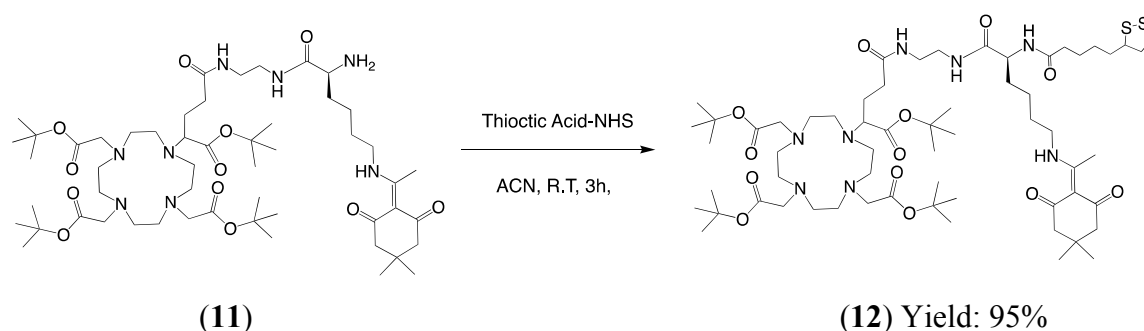
Figure III-9: Activation of Lysine-Fmoc-dde using TSTU.

Figure III-10: Synthesis of DOTAGA(tBu)₄-Lys-Fmoc-Dde (**10**).

The next step of the synthesis entailed the linker system which was based on lysine. Lysine-Fmoc-Dde was first activated to its ester form using TSTU (Figure III-9). The activated NHS ester of lysine-Fmoc-dde was then coupled to DOTAGA(tBu)₄-NH₂ via amide coupling to obtain the compound (**10**) (Figure III-10). This compound is unique in that it features the differently protected functional groups that can be successively deprotected and coupled at desired site to have a control over the topology of final compound.

Figure III-11: Synthesis of DOTAGA(tBu)₄-Lys-Dde-NH₂ (**11**).

Deprotection of the Fmoc group via the treatment with 20% diethylamine in acetonitrile afforded compound (**11**) with excellent yield and purity (98%) (Figure III-11). The compound exhibited the mass peak corresponding to the molecular ion at 1257.775 [M+H]⁺ using HR-MS.

Figure III-12: Synthesis of DOTAGA(tBu)₄-Lys-TA-Dde (**12**)

As demonstrated using the deprotected form of DOTAGA, thioctic acid could be easily coupled at the alpha amino position of the lysine linker (Figure III-12) to have a grafting function enabling attachment of this sophisticated system to the surface of the gold nanoparticle via the gold-sulphur interactions.

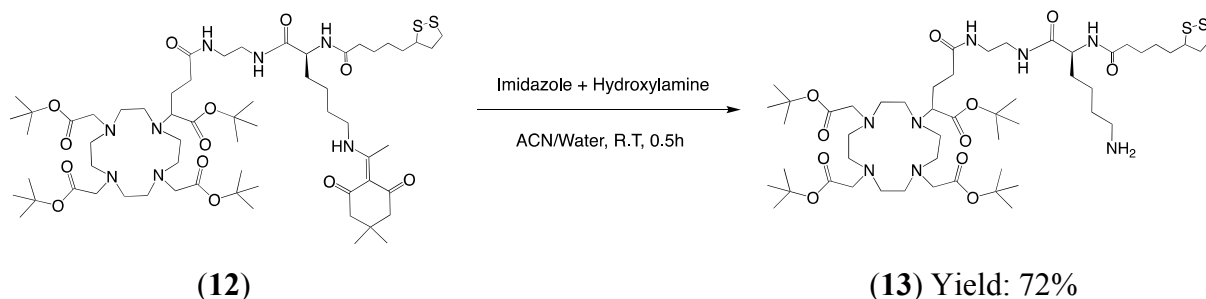


Figure III-13: Synthesis of DOTAGA(tBu)₄-Lys-TA-NH₂ (13)

In the second last step towards the generation of an important intermediate; compound (12) was deprotected to set the ϵ -amino group free using the equimolar ratio of imidazole and hydroxylamine hydrochloride in molar excess to that of the substrate (12). The reaction was carried out in solvent system containing ACN and water, to ensure that the polar (imidazole) and salt based (hydroxylamine hydrochloride) deprotection reagents were solubilized to elicit the reaction. Compound (13) was easily formed under the conditions indicated (Figure III-13) and was obtained in good yield (72%) after purification. Compound (13) represents the t-butyl protected form of the compound (8). As demonstrated in earlier section, compound (8) could be used for development of the amine functionalized gold nanoparticles. This affirmed the feasibility of using the ligands derived from compound (13) for the synthesis of gold nanoparticles. Compound (13) can be used as a crucial intermediate, the amino group of which could be modified using the relevant functions (like a chelating agent or a targeting ligand) resulting in a multi-functional ligand that can be deployed for the synthesis of gold nanoparticles as a part of pre-functionalization strategy (Figure III-2_B). Through this approach, the ligands bearing the relevant functions are used for the synthesis of gold nanoparticles that support dual functionality (bimodal imaging like PET-MRI or targeting) which are relatively easier for characterization unlike the post-functionalization of the gold nanoparticles.

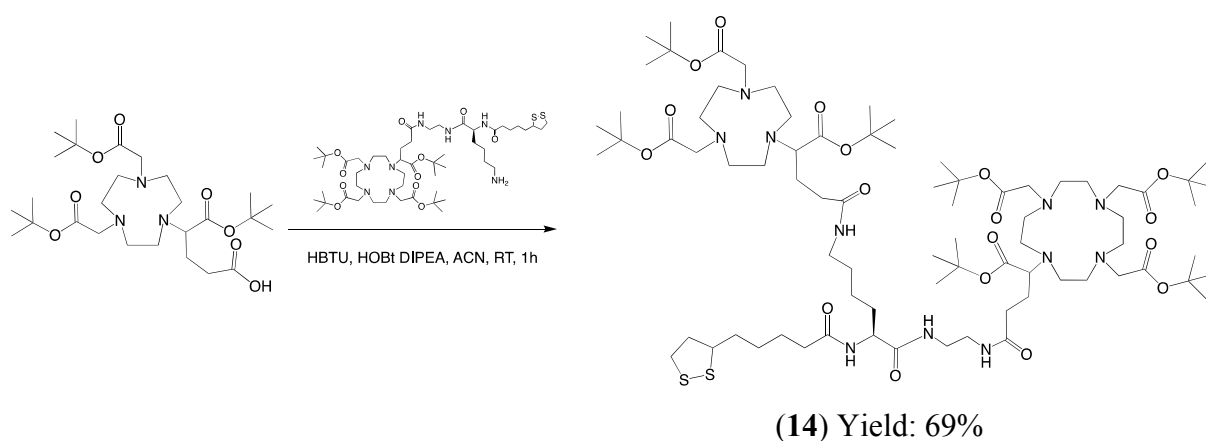


Figure III-14: Synthesis of DOTAGA(tBu)₄-Lys-TA-NODAGA(tBu)₃ (**14**)

The ϵ -amino group on the side chain of the compound (**13**) was derivatized with NODAGA(tBu)₃ using its NHS ester (Figure III-14). The resulting macromolecular compound (**14**) was obtained with a purity of 95% after flash chromatographic purification.

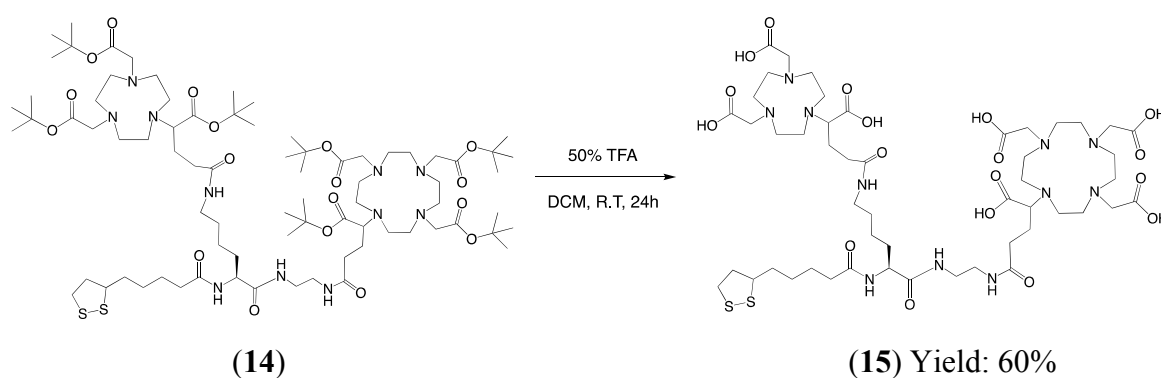


Figure III-15: Synthesis of DOTAGA-Lys-TA-NODAGA (**15**)

The t-butyl protected compound (**14**) was subjected to deprotection using 1:1 mixture of dichloromethane and TFA (Figure III-15). Deprotection could also be effected by use of conc. HCl or TFA as demonstrated for some of the simpler forms of t-butyl protected chelate compounds but could be harsh for the macromolecular structure described above. As a result, the deprotection was performed under milder conditions that ensured the integrity of the molecule which remains unaltered as revealed by the mass analysis that showed molecular ion peak at 1192.559 [M+H]⁺ and HPLC purity of 91%.

III-3.2 Gold nanoparticles based on DOTAGA-Lys-TA-NODAGA for PET-MRI:

Gold nanoparticles were developed employing the bifunctional ligand that was synthesized for PET-MRI application. Typically, the gold salts were reduced using NaBH_4 in the presence of equimolar amount of the ligand (**15**). This experiment was performed at the lab of Prof. Stephane Roux in Besançon. The gold nanoparticles thus developed were stable in terms of the colloidal stability of the dispersion. The hydrodynamic diameter of these nanoparticles was around 8nm as measured by DLS with gold core amounting to the size of 2.3nm as evidenced by the TEM measurements (analysis performed in Besançon). This was in alignment with the previous observations made for the DTDTPA functionalized gold nanoparticles. Moreover, stability assessment of these nanoparticles was performed using UV-visible spectroscopy and the zeta potential measurements. The optical properties of the gold nanoparticles are dependent on its size. Gold nanoparticles exhibit surface plasmon resonance owing to interaction of light with electrons on the gold nanoparticle surface resulting in strong extinction of light (absorption and scattering). The particular wavelength, or frequency, of light where this occurs is strongly dependant on the gold nanoparticle size, shape, surface and agglomeration state [112, 113]. UV-visible spectroscopy has been widely used to characterize the gold nanoparticles. However, gold nanoparticles having size around 2nm do not exhibit surface plasmon resonance and hence the UV-visible spectrum of the DOTAGA-Lys-TA-NODAGA nanoparticles appears without any sharp peak. Nonetheless, the changes in the UV-visible spectrum reflects a change in properties like size, shape and agglomeration state of the nanoparticles and serve as one of the stability indicating parameter.

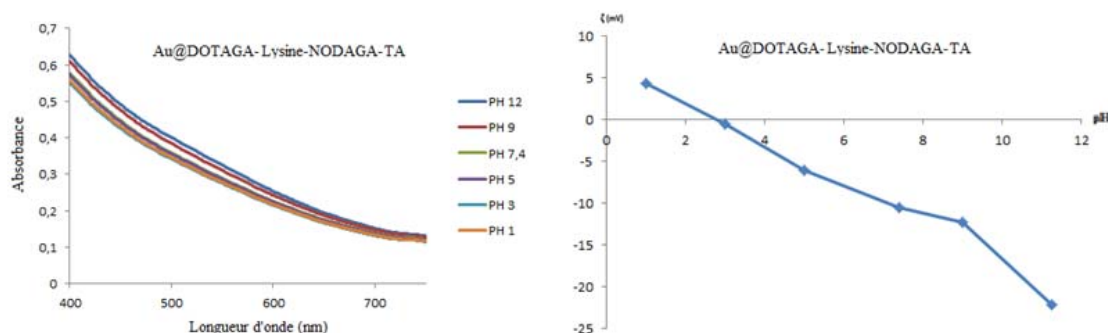


Figure III-16: UV-visible spectra of the Au@DOTAGA-Lys-TA-NODAGA nanoparticle solution and the zeta potential at different pH.

As can be seen from the Figure III-16, the dilute nanoparticle solution exhibited a unique spectrum in the range of 400-750nm, which remained unchanged for a pH ranging from 1 to 12. This property of the nanoparticle can also be useful for quantification of the nanoparticles in terms of the gold content once the extinction coefficient at a particular wavelength is

known or computed. To further assess and characterize the surface properties, zeta potential was measured over same pH range which confirmed the negative surface charge. A net negative surface charge of $\sim -10\text{mV}$ was observed at the physiological conditions at pH 7.4, which is believed to impart the colloidal stability to the nanoparticles. This can be expected owing to the presence of surface carboxylate groups from the chelate moieties. The DOTAGA moiety can be partially complexed with gadolinium, to improve the MRI contrast as well as increasing the radiosensitizing properties of these probes. On the other hand, NODAGA in small traces can be used for complexing the PET radio-isotope as the high sensitivity of the PET precludes the use of large amount of radioisotope and this is not expected to significantly alter the stability of nanoparticles. This has also been proven for the first-generation gold nanoparticles based on DTDTPA [106]. Above observations clearly demonstrate the ability of the ligands to yield stable gold nanoparticles that can be of value in PET-MRI imaging.

III-4 Radiolabelling and stability of the radiolabelled nanoparticles for PET-MRI:

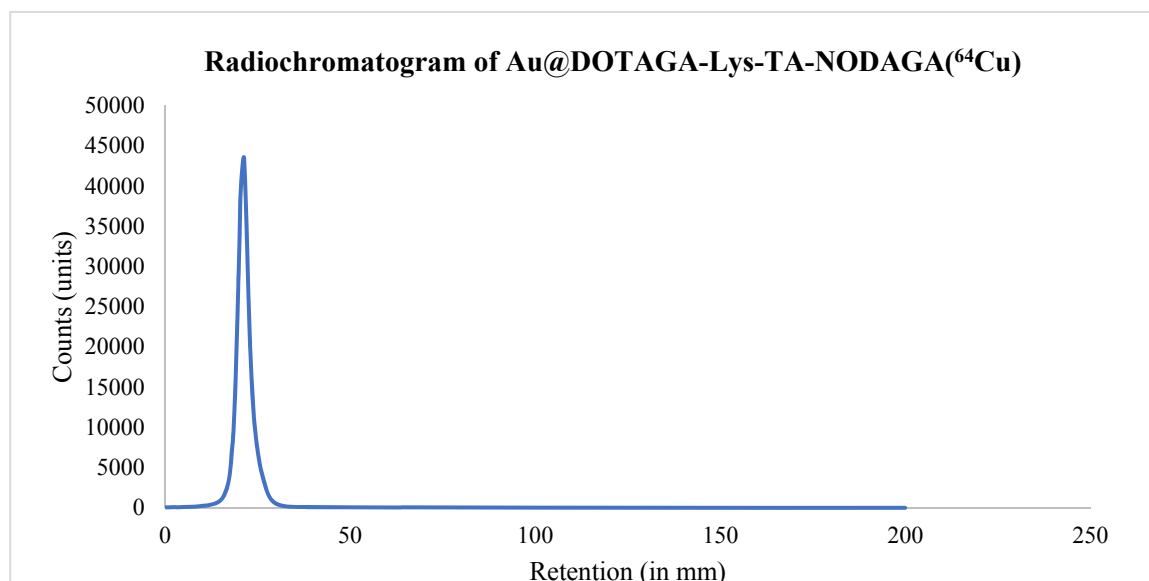


Figure III-17: Radiochromatogram of Au@DOTAGA-Lys-TA-NODAGA(⁶⁴Cu) as determined by ITLC using 0.1 M EDTA as mobile phase.

Following the demonstration of the synthesis of the nanoparticles using the ligand (**15**) the next step towards establishing the applicability of the nanoparticles was to radiolabel them. The Au@DOTAGA-Lys-TA-NODAGA nanoparticles were radiolabelled with ⁶⁴Cu in line with the strategy to use them as PET-MRI probe. Since, NODAGA forms rapid and stable complex with ⁶⁴Cu at ambient conditions unlike DOTAGA, it can be anticipated that the ⁶⁴Cu gets exclusively complexed by NODAGA. This holds true as well for gadolinium, however in opposite manner. Due to the presence of the abundant ligands (**15**) on the surface of the gold core in nanoparticles, the nanoparticles Au@DOTAGA-Lys-TA-NODAGA could be easily radiolabelled with ⁶⁴Cu by incubating at 37°C for 45min in 0.1M NH₄Ac buffer (pH 5.8). These conditions have been proven and observed to be optimal for radiolabelling with ⁶⁴Cu based on previous experience. As can be seen from the (Figure III-17), Au@DOTAGA-Lys-TA-NODAGA (⁶⁴Cu) exhibited a radiochemical purity of >95%. The radiolabelling protocol of the nanoparticles was quite facile since no purification was required as the relative amount of chelating agent compared to the radioisotope was quite high taking into account the anticipated dose of nanoparticles. Moreover, the presence of DOTAGA affords the opportunity of nanoparticles to be complexed with Gd for improving the MRI contrast and radiosensitizing properties of these nanoparticles.

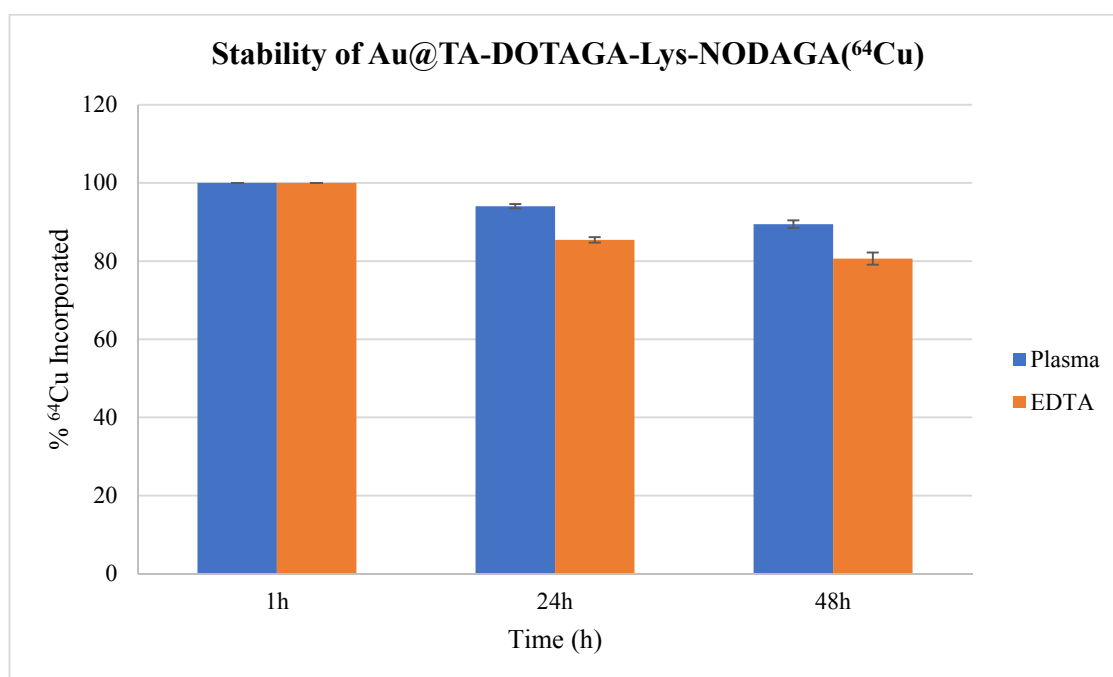


Figure III-18: Stability of Au@DOTAGA-Lys-TA-NODAGA(^{64}Cu) in plasma and EDTA.

To further investigate the stability of the Au@DOTAGA-Lys-TA-NODAGA(^{64}Cu) nanoparticles, the radiolabelled nanoparticles were subjected to incubation in human plasma and EDTA solution (chelate challenge study) at 37°C (Figure III-18). The incorporation of the ^{64}Cu into nanoparticles was found to efficient as the radiolabelled nanoparticles were stable and retained more than 90% and 80% of the incorporated ^{64}Cu at the end of 48h in plasma and 0.1M EDTA challenge solution. These observations justified the biological evaluation of these nanoparticles in relevant tumor model to investigate their pharmacokinetic properties.

III-5 Animal imaging and biodistribution studies in TSA tumor model:

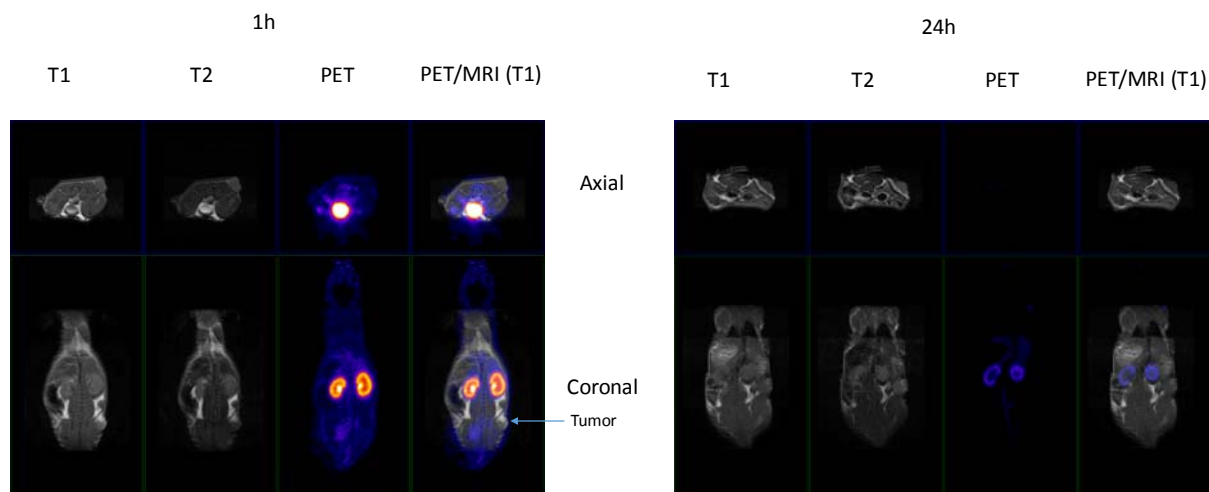


Figure III-19: PET-MRI imaging in TSA tumor models at 1h and 24h after injection of Au@DOTAGA(Gd)-Lys-TA-NODAGA(^{64}Cu).

To evaluate the targeting potential and understand the pharmacokinetics of the nanoparticles the radiolabelled nanoparticles were intravenously injected into mice bearing TSA tumor. The dose of the nanoparticles was calibrated taking into consideration the amount of the nanoparticles needed for the radiosensitization during the radiotherapy based on the previous experience with this type of gold nanoparticles. The nanoparticles were radiolabelled as explained earlier. 1mg of Au@DOTAGA(Gd)-Lys-TA-NODAGA(^{64}Cu) nanoparticles in PBS with activity of 10 MBq was injected via tail vein in each mouse ($n=3$). The PET-MR dual imaging was performed at 1 and 24 hours after the injection of the radiolabelled nanoparticles using a LabPET scanner (Trifoil Imaging) coupled in line with a small animal 3T MR small animal imaging system (MR Solutions) after anaesthetizing the mice with isoflurane (1.5-3% in air) [105]. After the last image acquisition, animals were terminated by isoflurane anesthesia followed by pentobarbital overdose. Blood, tumour and organs were collected, weighed and radioactivity in these samples was measured with a gamma-well counter. The counter was cross-calibrated to the dose calibrator used to measure the injected dose and the linearity range was determined for all the geometries used in *ex-vivo* counting. Data were then converted to percentage of injected dose and to percentage of injected dose per gram of tissue.

As can be seen from the axial and the coronal images (Figure III-19), the nanoparticles provided enhanced PET-MRI images with slight accumulation at the tumor site and major accumulation in kidneys and bladder at end of 1h. At 24h, the decrease in the intensity of the signals was evident indicating excretion of the nanoparticle preferentially via renal route. This

was further compounded by the biodistribution analysis based on the gamma counting the signals received from the recovered organs (Figure III-20).

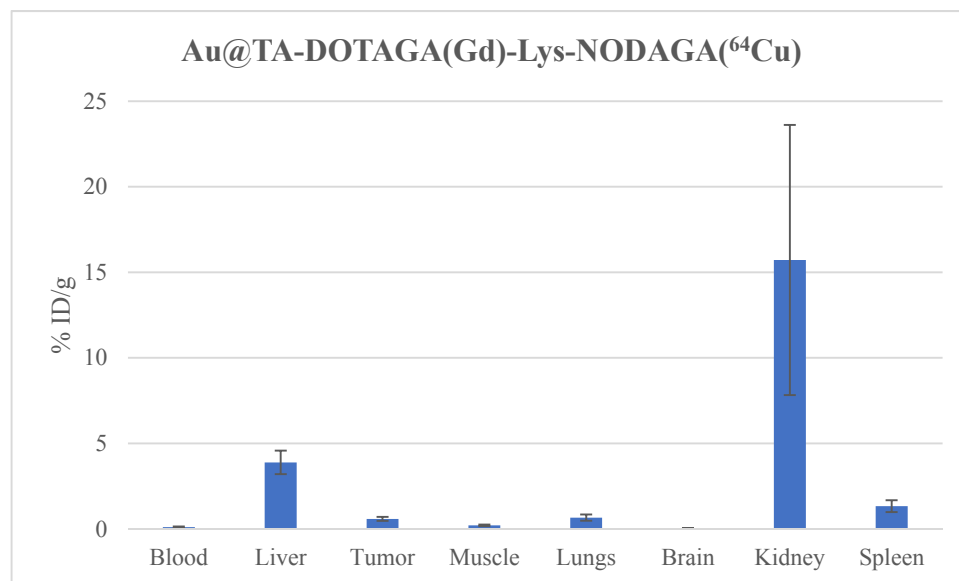


Figure III-20: Biodistribution of Au@DOTAGA(Gd)-Lys-TA-NODAGA(⁶⁴Cu) at the end of 24h.

At the end of 24h, the nanoparticles were observed to be mainly distributed into kidneys and to certain extent in liver, tumor, lungs and spleen. The stronger signals from kidneys (15.7 ± 7.89 %ID/g) compared to the signals from other organs could possibly indicate that the nanoparticles are in process of getting excreted. The accumulation in the tumor was very minimal (0.59 ± 0.11 %ID/g) and many factors could be attributed to this including the tumor model/size/physiology and hence it could be interesting to evaluate this multifunctional system in other tumor models. Nonetheless, the studies highlight the fact that the nanoparticles can be cleared from the body via renal excretion and do not suffer from the problem of biopersistence in major organs as is observed with many other inorganic nanoparticles. This clearly demonstrated the value of this multifunctional gold nanoparticles in cancer theranosis.

III-6 Development of PSMA targeted gold nanoparticles:

Due to the ease of its synthesis and the amenability to be grafted onto the macromolecular surface without significantly altering its properties, urea based PSMA inhibitors have been used for targeting nanoparticles for drug delivery [114, 115], macromolecular drug conjugates [116] and nanoparticles for imaging/brachytherapy [117-119]. Kasten et al., demonstrated feasibility of synthesis of the PSMA targeted gold nanoparticle wherein, the phosphoramidate peptidomimetic PSMA inhibitor was coupled to biotin and grafted non-covalently onto streptavidin coated gold nanoparticles using the streptavidin-biotin complex [120]. PSMA targeted gold nanoparticles containing a macrocyclic chelator can be of immense value in developing theranostic agents having value both as imaging (SPECT) and radiosensitizer. The monomolecular multimodal platform can be adapted to develop such novel tools as has been described in the following sections.

III-6.1 Synthesis of the DOTAGA-Lys-TA-Glu-PSMA

As an extension to the application towards the development of targeted gold nanoparticles based on pre-functionalization strategy, ligand bearing the targeting moiety and the macrocyclic chelator was synthesized utilizing the amino bearing intermediate/DOTAGA(tBu)₄-Lys-TA-NH₂ (**13**) (Figure III-13) and PSMA ligand. The approach entailed modification of the PSMA targeting ligand so as to develop a spacer and a coupling handle between the pharmacophore and the intermediate bearing the site of nanoparticle conjugation and the chelator. The PSMA ligand precursor was kindly provided by Dr. Victor Gonçalves.

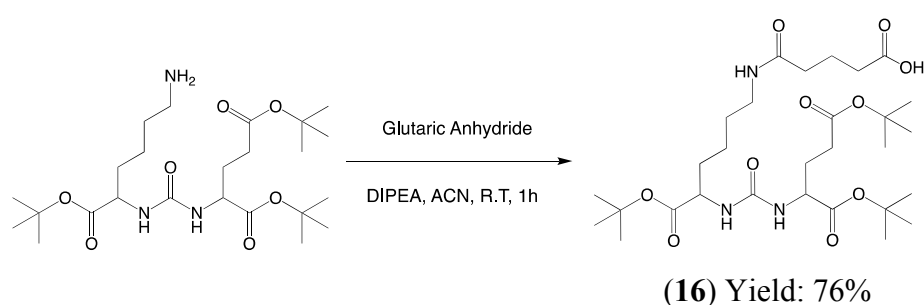


Figure III-21: Synthesis of PSMA(tBu)₃-Glutarate (**16**).

As has been demonstrated in some of the reports earlier, a glutarate arm was introduced at the lysine residue of the urea based ligand. This could be easily achieved with commercially available glutaric anhydride. The translucent compound (**16**) was obtained in moderate yield (76%) and provided the carboxylate site that could be used for further amide coupling (Figure III-21).

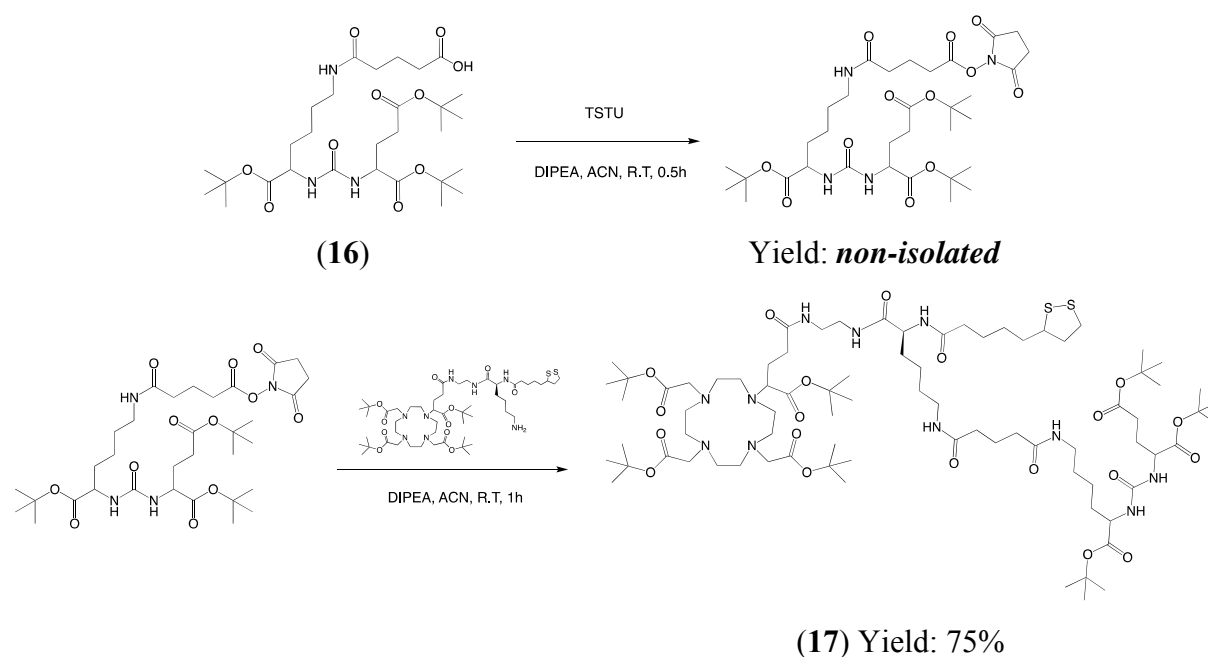


Figure III-22: Synthesis of DOTAGA(tBu)₄-Lys-TA-Glu-PSMA(tBu)₃ (17).

The carboxylate bearing compound (16) was activated to its NHS ester form using TSTU and then treated with the amino bearing intermediate (13) to afford the compound (17) (Figure III-22). The course of the synthesis was verified by LC-MS analysis and the purification was made using flash chromatography with C18 column employing the mobile phase (water: acetonitrile) containing TFA as is the case for most of the compounds.

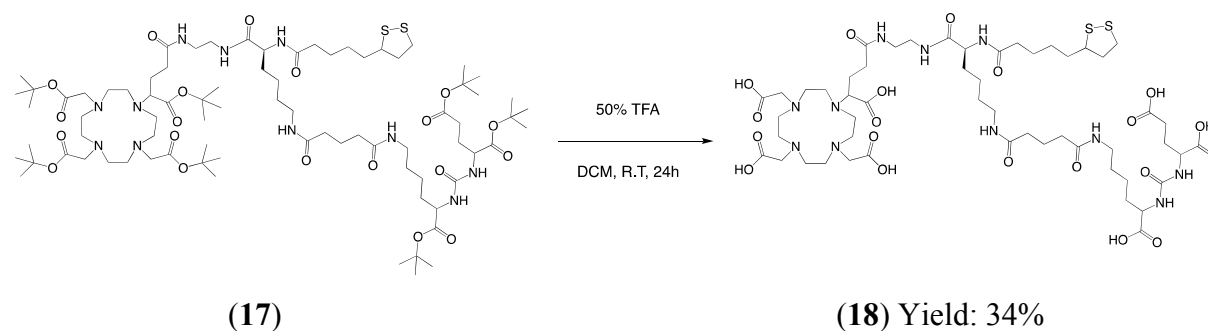


Figure III-23: Synthesis of DOTAGA-Lys-TA-Glu-PSMA (18).

Mild deprotection conditions were used to deprotect the t-butyl protected compound (17) as described in preceding sections. (Figure III-23). The compound was finally recovered as a TFA salt in the form of a white powder after purification. The compound was readily soluble in water and hence is considered valuable in development of targeted gold nanoparticles.

III-6.2 Determination of the PSMA binding activity using the enzymatic assay:

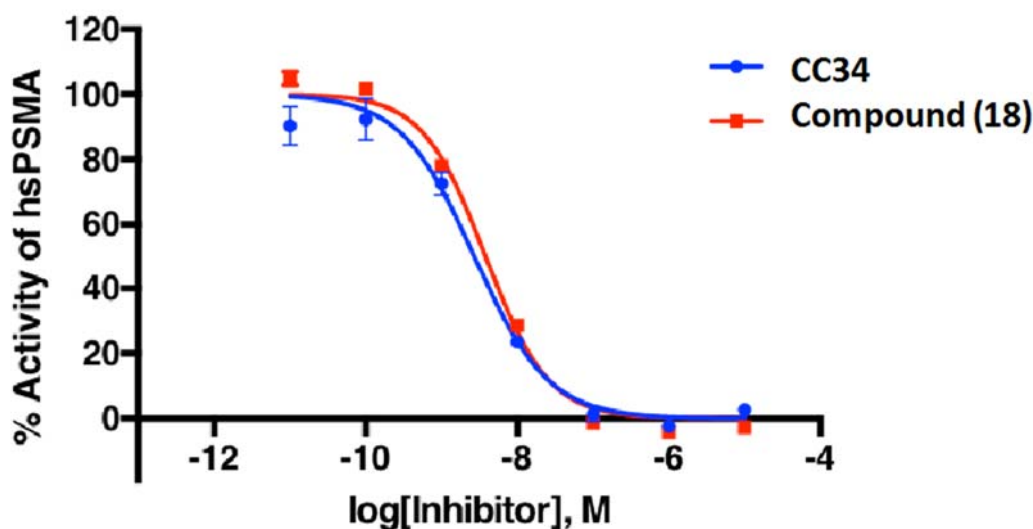


Figure III-24: Binding affinity of ligands (CC34 & 18) towards PSMA using enzymatic assay.

To evaluate the binding affinity of this ligand we performed the NAALDase assay using the commercially available assay kits from R&D Systems. The assay employs recombinant human PSMA that has ability to hydrolyse the substrate N-acetyl-L-Asp-L-Glu into N-acetyl-L-Asp and L-Glu. The L-Glu product is measured by fluorescence after its derivatization by *ortho*-phthaldialdehyde. This enzyme also has the ability to hydrolyse the ureido derivatives containing L-Glu which have been reported in numerous articles involving PSMA based theranostic agents. The extent of the released L-Glu as detected by fluorescence in relation to the quantity of the theranostic probe (ureido derivative) indicates the binding ability/potency of the PSMA based probe.

This assay has been routinely employed in our group particularly by Dr. Victor Gonsalves for evaluation of the PSMA based probes developed at ICMUB. CC34 is one such PET imaging probe which has shown a considerable promise born out of Master's thesis of Coline Canovas and developed in collaboration with Prof. Helmut Maecke for clinical imaging. The details concerning this compound and its background will be discussed extensively in Chapter IV that exclusively focusses on PSMA. As a control for the experiment, we compared head to head, the activity of our ligand with that of CC34 and it was observed that the binding or inhibitory activity of (18) was very close to that of CC34 (Figure III-24). This paved the way for employing (18) in the synthesis of the gold nanoparticles targeted towards PSMA.

III-6.3 Gold nanoparticle based on DOTAGA-Lys-TA-Glu-PSMA:

With the promising affinity towards PSMA, the ligand (**18**) was justified to be employed for the development of the targeted gold nanoparticles. Typically, the gold salts were reduced using NaBH₄ in the presence of equimolar amount of the ligand (**18**). These experiments were performed in collaboration with Prof. Stephane Roux at Université de Franche-Comté, Besançon. The gold nanoparticles developed were found to be stable in terms of the colloidal stability of the dispersion. The hydrodynamic diameter of these nanoparticles was observed to be around 7nm as measured by DLS (analysis performed in Besançon). These results were in agreement with the previous observations made with nanoparticles based on (**15**) and DTDTPA (first generation) functionalized gold nanoparticles. The stability of these nanoparticles was assessed using UV-visible spectroscopy and the zeta potential measurements.

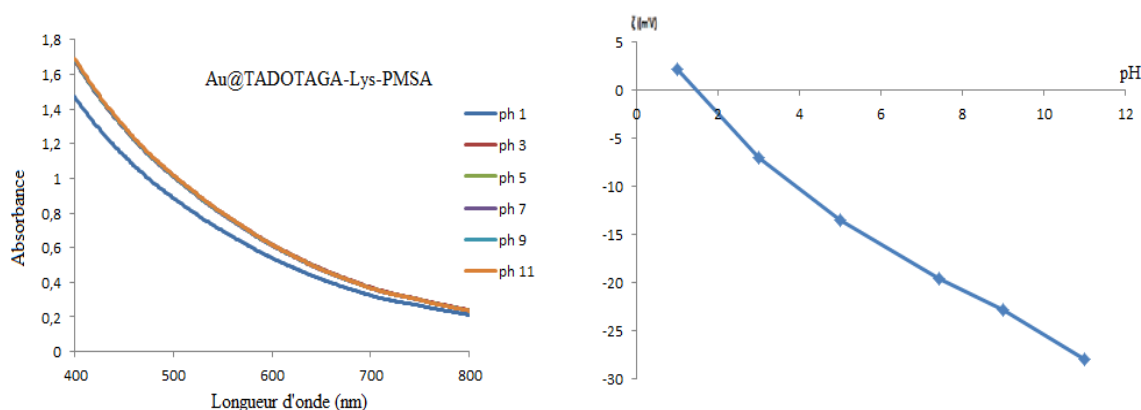


Figure III-25: UV-visible spectra of Au@DOTAGA-Lys-TA-Glu-PSMA nanoparticle solution and the zeta potential at different pH.

As can be observed from the above figure 4-5, the dilute nanoparticle solution exhibited a unique spectrum in the range of 400-750nm, that remained unchanged for a pH ranging from 1 to 12. Moreover, the zeta potential values over same pH range revealed a net negative surface charge at the physiological conditions (-20mV at pH 7.4). This can be expected owing to the presence of surface carboxylate groups from the chelate moieties as well as the PSMA ligand. The DOTAGA moiety on the nanoparticles can be partially complexed with gadolinium, to impart the contrast enhancing properties for MRI and improving the radiosensitizing properties of the nanoparticles. Alternatively, the DOTAGA can also be used in smaller amounts for complexation with SPECT relevant radioisotope like ¹¹¹In. This design of the ligand makes it versatile and indeed multi-functional yet meeting the criterion of stability as can be seen from above graphs. These observations justify the ability of the ligands to yield stable gold nanoparticles that can be of value in targeted imaging and therapy in prostate cancer management.

III-7 Radiolabelling and stability study of the PSMA targeted nanoparticles:

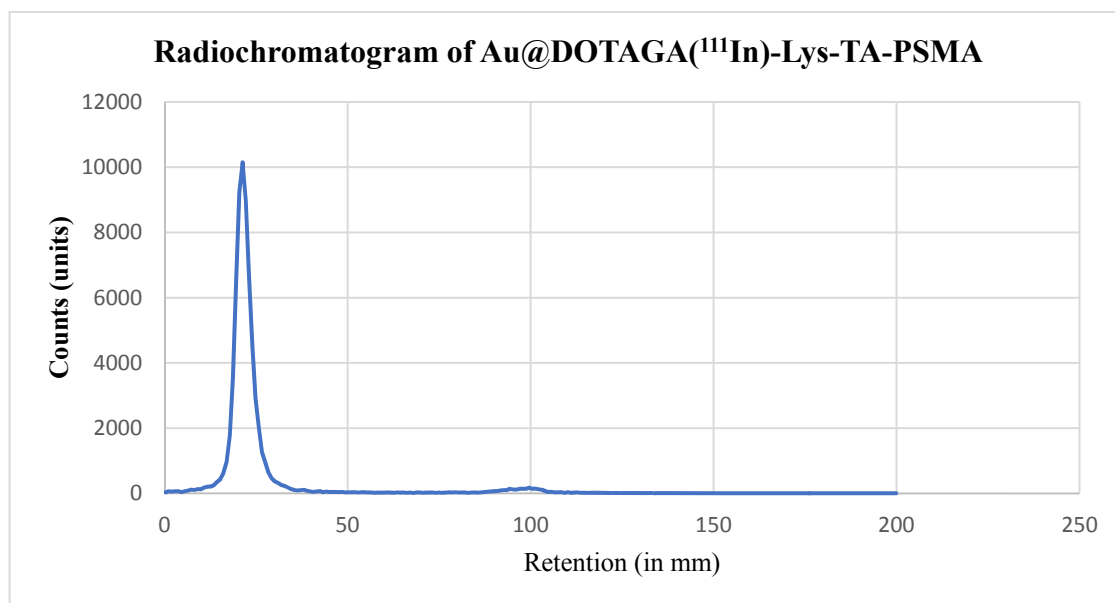


Figure III-26: Radiochromatogram of Au@DOTAGA(¹¹¹In)-Lys-TA-PSMA as determined by ITLC using 0.1 M EDTA as mobile phase.

Having demonstrated the affinity of the ligand (**18**) towards PSMA and successful synthesis of stable gold nanoparticles using it, the nanoparticles were further radiolabelled with ¹¹¹In. Radiolabelling with ¹¹¹In was made keeping in mind the propensity of the chelate (DOTAGA) to form a stable complex with ¹¹¹In, so that nanoparticles can be tracked and could find application in targeted SPECT imaging in prostate cancer. Due to presence of the abundant ligands (**18**) on the surface of the gold core in nanoparticles, the nanoparticles Au@DOTAGA-Lys-TA-PSMA could be easily radiolabelled with ¹¹¹In by incubating at 37°C for 1h in 0.1M NH₄Ac buffer (pH 5.8). As can be seen from the figure 4-6, Au@DOTAGA(¹¹¹In)-Lys-TA-PSMA exhibited the radiochemical purity of >95%. The radiolabelling protocol of the nanoparticles was quite facile in that there was no purification needed as the relative amount of chelating agent compared to the radioisotope was quite high. Moreover, this relative abundance can also permit some of the chelate to be complexed with Gd for improving the MRI contrast and radiosensitizing properties of these nanoparticles. To further assess the stability of the Au@DOTAGA(¹¹¹In)-Lys-TA-PSMA nanoparticles, the radiolabelled nanoparticles were subjected to incubation in human plasma and EDTA solution (chelator challenge study) at 37°C, as has been done with AGuIX nanoparticles in Chapter II.

III-8 Development of a PET-Optical ligand for gold nanoparticles:

In another interesting application towards development of multimodal gold nanoparticles, ligands for the fabrication of gold nanoparticles were envisaged for PET-optical imaging. This entails development of a monomolecular multimodal platform that encompass; PET chelator, fluorescent dye and a gold conjugatable handle. Following section describes in a stepwise manner the realization of this ligand and its photophysical characterization.

III-8.1 Synthesis of a PET-Optical ligand for gold nanoparticles

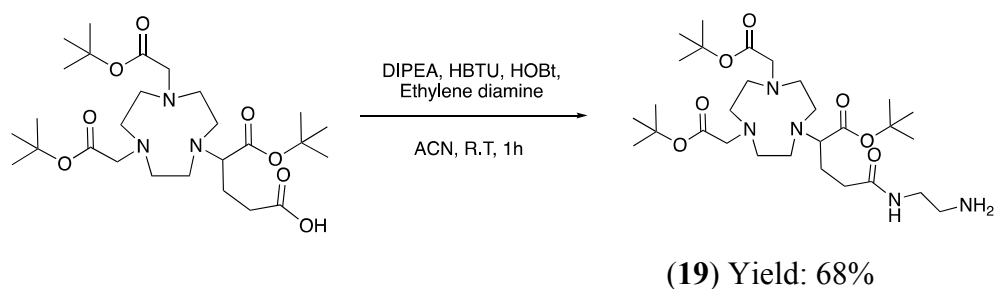


Figure III-27: Synthesis of NODAGA(tBu)₃-NH₂ (19).

The synthesis commences with NODAGA(tBu)₃ which has been a key starting compound in majority of the PET based imaging probes in our group. NODAGAtBu₃ is converted into its amine bearing form NODAGA(tBu)₃-NH₂ through classical coupling chemistry using HBTU and HOBT as coupling agents (Figure III-27). Possibility of the covalent dimers formation necessitates the use of the ethylene diamine in excess (eq. 50). Post reaction work-up was necessary to get rid of the excess of the reagents. This involved washing of the organic phase (dichloromethane) successively with acidic, basic and neutral aqueous solutions followed by drying over MgSO₄. The compound was finally purified by flash chromatography using C18 column using water (0.1%) and acetonitrile (0.1%) as eluents. The compound (19) was obtained in good yield of 68% as a TFA salt.

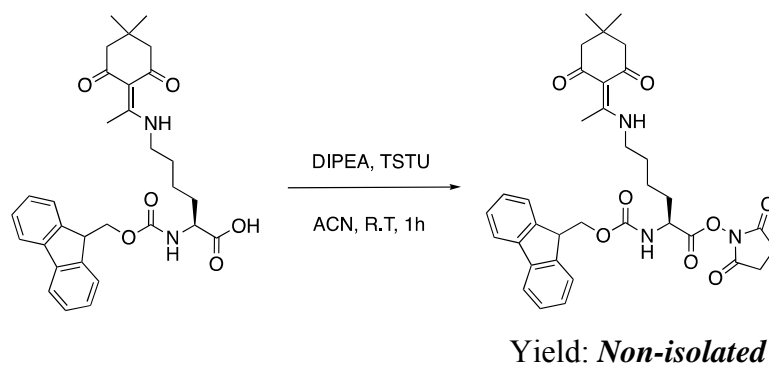


Figure III-28: Synthesis of Lysine-Fmoc-Dde-NHS.

The next step entails use of the appropriately protected lysine as a linker which in our case

has been Fmoc-Lys(Dde)-OH, as explained in preceding sections. The lysine (carboxylate) was activated to obtain an NHS ester (in-situ). The NHS ester formation could be easily verified by LC-MS as the ester is fairly stable during the course of chromatographic analysis.

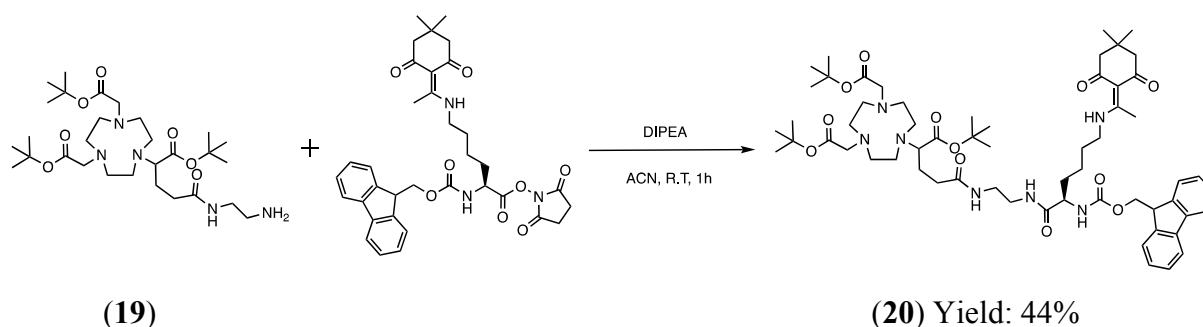


Figure III-29: Synthesis of NODAGA(tBu)₃-Lys-Fmoc-Dde (**20**).

The activated Fmoc-Lysine-Dde was coupled to NODAGA (tBu)₃-NH₂ through formation of a peptide link. The compound could be recovered with the yield of 44% after C18 chromatographic purification (Figure III-29). This compound (**20**) represents a very important intermediate owing to the presence of differently protected groups which could be exploited in diverse manner in order to achieve the desired placement of the functional moieties over the course of subsequent deprotection-coupling reactions.

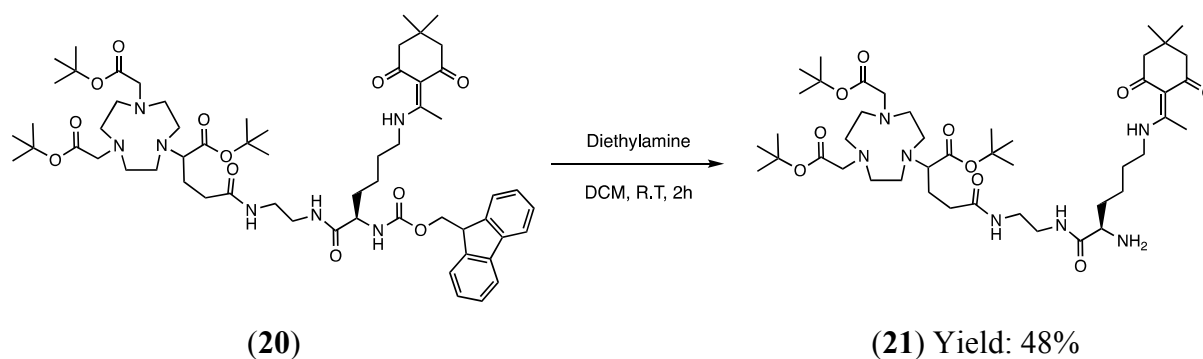
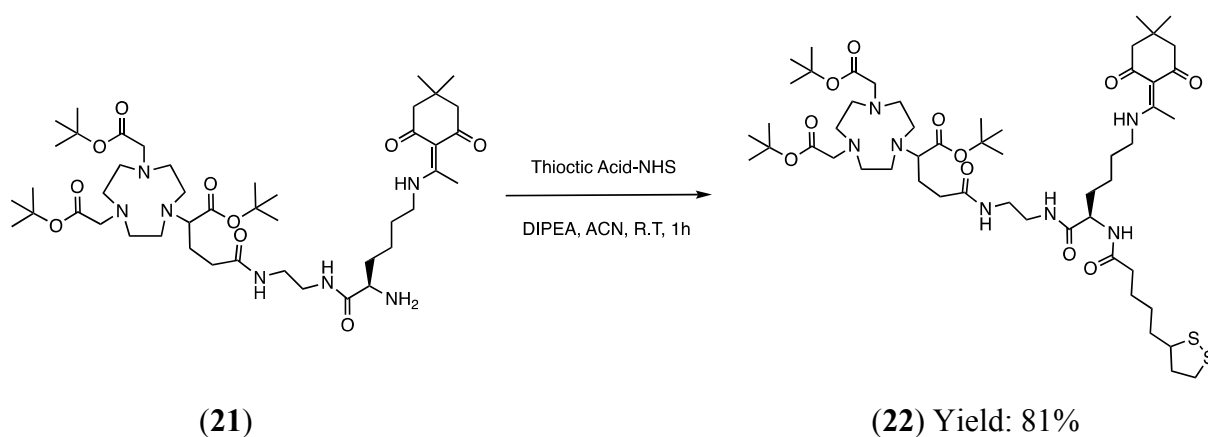
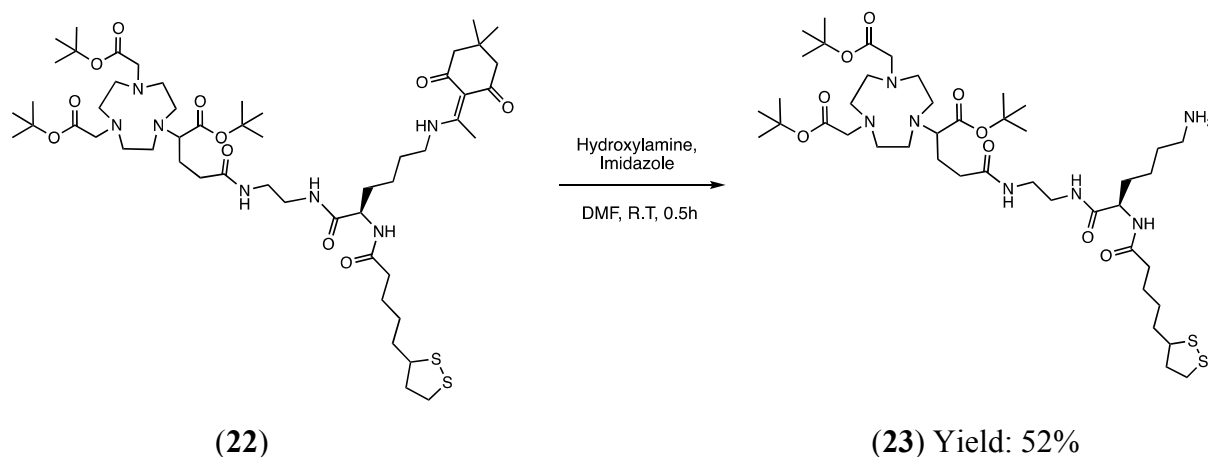


Figure III-30: Synthesis of NODAGA(tBu)₃-Lys-Dde-NH₂ (**21**)

As can be seen in Figure III-30, the α -amino group on the lysine was set free by cleaving off the Fmoc through a deprotection step mediated by diethylamine to get compound (**21**) that was chromatographically purified and recovered as cream white powder with a yield and purity of 48% and 97% respectively. In a manner analogous to the previous approach, it was necessary to place an arm bearing the sulfur (thiol/disulphide) function between the chelator and prospective gold surface. This was achieved by attaching lipoic acid or thioctic acid to the alpha amino group that was generated in compound (**21**). The use of lipoic acid has been proven to be valuable in developing functionalized gold nanoparticles via a post synthetic functionalization approach [121].

Figure III-31: Synthesis of NODAGA(tBu)₃-Lys-TA-Dde (**22**)

In an attempt to develop an integrated molecule bearing the grafting function, compound (**21**) was amide coupled to thioctic acid by employing the pre-synthesized thioctic acid NHS ester (Figure III-31). Compound (**22**) was characterized by HR-MS and revealed the anticipated molecular peak at 1066.629 [M+H]⁺.

Figure III-32: Synthesis of NODAGA(tBu)₃-Lys-TA-NH₂ (**23**)

Deprotection of the dde yielded the intermediate compound bearing the free amino group at the ε position (Figure III-32). This purified compound (**23**) was obtained as a TFA salt owing to presence of the TFA (0.1%) in the mobile phase with moderate yield and excellent purity of 97%. This compound was further coupled to fluorescent dye (Cy5).

Cy5 dye is a traditional far-red–fluorescent label for protein and nucleic acid conjugates used for imaging, flow cytometry, and genomic applications ideally suited for the 633 nm or 647 nm laser lines. A significant advantage to using long wavelength dyes such as Cy5 dye over other fluorophores is the low auto-fluorescence of biological specimens in this region of the spectrum. Although less superior compared to the NIR dyes, Cy5 dye has relatively higher quantum yield and brightness and hence finds application in optical imaging. Cy5 was kindly provided by Prof. Anthony Romieu and was synthesized based on the scheme depicted in Figure III-33. The 2,3,3-trimethylindolenine is subjected to a nucleophilic substitution

reaction with 6-bromohexanoic acid and ethyl iodide so as to develop two intermediates; one bearing the longer carboxylate side arm and the other short ethyl arm. The hexamethine chain was introduced between these two intermediates so as to obtain Cy5 that was purified over silica using flash chromatography to obtain the pure Cy5.

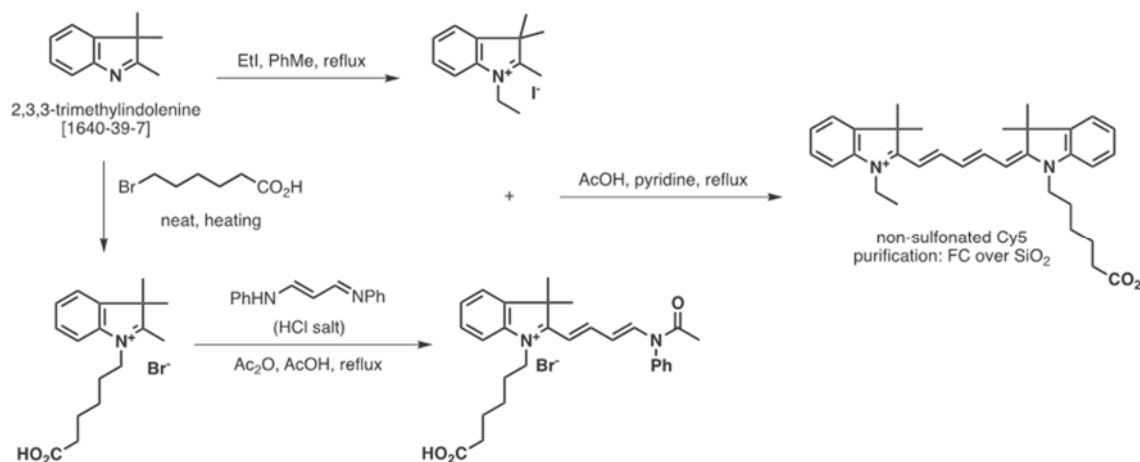


Figure III-33: Synthetic scheme for the Cy5 fluorescent dye.

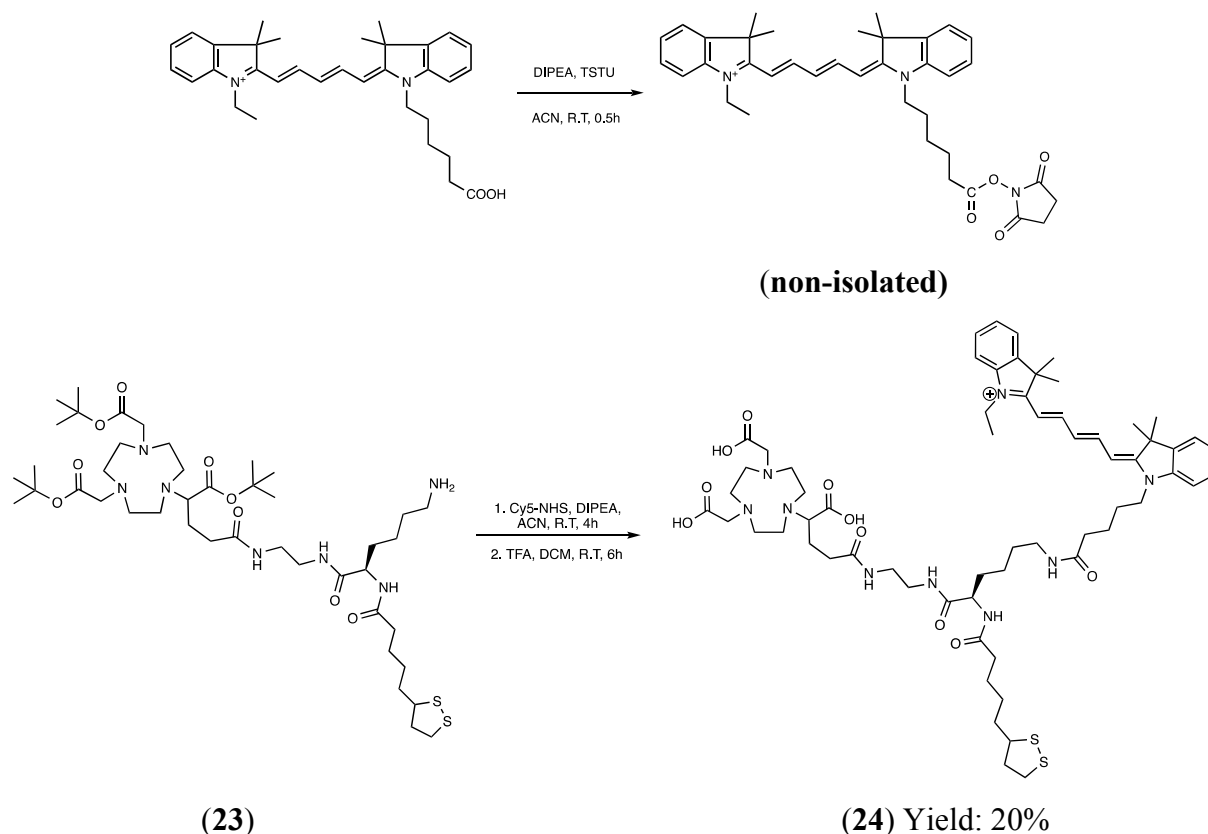


Figure III-34: Synthesis of NODAGA-Lys-TA-Cy5 (**24**)

Cy5 was activated to its NHS form using TSTU in DMF and treated with compound (**23**) to obtain an intermediate which was confirmed by LC-MS (Figure III-34). This intermediate was treated in-situ with TFA to deprotect the t-butyl group present on the chelator. Compound (**24**) was finally obtained after purification using semi-prep HPLC with a purity of 94%.

III-8.2 Photo-physical characterization of the PET-Optical probe (24):

The photo-physical properties of (**24**) were studied in PBS at room temperature. The stock solution of compound **24** was prepared in DMSO and diluted into PBS for the analysis. The photophysical data has been summarized in (Table III-1). The PET-Optical probe displays long wavelength absorption and emission bands that match closely to that of disulfonated Cy5.0 (reference dye) in aqueous solutions. The compound has an absorption maximum of 644 nm with a quantum yield of 10%, as a result it is well suited for imaging using currently available filter sets optimized for Cy5. The aqueous solution of the probe exhibited no indication of aggregation which otherwise would manifest itself as a second absorption band around 60nm shorter from the main peak. The short wavelength shoulder preceding the main peak in the absorption spectrum is a common feature of virtually all cyanine based fluorochromes and is even observed in less polar solvents such as DMSO and MeOH where there is least tendency for aggregation. The formation and presence of dimers or aggregates is undesirable as they likely result in intermolecular quenching of fluorescence emission [122].

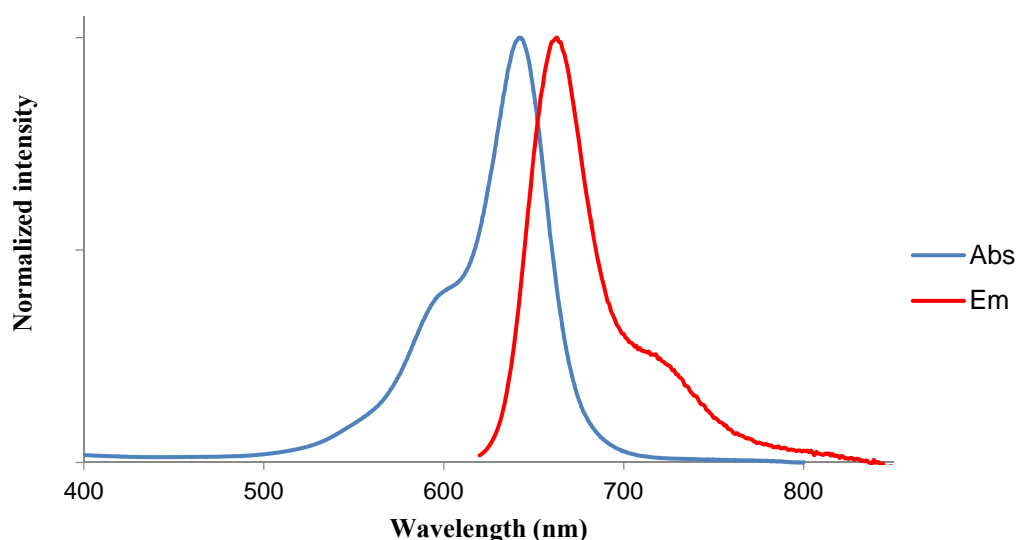
Absorption and fluorescence spectrum of PET-Optical probe

Figure III-35: Absorption and emission spectrum of the purified compound (**24**) in PBS using UV-Vis and fluorescence spectroscopy.

Table III-1: Photophysical properties of the trifunctional probe (**24**) in PBS at 298K.

Compound	λ_{abs} (nm)	λ_{em} (nm)	ϵ ($\text{M}^{-1}\cdot\text{cm}^{-1}$)	Φ (%)
24	644	665	120125	10

The PET-Optical ligand (**24**) described above has the potential for synthesis or functionalization of the gold nanoparticles that can be used for multimodal imaging.

III-9 Development of amine functionalized NODAGA ligands for gold nanoparticle synthesis:

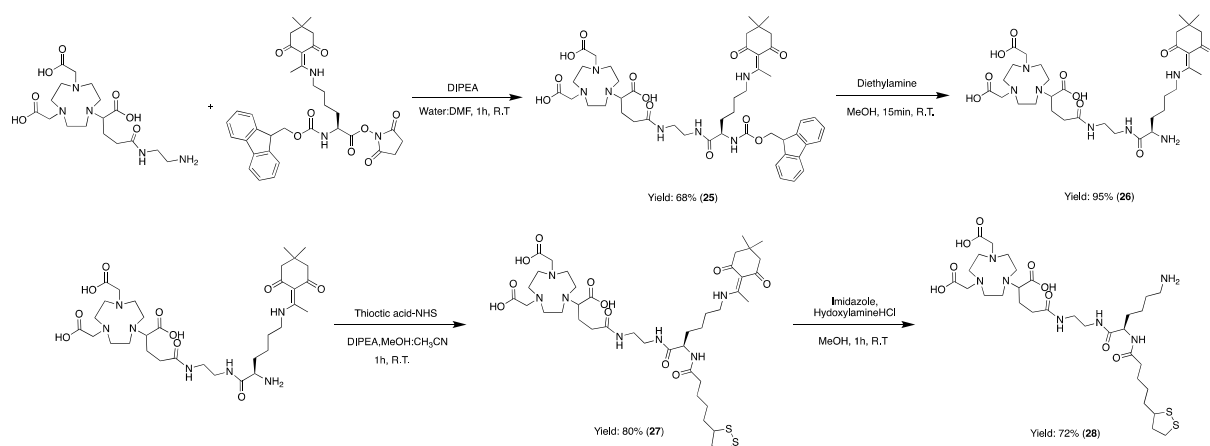


Figure III-36: Synthesis of NODAGA-Lys-TA-NH₂.

In an attempt to develop amino functionalized gold nanoparticles for PET imaging, ligand was developed employing the NODAGA-NH₂ as a starting compound as against the t-butyl protected NODAGA-NH₂ i.e NODAGA(tBu)₃-NH₂. This approach is amenable when the gold nanoparticles based on post-functionalization strategy (Figure III-2_A) are being developed unlike the pre-functionalization route where it is essential to have the chelate moiety protected as demonstrated previously for the synthesis of ligands for PET-MRI (DOTAGA-Lys-TA-NODAGA), PSMA targeting (DOTAGA-Lys-TA-Glu-PSMA) and PET-Optical (NODAGA-Lys-TA-Cy5). Synthesis of NODAGA-Lys-TA-NH₂ (**28**) using NODAGA-NH₂ can be realized by using correct combination of solvent and appropriate sequence of coupling-deprotection (Figure III-36). The overall yield of the process in terms of final compound was 37% which was considered very good. The purity of compound (**28**) as determined by HPLC was found to be 94%. This ligand (**28**) has been successfully demonstrated to be useful in development of multifunctional gold nanoparticles and will be employed in future projects encompassing targeted multimodal imaging in oncology as well as other disease areas.

III-10 Conclusions:

The objective of this chapter was to develop novel multifunctional ligands that find application in fabrication of the gold nanoparticles for multimodal theranosis. This has been accomplished through multistep chemical synthetic schemes encompassing appropriate selection of chelator for PET/SPECT/MRI imaging, fluorescent dye, and/or a targeting ligand capitalizing on leveraging the expertise of Chematech and ICMUB in Dijon. Following are the highlights that summarize milestones achieved in this direction:

- A novel PET-MRI ligand has been successfully synthesized and has been demonstrated to be useful in fabricating stable gold nanoparticles for cancer theranosis. These nanoparticles have been investigated for their pharmacokinetics and biodistribution properties in TSA tumor model using PET-MRI.
- PSMA targeting multifunctional ligand has been synthesized that has been proven to be valuable in terms of its affinity for PSMA. Furthermore, this ligand could be applied in the development of targeted gold nanoparticles that demonstrated good colloidal and radiochemical stability for prospective theranostic applications.
- A PET-Optical bimodal probe/ligand has been synthesized and characterized for its photophysical properties. This probe can be of high value in synthesis or functionalization of gold nanoparticles for multimodal imaging/theranostics.
- Amine bearing multifunctional ligands containing different chelators have been synthesized via diverse synthetic schemes that demonstrate versatility of the approach along with their application in developing amine functionalized gold nanoparticles.

Above summary points clearly demonstrate the value of the developed multimodal ligands in developing gold nanoparticulate systems that find diverse applications in managing cancer. Moreover, this work further strengthens the interdisciplinary collaborative efforts between teams at Dijon and Besançon, as this work will also be useful in prospective joint research projects.

Chapter IV. PSMA targeted multimodal imaging

IV-1 Introduction:

Prostate cancer (PCa) is one of the most common malignancy observed in men, with an estimated 1.4 million incident cases diagnosed worldwide in 2013 and this has been projected to increase as the population ages [123].

There are quite a few biomarkers associated with prostate cancer however, until recently diagnosis used to be typically based on the digital rectal exam and blood prostate-specific antigen (PSA) testing. PSA is secreted by the prostate cells and released into blood circulation. However, elevated serum PSA levels do not always necessarily correlate with malignancy, as it could be also due to condition other than prostate cancer. As a result of these false negatives, there is a scepticism regarding the value of broad PSA testing in diagnosis of prostate malignancies [124][125]. Recently, PCa diagnosis and staging has moved to the morphologic imaging with computed tomography (CT) and magnetic resonance imaging (MRI), as well as analysis of bone metabolism with ^{99m}Tc - methylene diphosphonate scintigraphy [126].

In order to address the anomalies that existing diagnostic toolkit presents, novel agents based on molecular imaging that will more accurately diagnose and stage prostate cancer are being developed. These tools must not only diagnose but also aid in monitoring therapy that will lead to a better treatment planning and result in improved patient outcome. PSMA based molecular theranostics represents one such arena.

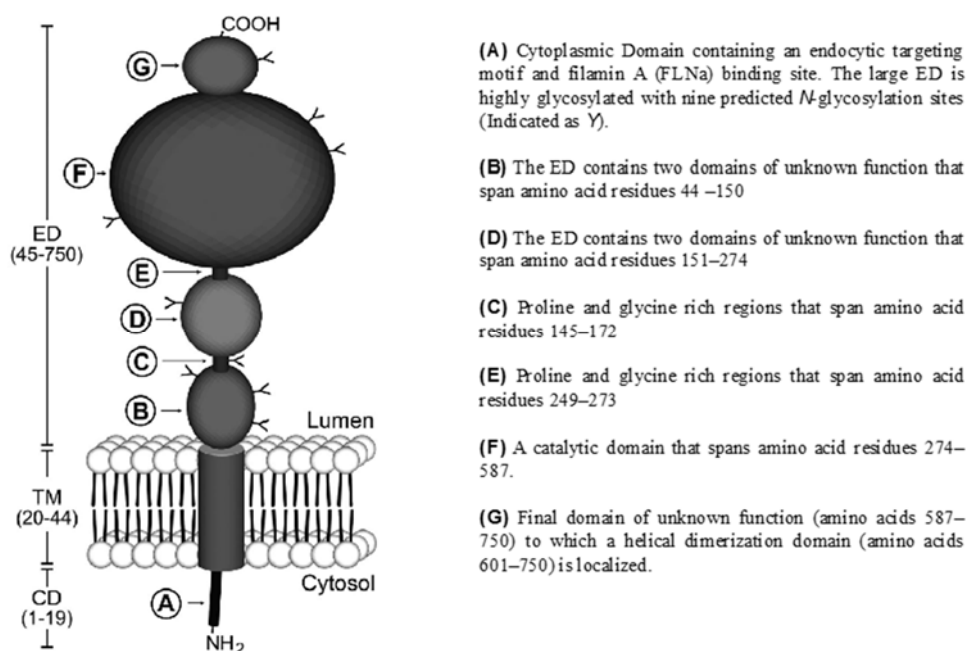


Figure IV-1: Schematic diagram of prostate-specific membrane antigen (PSMA) structure.

Adapted from [127].

IV-1.1 PSMA as a biomarker in prostate cancer:

PSMA is a type II transmembrane glycoprotein which is negatively regulated by androgen and is observed to be significantly overexpressed in androgen-independent prostate cancer [128]. With a molecular weight of 100kD, it is composed of 750 amino acids and has three distinct parts: a 707-amino acid containing portion that orients in an extracellular region, 24 amino acids region that spans the cell membrane and a short cytoplasmic tail which entails 19 amino acids (Figure IV-1).

PSMA has been found to be a key player in prostate carcinogenesis, glutamatergic neurotransmission and folate absorption. Owing to the diverse functions and the varied tissue distribution, there are different terms attributed to this protein, the most widely used being glutamate carboxypeptidase II (GCPII). This protein also has capacity to metabolize the brain neurotransmitter N-acetyl aspartyl glutamate (NAAG), as a result it is also named as NAALADase. As a folate hydrolase FOLH1, it removes γ -linked glutamates from poly- γ -glutamated folic acid in the proximal small intestine. [129-132].

Upon binding of the PSMA ligand to the cell membrane bound PSMA (target) it undergoes internalization through clathrin-dependent endocytosis [133]. This results in enhanced accumulation of ligand assembly (ligand conjugated chelate complexed radionuclides/drugs) into the cells in spite of the small volume of the afflicted site. This in turn enables high quality imaging for diagnostic procedures as well as high local dose for therapeutic applications [134, 135].

Recently, several monoclonal antibodies as well as small molecules with high binding affinity to the extra-cellular domain of PSMA have been developed [136]. Monoclonal antibodies, owing to their large size (150kD) and high blood circulation half-life, have poor tumor penetration that make them less attractive for molecular imaging unlike their small sized counterparts. In this context, the based small molecule inhibitors of PSMA have been observed to be quite promising owing to their suitable pharmacokinetic features and rapid blood clearance that improves the tumor to background signal [137]. So far, many bio-distribution studies have been performed to optimize the protocols for imaging with this small molecule based contrast agents.

IV-2 PSMA inhibitors in prostate cancer theranosis:

With the advanced ongoing investigations, the scientific community has been able to better understand the molecular pathophysiology of prostate cancer in greater details. This knowledge has resulted in the development of the ligands that specifically targets the PSMA expressed on the prostate cancer cells. The ability of the PSMA to also act as an enzyme facilitates the in-vitro screening of such ligands using easy to perform biochemical assays. These ligands when coupled to a pertinent chelating moiety could be used for molecular imaging as well as therapy. Subsequent section highlights in the brief the approaches that have been developed in this direction.

IV-2.1 Anti-PSMA monoclonal antibodies in prostate cancer theranosis:

ProstaScint® (Capromab Pendetide) developed by Cytogen Corporation, Princeton, NJ, USA has been the first antibody-chelate conjugate approved for the prostate cancer diagnosis based on SPECT imaging. It comprises the monoclonal antibody (7E11-C5/ Capromab) conjugated to diethylenetriaminepentaacetic acid (DTPA) which is labelled with ¹¹¹In. ProstaScint® has not found its widespread use as it binds to the intracellular domain of PSMA (the amino terminus) restricting its accessibility only to the necrotic cells and not the general population of cancer cells [138, 139].

To overcome this hurdle, monoclonal antibodies binding the extracellular domain of PSMA have been developed. A humanized monoclonal antibody J591 has been conjugated to chelators like 1,4,7,10-tetraazacyclododecane-1,4,7,10-tetraacetic acid (DOTA) and desferoxamine (DFO) which could be labelled with different radioisotopes for imaging (^{99m}Tc, ¹¹¹In, ⁸⁹Zr, ⁶⁴Cu) as well as therapy (¹⁷⁷Lu, ⁹⁰Y)[140, 141]. Of these, ¹¹¹In-DOTA-J591 was found to be superior in terms of pharmacokinetics and tumor-to-blood signal ratios in the nude mice with PSMA-positive LNCaP tumors. This led to the drug being tested in clinical trials, where it was observed to be superior to ProstaScint® owing to its ability to unveil soft-tissue and bone metastases [141, 142]. Attempts have been made to produce antibodies with better binding profiles for theranostic applications. However, despite the efforts the major drawback with monoclonal antibodies associated with their inherent properties still persists; longer turnover (circulation) time and slow clearance. This impedes the compliance in the clinical setting with respect to the time between the administration of the contrast agent and imaging session. This could be of more concern in therapeutic applications (¹⁷⁷Lu/⁹⁰Y) where extra-tumoral dose deposition needs to be controlled [143, 144]. In order to address the drawbacks associated with the full length antibodies, newer and shorter formats like antibody fragments (Fab, Fab', ScFv), nanobodies, diabodies and minibodies have been employed [145]. These tools have improved tumor penetration and faster clearance resulting in excellent

tumor/background signals in relatively shorter period of time, allowing the imaging to be done in one setting or same day [146].

Although with limited clinical success, immuno-imaging has been one of the pioneering approaches towards the prostate cancer diagnosis and necessitates further fine tuning to optimize the pharmacokinetics of the imaging agents. Table IV-1 summarises the list of the important developments in the antibody based PSMA imaging probes.

Table IV-1: Antibody and antibody fragments based conjugates for PSMA theranosis

Antibody/Protein	Chelating agent	Radionuclide	Application	Reference
7E11/Capromab (MAb)	DTPA	¹¹¹ In	SPECT Imaging	[138]
	DOTA	¹³¹ I, ¹¹¹ In	SPECT Imaging	[147]
	DTPA	^{99m} Tc	SPECT Imaging	[140]
J591	DOTA	¹⁷⁷ Lu, ⁹⁰ Y	Radiotherapy/SPECT imaging	[148]
	DFO	⁸⁹ Zr	PET Imaging	[149]
3/A12, 3/F11, 3/E7, 3/A12-Fab, 3/A12-F(ab)2 (MAb)	DOTA	⁶⁴ Cu	PET Imaging	[150]
JVZ-007 (Nb)	DTPA	¹¹¹ In	SPECT Imaging	[151]
IAB2M (Mb based on J591)	DFO	⁸⁹ Zr	PET Imaging	[146]

IV-2.2 Small molecule based PSMA inhibitors in prostate cancer theranosis:

Chemically synthesized low-molecular-weight PSMA-targeting radioligands have been shown to detect metastatic or recurrent PCa with high specificity and sensitivity. In comparison to mAbs, they are more potent and have excellent tissue penetration, half-life of circulation, and production-related costs [152, 153].

With the advances in the *in-silico* tools, it has been possible to perform docking studies to identify the best fitting (affinity) PSMA inhibitors using a high-resolution crystal structure of PSMA/binding motif. The active site of PSMA comprises a binuclear Zn⁺² active site and the two sub-pockets namely S1 and S1'. The urea and carboxylate groups are primarily involved

in interactions at the Zn^{+2} active site and the S1' sub-pocket of PSMA. In addition to this, there is S1-accessory hydrophobic pocket that entails potential lipophilic interactions with the PSMA inhibitors. In the context of the above binding features, the glutamate–urea–lysine binding structural motif has been a building block for the synthesis of potent PSMA inhibitors [154-157].

Urea based PSMA inhibitors were first synthesized and evaluated by Kozikowski and co-workers in 2001[158]. Later in 2002, Pomper's group from John Hopkins School of Medicine (Baltimore, MD, USA) for the first time published the synthesis and preclinical evaluation of radiolabelled urea-based PSMA inhibitor abbreviated as ^{11}C -MCG, which refers to ^{11}C -(S)-2-[3-((R)-1-carboxy-2-methylsulfonyl-ethyl)-ureido]-pentanedioic acid [159]. Having published numerous articles, this group has been one of the major contributor toward development of PSMA based theranostics.

Since the first report of the urea based PSMA inhibitors, different variants have been developed and labelled with radio-isotopes for imaging modalities like SPECT (^{99m}Tc , ^{111}In) and PET (^{68}Ga , ^{64}Cu) as well as for therapeutics (^{177}Lu). Some of these probes have even shown good clinical value after being tested in humans [160-162].

In order to label the urea-based PSMA precursors with radiometals, it is necessary to attach the chelator to the peptidomimetic structure of the PSMA inhibitors. However, as the active site of the PSMA/enzyme is hidden about 20 Å inside from its extracellular surface it is necessary to have a linker/spacer between the urea moiety and the sterically bulkier radiometal chelate complex. Introduction of the spacer/linker not only ensures the easy access of the PSMA inhibitor to the binding site but also gives an opportunity to alter the binding properties through the lipophilic interactions between the receptor and the inhibitor. Moreover, structural changes in the linker can influence lipophilicity, charge, plasma protein binding and molecular weight of the probes which have substantial effect on its pharmacokinetics. Thus, the overall potential of the PSMA based radiopharmaceuticals cumulatively depends on the relevant combination of the urea moiety, chelator moiety and particularly the nature of the spacer [71, 163]. Amongst several candidates that have been developed for PSMA theranosis below section will discuss some of the candidates that have shown promise at the preclinical and clinical level.

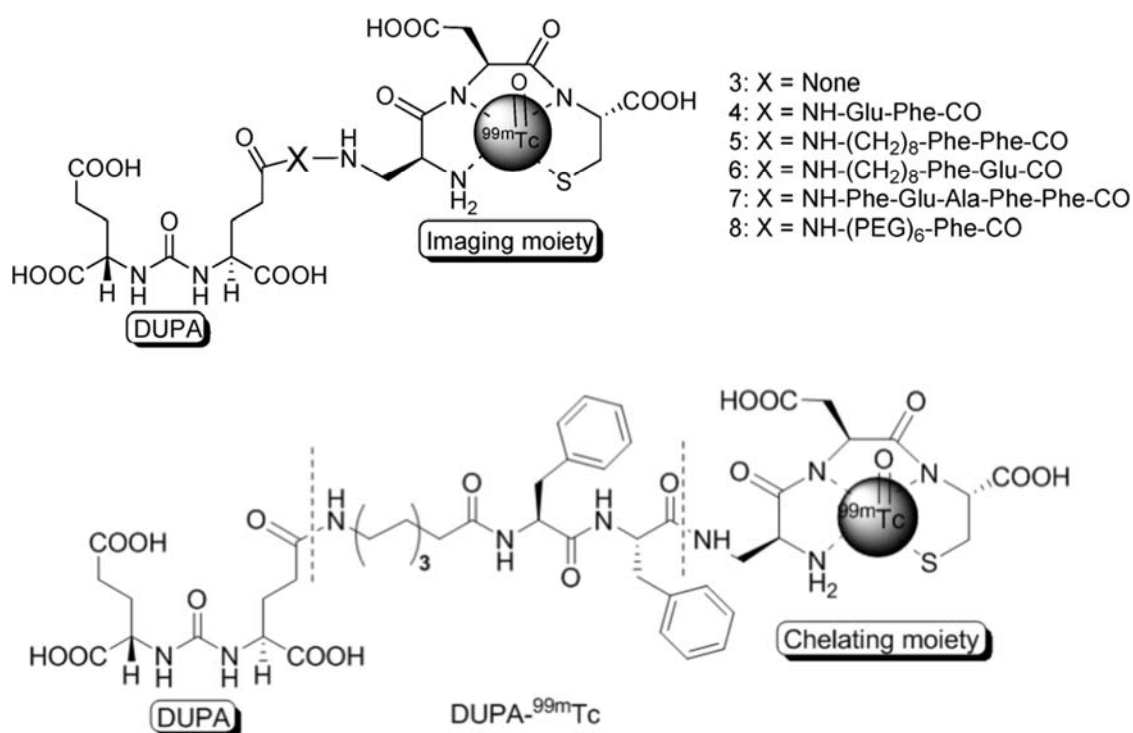


Figure IV-2: PSMA targeted probes for SPECT imaging (adapted from [153, 164]).

Low and his group from Purdue University has done some significant work in developing PSMA based imaging probes for SPECT imaging. Using the computational docking studies, PSMA inhibitors were developed taking into account the receptor topology. Figure IV-2 depicts the ^{99m}Tc labelled Glu-Urea-Lysine-Peptides that have shown promising PSMA binding affinities in nanomolar range as well as good tumor localization in LNCaP xenografts in nude mice [153, 164].

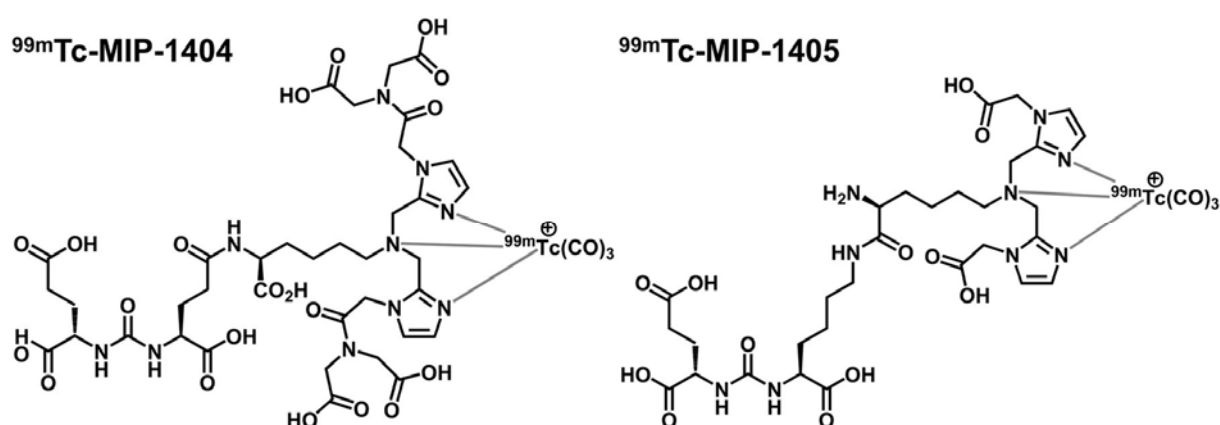


Figure IV-3: PSMA targeted probes based on single amino acid chelators (SAAC) for SPECT imaging (Adapted from [165]).

On the similar lines as above, Hillier et al., developed SPECT imaging agents one bearing Glu-Urea-Lys and other bearing Glu-Urea-Glu as pharmacophoric moiety. These functions

have been coupled to the SAAC (single amino acids) chelators CIM (2,2'-(2,2'-(azanediylbis(methylene))bis(1H-imidazole-2,1-diyl))diacetic acid) or TIM (2,2', 2'',2''-((2,2'-(2,2'-(azanediylbis(methylene))bis(1H-imidazole-2,1-diyl)) bis(acetyl)) bis(azanetriyl)) tetraacetic acid). The two promising leads ^{99m}Tc -MIP-1404 and ^{99m}Tc -MIP-1405 have been tested in humans and were found to detect the bone metastatic lesions and soft-tissue PCa lesions including sub-centimeter lymph nodes [165, 166] (Figure IV-3). In addition to above, there have been few other ^{99m}Tc based PSMA inhibitors that have been reported which can be referred to in recent review [167].

In recent years, PET imaging has gained a wide spread attention in oncology and PSMA has been no exception to this. Numerous preclinical and clinical studies have been published demonstrating use of PSMA based PET probes of which PSMA-11 (HBED-CC-PSMA), and PSMA-617 are the most promising ones.

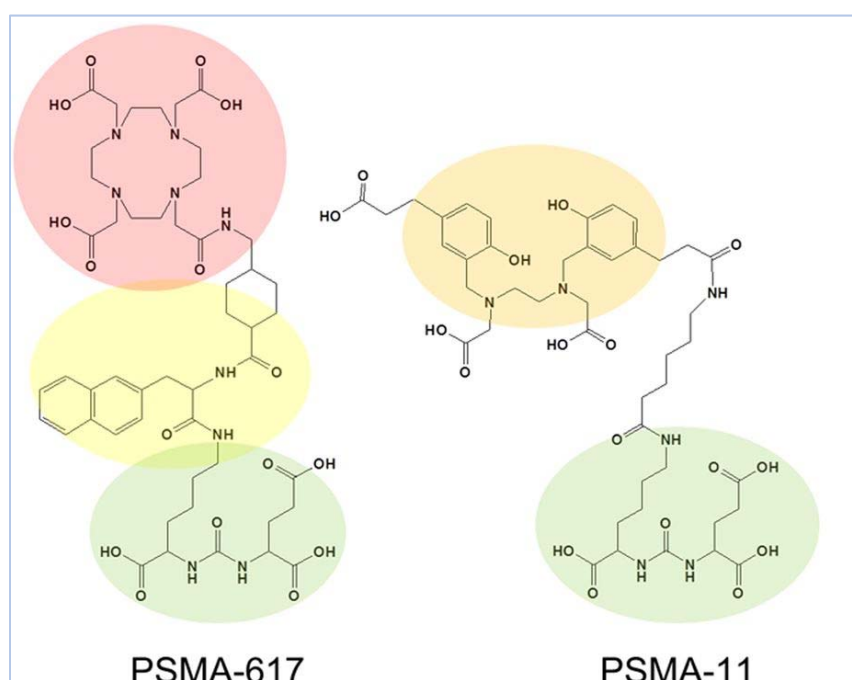


Figure IV-4: Rationally developed PSMA inhibitors for nuclear imaging and medicine by Eder and co-workers (Adapted from [168]).

As demonstrated by Eder et al., PSMA-11 (HBED-CC-PSMA) has been developed by coupling the peptidomimetic structure Lys-urea-NH-Glu to the spacer 6-aminohexanoic acid (Ahx) and then functionalizing it with the chelator *N,N'*-dis[2-hydroxy-5-(carboxyethyl)benzyl] ethylenediamine-*N,N'*-diacetic acid (HBED-CC) to obtain HBED-CC-Ahx-Lys-urea-Glu (HBED-CC-PSMA or PSMA-11)(Figure IV-4). In addition to being a chelating agent HBED-CC also serves as a lipophilic moiety owing to the presence of the two phenolic rings. An aliphatic spacer such as Aca is sufficient for providing the requisite

lipophilicity and retaining the affinity of the ligand towards PSMA ($K_i = 12.1 \pm 2.1$ nM)[169]. Based on the several clinical studies using PET/CT, ^{68}Ga -PSMA-11 holds diagnostic value in PC patients having biochemical recurrence with curative treatment option, in primary staging of patients with a high risk for metastases (Gleason Score > 7 and PSA > 10 ng/mL) and in patients with a high suspicion of PC [170-174]. However, owing to the high selectivity of the complexing agent HBED-CC for ^{68}Ga , the radiotracer (PSMA-11) is not suitable for radiolabelling with therapeutic radiometals such as ^{177}Lu or ^{90}Y .

In order to mimic the proven additional biologic interactions of HBED-CC with the binding pocket, PSMA-617 was developed. PSMA-617 is the DOTA-conjugated PSMA inhibitor that has been sustainably refined and advanced with regards to its tumor-targeting and pharmacokinetic attributes by systematic chemical modification of the linker region. ^{68}Ga -PSMA-617 was found to be comparable with ^{68}Ga -PSMA-11 in humans as PET diagnostic tracer, which paved the way for further exploration into radiotherapy [175]. Currently undergoing extensive investigations in human clinical trials, ^{177}Lu -PSMA-617 has emerged as a promising new option for therapy of metastasized castration resistant prostate cancer [168, 176-178]. The chelator moiety of PSMA-617 has been replaced with different chelators like DTPA, NOTA, NODAGA and CIM PCTA to give a series of compounds in a work demonstrated by Wüstemann et al [179].

In an ongoing effort to develop novel PET traces in our group, CC34 has emerged to be a leading hit developed in collaboration with University of Freiburg (Figure IV-5).

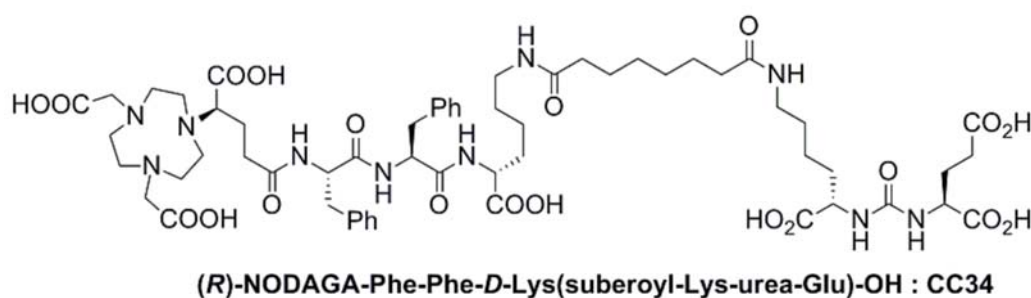


Figure IV-5: (R)-NODAGA-PSMA/CC34: A Versatile precursor for nuclear imaging of PSMA-positive tumors developed at ICMUB, Dijon (Adapted from [180]).

CC34 is versatile in terms of its ability to be radiolabelled by ^{68}Ga , ^{64}Cu and ^{111}In . ^{68}Ga -CC34 was found to be comparable to ^{68}Ga -HBED-CC-PSMA in terms of tumor uptake and tumor to background tissue ratios. Moreover, ^{64}Cu -CC34 enabled high contrast imaging of PSMA positive tissues characterized by elevated expression of PSMA. This could be of value when delayed imaging is required [180].

IV-2.2.1 Optical and PET-Optical imaging of PSMA:

Optical imaging of prostate cancer based on high sensitivity fluorescence can be of considerable value in intraoperative prostate cancer imaging. In this context, quantum dots and more advanced dyes, such as indocyanine green (ICG), which emits in the near-infrared (NIR) region of the spectrum, enable reasonable tissue penetration of emitted (and detected) light. NIR region (>700 nm) facilitates deep-tissue imaging by improving the signal to background ratio through reduction in scattering events, as the NIR photons travel through the biological tissue.

A typical approach in development of PSMA targeted fluorescent imaging agent involves conjugation of the fluorescent dye to an anti-PSMA antibody or chemical ligand.

Monoclonal antibody J591 conjugated with a linkable ICG derivative was able to depict PSMA+ tumors with high contrast compared to PSMA tumors until 10 days after injection of low dose of reagent (0.25 mg/kg) in mice [181]. To overcome the longer tumor accumulation time associated with antibodies, Watanabe et al, conjugated ICG to anti-PSMA minibody which exhibited faster tumor penetration in around 6h [182] whereas, conjugation of XX70 to scFv has also been performed [183]. Using urea based small molecule ligands for optical imaging offers a smart and cost-effective approach as they are internalized into PSMA expressing cells just like their antibody counterparts however with better favourable pharmacokinetic features much suited in intra-surgical realms.

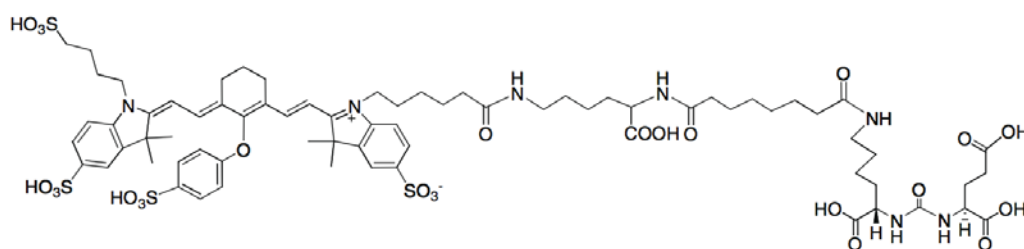


Figure IV-6: PSMA targeted optical imaging probe based on YC-27 (adapted from [184]). Pomper's group reported the synthesis of YC-27 (Figure IV-6) by coupling the urea based pharmacophore to activated NIR dye, IRDye800CW-NHS with a suberate-lysine spacer in between. YC-27 demonstrated a PSMA inhibitory activity of 0.37 nM and was able to generate tumor-to-normal tissue ratios of at least 10 in PSMA-expressing PC3-PIP beginning 18h after injection [184, 185]. Moreover, it was demonstrated that such probes could be used for fluorescence guided laparoscopic surgery. Kularatne et al. likewise have synthesized fluorescent (fluorescein and rhodamine) urea derivatives that exhibited PSMA uptake in endosomes [164]. Recently, Bao et al. has reported a series of optical probes with a small

PEG spacer between the urea moiety of PSMA and the fluorescent dyes like Cy5.5, Cy7 and ZW800 for intraoperative assistance [186].

Although, quite a few fluorescent PSMA probes have been reported, the dual imaging modality in the context of PSMA has been less explored. A bimolecular approach has been revealed in which the extracellularly binding PSMA antibody (D2B) has been conjugated independently by DTPA (^{111}In) and IRDye800CW for SPECT/Optical imaging [187]. This approach is not so elegant owing to complex conjugation protocol and heterogeneous species that are difficult to characterize. Our group has worked extensively in the development of monomolecular bimodal probes which could be employed in such applications.

Owing to the complexity of the synthesis, only one example of monomolecular SPECT/Optical imaging probe with the small molecular PSMA inhibitor could be retrieved. Banerjee et al., in 2011 reported this dual imaging probe, which was synthesized through series of coupling and deprotection steps to arrive at a macromolecular structure as depicted in Figure IV-7. It encompasses a DOTA chelator and IRDye800CW (NIR dye) assembled through lysine based linker which in turn is linked to urea moiety. This study demonstrated efficient chemical and radiochemical synthesis of a dual modality PSMA-binding compound, that could provide sequential imaging by SPECT and NIRF at radiotracer levels in preclinical models [188].

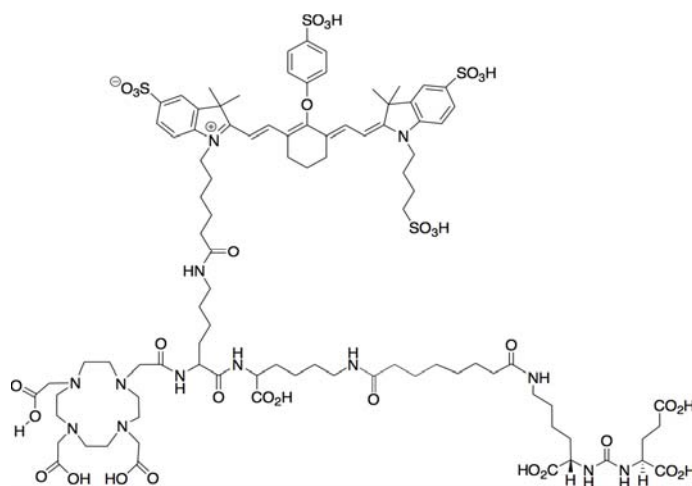


Figure IV-7: Bimodal probe for SPECT-optical imaging (Adapted from [188]).

The objective of our project was to develop a PET-Optical imaging probe through the right combination of chelator and fluorescent dye. Subsequent sections of this chapter, details the approach and methodology adopted in achieving this goal.

IV-3 Synthesis of PSMA targeted monomolecular PET-Optical imaging probe:

IV-3.1 Synthesis of chelator-linker moiety:

The development of the bimodal probes began by the synthesis of lysine-chelator intermediate. This involved first, activation of Fmoc-dde-lysine-OH to its NHS ester, as also been the case for other synthesis in chapter III. The activated Fmoc-dde-lysine-OH was subsequently coupled to NODAGA-NH₂ (Figure IV-8). Although, it might be more suitable to use the protected form of the NODAGA-NH₂, we demonstrate here that even the deprotected form could be used to obtain the desired compound by the appropriate choice of solvent, during the course of synthesis.

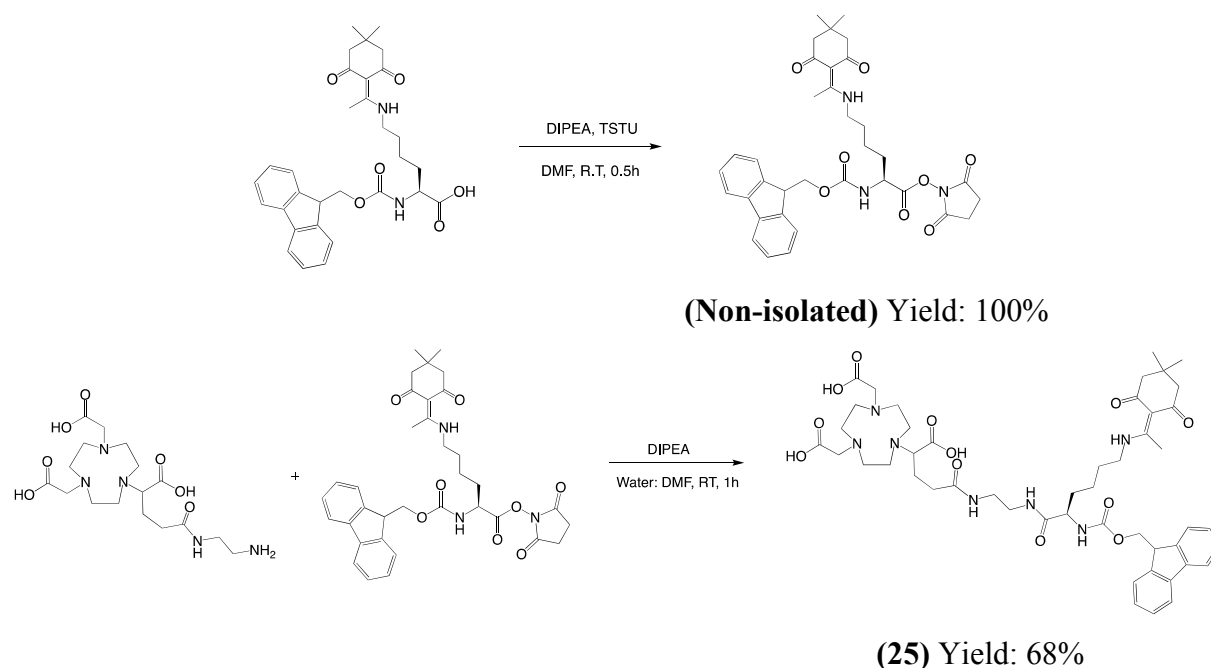


Figure IV-8: Synthetic scheme for the NODAGA-Lys-Fmoc-Dde (**25**).

Compound **25** was obtained in good yield and excellent purity of about 99%. This compound is valuable and versatile in terms of its amenability to be customized based on the topology of subsequent compounds desired. For instance, this compound has also been demonstrated to be of use in the synthesis of multifunctional ligands for gold nanoparticles as explained in chapter III. To introduce an extra space between the linker and the PSMA ligand, the Dde group on the amino group of lysine side chain was deprotected. Dde has been widely used as a protecting group for primary amines in peptide chemistry and is typically cleaved under nucleophilic conditions using 2% v/v hydrazine in DMF. Dde is stable under conditions used for deprotection of Fmoc and Boc, however, Fmoc is readily deprotected in the presence of 2% v/v hydrazine in DMF, therefore defeating the potential of a dual Dde/Fmoc protecting group strategy. This necessitated the orthogonal deprotection strategy that involved use of hydroxylamine and imidazole (30 eq. of each)[111]. The orthogonal Dde deprotection could

be easily achieved within an hour or less and could be even carried out in an aqueous methanolic solution (Figure IV-9). The compound was further purified by flash chromatography.

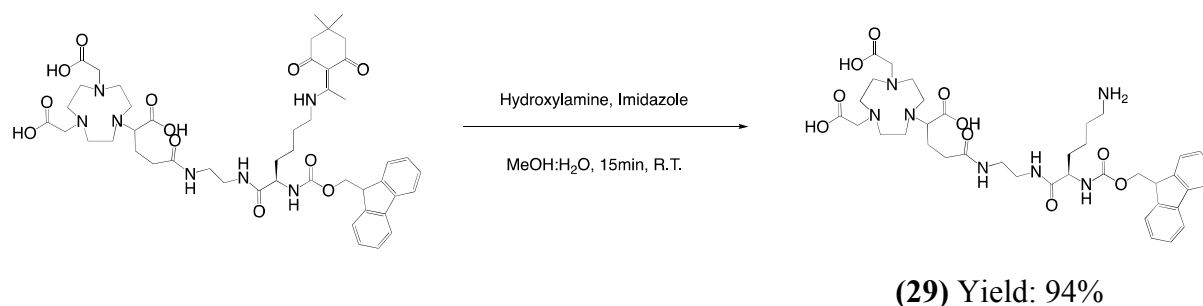


Figure IV-9: Synthetic scheme for the NODAGA-Lys-Fmoc-NH₂ (**29**).

IV-3.2 Synthesis of PSMA ligand and its derivative:

The design of the urea based pharmacophore has been reported widely in the literature. The *t*-butyl protected Glu-Urea-Lysine was kindly obtained from Dr. Victor Gonçalves and further derivatized.

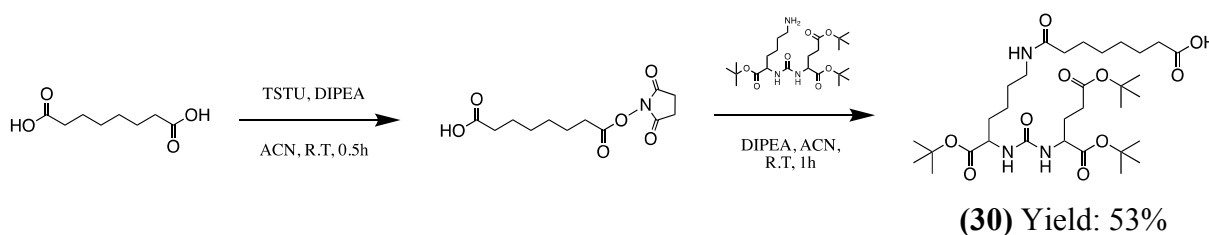
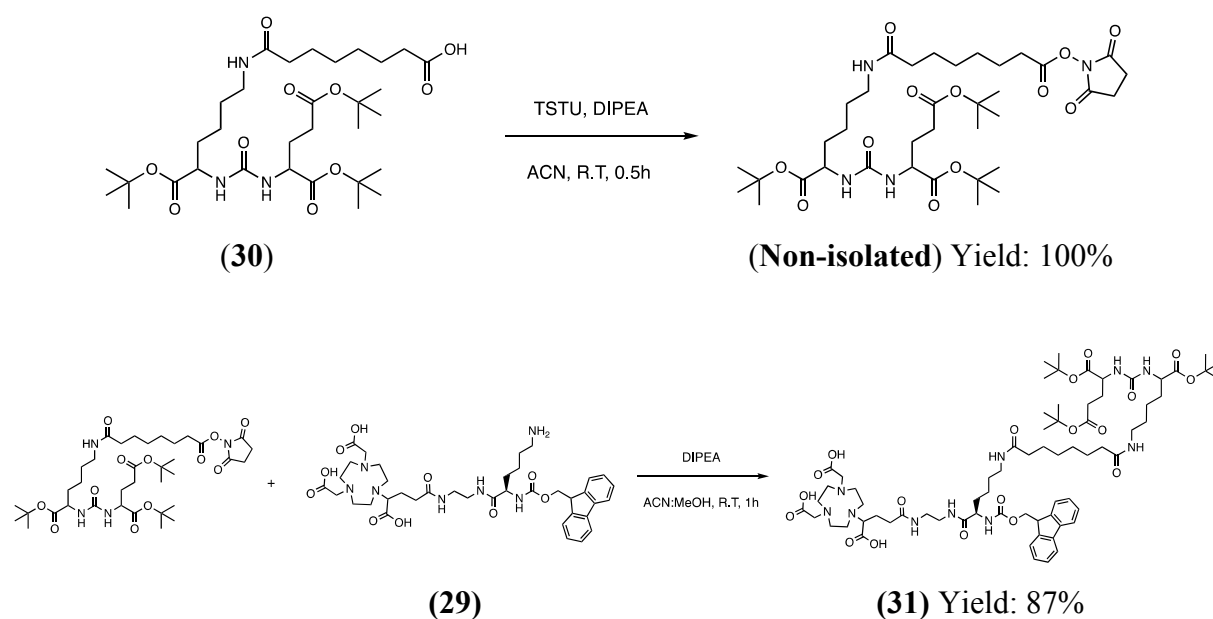


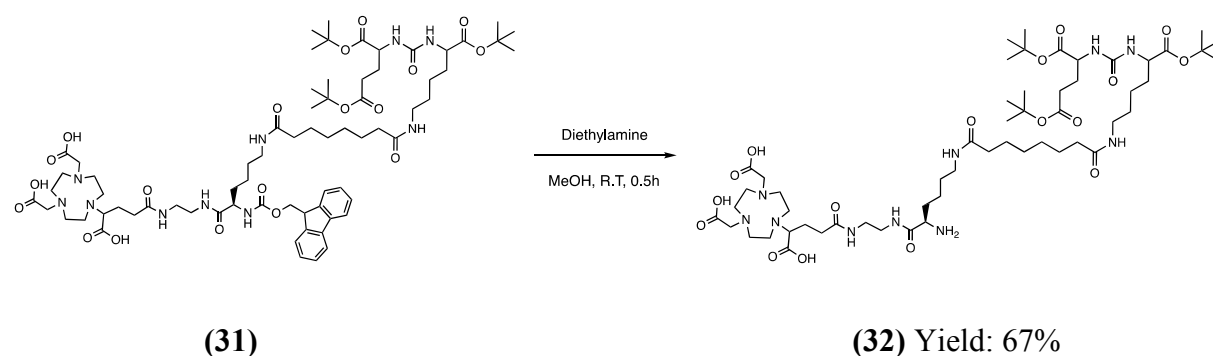
Figure IV-10: Synthetic scheme for the PSMA (tBu)₃-Suberate (**30**).

A suberate spacer was introduced between the lysine of the urea pharmacophore and chelator-linker moiety. This will ensure steric flexibility and accessibility of the ligand to the binding region seated inside the PSMA/enzyme. An ideal approach in doing so would be to use suberate anhydride, but owing to its inherent challenges in the synthesis and characterization, we adopted another approach. Monofunctional NHS of suberate was synthesized by using one equivalent of TSTU and DIPEA, which was then coupled to protected PSMA ligand (Figure IV-10). As anticipated, dimers were also observed during synthesis which could be separated from the monosubstituted suberate of PSMA ligand using flash chromatography. Compound **30** was obtained as a translucent semisolid with a purity and yield of 90% and 53% respectively.

IV-3.3 Synthesis of chelator-linker-PSMA ligand:

Figure IV-11: Synthetic scheme for the NODAGA-Lys-Fmoc-Sub-PSMA(tBu)₃ (**31**).

NHS ester of the compound **30** could be easily synthesized by TSTU coupling in the presence of base and was verified by LC-MS. Compound **29** was then coupled to the protected PSMA ligand via the available ϵ -amino group present on the chelate-linker moiety (Figure IV-11). The obtained product was purified using C18 based flash chromatography using water (0.1%TFA) and acetonitrile (0.1%TFA) as eluents. Compound **31** was recovered as a white powder after lyophilisation.

Figure IV-12: Synthetic scheme for the NODAGA-Lys-Sub-PSMA(tBu)₃-NH₂(**32**).

Compound **31** was subjected to Fmoc deprotection wherein, it was treated with 50% diethylamine in methanol (Figure IV-12). The deprotection was complete in 30min and the product was subjected to flash purification. Simple work-up was not possible with such a macromolecular and amphoteric structure and hence chromatographic purification was

imperative. The product revealed a HPLC purity of about 98% and could be characterized by HRMS in which a molecular peak was evident at 1193.701 $[M+H]^+$.

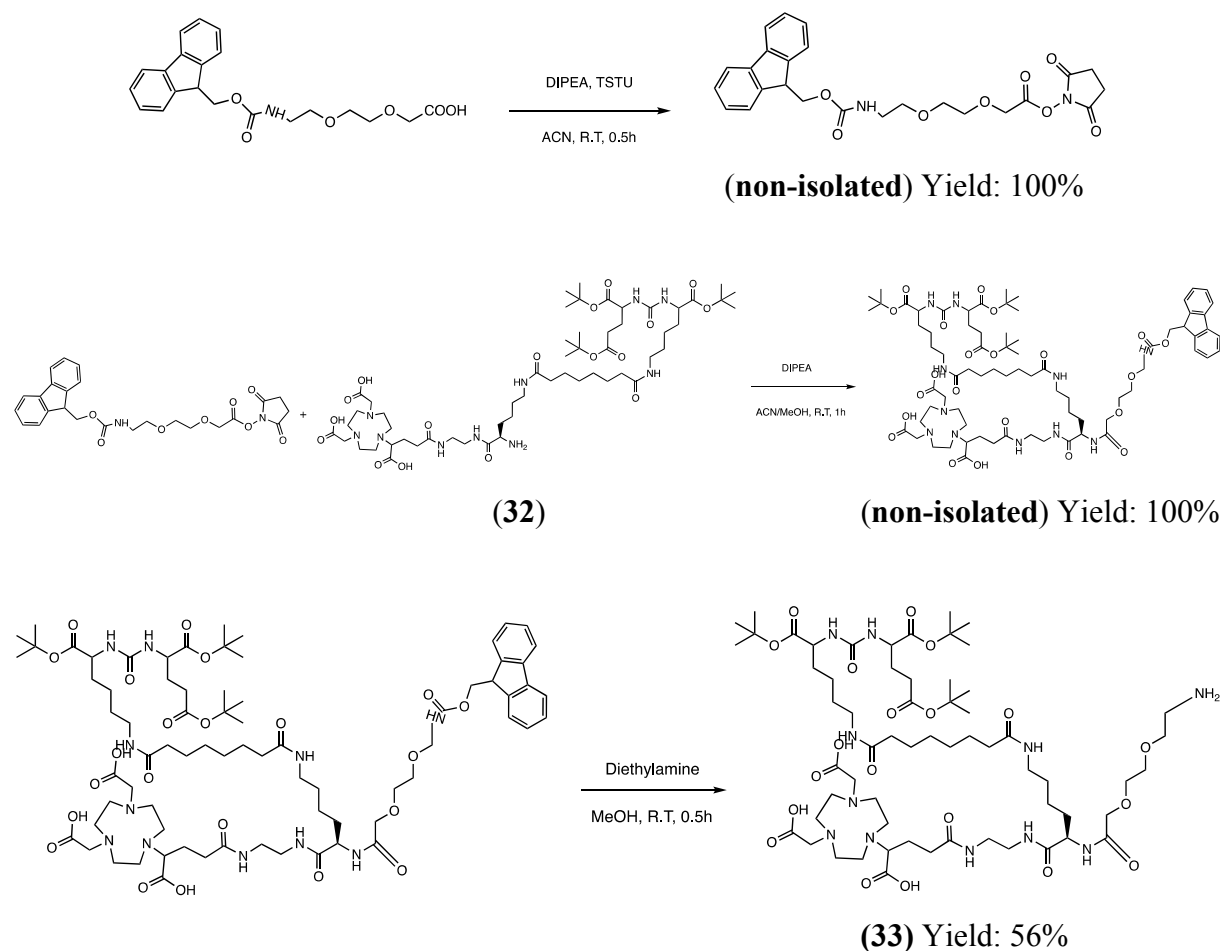


Figure IV-13: Synthetic scheme for the NODAGA-Lys-Sub-PSMA(tBu)₃-PEG₂-NH₂(**33**).

In the following steps, we decided to adopt a strategy that entailed use of a PEG spacer between the generated α -amino group in compound **32** and the prospective fluorescent dye. This was accomplished by use of a hetero bifunctional PEG spacer; Fmoc-O₂Oc-OH (Iris Biotech). Fmoc-O₂Oc-OH was activated to its NHS ester again by its coupling with TSTU in presence of DIPEA and was then coupled to compound **32** (Figure IV-13). Taking cue from the previous Fmoc deprotection success, the Fmoc deprotection was attempted in a same reaction mixture. The resulting compound **33** could be easily obtained in a one pot process and with moderate yield of 56%. Compound **33** as can be seen from the structure is amphoteric with chelating moiety quite polar with three carboxyl groups whereas the PSMA ligand bears three t-butyl protected sites affording the lipophilicity. The presence of the protected groups ensured the molecule retained its amenability to chromatographic separation/purification.

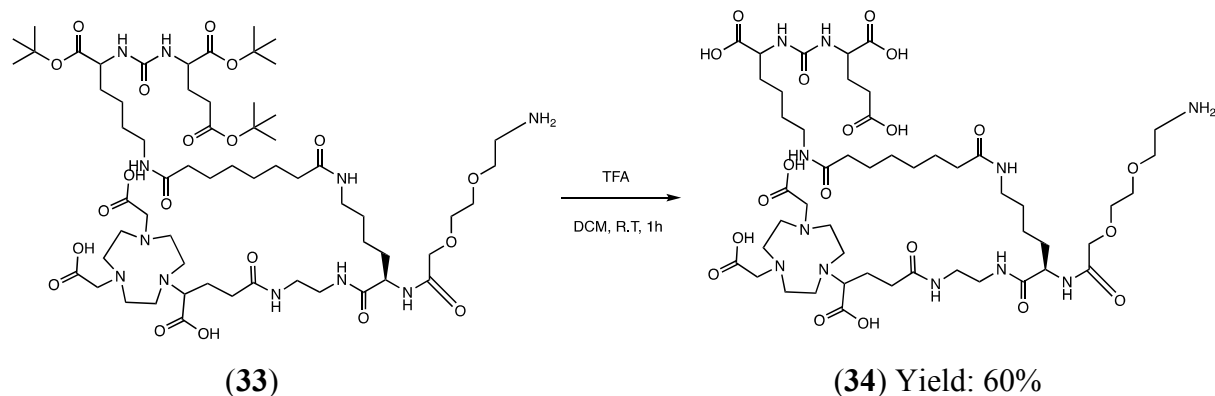


Figure IV-14: Synthetic scheme for the NODAGA-Lys-Sub-PSMA-PEG₂-NH₂ (**34**).

The deprotection of the t-butyl group was envisaged before the conjugation to the dye, in order to minimise the cycles of the reaction to which the dye could be subjected as the dye has been observed to be quite sensitive towards multiple reaction in terms of degradative stability. As a result, deprotection was performed before by using 1:1 mixture of dichloromethane: trifluoroacetic acid (Figure IV-14). The t-butyl groups on the PSMA ligand were cleaved off in an hour. The product was purified by semi-preparative HPLC to get the compound **34** with a purity of around 96%.

IV-3.4 Synthesis of bioconjugatable IR-783:

IR-783 is a commercially available NIR dye. Unlike most of the other NIR dyes like for example IRDye800CW, IR-783 is not very expensive. However, in its native form it lacks any bioconjugatable group and has to be chemically modified to have functional groups like –COOH/NH₂. Achilefu et al. demonstrated that Suzuki coupling could be employed to introduce carboxy phenyl moiety through a C-C bond formation at the meso carbon of the heptamethine chain of the NIR dye (Figure IV-15) [189, 190]. In another approach, aryl ether modified cyanine derivatives have been synthesized through the nucleophilic substitution at the chloro position [191]. These carboxylates bearing NIR dye could be then used to attach a peptide/protein through coupling chemistry. Although these modified NIR dyes are water-soluble, such fluorophores containing an additional aryl group show an increased tendency to aggregate in aqueous solution and the aryl-ether linkage in some of these fluorophores is vulnerable to cleavage [192].

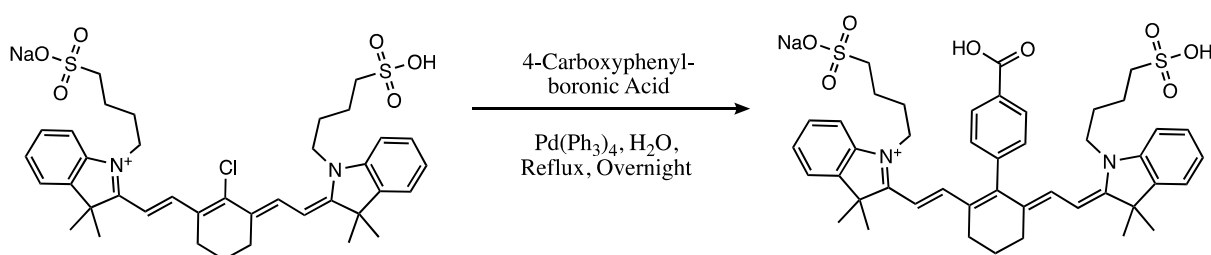


Figure IV-15: Suzuki coupling mediated derivatization of IR-783. Adapted from [189].

In order to overcome the drawbacks associated with the presence of an extra aryl ring, use of an alkyl chain was envisaged. As demonstrated by Hilderbrand and co-workers, IR-783 could be easily modified into its alkyl-thio ether derivatives through nucleophilic substitution reaction at the meso position. Such fluorophores were directly labelled to a vascular cellular adhesion molecule-1 (VCAM-1) targeting peptide. This enabled monitoring of Endothelial cell internalization of the VCAM-1 targeted phage via near-infrared fluorescence microscopy [48].

Following the similar approach compound **35** has been synthesized. The reaction was quite straight forward with the product being obtained by overnight stirring of IR-783 with 3-mercaptopropionic acid in the presence of a base (Figure IV-16). The compound was purified by semi-preparative HPLC to get a purity of 99%.

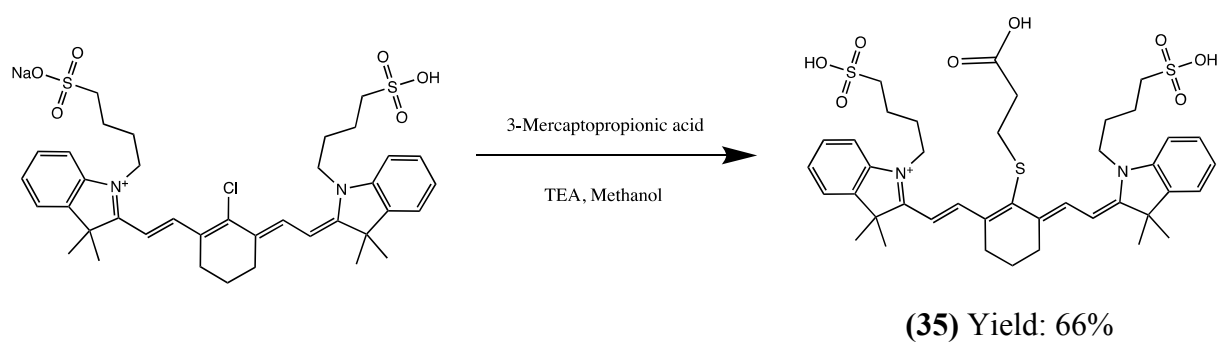


Figure IV-16: Synthetic scheme for the IR-783-Propionic Acid (35)

IV-3.5 Synthesis of chelator-linker-PSMA ligand-IR783:

The carboxy functionalized IR-783 was activated through TSTU in the presence of triethylamine to get the activated form of the dye (NHS ester), which could be then coupled to compound **34** (Figure IV-17).

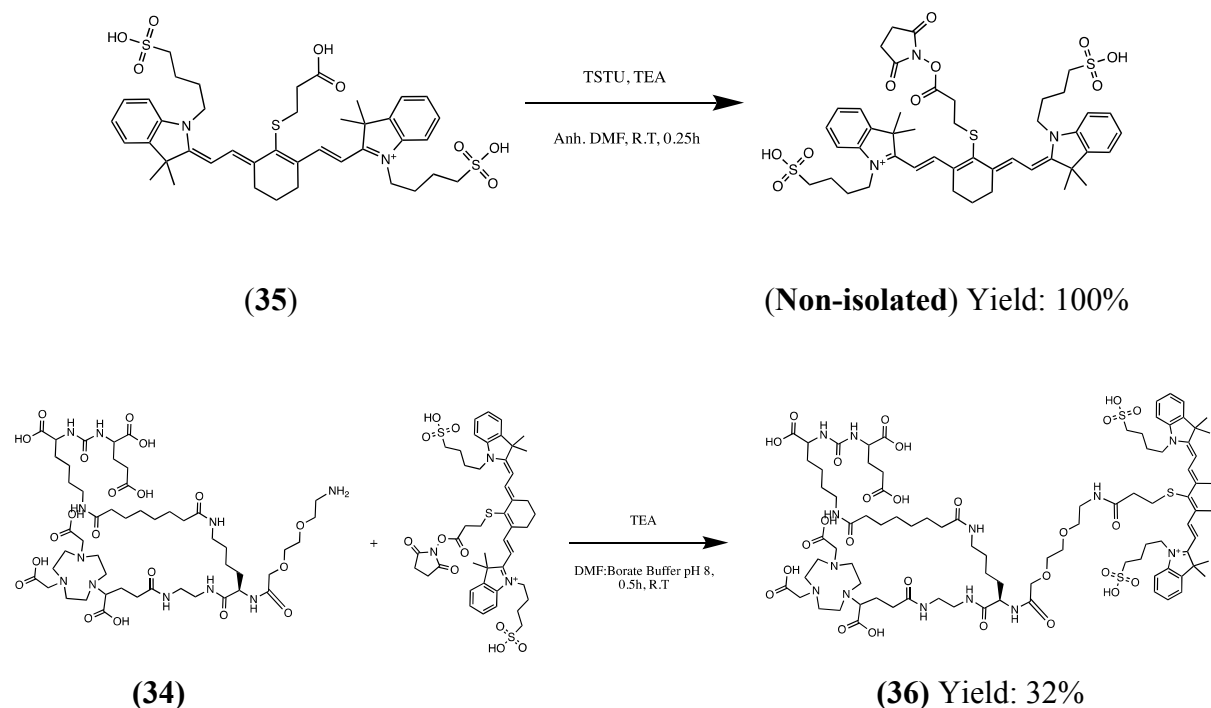


Figure IV-17: Synthetic scheme for the PSMA-Suberate-NODAGA-Lys-PEG₂-PA-IR783

(36)

The presence of several carboxylate groups in compound **34** necessitated use of large amount of the base to have the reactive amino group that could participate in coupling reaction. However, conducting the reaction under such conditions resulted into inexplicable degradation of the dye in DMF as solvent. In order to mitigate the degradative potential, we performed the coupling reaction in partially aqueous solution. As indicated in the reaction scheme the coupling was carried out in DMF and Borate buffer at pH 8. This significantly reduced the in-situ degradation of the dye and the compound **36** could be obtained in moderate yield of around 32% with excellent purity profile (Figure IV-18).

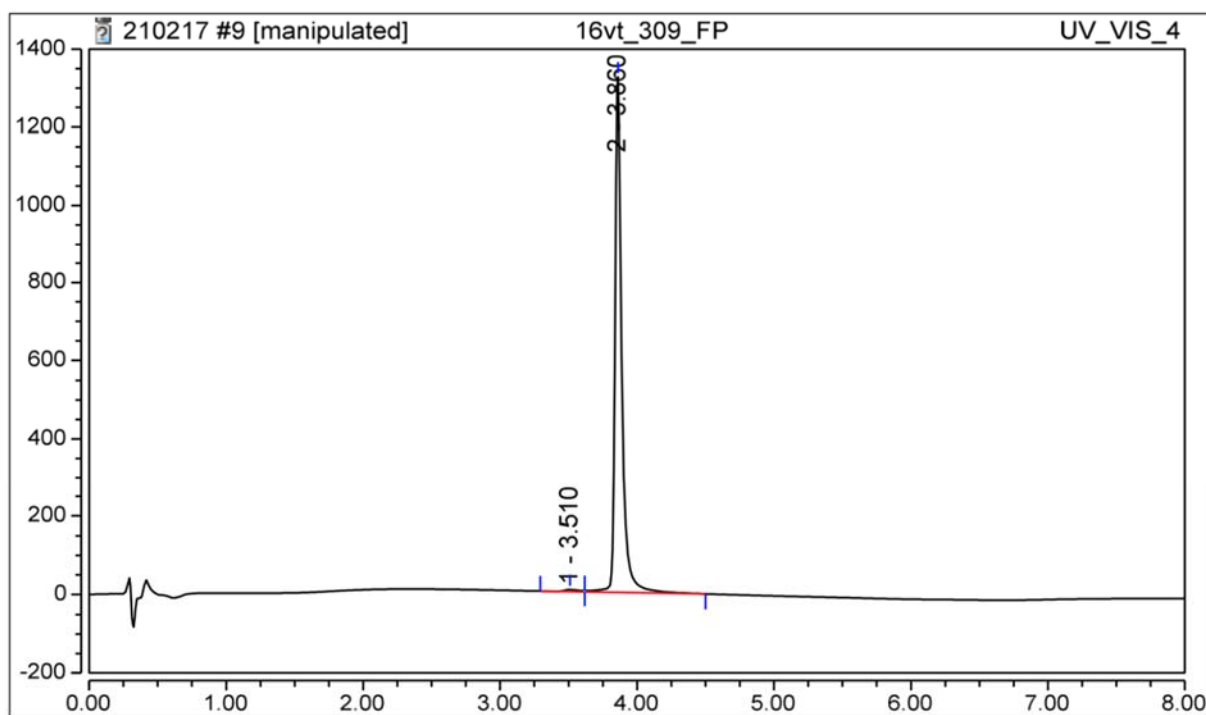


Figure IV-18: HPLC spectrum of the purified compound **36** at 780nm.

IV-4 Characterization of the PET-Optical probe

IV-4.1 Photophysical characterization of the PET-Optical probe:

In order to evaluate the potential of the optical probe, it is essential to estimate its photophysical parameters; $\lambda_{\text{abs-max}}$, $\lambda_{\text{em-max}}$, molar extinction coefficient (ϵ) and quantum yield (Φ). When the photon traverses through the fluorophore it induces a molecular electronic transition from a lower electronic state, usually the lowest in energy (ground state, S_0), to a state of higher energy (excited states, S_1 , S_2 ,...). Experimentally, the efficiency of light absorption at a fixed wavelength by a fluorophore is characterized by the *molar extinction coefficient* $\epsilon(\lambda)$ (commonly expressed in $\text{L}\cdot\text{mol}^{-1}\cdot\text{cm}^{-1}$) and follows the Beer-Lambert law where $A(\lambda)$ represents the absorbance at the wavelength λ , l , the absorption path length (in cm) and c , the concentration (in $\text{mol}\cdot\text{L}^{-1}$).

$$A(\lambda) = \epsilon(\lambda) \cdot l \cdot c$$

Quantum yield (Φ_F), is another important parameter which compares the photon input and output and represents the fraction of excited molecules that return to the ground state S_0 with the emission of fluorescence photons. The product of the two parameters $\epsilon(\lambda)$ and Φ_F , results in the other important parameter; brightness, which relates to the absorption and emission capacity of the fluorophore. These parameters enable comparative analysis of different fluorophores at the same wavelength.

Absorption & Fluorescence Spectrum of bimodal PSMA probe

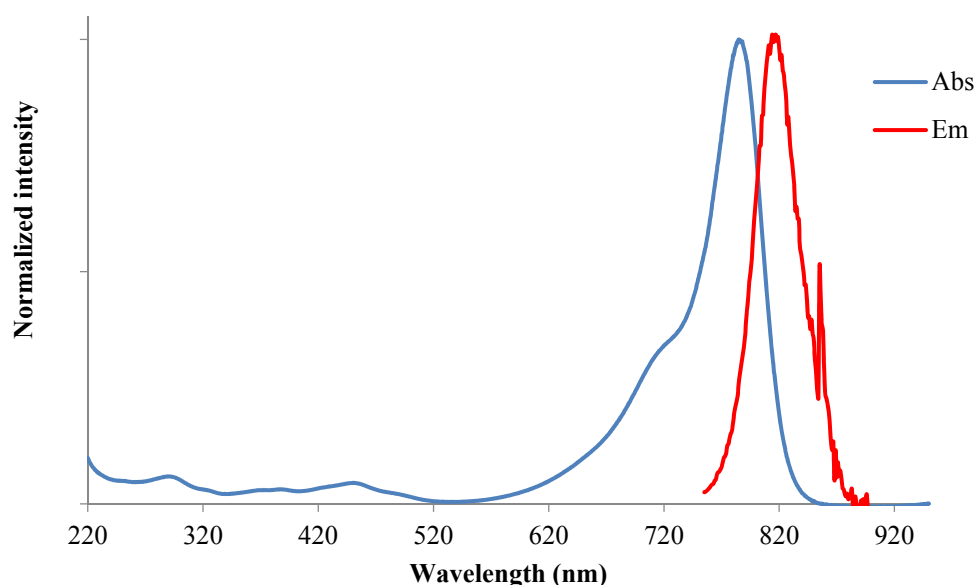


Figure IV-19: Absorption and emission spectrum (at λ_{exc} of 740nm) of the purified compound (36) in PBS (pH 7.4) using UV-Vis and fluorescence spectroscopy.

Table IV-2: Photophysical properties of the PET-Optical probe in PBS at 298K

Compound	λ_{abs} (nm)	λ_{em} (nm)	ϵ ($\text{M}^{-1}\cdot\text{cm}^{-1}$)	Φ (%)
36	785	819	197350	2.5

The photophysical properties of **36** were studied in PBS at room temperature. The data has been summarized in Table IV-2. The bimodal fluorophore displays long wavelength absorption and emission bands that match closely to that of ICG in aqueous solutions (Figure IV-19). The compound has an absorption maximum of 785 nm, as a result it is well suited for imaging using currently available filter sets optimized for ICG. The quantum yield of the probe was computed to be 2.5% which is characteristic of ICG like dyes. Although, this is relatively lower compared to other dyes like Cy5, the NIR window compensates for this by providing high signal to noise ratio (low auto-fluorescence). The aqueous solution of the probes revealed no indication of aggregation which otherwise would manifest itself as a second absorption band around 70nm shorter from the main peak. The short wavelength shoulder preceding the main peak in the absorption spectrum is a common feature of virtually all cyanine based fluorophores and is even observed in less polar solvents such as DMSO and MeOH where there is least tendency for aggregation. The formation and presence of dimers or aggregates is undesirable as they likely result in intermolecular quenching of fluorescence emission [122].

IV-4.2 Radiolabelling and stability of the PET-Optical probe:

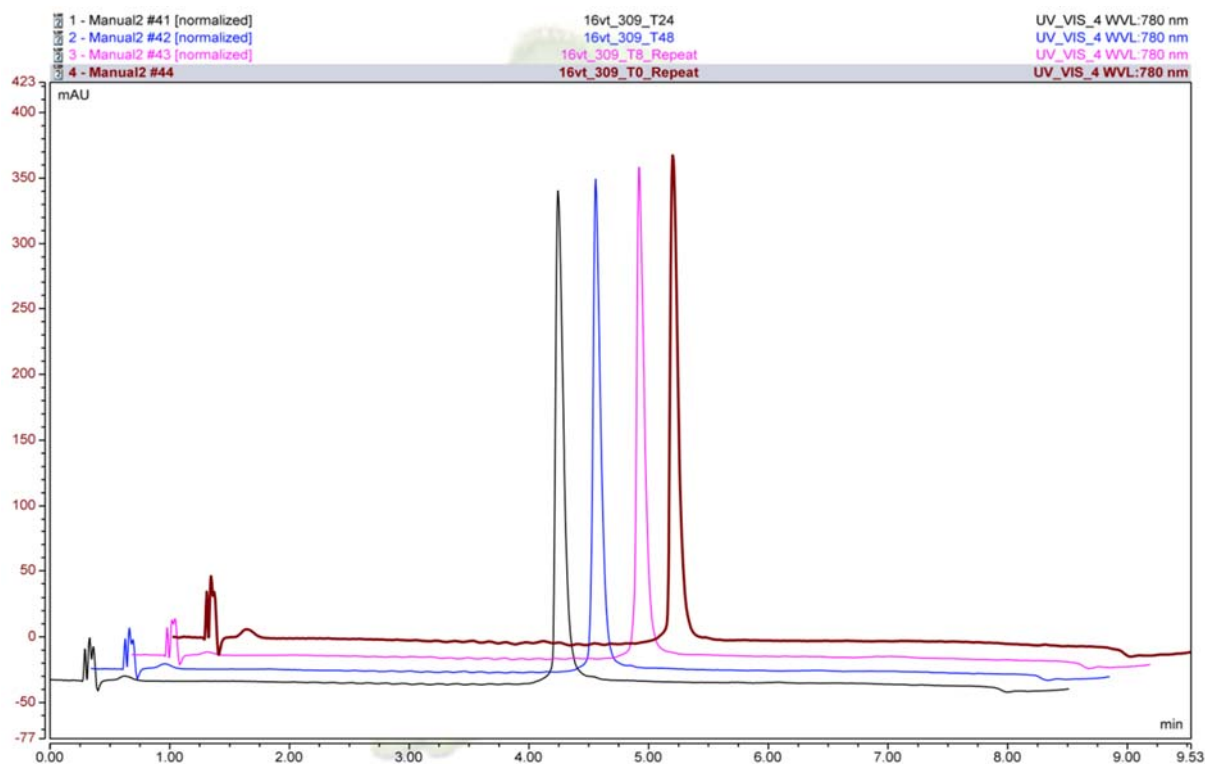


Figure IV-20: Plasma stability of the bimodal probe **36** at 37°C evaluated by HPLC at 780nm. The bimodal probe is expected to remain stable in terms of its optical/fluorescent properties as well as radiochemical properties after complexation at the physiological conditions. The stability of the bimodal probe was assessed by incubating the probe in human plasma at 37°C at the concentration of 0.5mg/mL over a period of 48h. Aliquots were withdrawn at t_0 , t_8 , t_{24} and t_{48} and extracted into equal volume of methanol. This analysis represents the typical approach for the bioanalysis of the drugs during the pharmacokinetics studies, wherein the plasma recovered from the subjects is treated with a suitable organic solvent to precipitate the serum proteins and extract the drug into a solvent system that can be quantified chromatographically.

Sowell et al., have demonstrated that IR-783 has propensity to bind to HSA with a binding affinity of around $6.5 \times 10^6 \text{ M}^{-1}$ [193]. Although there has been structural modification of the dye IR783 in the bimodal probe, it can still be expected to have binding behaviour similar to that of the native dye IR783. Extraction of the plasma by methanol ensures serum protein precipitation and release of the probe that can be analysed by HPLC. The probe was found to be stable in plasma at 37°C over a period of 48h as can be seen from the overlaid chromatograms (figure 3-20) that depict no change in the retention time of the probe or appearance of new peaks when the absorbance was measured at 780nm. The peaks corresponded to the molecular species of the probe as confirmed by the mass analysis (LC-

MS). This ensured that the optical/fluorescent properties of the probe remained unaffected at the physiological conditions.

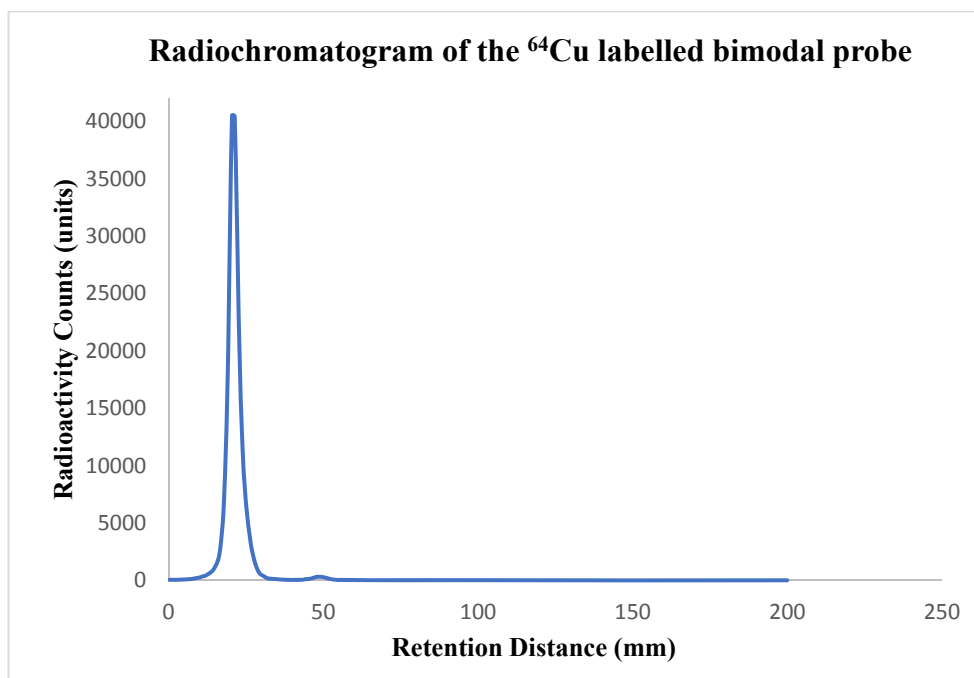


Figure IV-21: Radiochromatogram of the ⁶⁴Cu labelled bimodal probe obtained after ITLC-SA using 0.1M EDTA as a mobile phase.

Stability studies were also performed to further understand the probe stability under radiolabelled conditions (with ⁶⁴Cu) with end-point being radiochemical purity. Radiolabelling of the compound **36** was performed using ⁶⁴Cu, as it is one of the most suitable radio-isotope for PET imaging. The chelator NODAGA exhibits excellent complexation properties for ⁶⁴Cu and ⁶⁸Ga and hence this probe could be also useful in PET studies with ⁶⁸Ga. The complexation was performed by incubating (37°C) the compound with ⁶⁴Cu in ammonium acetate buffer at pH 5.8 for 45min. The quality control of the radiolabelling was performed by radio ITLC. Briefly, a micro-droplet was spotted onto the ITLC plates (ITLC-SA) and the chromatography was performed by using 0.1M EDTA as a mobile phase. The ITLC plates were read using the radio-scanner. Figure IV-21 shows the radio-chromatogram of the ⁶⁴Cu complexed probe at t_0 which exhibits a good radiochemical purity of around 99%. The radiolabelled probe was further subjected to EDTA challenge study and plasma stability. The EDTA challenge protocol involved incubating the labelled probe in HEPES buffer (pH 7, 0.5M) containing EDTA (50mM). This enables to have an insight into the resistance of the labelled probe toward trans-chelation by the potential sequestering agents present in the physiological fluids. The radiolabelled probe was found to have an excellent stability towards trans-chelation as the radiochemical purity remained above 90% with no change in the retention time of the peak or emergence of new peak over a period of 48h. Similar results

were obtained also for the plasma stability experiments over a period of 48h when incubated at 37°C. The cumulative stability studies as described above justifies the utility of the probe for its bimodal imaging potential.

IV-4.3 Binding affinity measurements using NAALDase assay:

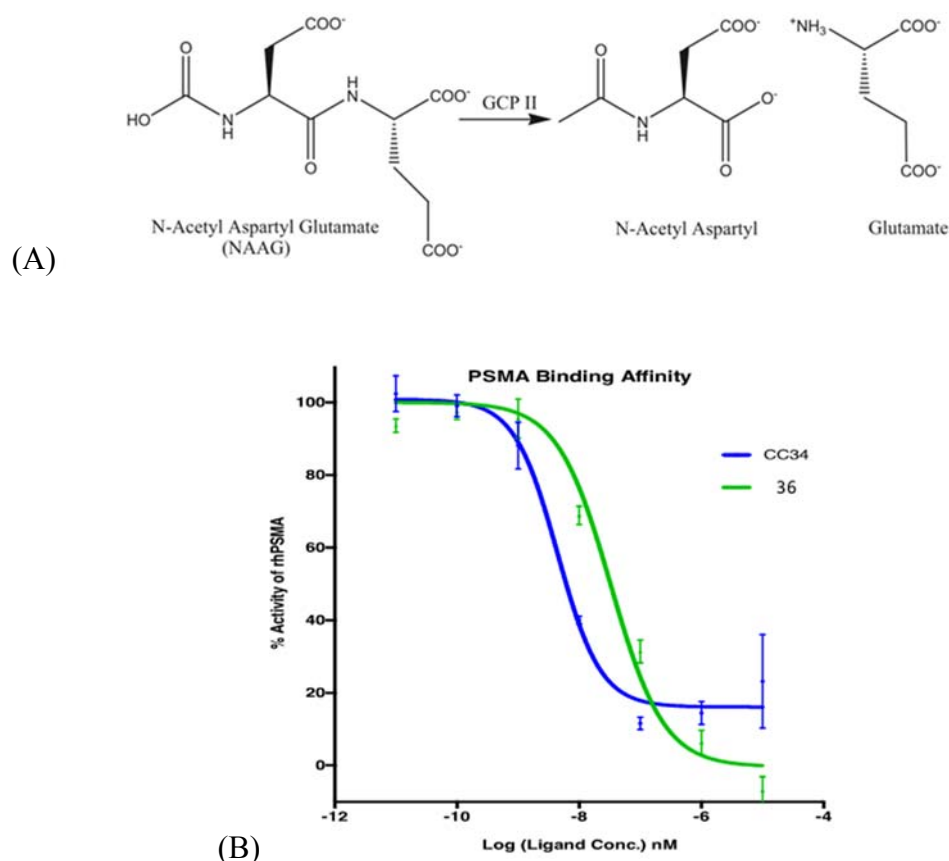


Figure IV-22: Enzymatic activity of the PSMA/NAALADase A) Breakdown of the enzyme substrate/NAAG (Adapted from [136]). B) Binding affinity measurements of the PSMA based diagnostic probes using in-vitro assay.

In order to understand the tumor localization and the binding potential of the probe towards PSMA receptors, it is essential to perform the in-vitro studies using appropriate cell models that express the PSMA receptors at adequate levels. For instance, LNCap cells have been widely used as reported by several research groups working in this arena[167]. Alternatively, biochemical assays based on enzymatic activity could be performed which can be an excellent tool to reflect the PSMA targeting ability of the PSMA inhibitors. The binding affinity of the compound **36** towards PSMA was found to be very good based on the NAALDase assay. The assay is based on the principle that PSMA hydrolyses the substrate N-acetyl-L-Asp-L-Glu into N-acetyl-L-Asp and L-Glu. The L-Glu product is measured by fluorescence after its derivatization by ortho-phthaldialdehydewhich was performed based on the protocol provided by the vendor (R&D Systems, Bio-Techne Ltd, UK). Typically, rhPSMA (recombinant

human PSMA) at the concentration of 0.4 μ g/mL is mixed with the bimodal probe/inhibitor in HEPES buffer (50mM, pH 7.5) and incubated for 1h at 37°C. The reaction is stopped by transient heating at 95°C for 5 min, followed by addition of ortho-phthaldialdehydecontaining buffer. The resulting solution is incubated at room temperature for 10min and then analysed by fluorescence spectrometry at the excitation and the emission wavelengths of 330nm and 450nm respectively in an endpoint mode. The specific activity of PSMA is then calculated as below:

$$\text{Specific Activity} = \frac{\text{Adjusted Fluorescence (RFU)} \times \text{Conversion factor (pmol/RFU)}}{\text{Incubation time (min)} \times \text{amount of enzyme}(\mu\text{g})}$$

#Adjusted fluorescence – adjusted for blank substrate

Conversion factor – derived from the calibration standard L-glutamic acid.

The above analysis was performed with various concentrations/dilutions of the substrate and the resulting activity of the PSMA was used to calculate a plot between the two parameters. As can be seen in the Figure IV-22, a sigmoidal curve was obtained which is typical of an enzyme activity v/s substrate concentration curve or a pharmacodynamics dose response curve. As the concentration of the inhibitor increases the activity of the enzyme decreases proportionally and then reaches a plateau where there is a saturation and all the active sites on the enzyme are blocked. The mid-point of the linear region of the curve is a useful indicator for the interpretation of such sigmoidal relationship. In this context, it is referred to as IC₅₀ or Inhibitor Concentration₅₀ which is defined as the concentration of the inhibitor that is needed to reduce the activity of the enzyme to half or 50% of its initial activity. Figure IV-22 depicts two-sigmoidal curve one representing the bimodal probe and the other CC34 which has been used here as a reference compound. The curves were obtained by plotting the activity of PSMA versus the logarithms of molar concentration and fitting of the data points using non-linear regression employing GraphPad Prism software. The IC₅₀ of the bimodal probe was observed to be 3.26 x 10⁻⁸ M or 0.326 nM which was around 14 times lower to the reference compound CC34 (4.47 x 10⁻⁹ M or 4.47 nM). Nonetheless, the bimodal probe can be considered to be significantly potent towards its PSMA binding affinity that reflects the PSMA targeting potential of this bulky probe. The lower affinity compared to CC34 could be because of its bulky macromolecular nature partly afforded by the fluorescent dye which in turn could induce or alter the nonspecific interactions between the probe and the PSMA.

IV-5 Conclusions:

The objective of this chapter was to develop a new bimodal imaging probe targeted towards PSMA for prostate cancer theranosis. This has been realized through a multistep chemical synthesis encompassing appropriate selection of chelator for PET imaging and NIR fluorophore capitalizing on the collective expertise of Chematech and ICMUB in Dijon. Following aspects represent the conclusive remarks towards accomplishing this objective:

- The PSMA targeted PET-Optical imaging probe has been successfully developed through strategic synthetic schemes and chromatographic purifications, with moderate yields and excellent purity and spectroscopic characterization.
- The bimodal probe has been evaluated for its photo-physical characteristics that demonstrate its equivalence with ICG dye which has been the only FDA approved NIR dye for imaging in humans.
- The radiolabelling protocol using ^{64}Cu for this probe has been facile and efficient and affords a stable compound in terms of the radiochemical purity and this could also be adapted for other PET isotopes like ^{68}Ga .
- The probe has exhibited to have very good stability at the physiological conditions through determination of its stability in human plasma at 37°C up to 2 days for its optical as well as radio-chelating properties.
- *In-vitro* enzymatic assay for PSMA/NAALDase inhibition revealed a good binding affinity of the probe towards the PSMA receptor highlighting its potential for targeting PSMA positive prostate cancer.

Moreover, the approach described in this chapter could easily be adapted to other cancer targeting ligands. Biological investigation of this probe in the PSMA positive xenograft rodent model represents the immediate perspective of this project to truly realize the theranostic potential of this system.

Chapter V. Bimodal imaging probes for bioconjugation to antibody fragments and nanoparticle functionalization

V-1 Multimodal imaging probes for bioconjugation:

Design of the multi-modal contrast agents has been one of the thrust areas of the research in the imaging sciences. Combination of the two imaging modalities can be really advantageous if they complement each other in revealing the correct biological information for preclinical and clinical use. This approach has given rise to hybrid imaging modalities like PET/MRI, SPECT/CT, PET/OI and PET/CT. Hybrid imaging helps in retrieving the information that otherwise would not be available with individual modality. For instance, a combination of functional information (from PET) and anatomic/spatial information (obtained by CT) into a single image provides an advanced diagnostic [29, 194]. To successfully leverage such symbiosis, it is necessary to develop tracers that can have dual/multiple functionality. Tracers coupled to the antibodies/peptides/chemical ligands enable molecular and tissue level investigations. These tracers could be a radioisotope/heavy metal complexed by chelator moiety, metals in colloidal form (nanoparticles), an organic fluorescent dye or a combination of any of these. Realization of the above systems necessitates chemical synthesis of structures which encompass tracers that support different imaging modalities (PET-MRI, PET-OI, MRI-OI etc.) and could be grafted onto antibodies/antibody fragments/peptides or nanoparticles. In a PET-OI arena, using a same bimodal probe for PET imaging for diagnosis and later for intra-operative surgical assistance based on the optical imaging presents a more rational and valuable approach than development of probes independently. In the context of bioconjugation, the sequential conjugation with two different probes, which can present many process and characterization related challenges can be overcome using the bimodal probes. Our research interests particularly lie in developing such probes and has been testified by our previous work in this arena.

Bimodal probes based on BODIPY and DOTA have been developed by our group for targeted SPECT/Optical imaging of neuroendocrine tumors and lipopolysaccharide detoxification [195, 196]. To capitalise and extend application of such probes, Maindron et al., developed a SPECT-Optical probe for conjugation to trastuzumab using an isothiocyanate handle. The compound was called TBK-686 for TrisDOTA-BODIPY-Lysine- 686 nm. It comprises of a central bodipy which is linked to DOTA and conjugation site (-NCS) on one side (via click chemistry), whereas on the other side it bears two additional DOTA molecules (Figure I-1). The accumulation of the bioconjugate of this probe in HER-2 expressing tumors in mice demonstrated by both in vivo and ex vivo SPECT/optical imaging provided for the potential of such probes in bimodal imaging [197]. Another probe that has been developed at Chematech/ICMUB for PET-Optical imaging is NODAGA-Lys-Cy5-NCS. Use of NODAGA

Chapter V. Bimodal imaging probes for bioconjugation to antibody fragments and nanoparticle functionalization

as chelating agent makes it suitable for radiolabelling with PET radio-isotopes like ^{64}Cu and ^{68}Ga . This probe has been deployed for conjugation with monoclonal antibody that targets *Aspergillus Fumigatus* within the purview of another European project MATHIAS. Thus, developing bimodal probes involves synthesis of complex chemical molecules that can cater to diagnosis of broader set of disease conditions.

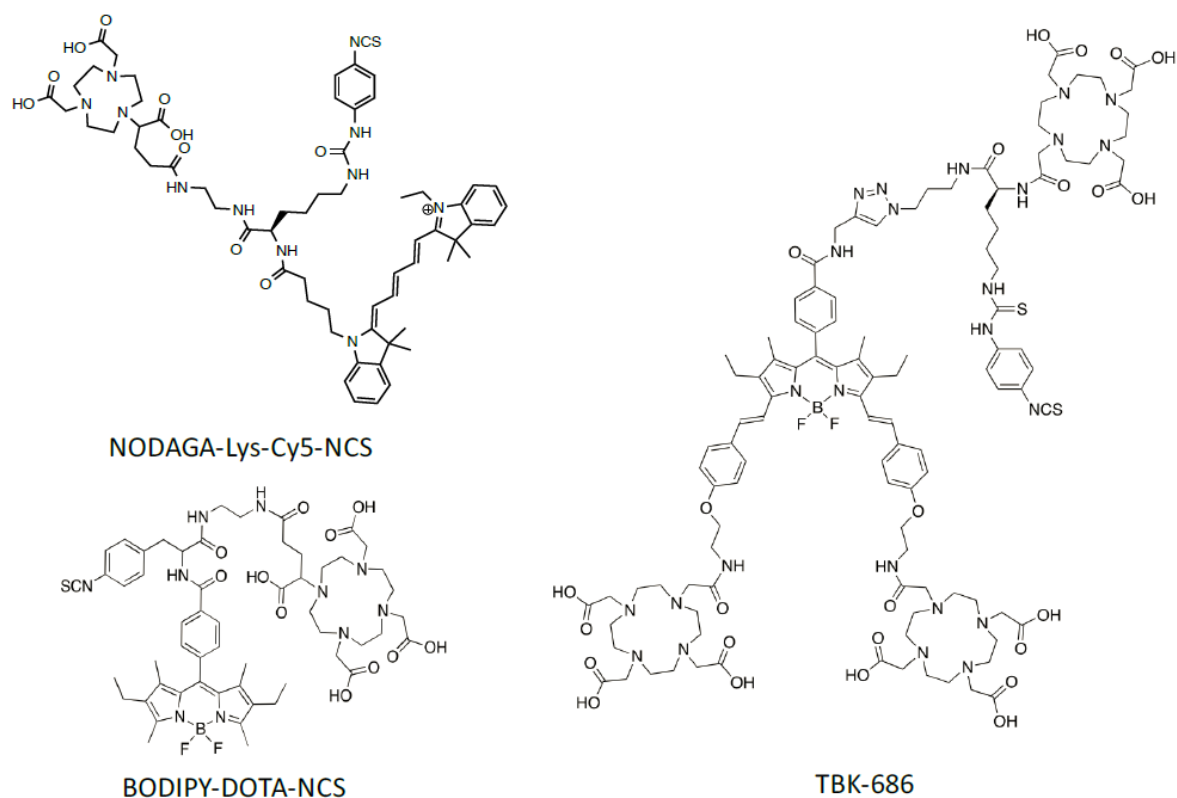


Figure V-1: Bimodal probes developed at ICMUB, Dijon for bioconjugation applications. Although challenging, this integrated approach enables development of unique tracer combinations having potential value in multimodal imaging. In the following chapter, we discuss the development of PET-Optical imaging tracer based on the Monomolecular Multimodal Imaging Probe (MOMIP) platform that has been one of the mainstays of the research conducted in our group at ICMUB and Chematech, Dijon. The central theme in developing this multimodal platform has been to develop first a linker system which is typically an amino acid or a short peptide and then subsequently extending this system by functionalizing it with a chelator, fluorescent dye and a bioconjugatable handle which enables this platform to be appended to a protein/peptide or a nanoparticle. In the sections following the synthesis, this probe has been further demonstrated to be valuable in site specific conjugation of the antibody fragments as well as the functionalization of the nanoparticles.

V-2 Synthesis of trifunctional probe for PET-Optical imaging:

V-2.1 Synthesis of bifunctional chelating agent:

The synthesis begins with NODAGA(tBu)₃ which has been a key starting compound in majority of the PET based imaging probes. NODAGA(tBu)₃ is converted into its amine bearing form NODAGA(tBu)₃-NH₂ through classical coupling chemistry using HBTU and HOBT as coupling agents (Figure V-2). Possibility of the covalent dimers formation necessitates the use of the ethylene diamine in excess (eq. 50). Post reaction work-up was necessary to get rid of the excess of the reagents. This involved washing of the organic phase (dichloromethane) successively with acidic, basic and neutral aqueous solutions followed by drying over MgSO₄. The compound was finally purified by flash chromatography using C18 column using water (0.1%) and acetonitrile (0.1%) as eluents. The compound (**19**) was obtained in good yield of 68% as a TFA salt. This compound was synthesized in the same manner as the one indicated in Chapter III.

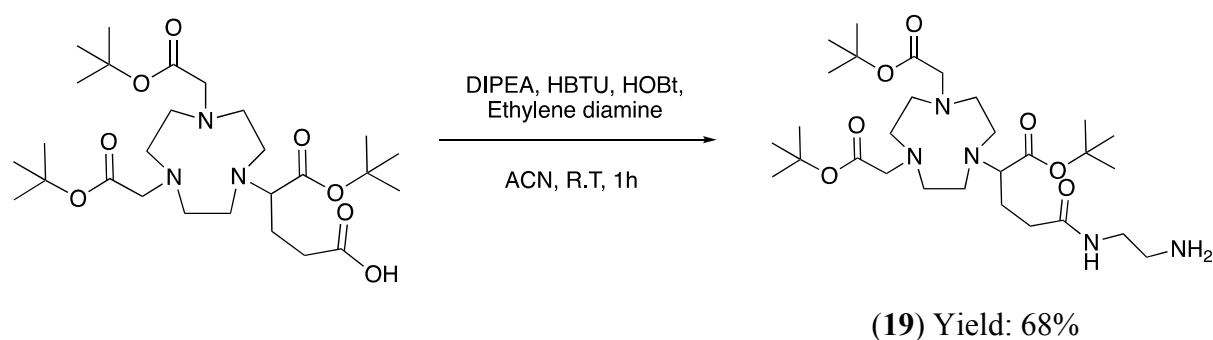
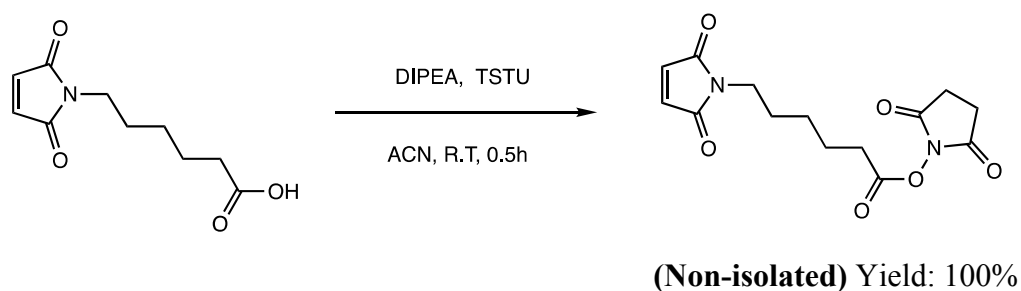


Figure V-2: Synthesis of NODAGA(tBu)₃-NH₂ (**19**)

V-2.2 Synthesis of the linker system bearing chelator and conjugation site:

The next step in the synthesis was to build a building block containing a maleimide (bioconjugation site) and linker system bearing appropriately protected site. Choice of a suitable lysine derivative is very crucial while dealing with maleimide as it is very sensitive and prone to be attacked by variety of the reagents employed in deprotecting reactions used typically in peptide chemistry.



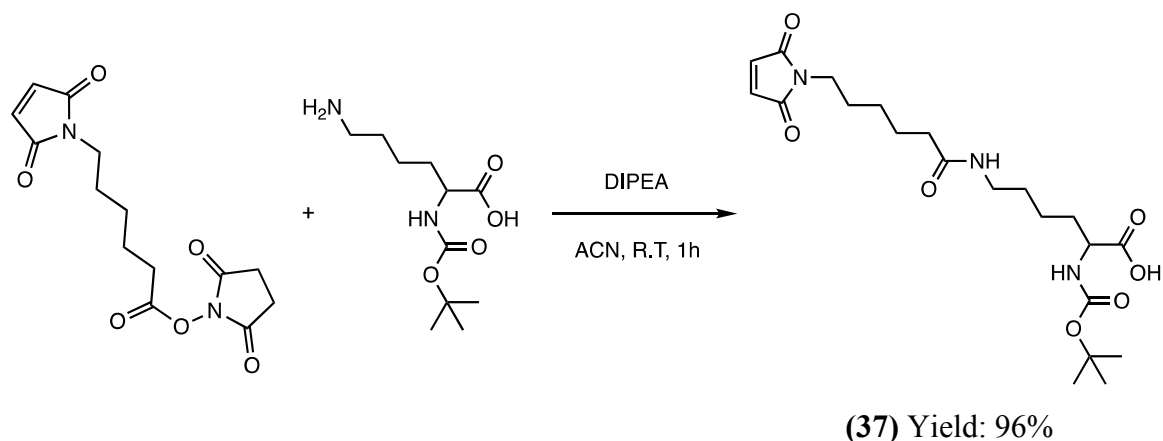


Figure V-3: Synthesis of 6-Maleimido-hexanoic-Lysine-Boc (**37**).

In this context, 6-maleimido-hexanoic acid (6-MHA) was first reacted with Boc-lysine-OH, wherein the carboxylate group over 6-MHA was activated to NHS ester by TSTU which was then amide coupled with the ϵ -NH₂ of Boc-lysine-OH (Figure V-3). The compound (**37**) was purified via C18 flash chromatography that led to a pure compound with HPLC purity of around 97%.

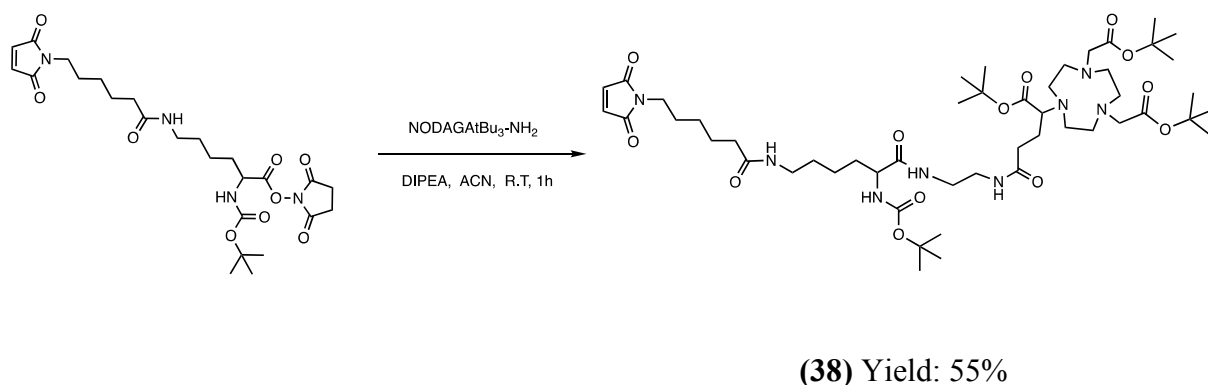
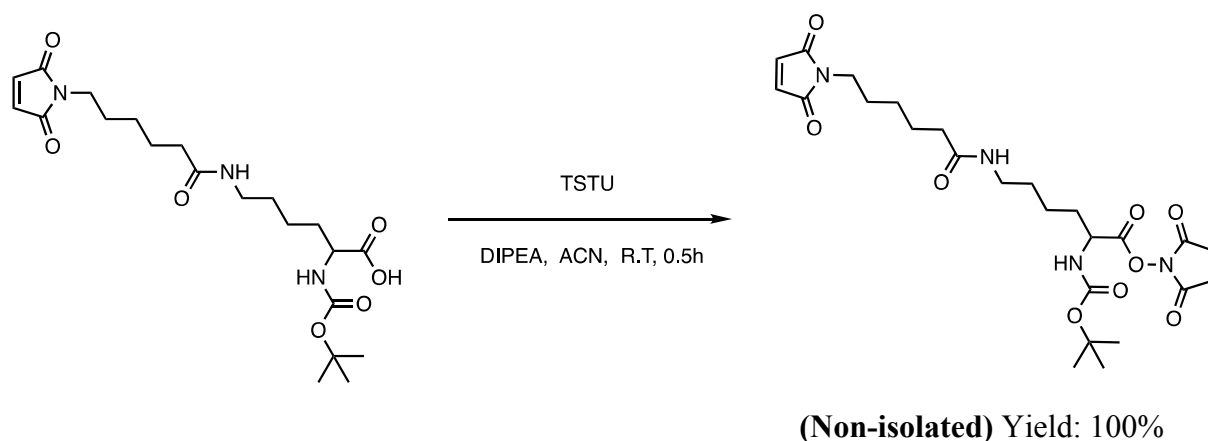


Figure V-4: Synthesis of 6-Maleimido-hexanoic-Lysine-Boc-NODAGA(tBu)₃ (**38**).

As depicted in the scheme above (Figure V-4), the maleimide-lysine linker system was further

Chapter V. Bimodal imaging probes for bioconjugation to antibody fragments and nanoparticle functionalization

integrated with the chelator bearing moiety NODAGA(tBu)₃-NH₂. The carboxylate functional group on the maleimide-lysine system was activated using TSTU to afford an intermediate NHS ester (in-situ). Once the ester formation was verified (by LC-MS) it was appended onto the amino group of NODAGA(tBu)₃-NH₂, that resulted in a product bearing a maleimide, protected NODAGA and t-butoxy carbonyl (Boc) protected α -amino group (**38**).

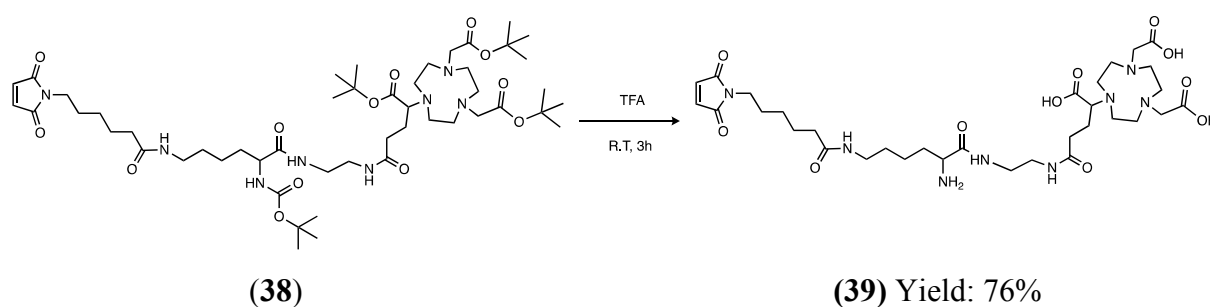


Figure V-5: Synthesis of 6-Maleimidohexanoic-Lysine-NODAGA-NH₂ (**39**)

To set free the protected α - amino group present on the compound (**38**), it was treated with TFA (Figure V-5). Treatment with TFA not just enabled deprotection of the t-butoxy group but also deprotection of the tert-butyl group present on NODAGA. Thus, this step strategically afforded deprotection of two different sites in one step to yield a compound which was purified by flash chromatography to obtain the pure product (**39**). This compound was observed to be quite hygroscopic and hence needed to be stored away from moisture.

V-2.3 Synthesis of a trifunctional probe using bioconjugatable IR-783:

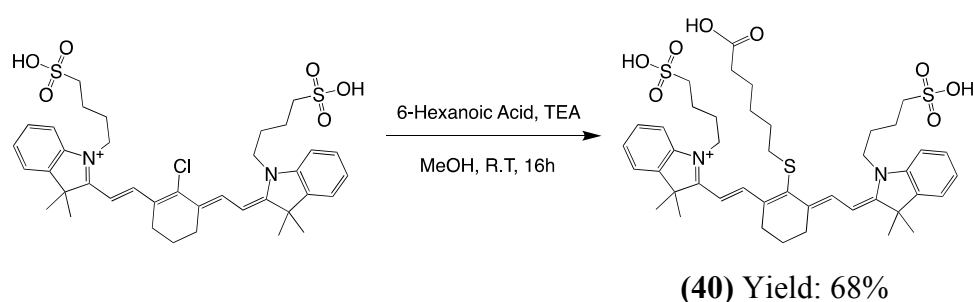


Figure V-6: Synthesis of IR-783-Hexanoic Acid (**40**)

The third aspect of developing a trifunctional probe involved the development of near infrared dye (NIR dye). The NIR dye used to address this part, entailed use of the commercially available dye IR-783. As has been demonstrated earlier, IR-783 can be exploited for bioconjugation applications by introduction of the carboxylate group at the meso position on cyclohexyl ring using Suzuki coupling [198] or using thiol mediated nucleophilic substitution reactions [48]. Owing to simple work up and ease of purification we adopted the second

approach. The chloro- group on the cyclohexyl ring was displaced by 6-mercaptohexanoic acid by overnight stirring in the presence of triethylamine/TEA (base) (Figure V-6). The product was purified by semi-preparative HPLC to afford the product **(40)** with a purity of around 98%.

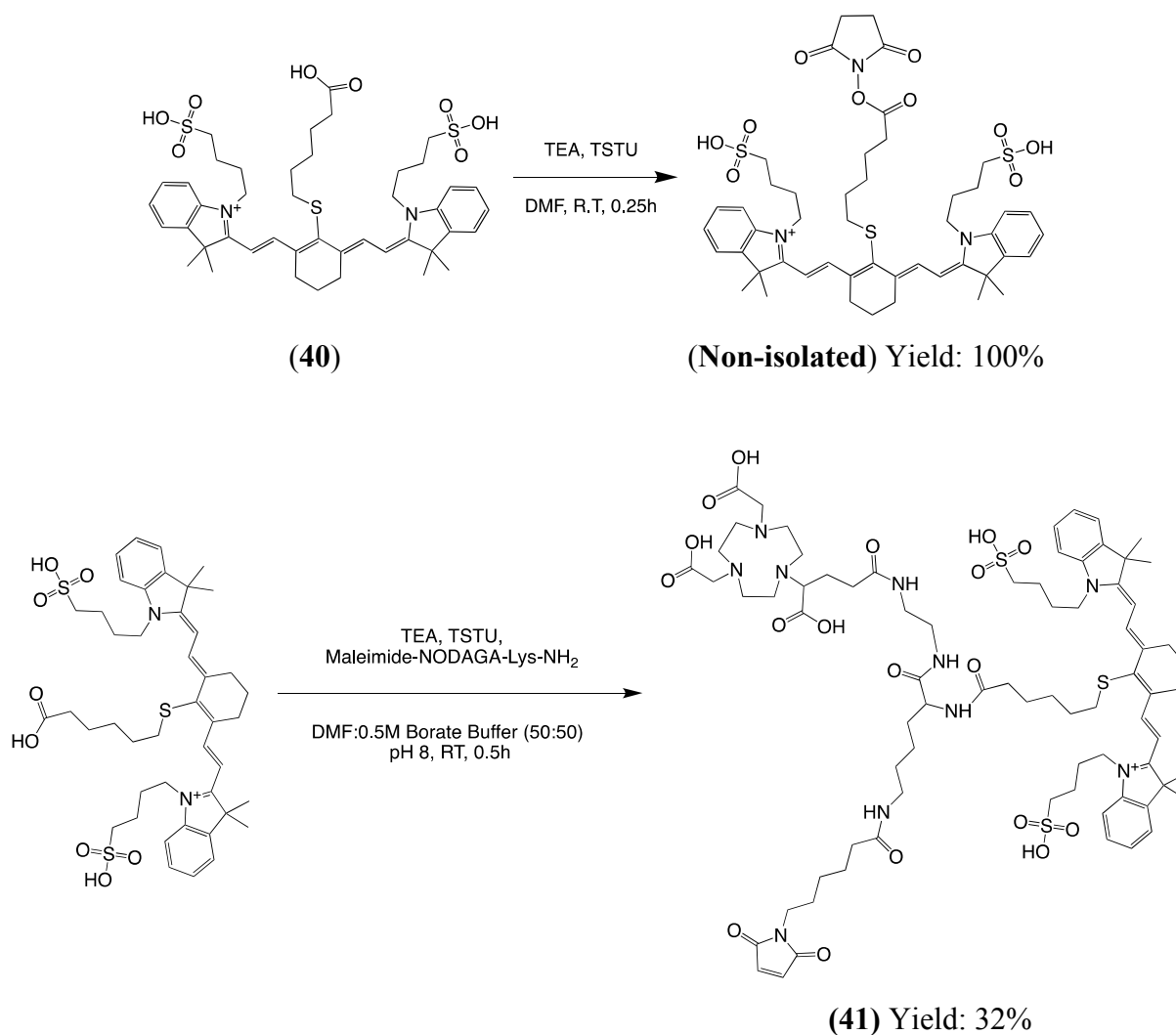


Figure V-7: Synthesis of 6-Maleimido-hexanoic-Lysine-NODAGA-HA-IR783 (**(41)**)

Introduction of the carboxylate function improves the bioconjugatability of the compound **(40)** in terms of the peptide chemistry. This function could be easily activated by the coupling agent TSTU to afford the NHS ester of the compound **(40)** as has been verified by LC-MS. The next critical step involved the final assembly of the molecule by forming a peptide link between the activated **(40)** and the amine bearing **(39)**. Initial attempts to perform this reaction in DMF alone caused a significant degradation of the dye, possibly due to base promoted degradation in DMF. This could be alleviated considerably by performing the reaction in partially aqueous conditions [199].

Chapter V. Bimodal imaging probes for bioconjugation to antibody fragments and nanoparticle functionalization

As can be observed in Figure V-7, the peptide coupling was performed in a 50:50 mixture of DMF and borate buffer (0.5M, pH 8). Immediately after the reaction was complete the final compound was purified by semi-preparative HPLC to obtain the pure product (**41**) with a purity of around 99% as detected by HPLC at 780nm (Figure V-8).

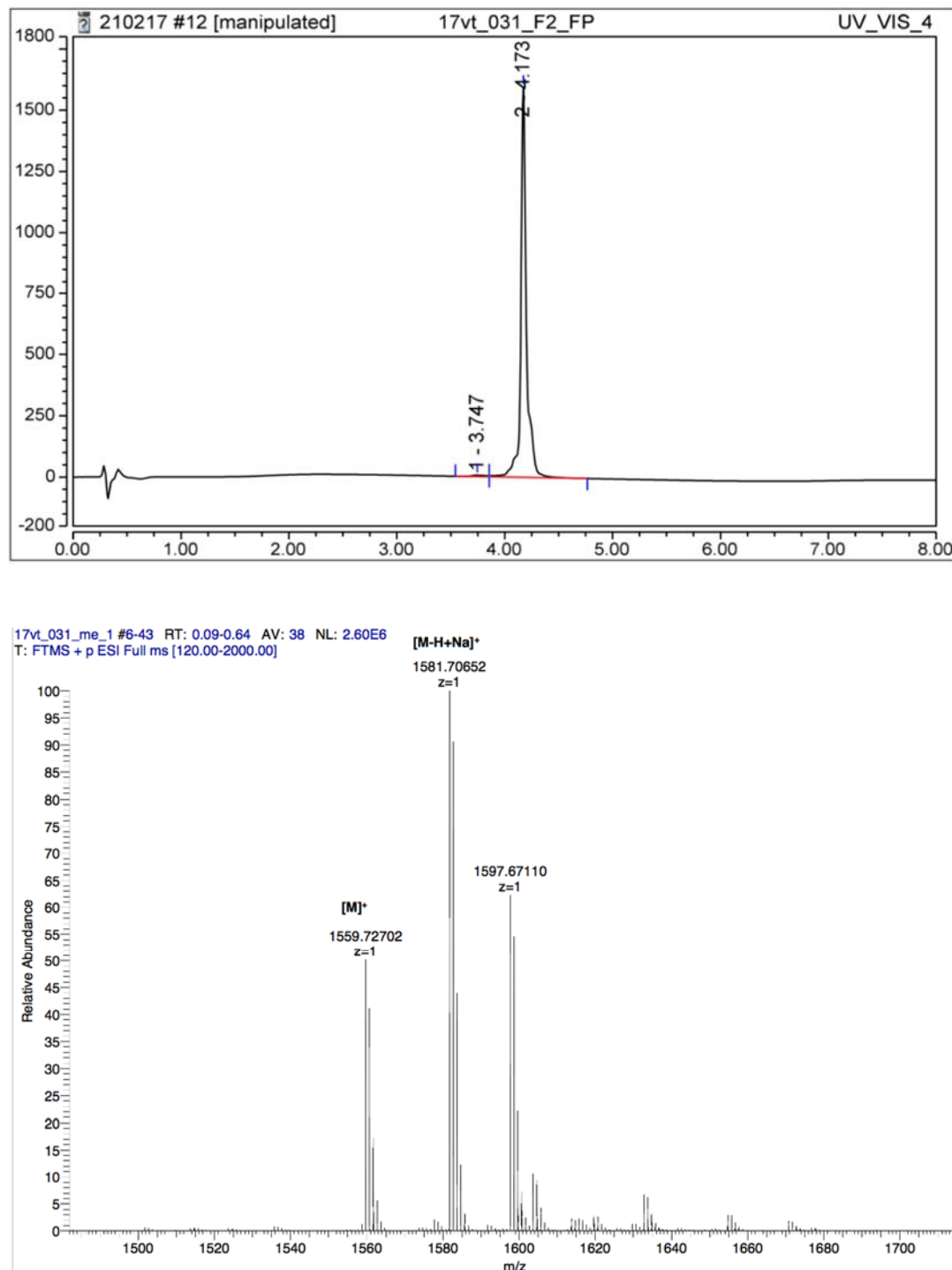


Figure V-8: HPLC chromatogram at 780nm and HR-MS spectrum of the purified compound (**41**).

V-3 Photo-physical characterization of the trifunctional probe:

The photo-physical properties of (**41**) were studied in PBS at room temperature. The data has been summarized in (Table V-1). The bimodal fluorochrome displays long wavelength absorption and emission bands that match closely to that of ICG in aqueous solutions (Figure V-9). The compound has an absorption maximum of 785 nm with a quantum yield of 2%, as a result it is well suited for imaging using currently available filter sets optimized for ICG. The aqueous solution of the probe exhibited no indication of aggregation which otherwise would manifest itself as a second absorption band around 70nm shorter from the main peak. The short wavelength shoulder preceding the main peak in the absorption spectrum is a common feature of virtually all cyanine based fluorochromes and is even observed in less polar solvents such as DMSO and MeOH where there is least tendency for aggregation. The formation and presence of dimers or aggregates is undesirable as they likely result in intermolecular quenching of fluorescence emission [122].

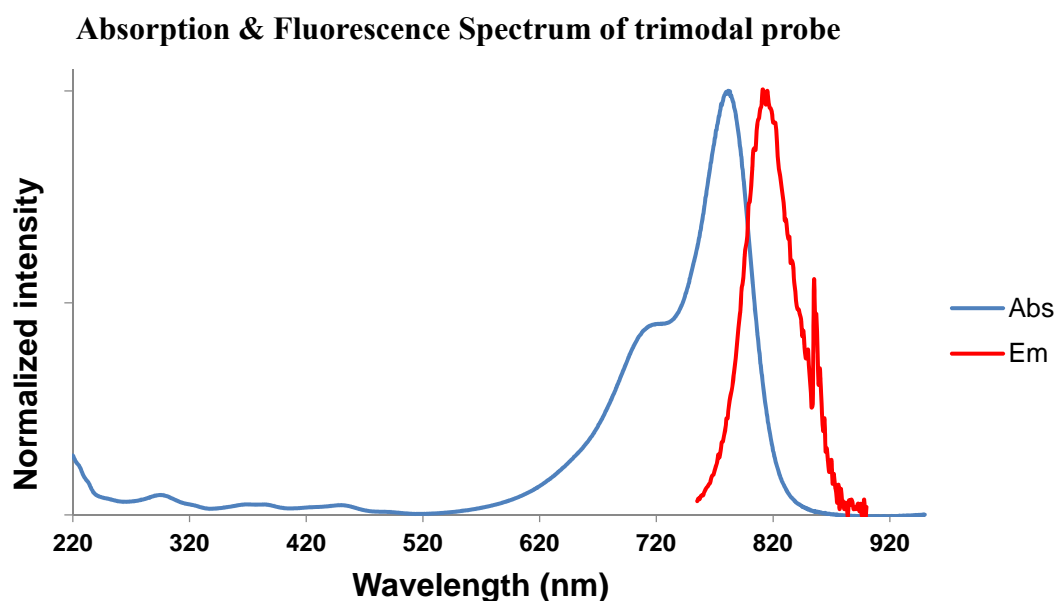


Figure V-9: Absorption and emission spectrum of the purified compound **41** in PBS using UV-Vis and fluorescence spectroscopy.

Table V-1: Photophysical properties of the trifunctional probe (**41**) in PBS at 298K.

Compound	λ_{abs} (nm)	λ_{em} (nm)	ϵ ($\text{M}^{-1}.\text{cm}^{-1}$)	Φ (%)
41	785	811	178470	2

Having demonstrated the development of this multimodal probes based on the well-designed synthetic schemes, purification protocols and pertinent characterization, it was necessary to

Chapter V. Bimodal imaging probes for bioconjugation to antibody fragments and nanoparticle functionalization

justify the applicability of this probe in diverse situations. Subsequent chapter deals with the applications covered in the context of antibody bio-conjugation and nanoparticle functionalization.

V-4 Chemical biology of the antibody drug conjugates:

Antibody–drug conjugate (ADC) encompasses a recombinant monoclonal antibody (mAb) which is covalently linked to a cytotoxic moiety through a synthetic linker system. Such an integrated modality combines the potency of highly cytotoxic anti-cancer compounds (typically 200-1000 Da) with the high selectivity and stability of mAbs [79]. Using this approach of targeted delivery, the eradication of the tumor cells can be realized whilst sparing the normal cells which have not been targeted by the antibody. Thus, mAbs provide an ideal delivery platform based on a magic bullet concept for molecular targeting of tumor cells. However, the realization of this theory has taken decades to implement and it is only recently that there has been surge in the number of ADCs that are in clinical development with only handful of market approvals hitherto [200]. The concept of ADCs can be equally extended to imaging or radiotherapy by conjugating a chelating moiety capable of sequestering a radioisotope that has implications in nuclear imaging/radiotherapy. Diverse strategies have been developed for chemical conjugation of the monoclonal antibodies with cytotoxic payloads or imaging probes which will be summarized in following sections (Figure V-10).

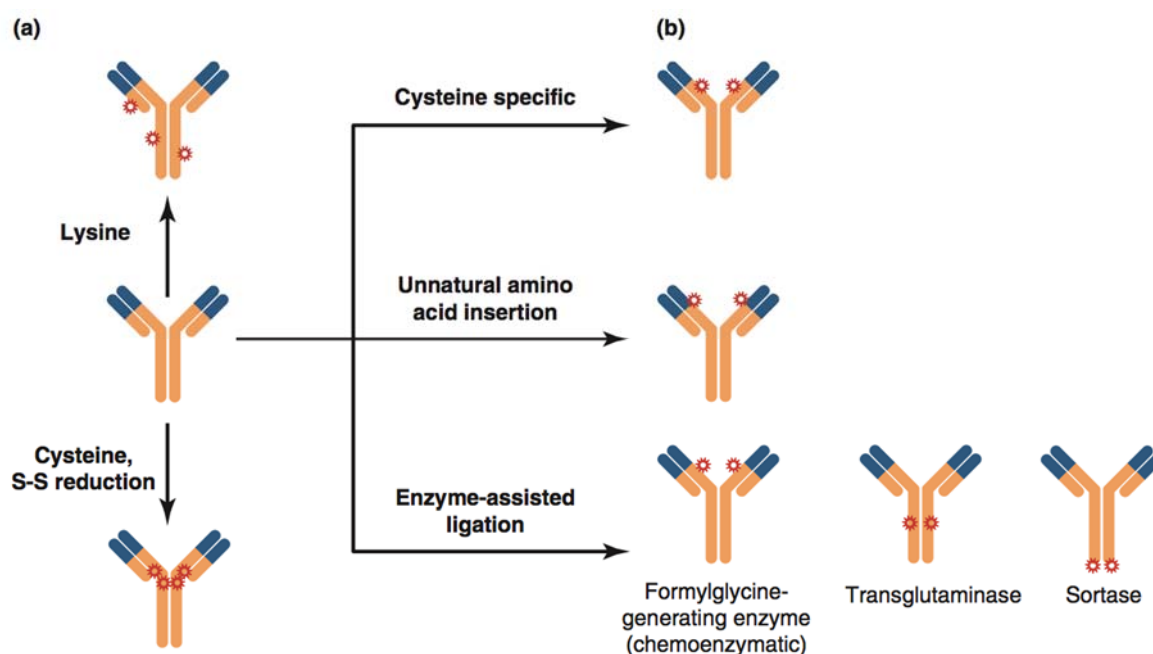


Figure V-10: Antibody–drug conjugate (ADC) products of random conjugation comprise chemically heterogeneous species (a), whereas site-specific conjugation methods produce homogeneous product profiles (b). Adapted from [201].

V-4.1 Non-specific Conjugation through Native Residues

The most common naturally occurring amino acids such as lysine and cysteine are attractive reactive sites for antibody conjugation. A typical IgG antibody has over 80 lysines of which

about 20 residues are found at solvent-accessible sites. Unlike lysine, cysteine residues are less abundant in IgGs but are more uniformly and symmetrically distributed. In an IgG antibody there are 16 cysteine pairs that arise from 12 intra-chain and 4 inter-chain disulfide linkages. The four inter-chain disulfide bonds are the main targets for conjugation owing to their solvent accessibility and apparent ease of reduction [202, 203].

The prime advantage of linkage via the native lysine residues is the ease of reactivity and obviation of prior processing/modification of the antibody. However, conjugation at these natural sites results in variability and heterogeneity of the resulting conjugates with a wide range of drug to antibody ratios (DAR). Moreover, the non-specific conjugation often results in alteration of electrostatic properties (with corresponding change in pI) and hydrophobicity of the parent antibody [204, 205]. It has been reported that most of the solvent-accessible lysine residues are localized in the CH₂ domain and conjugation at these sites can have destabilizing effect on the antibody making it susceptible to aggregation [206].

Presence of a reactive thiol group is the prime feature of the amino acid cysteine which serves the essential roles in the structure and function of several proteins. Conjugation of thiol-reactive probes to proteins via the cysteine residues has been a practised method for protein labelling, and has also been extended to the generation of ADCs. Using the native cysteine residues for ADC synthesis involves partial reduction of inter-chain disulfide bonds and results in a heterogeneous mixture of ADCs that differ in terms of conjugation site, DAR and number of intact inter-chain disulfide bonds [207].

Although use of the cysteine residues for the conjugation entails processing of the antibody to chemically reduce the disulfide bonds, this approach yields ADCs that are less heterogeneous compared to ADCs generated via lysine conjugation. This is apparent owing to the limited number of potential sites (8 sites) making it easier to characterize the resulting products. Cysteine conjugated ADCs can thus have favourable implications on the pharmacokinetics and pharmacodynamics due to reduced variability amongst the heterogeneous species [207, 208].

Despite the inherent challenges associated with the use of the native residues, the clinically approved ADCs viz. gemtuzumab ozogamicin (Mylotarg), trastuzumab emtansine (Kadcyla) and brentoximab vedontin (Adcetris) utilize native lysines or cysteines. On the similar lines, antibody conjugates like ⁹⁰Y-Ibritumomab tiuxetan (Zevalin) and ¹³¹I-Tositumomab (Bexxar) have also been approved for targeted immuno-radiotherapy.

V-4.2 Conjugation through genetically engineered sites

In order to overcome the inherent heterogeneity associated with non-specifically conjugated ADCs, antibodies have been engineered to possess reactive sites or amino acids that can be readily used for bioconjugation. Attesting to this concept, THIOMABs platform has been developed by Junutula and co-workers, wherein cysteines residues are engineered onto antibody to enable thiol conjugation at these specific sites. Such ADCs based on site specific–drug conjugates are much superior compared to their conventional counterparts as these conjugates exhibit uniform spatial distribution of the linker-drugs over the antibody surface and display superior safety profiles. On the flip side, a reduction step prior to conjugation might be necessary along with the liability of aggregation caused by disulfide bridging between antibodies [209-211].

On the similar lines, Jeffrey et al. (Seattle Genetics, USA) have recently reported an anti-CD70–pyrrolobenzodiazepine linked through engineered cysteine residues. Previous attempts to prepare the conjugates employing the reduced hinge cysteine residues led to significant ADC aggregation owing to the combination of higher DARs and hydrophobicity of the pyrrolobenzodiazepines. These problems could be circumvented by using the engineered cysteine residue that limited the DAR to 2 [212]. Many ADC candidates based on the engineered cysteine residues are currently under clinical development and can be traced in a recent review published by Beck and co-workers [79].

V-4.3 Enzymatic Bioconjugation:

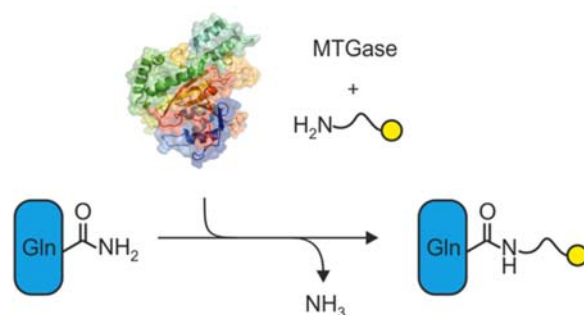


Figure V-11: Transglutaminase mediated protein cross-linking. Adapted from [213].

The ability of an enzyme to catalyse bond formation has been utilized in the development of site-specific conjugation. Enzymes like transglutaminases and glycotransferases have been found to be quite valuable for these applications.

Typically, microbial transglutaminase (MTGase) catalyses an isopeptide bond formation between the γ -carbonyl amide group of glutamines and the primary amine on the linker/drug (Figure V-11). Microbial transglutaminase has been utilized to modify antibodies, including synthesis of homogeneous ADCs [214, 215]. MTGase has also been used to produce

homogeneous trastuzumab-MMAE conjugate using a chemo-enzymatic conjugation strategy that involved at the first, use of peptide-N-glycosidase F (PGNase F) to clip-off the glycan attached to asparagine residue (N297) in the vicinity of conjugation site, glutamine 295 (Q295). This was followed by MTGase treatment, to mount the azide handle on the antibody that could be later used for strain-promoted azide-alkyne cycloaddition (SPAAC) chemistry involving alkyne derivated auristatin (MMAE) [213].

In another interesting amalgamation of polymer chemistry, radiotherapy, and enzymatic conjugation deployed on antibody, Grünberg et al., enzymatically conjugated DOTA (1/3/5) functionalized short length (10 amino acids) polylysine to the heavy chain of chimeric monoclonal anti-L1CAM antibody chCE7agl. These immunoconjugates were radiolabelled with ¹⁷⁷Lu for exploring the potential of these systems for radiotherapy [216]. As a commercially viable technology, ADCs developed based on MTGase have been in clinical development under joint collaboration of ETH, Switzerland and Marseille, France.

Glycoengineering of the antibody/protein enables to alter the antibody through its glycan regions. Modifications at the glycan site reduces the risk of alteration of the binding affinity which otherwise could be possible with Lysine/cysteine based conjugations. Chemical oxidation of *cis*-glycol groups of the glycans (galactose/sialic acids) using sodium periodate (NaIO₄) results in the generation of an aldehyde moiety, that could be used for coupling with nucleophilic ligands/drugs [217, 218]. To prevent the lack of specificity with the chemical oxidation, glycotransferases could be used to graft a chemically active sugar moiety to a glycosylation site on an antibody. Glycotransferases encompass a family of proteins that play a role in the synthesis of oligosaccharides and transfer of a sugar residue from an activated sugar nucleotide to a sugar acceptor or glycoprotein/lipid.

The glycans attached to N-glycosylation site Asn-297 of the Fc fragment can be degalactosylated so as transfer C2-keto-Gal onto it through enzymatic action of mutant glycotransferase. The C2-keto Gal then serves as an anchoring point to which biomolecules can be coupled. Boeggeman et al., developed fluorescent conjugates of trastuzumab using this methodology by employing aminooxyacetamide derivative of Alexa Fluor 488 [219]. Likewise, Zhou et al., have demonstrated the synthesis of MMAE based ADCs through enzymatic remodelling of trastuzumab mediated via galactosyl and sialyltransferases [218]. A recent review by Pradman Qasba summarises the use of glycosyltransferases in antibody drug conjugation [220]. Several other enzymes like formylglycine generating enzyme, sortase, protein farnesyl transferase, biotin ligase, etc. have been implicated in the development of conjugates via enzymatic/chemo-enzymatic approaches [221].

V-4.4 Labelling strategies in antibody conjugation:

Table V-2: Labelling chemistries for antibody conjugates. Adapted from [200].

Reaction Chemistry	Reaction scheme	ReactionRate	Conjugation Site in Protein
Amine-NHS	<p>Primary amine + NHS-Ester → Amide bond + NHS</p>	fast	Lysine, terminal amine
Thiol-Maleimide Michael Addition	<p>Reactive thiol + Maleimide → Thioether bond</p>	fast	Cysteine
Oxime Ligation	<p>p-Acetylphenylalanine + Aminoxy reagent → Oxime bond</p>	slow	p-Acetylphenylalanine
Cycloaddition CuAAC	<p>Azide Amino Acid + Terminal alkyne → Stable triazole</p>	slow	Azidohomoalanine
Cycloaddition SPAAC	<p>Azide Amino Acid + Dibenzocyclooctyne → Stable triazole</p>	slow	Azidohomoalanine
Inverse-electron-demand Diels-Alder reaction	<p>trans-Cyclooctene + Tetrazine reagent → Substituted cyclohexene</p>	very fast	trans-Cyclooctene-Lysine

Some of the major reaction chemistries that govern the bio-conjugation of the drugs or imaging/chelating agents to the monoclonal antibodies or proteins have been depicted in Table V-2. Chemical conjugation is a crucial step in appending a detectable tracer or drug to an antibody/fragment/protein and should proceed quickly with high efficiency under moderate aqueous conditions. Moreover, resulting immune-conjugate should result in optimal tracer to antibody ratio and must be stable under *in vivo* conditions.

NHS esters are widely used in labelling proteins and are typically formed by activation of carboxylate group with a relevant coupling agent (e.g: TSTU, carbodiimide etc.). NHS ester based compounds react with primary amines (nucleophilic substitution) under slightly alkaline conditions (pH 7.2 to 9) to yield stable amide bonds whilst releasing N-hydroxysuccinimide (NHS) as by-product. The payload on the approved ADC Kadcyla (Trastuzumab emtansine) has been conjugated to antibody using this approach via a heterobifunctional linker SMCC. Likewise, several fluorescent dyes and chelating agents are available commercially as their NHS esters.

Thiol reactive chemistry has been extensively used for conjugation reactions wherein the unique nucleophilicity of thiol enables it to undergo reactions with α -halocarbonyl

compounds, perfluoroaromatic molecules, Michael acceptors (maleimide and vinyl moiety), 2-cyanobenzothiazole, phenyloxadiazole sulfone, etc [80]. Although, maleimide-thiol conjugates are potentially vulnerable to exchange reaction with free thiol present on the endogenous albumin it's unclear if it is significant in terms of kinetics to have an impact on the pharmacokinetics/dynamics. [222]. Nonetheless, the Michael addition reaction between thiol from the cysteine residues and the maleimide have a special place in ADC chemistry as most of the site-specific approaches rely on use of cysteine residues. The EMA (European Medicines Agency) and FDA (Food and Drug Administration) approved ADC, Adcetris (brentuximab-vedotin) has been manufactured through this methodology. In addition to the conventional Michael reaction, derivatives of maleimides like dibromomaleimides have shown promise as disulphide bridging agents with better control over DAR without impairing the integrity of the antibody chains [223-225]. Click chemistry has found widespread applications in conjugation of tracer molecules to monoclonal antibodies. Click chemistry based cycloaddition reactions (CuAAC, SPAAC) are rapid and modular with higher yields and nontoxic by-products, remain stable in physiological conditions and utilize benign solvents [86, 87]. Inverse Electron-Demand Diels-Alder (iEDDA) cycloaddition has been the recent addition to the toolbox of bioorthogonal chemistry for ADCs. Reaction between 1,2,4,5-tetrazines and trans-cyclooctene (TCO) was introduced in 2008 and is currently being explored for varied applications owing to its extremely fast kinetics ($k > 800 \text{ M}^{-1} \cdot \text{s}^{-1}$, fastest biorthogonal reaction). Moreover, the recent commercial availability of a wide range of tetrazine and TCO reagents has made iEDDA reactions a popular choice for bioconjugation applications. On the flip side tetrazines could be susceptible to degradation in biological environments and TCO can have the tendency to get buried in the hydrophobic pockets of the protein that could influence the efficiency of the conjugation [88, 89]. Since the labelling strategies are driven by the chemistry approaches, they can also be employed for the surface functionalization of nanoparticles, as has been demonstrated in the following sections.








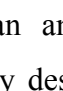
V-4.5 Difference between conjugates of mAb fragments and full scale mAb?

Monoclonal antibodies/IgGs have a distinct structural feature with each structural sub-unit having a specific function. This modular nature of the immunoglobulins has enabled to engineer “customized” platforms for the optimized pharmacological applications. Pharmacokinetics/dynamic aspects like; half-life, biodistribution, valency, affinity, tissue penetration and apparently bioactivity could be varied and controlled by selection of appropriate molecular domains or genetic features, allowing a control over both safety and efficacy of antibody products. Certolizumab pegol (Cimzia) and Ranibizumab (Lucentis) are the antibody

Chapter V. Bimodal imaging probes for bioconjugation to antibody fragments and nanoparticle functionalization

fragment based products currently approved by FDA. Cimzia is Fab fragment indicated for Crohn's disease, rheumatoid/psoriatic arthritis and ankylosing spondylitis, whereas Lucentis is a PEGylated Fab' fragment indicated for age related macular degeneration [226].

Table V-3: Different antibody formats and their properties. Adapted from [227].

Format	Composition	Valency	Approx. MW (kDa)	Typical Serum $t_{1/2}$	Clearance Route
 Intact IgG	$(V_H + V_L)_2$	Bivalent	150-160	1-3 weeks	Hepatic
 F(ab') ₂	$(V_H C_H1 + V_L + C_L)_2$	Bivalent	110	8-10 h	Hepatic
 Minibody	$(scFv + C_H3)_2$	Bivalent	75	5-10 h	Hepatic
 Fab	$V_H C_H1 + V_L + C_L$	Monovalent	50-55	12-20 h	Renal
 Diabody	$(scFv)_2$	Bivalent	50	3-5 h	Renal
 scFv	$V_H + V_L$	Monovalent	28	2-4 h	Renal
 Nanobody	$V_H H$ (Camelid)	Monovalent	12-15	30-60 m	Renal
 Affibody	Z domain of protein A (<i>S. aureus</i>)	Monovalent	7	30-60 m	Renal

Choice of an antibody or its fragment for therapeutic purpose is influenced by the pharmacology desired while treating the disease. Likewise, the selection of an antibody or antibody fragments has considerable influence on the properties of the imaging tracer developed from them. Many therapeutic antibodies could be of value in imaging due to similarities in the desired characteristics of targets like high expression in disease state and low expression in normal tissue, but not all therapeutic targets will be ideal for imaging, and vice versa. It is preferable that an imaging agent be biologically inert and this can be to certain extent possible as the expected antibody concentration for imaging is several folds lower than that needed to elicit therapeutic effect. In terms of the pharmacokinetics and biodistribution, therapeutic antibodies should achieve significant concentrations at the target site/tissue over time (high area-under-the-curve) whereas, imaging agents need to achieve high contrast in shorter time frame. Extended serum half-lives (1–3 weeks) of intact antibodies serves to be a major impediment to successful use of antibody as an imaging agent as several days will be needed to achieve a good signal to noise ratio (disease site to normal tissue background) and also result in exposure of the organism or patient to radioactivity for an extended amount of

time [228].

This can be addressed by harnessing protein engineering strategies that enable generation of the smaller and modular formats or by employing the antibody fragments developed from the parent antibody like Fab, F(ab')₂, Fab', scFv, etc [228, 229]. Table V-3 exemplifies various antibody based formats along with their characteristics and properties. Reformatted or enzymatically modified antibodies have Fv (fragment variable) domain that preserves the antigen binding properties, but typically lack the Fc region, eliminating complement- and effector cell-mediated immune interactions. Excision of the Fc region also prevents recycling that is mediated through the neonatal Fc receptor (FcRn) pathway, which facilitates visualization of targeted/diseased sites via faster target site penetration, rapid blood clearance and improved contrast.

The radiation exposure to the patient also can be minimized together by deploying radionuclides that decay more rapidly and the expedited clearance of antibody fragments. Typically, lower-molecular weight antibody fragments and proteins (below ~50 kDa) undergo elimination via renal clearance as their size is lower than the renal threshold [230].

V-5 Activatable fluorescent molecular imaging probes based on antibody/antibody fragments:

Molecular imaging with target-specific activatable “smart” probes, that yield fluorescence only at the intended target, enables sensitive and specific cancer detection. Different strategies have been employed to accomplish this viz. enzymatic activation of the fluorescent probe at the pathological site, pH mediated fluorophore activation or exploiting the fluorophore-protein interactions. The last strategy being the most facile in that it harnesses the natural phenomenon of dimerization of some of the fluorescent dyes.

Dimerization and quenching of fluorescent probes has been observed to occur in concentrated aqueous solutions. When conjugated to proteins, fluorophore dimerization and quenching can still occur at low concentration and this phenomenon could be exploited as a mechanism for fluorescence activation. Upon conjugation to the monoclonal antibodies/proteins, the fluorophores tend to dimerize owing to steric closeness as fluorophores are localized onto proteins. These fluorophore-antibody conjugates exhibit minimal fluorescence owing to quenching. However, upon injection into body, when these conjugates are internalised by the cancerous cells the catabolism/metabolism of the protein causes changes in the conformation of the proteins leading to activation of the fluorophore [231]. This phenomenon has been leveraged in the development of in-vivo activatable fluorescent conjugates (Figure V-12).

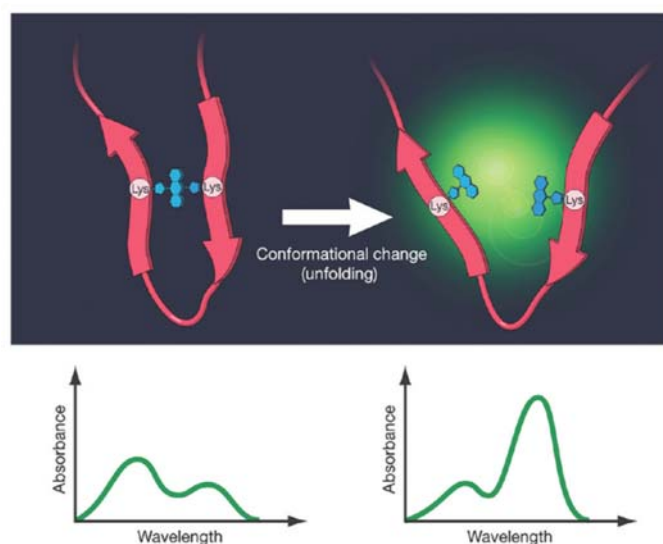


Figure V-12: Quenching and activation mechanism involving H-dimer formation after binding to the protein [231].

Nakajima et al., have demonstrated development of monoclonal antibody conjugate of indocyanine green (ICG) for in vivo activatable smart probes for molecular imaging of PSMA positive cancers. Before binding to PSMA and cellular internalization, the conjugate yielded

minimal light however, after binding and subsequent internalisation an 18-fold activation was observed enabling the specific detection of PSMA+ tumors up to 10 days after injection with a dose as low as (0.25 mg/kg) of the conjugate [232].

mAb-ICG/ICG like dye conjugates have drawback that inspite of purification, there could be some dye remaining non-covalently bound to the mAb. This non-covalent fraction when released from the mAb into the circulation could lead to higher nonspecific background signals, particularly in the liver and the intestine. To address this, a short polyethylene glycol (PEG) spacer was inserted between ICG and the minibody which diminished the background signals in a mouse PSMA xenograft model. However, the flip side of this could be altered binding affinity of the minibody, which needs to be taken into account [233].

Given the complexity of the synthesis of the bimodal probe for bioconjugation, the objective of this piece of work was to develop the bimodal probe for PET-Optical imaging (as described earlier) and apply it to the site-specific labelling of the antibody fragment. The bimodal conjugate developed based on the antibody fragment can be considered to be the first of its kind in terms of the bimodality combined with its bioactivatable features. Following sections describe the approach and methodology used in accomplishing this objective including the physico-chemical and biological characterization.

V-6 Development of HER-2 targeted bimodal probe based on antibody fragment:

Breast cancer is one of the most commonly occurring tumors in oncology. In 20% of cases, tumors overexpress the HER-2 transmembrane receptor (Human Epidermal Growth Factor Receptor 2). At the clinical level, HER-2 positive tumors are associated with an increased risk of local or regional recurrence and impaired overall survival [234]. In order to effectively locate the lesions, it becomes imperative to observe the spread of the malignancy across the region using a suitable imaging technique. Moreover, it can be of considerable value for oncologist to provide delineation of the cancer tissue from the normal ones for effective surgical resection. An ideal probe must not only provide the spatial information of the tumor during the diagnostic assessment but also offer imaging (optical) guided operative assistance during surgery.

Although quite a few studies report the development of trastuzumab based probes for PET or SPECT or Optical imaging as a standalone monomodal probes, the number of bimodal probes reported for HER-2 has been very limited. Group led by Eva M. Sevick-Muraca, has reported development of trastuzumab based bimodal probes based on sequential conjugation for SPECT-Optical imaging [235, 236]. However, there are barely any reports of bimodal trastuzumab conjugates based on the monomolecular approach (except one developed by our group for SPECT-Optical (Figure V-1)). The development of a HER-2targetingmonomolecular bimodal probe essentially aims to address this lacuna, compelling the need for the proposed work. Aligning with this objective, our aim is to site specifically label the F(ab') fragments of trastuzumab with the monomolecular bimodal probe, so as to develop HER-2 targeted PET-Optical probes that accumulate rapidly into the tumor.

The first part of the work involves synthesising the fragments from the full-scale antibody. Obtaining the fragments of the antibody is quite common in a typical drug discovery set up, wherein, to investigate the distinct regions of an immunoglobulin, it is necessary to cleave them with proteolytic enzymes. To examine the effects mediated by specific binding of antibody to cells in vitro or to localize antibodies to certain organs in vivo, it might be necessary to get rid of the nonspecific effects of Fc-receptor binding. The affinity of antibody for an antigen on the surface of viable cells can only be gauged accurately using monovalent antigen-binding fragments (Fab)[237].

Typically, the fragmentation of the antibody to the monovalent Fab fragment is carried out using papain digestion whereas, the bivalent F(ab')₂ fragment is obtained by pepsin digestion. Papain digestion produces Fab fragments from IgG of all subclasses from all species, however pepsin does not exert its action universally. While employing pepsin or papain for

first time on an antibody, pilot experiments are necessary to determine the optimal reaction conditions [238].

V-6.1 Synthesis of $F(ab')_2$ of trastuzumab:

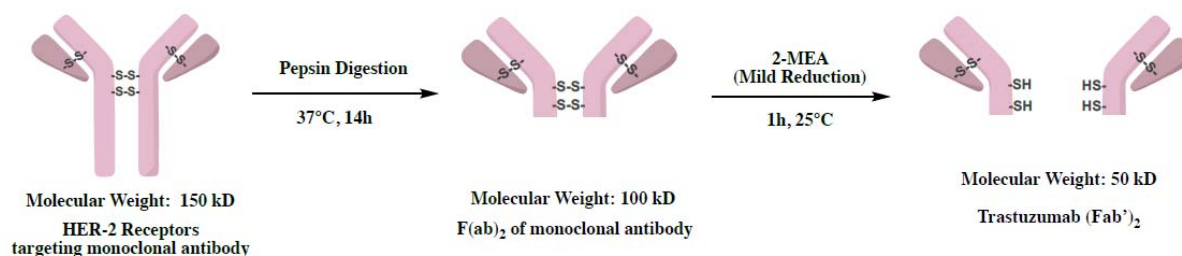


Figure V-13: Synthesis scheme for Trastuzumab- $F(ab')_2$.

Trastuzumab (drug substance) was recovered from the marketed formulation - Herceptin (Roche) by reconstituting the lyophilisate with minimal quantity of phosphate buffer (20mM, 0.05% NaN_3). The reconstituted solution was desalted by using HiTrap desalting column on the AKTA Explorer purification system. The fractions were collected based on the position of the protein peak detected at 280nm. The fractions were pooled and concentrated using Vivaspin (5mL, MWCO-30kD) to get the concentration of around 20mg/mL measured using UV spectrophotometer. The $F(ab')_2$ formation was verified by mass analysis using MALDI. Trastuzumab $F(ab')_2$ was generated by enzymatically cleaving the monoclonal antibody at the hinge region. 10mg of trastuzumab was buffer exchanged in 20mM sodium acetate buffer pH 4.5 and incubated with pepsin at 37°C for 12h (Figure V-13). After the digestion was complete the enzyme was inactivated by addition of Tris buffer pH 8.0. The reaction mixture was purified using ProteinA affinity chromatography based on 'bind and elute' principle. During the 'binding' phase of the chromatographic step, the Fab binding region exclusively binds to the protein A, whereas the digested Fc region is washed-off. The 'elution' phase conditions (pH 3) causes the release of the $F(ab')_2$ from the chromatographic media with good purity. The relevant fractions were pooled and concentrated using ultrafiltration and buffered exchanged in phosphate buffer.

V-6.2 Reduction of $F(ab')_2$ fragments:

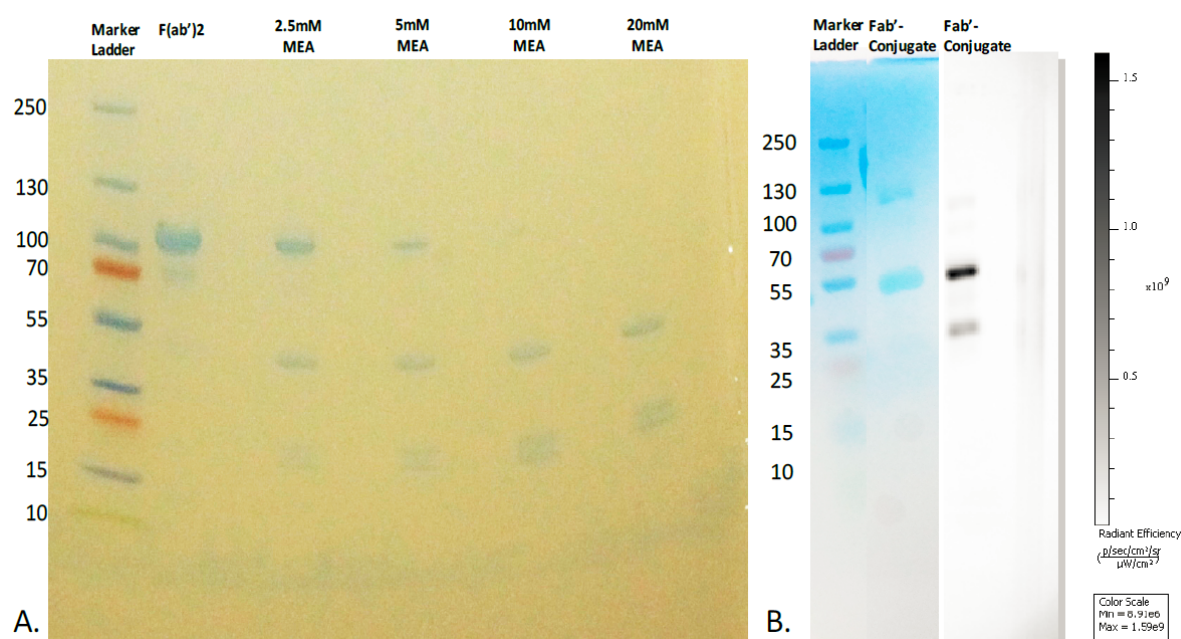


Figure V-14: SDS Gel electrophoresis of the A) $F(ab')_2$ and the effect of reduction using different concentration of 2-MEA. B) Fab'-conjugate without and with fluorescent detection.

Reduction of the disulphide bonds present in the antibody can be brought about to generate individual antibody chains. However, for the synthesis of conjugates it is preferable that only the disulphide bonds in the hinge region are reduced. This can be realized by using mild reducing agent and by optimising the concentration of the reducing agent. The intra-chain disulphide bonds are generally more stable to reduction compared to the once present between the antibody chains. Hence, reduction performed under optimal conditions is less likely to cause any conformational damage to the antibody or its domains. Various reducing agents like DTT (Dithioerythritol), TCEP, 2-mercaptoethanol, cysteine and 2-mercaptoethylamine could be used in protein chemistry each with its own merits and demerits. Dithiothreitol is a popular reducing agent for many protein research applications and is most commonly used in reducing polyacrylamide electrophoresis (SDS-PAGE). TCEP has been widely used in ADC chemistry as it is odour free, effective at room temperature, efficient at lower concentrations, stable and compatible with wide range of solutes which makes it possible to perform reduction and conjugation in same reaction mixture. Of the all reducing agents mentioned above, 2-mercaptoethylamine (2-MEA) is a relatively mild reducing agent and finds application in the instances where only the hinge disulphide are needed to be reduced. 2-MEA is particularly suitable for reduction of the $F(ab')_2$ for the generation of Fab' fragments. Zhou et al reported the reduction of the $F(ab')_2$ using 2-MEA to develop Doxorubicin-PEG-anti-

Chapter V. Bimodal imaging probes for bioconjugation to antibody fragments and nanoparticle functionalization

CD20 Fab'conjugates [239]. Fab' fragment of the trastuzumab was generated by treating 1mg/mL of the F(ab')₂ in the phosphate buffer with 10mM of 2-MEA and incubating at room temperature for 1h (Figure V-13). In order to arrive at this optimal concentration, F(ab')₂ was treated with varying concentration of 2-MEA (5-50mM) and gel electrophoresis was performed to verify the Fab' formation. As can be seen from the Figure V-14, the concentration of 10mM of 2-MEA was found to be optimal in complete reduction of the F(ab')₂ with the generation of Fab' band at around 55kD, whilst generating minimum of low molecular weight species.

V-6.3 Conjugation of the bimodal probe to Fab' fragment:

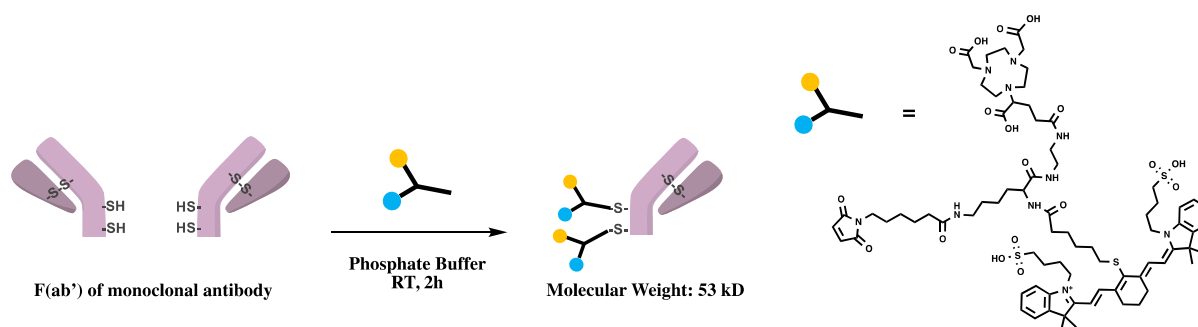


Figure V-15: Development scheme for trastuzumab-F(ab')-conjugate of the trifunctional probe (41)

Following the reduction of the F(ab')₂, the reaction mixture was purified by HiTrap desalting column. The Fab' fragment was recovered from the identified fractions and concentrated to around 1mg/mL and treated with 20-fold excess of the bimodal probe and incubated at room temperature for 2h. The conjugate was purified by protein A chromatography and the relevant fractions were pooled and buffered exchanged into phosphate buffer (20mM, pH 7.2) at the concentration of around 1mg/mL. Alternatively, purification can also be performed by Size Exclusion Chromatography. The purified conjugate was further characterized using MALDI spectroscopy, gel electrophoresis/SDS-PAGE and UV-Visible spectroscopy. As a positive control for the experiment, Fab' fragment was also treated with iodoacetamide in a manner analogous to bimodal probe. Iodoacetamide reacts irreversibly with the thiol groups on the reduced fragments via nucleophilic substitution reaction generating the Fab' fragments that cannot undergo re-oxidation to F(ab')₂, thus serving as useful control during analysis (particularly mass analysis).

V-6.4 Characterization of the bimodal conjugate:

In order to identify the number of probes conjugated to antibody or its fragment, it is essential to analyse the PAR (probe to antibody ratio), which is analogous to DAR (drug to antibody

ratio). This can be assessed by UV-Visible analysis, mass analysis or hydrophobic interaction chromatography. In this case, MALDI analysis was performed to evaluate the PAR using sinnapinic acid as a matrix and the mass spectroscopic parameters typically used for the biological proteins like monoclonal antibodies. As can be seen from Figure V-16, trastuzumab shows a peak at 148441 Da, that corresponds to its M_w , whereas the $F(ab')_2$ exhibits a peak at 97496 Da demonstrating the digestion of the F_c region of the antibody. $F(ab')_2$ that was optimally reduced with 2-MEA and subsequently capped with idoacetamide showed a peak corresponding to 48744 Da. Absence of any $F(ab')_2$ peak in the idoacetamide capped $F(ab')$ sample/spectrum proves that conjugation protocol was satisfactory. Similar observations were made for trastuzumab Fab' -bimodal probe conjugate, wherein the conjugate peak was observed at 51958 Da, this translates to the probe to fragment ratio of ~ 2 , as calculated below:

$$PAR = \frac{\text{Molecular weight of the conjugate} - \text{molecular weight of idoacetamide capped } F(ab')}{\text{Molecular weight of bimodal probe}}$$

This demonstrates that the two thiol groups present at the hinge region of the $F(ab')$ have been successfully conjugated to the bimodal probe in a site-specific manner. This was further compounded by the results from the SDS-PAGE analysis. SDS-PAGE analysis revealed main band/peak corresponding to the conjugate at around 50kD which was easily detected using coomassie blue staining and was also verified using fluorescent detection.

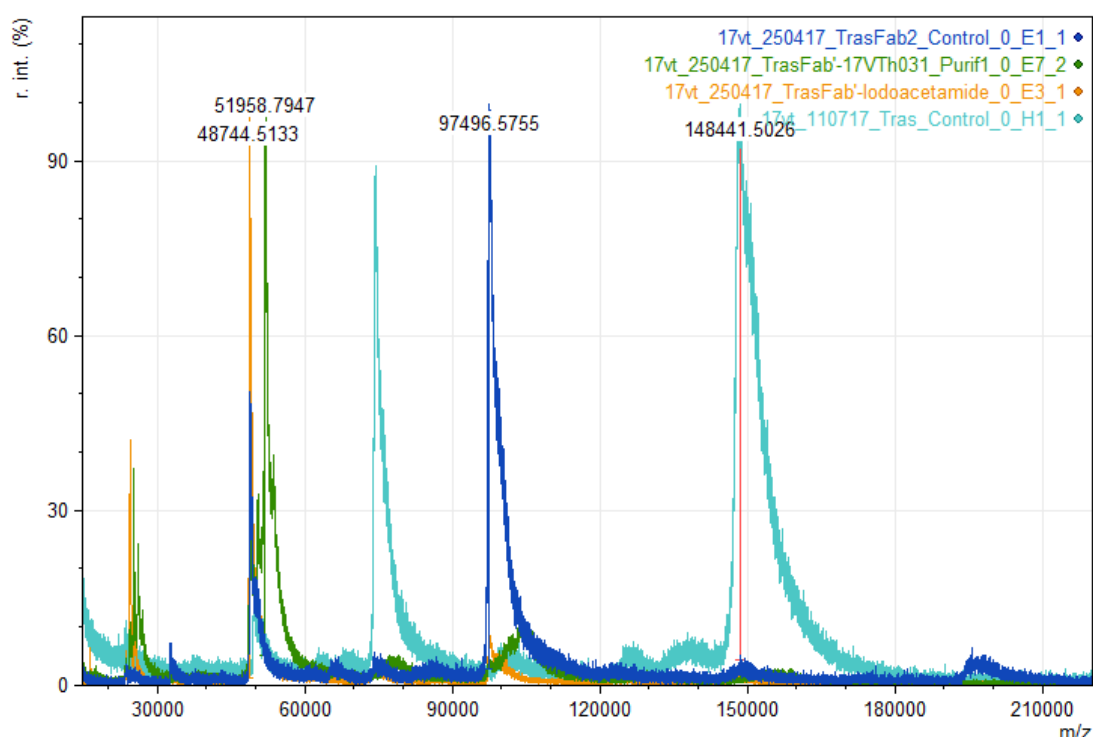


Figure V-16: MALDI analysis of the trastuzumab Fab' -bimodal probe conjugate.

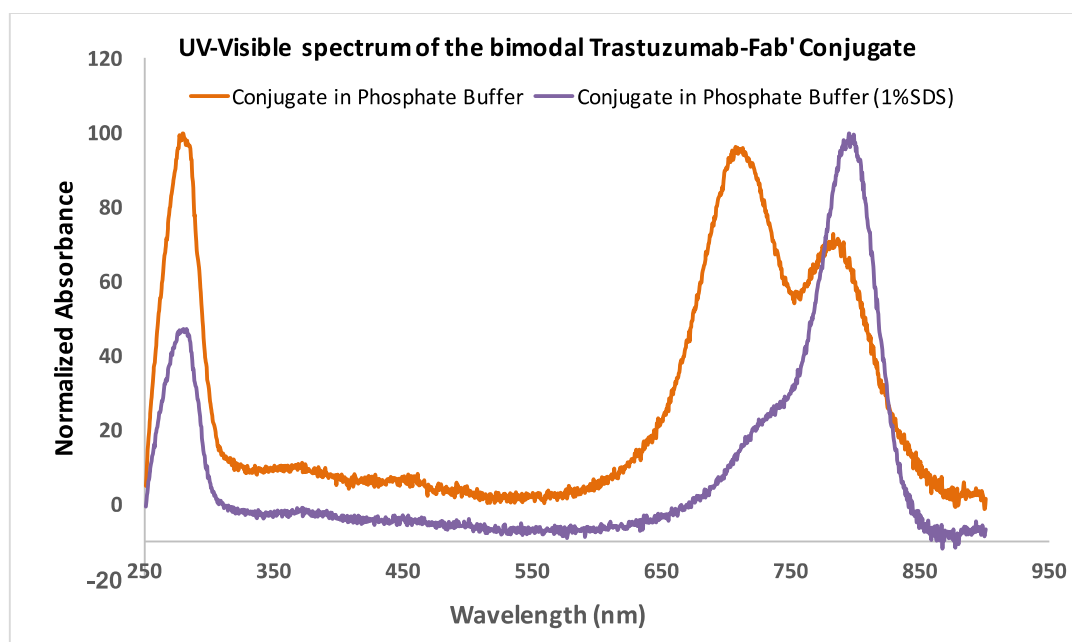


Figure V-17: UV-visible spectrum of the Fab'-bimodal probe in phosphate buffer (with or without 1% SDS).

A UV-visible spectrophotometric analysis of the conjugate was performed in phosphate buffer in the presence and absence of SDS. As can be seen from the Figure V-17, the conjugate spectrum in phosphate buffer revealed three peaks; one at 280nm corresponding to the protein absorption and the other two at 710nm and 786nm corresponding to the fluorescent dye peak. However, the peak at 710nm exhibits higher absorbance compared to the ones at 786nm. As explained earlier, this is due to the phenomenon of quenching/dimer formation mediated by interactions of the fluorescent dye with the protein as well as the other dye molecules conjugated to protein in its vicinity. When the spectrum was recorded in the presence of 1% SDS (in phosphate buffer) these interactions were found to disappear as evident from the spectrum that revealed only two peaks one for the protein (280nm) and another for the fluorescent dye (795nm). This observation is in line with those described in the literature for a potential bioactivatable probe.

It could be expected that an analogous effect might be observed under physiological conditions, wherein the internalized antibody fragment conjugate would be catabolized so as to digest the antibody fragment/protein releasing the fluorescent dye which under the activated state will exhibit its fluorescence.

V-7 Animal imaging in breast cancer model:

Pilot imaging studies were performed in BT-474 xenograft tumor model in NOD-SCID mice (n=3). The bimodal probe was injected intravenously and the optical imaging scans were recorded with 760/845 nm filters at 1h, 4h and 24h. At the end of 24h animals were sacrificed and the organs were retrieved to see the probe distribution in the organs.

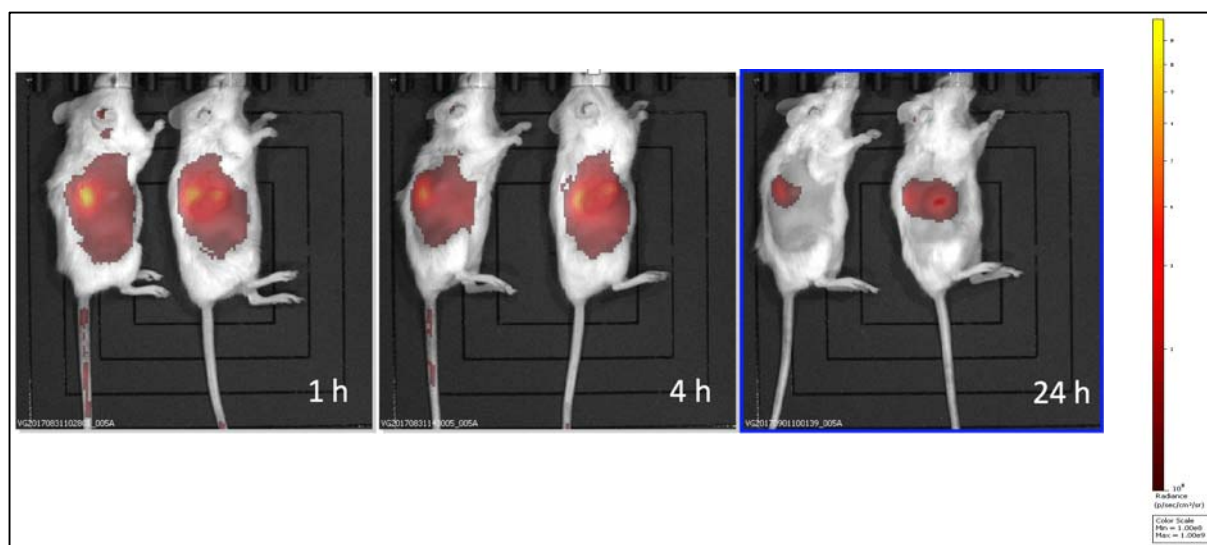


Figure V-18: Optical imaging scans performed on the mice at 1h, 4h and 24h demonstrating localization of the probe in tumor.

BT-474 xenograft tumor model can be useful to evaluate the theranostics targeting the HER-2 positive breast cancer as it expresses the HER-2 receptors. As can be observed from images (Figure V-18), the conjugate was rapidly localized in the tumor and the kidneys. Unlike the full antibody, the Fab' fragment is rapidly cleared from the circulation as its M_w is closer to the renal threshold. Signals from the liver were also observed to be strong. This was evident from the images at the end of 1h and 4h. At the end of 24h, the collective broad signals reduced in its intensity, owing to possible excretion of the conjugate. These observations were consistent with the results reported for the ^{111}In labelled DTPA conjugated Fab fragments of trastuzumab wherein, relatively high tumor uptake (7.8% ID/g) and tumor/background ratios (>25:1) were recorded [240].

Typically, the optical/radioactivity in kidneys is high when conjugates are based on antibody fragments as the fragment tends to have higher renal uptake. This can be mitigated by administration of cationic amino acids (e.g., l/d-lysine or l-arginine) so as to competitively inhibit the charge interactions between Fab and renal tubular cell membranes. Alternatively, administration of total parenteral nutrition (TPN) solutions that include l-lysine could help in reducing the renal uptake of the antibody fragment based conjugates [241].

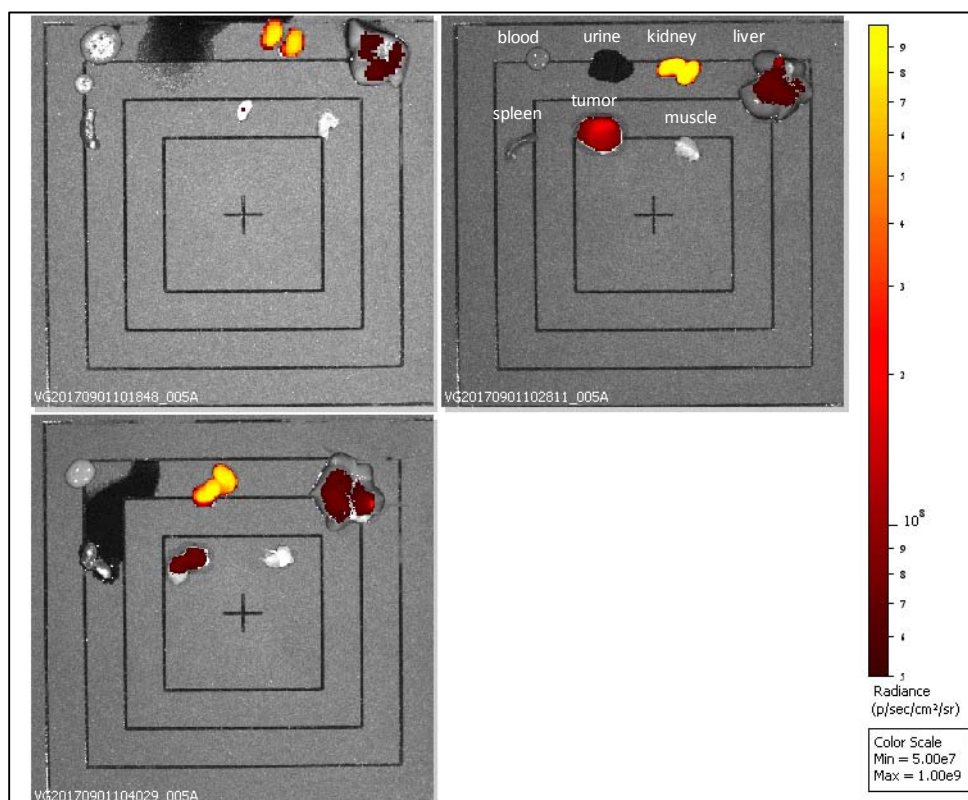


Figure V-19: Biodistribution of the bimodal probe based on the fluorescence/optical signals observed from the retrieved organs.

Our observations were further augmented by the biodistribution studies, that entailed imaging analysis of the organs retrieved at the end of 24h. As can be seen from the Figure V-19, the fluorescent signals were still noticeable in the tumor, in addition to the ones seen in kidneys and liver. However, it was difficult to quantify the organ wise biodistribution of the probe owing to the inherent variability/sensitivity of the fluorescent signals unlike the radioactivity based imaging modalities. Nonetheless, above imaging data clearly validate the tumor targeting ability of the bimodal probe.

V-8 Development of the multifunctional nanoparticles:

Nanomedicine has played a seminal role in diagnosis and therapy of varying types of cancer as evidenced through the approval of diverse set of nanoparticles by the regulatory health authorities across the world [242]. By virtue of the enhanced permeability and retention effect (EPR effect), nanoparticles have been able to traverse the leaky vasculature and target the cancer tissue. To further understand the targeting potential of the nanoparticles, they have been functionalized with targeting ligands like chemical ligands, peptides, antibody or its fragments. Nanoparticles bearing multiple functionalities can have wider implications in terms of addressing the diagnostic and therapeutic concerns employing a single modality. In this context, silica nanoparticles represent one of the versatile platforms for imaging and drug delivery applications. Multifunctional silica nanoparticles have been described in literature as contrast agents that combine diverse imaging modalities: like optical imaging and positron emission tomography (PET), optical imaging and MRI, and optical imaging with both MRI and computed tomography [243-245]. In the arena of theranostics, these systems have been demonstrated to combine imaging and therapy: MRI and gene delivery, optical imaging and drug delivery, and optical imaging and photodynamic therapy [246-248].

As described in detail in Chapter II, AGuIX nanoparticles are one of the most advanced silica nanoparticles in terms of its efficacy at the pre-clinical and clinical stages (Phase I) for imaging and radio-sensitizing applications. Owing to its rich surface chemistry, diverse functionalization strategies have been investigated to conjugate targeting ligands [35, 249], fluorescent dyes [35], photosensitizers [250] and chelating agents [251] onto the AGuIX nanoparticles. Multi functionalization of the nanoparticles is a multistep process that entails grafting of one modality after other in a sequential manner. This makes it difficult to exert control over the precision of process and accurate characterization of the macromolecular system. To address this, we capitalized on the monomolecular imaging platforms (MOMIPs) developed in our group and synthesized a trifunctional probe containing PET chelator and NIR dye and grafting functionality – maleimide that could be used to append it to the AGuIX nanoparticles, resulting into a multifunctional system capable of PET-MRI-Optical imaging and radiosensitization.

The following sections describe the development and characterization of an advanced multifunctional modality based on AGuIX platform by functionalizing the AGuIX nanoparticles with the bimodal PET-Optical probe described at the beginning of this chapter.

V-9 Chemical functionalization of AGuIX using bimodal probe:

V-9.1 Thiolation of the AGuIX:

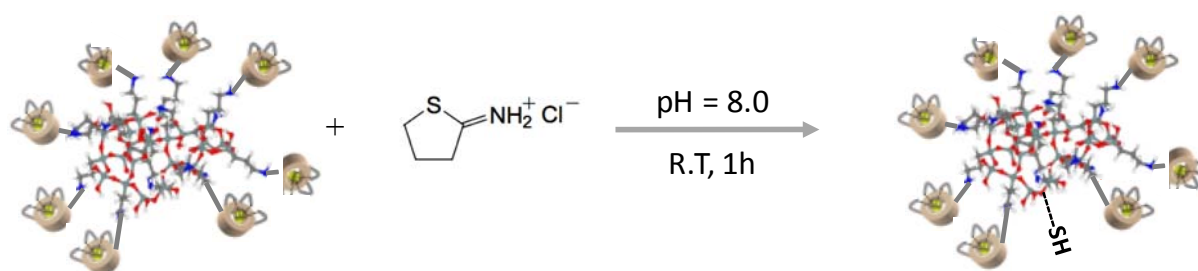


Figure V-20: Thiolation of the AGuIX nanoparticles using Traut's reagent.

The surface chemistry of the AGuIX nanoparticles enables it to be chemically conjugated to different tracers. Typically, AGuIX nanoparticles possess $-NH_2$ groups that stem from the APTES group that occupy the nanoparticle surface. Alternatively, there are also surface $-COOH$ groups from free chelators which can be employed as a conjugation site. The amide coupling at this site can be performed by classical carbodiimide chemistry or employing pre-activated ligands [35, 252]. In order for the trifunctional probe to be grafted on the nanoparticles based on thiol-maleimide chemistry, it was necessary to thiolate the nanoparticles. The thiolation was performed by treatment of the nanoparticles with Traut's reagent using 10-fold excess to the gadolinium at pH 8 for 1h (Figure V-20). The nanoparticles were purified by 6 ultrafiltration cycles using the Vivaspin (MWCO -3kD). The purified nanoparticles were characterized by Ellman's assay, T1 measurements, and DLS measurements.

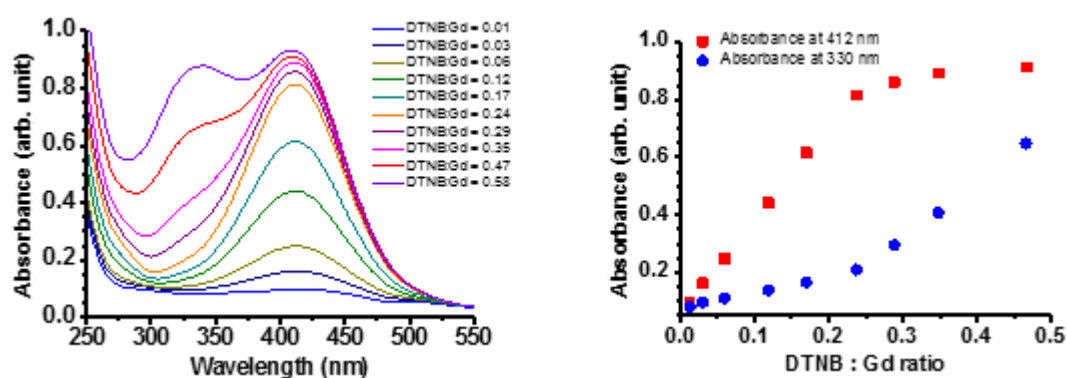


Figure V-21: Determination of the thiol content by the Ellman's reagent.

Ellman's Reagent (5,5'-dithio-bis-[2-nitrobenzoic acid])/DTNB can be used to determine the amount of sulfhydryl groups present in a sample (nanoparticles/protein/aminoacids) using the standard curve generated by of a sulfhydryl-containing compound such as cysteine or by

Chapter V. Bimodal imaging probes for bioconjugation to antibody fragments and nanoparticle functionalization

employing the extinction coefficient of TNB ($14,150\text{M}^{-1}\cdot\text{cm}^{-1}$ at 412nm). Ellman's Reagent (DTNB) reacts with sulfhydryl groups, to form mixed disulfides and colored TNB, whose color can be measured at 412nm the extent of which reflects the number of thiols present in sample.

A series of DTNB:Nanoparticles (Gd) ratios were tested to arrive at an estimate of the thiol as can be seen from Figure V-21. The thiol content of the nanoparticles was found to be around 2.5 thiols per nanoparticle, which was considered optimal for further conjugation as excessive thiolation might potentially cause nanoparticles to clump by inter-particulate disulphide bridging.

V-9.2 Conjugation of the bimodal probe to AGuIX:

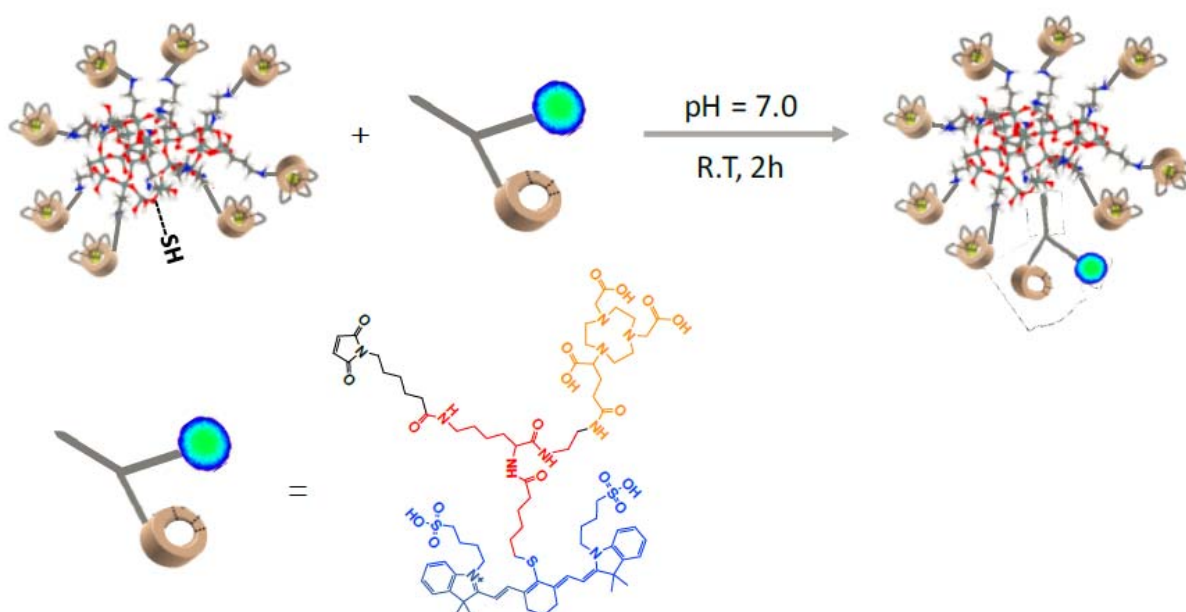


Figure V-22: Bioconjugation of the bimodal probe to the thiolated nanoparticles via thiol-maleimide/Michael addition reaction.

After the purification of the thiolated nanoparticles, the nanoparticles were immediately treated with the trifunctional probe at the pH of 7 (Figure V-22). Thiol maleimide conjugation works well in the pH range of 6.5-7.5 and results in the formation of stable thioether linkage. The thiol:maleimide or nanoparticle:trifunctional probe were taken in equal stoichiometric ratio and the reaction mixture was incubated at room temperature protected from light. Unlike NHS esters, the maleimide moiety is stable towards hydrolysis and molar excess was unnecessary. Moreover, the higher concentration of the reaction mixture ensured that reaction proceeded quickly to completion without any degradation. The functionalized nanoparticles were purified by 5 ultrafiltration cycles using the Vivaspin (MWCO-3kD) and lyophilized to

a green powder with a yield of around 50%. The purified nanoparticles were characterized by T1 measurements, DLS, HPLC and UV-Vis measurements.

V-10 Characterization of the functionalized nanoparticles:

V-10.1 Physico-chemical characterization of nanoparticle properties:

Nanoparticles that are currently approved for diagnosis and therapy have varied sizes and most of them are over 100nm [242]. AGuIX nanoparticles are unique in this regard as they are relatively smaller and have a size of about 5 nm and correspond to M_w of 8-10,000 Daltons. These physico-structural features make AGuIX suitable for the imaging applications as they are rapidly localized into tumor and cleared from the circulation through renal clearance [6, 100].

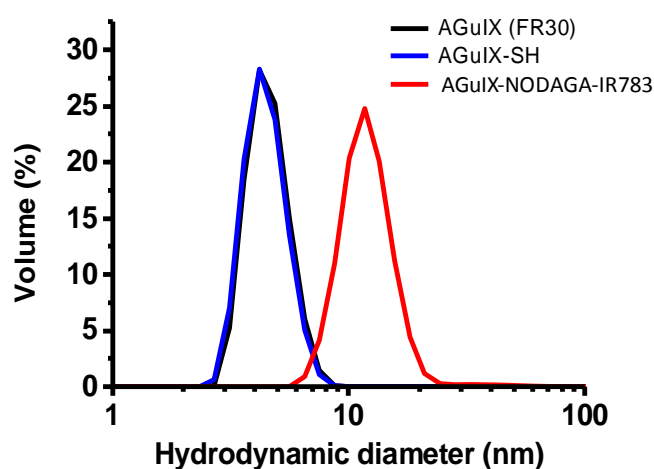


Figure V-23: Dynamic light scattering analysis of the nanoparticles.

The hydrodynamic diameter of the nanoparticles was measured using Dynamic Light Scattering (DLS) studies. The size of the pristine AGuIX nanoparticles was found to be 4.6 ± 0.9 nm whereas the thiolated nanoparticles exhibited a resembling size of 4.5 ± 0.9 nm (Figure V-23). Upon grafting of the macromolecular probe the D_H of nanoparticles increased to 12.1 ± 3.0 nm. Relaxometric measurements revealed that r_1 increased significantly after thiolation and slightly after grafting with the probe. r_2 increased significantly in both steps leading to a significant change in r_2/r_1 . The relative content of Gd reduces considerably and this is reasonable given the bulky structure of the probe.

Chromatographic analysis of nanoparticles is quite unusual and daunting task. Nonetheless, HPLC analysis of the nanoparticles revealed valuable information upon the structural changes caused to the nanoparticles (Figure V-24). AGuIX nanoparticles typically exhibit a retention time of 13nm at 295nm. Upon grafting the nanoparticle retention time shifted to right with elution at 18nm, and this could be due to increase in its hydrophobicity.

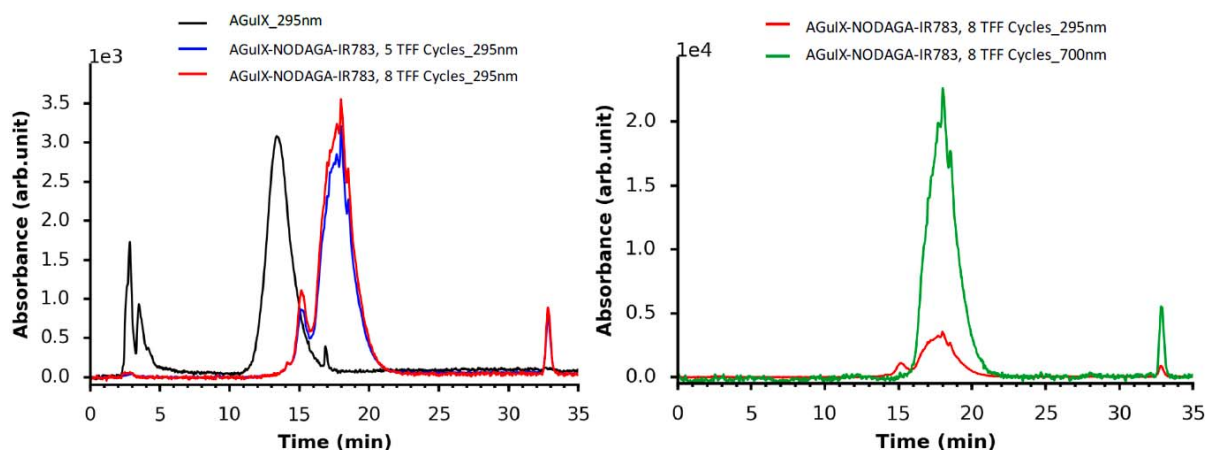


Figure V-24: HPLC analysis of the nanoparticles at 295nm and 700nm.

The presence of the small peak before the main peak of functionalized nanoparticles could be due to the residual underivatized nanoparticles. Furthermore, this was verified by performing the analysis at 700nm which clearly demonstrated the functionalization of the nanoparticles. In addition to the chromatographic analysis, battery of tests was conducted to further characterize the functionalized nanoparticles. The hydrodynamic size (diameter) of the nanoparticles increased from $4.6 \pm 0.9\text{nm}$ to $12.1 \pm 3.0\text{nm}$ after the functionalization owing to apparent increase in the size of the nanoparticles due to the bulky nature of the bimodal probe. The hydrodynamic size of the nanoparticles was least affected after thiolation of the nanoparticles. Increase in the relaxivity (r_1) and the corresponding increase in r_2/r_1 of the functionalized nanoparticles indicate increase in the rotational correlation time resulting from the grafting of a probe. The overall functional properties of the nanoparticles were not affected after the functionalization, which justifies the feasibility of synthesis of such multifunctional probes. Table V-4 & Table V-5 summarise the characteristics of the nanoparticles.

Table V-4: Summary of the characteristics of the pristine/functionalized AGuIX nanoparticles

Features	Methods	AGuIX (FR30)	AGuIX-SH	AGuIX-NODAGA-IR-783
D_H (nm)	DLS	4.6 ± 0.9	4.5 ± 0.9	12.1 ± 3.0
Relative quantification of SH	Ellman's assay	-	Gd : SH ~ 10 : 2	-
r_1 ($\text{mM}^{-1} \cdot \text{s}^{-1}$)	Relaxometry	13.51	16.82	16.91
r_2/r_1		1.35	1.39	1.83
Retention time (min)	HPLC	13.4	N/A	18
Purity (%)		80.2		95.7
Content of Gd ($\mu\text{mol}/\text{mg}$)	ICP-OES	0.8903	-	0.3185

Table V-5: Summary of the relaxometric characteristics of the nanoparticles at 37 °C (1.4 T & 60 MHz).

Sample	Concentration (mM)	T1	r ₁	T2	r ₂	r ₂ /r ₁
AGuIX (FR30)	200	0.37	13.51	0.274	18.25	1.35
AGuIX-SH	70.78	0.84	16.82	0.604	23.39	1.39
AGuIX-NODAGA-IR-783	45.83	1.29	16.91	0.705	30.94	1.83

V-10.2 Photophysical characteristics of the functionalized nanoparticles:

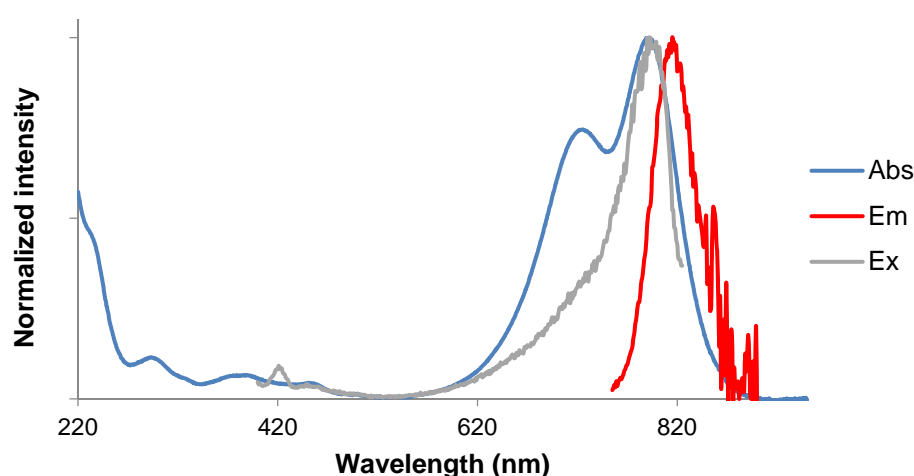


Figure V-25: Absorption and emission spectrum of the functionalized nanoparticles in PBS using UV-Vis and fluorescence spectroscopy.

Table V-6: Photophysical characteristics of the functionalized nanoparticles in PBS.

Compound	λ_{abs} (nm)	λ_{em} (nm)	Φ (%)
AGuIX-NODAGA-IR783	792	815	0.4

The functionalized nanoparticles were very readily dispersible in PBS. The photophysical measurements were performed by serially diluting the stock solution of 1mg/mL in PBS. The λ_{abs} and λ_{em} were observed to be 792nm and 815nm respectively (Figure V-25). Values for molar extinction coefficient could not be calculated as the functionalized nanoparticles represent a complex macromolecular structure without any assignable molecular weight. The shoulder peak at 725nm might signify the presence of inter-nanoparticulate interactions. Nonetheless, these functionalized nanoparticles have photophysical similarities to ICG making it a valuable candidate for imaging.

V-11 Radiolabelling and stability of the functionalized nanoparticles:

The functionalized nanoparticles bear three different modalities; viz Gadolinium complexed DOTAGA chelates, NIR dye and NODAGA, a PET chelator. The nanoparticles were radiolabelled with ^{64}Cu as its decay characteristics ($t_{1/2} = 12.7$ hours; β^+ , 0.653 MeV [17.8 %]; β^- , 0.579 MeV [38.4%]) are well suitable for PET imaging [253]. The functionalized nanoparticles were dispersed in AcONH₄ Buffer (pH 5.5) and incubated with ^{64}Cu at 37°C for 45min. The radiochemical purity of the radiolabelled nanoparticles was found to be >95% as determined by ITLC using 0.1M EDTA as a mobile phase (Figure V-26).

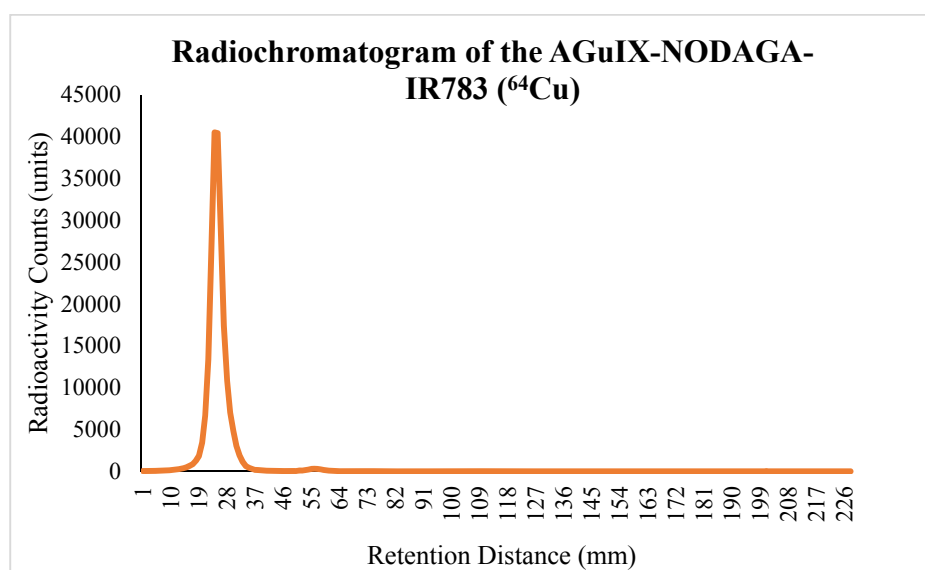


Figure V-26: Radio chromatogram of the ^{64}Cu labelled AGuIX-NODAGA-IR783 obtained after ITLC-SA using 0.1M EDTA as a mobile phase.

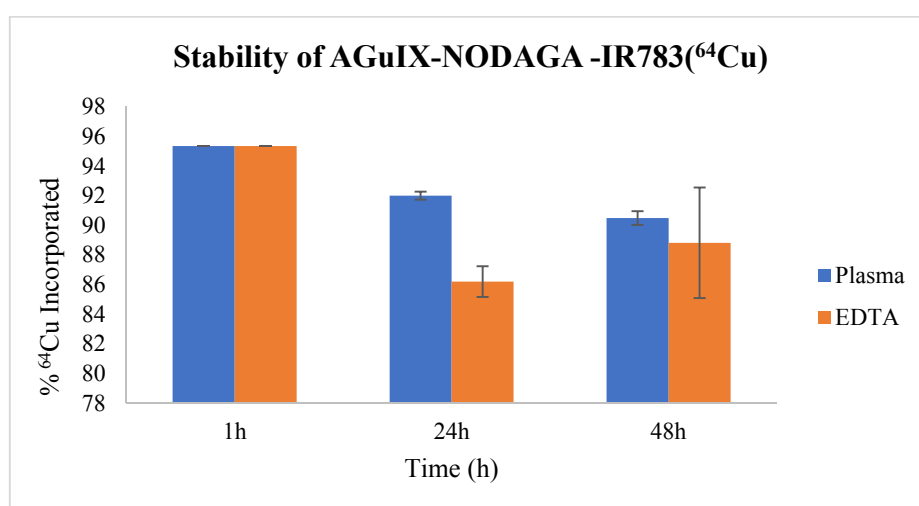


Figure V-27: Stability of the radiolabelled nanoparticles AGuIX-NODAGA-IR783 (^{64}Cu) in human plasma and EDTA.

Furthermore, stability investigations at 37°C in human plasma and EDTA (EDTA challenge) revealed that the radiolabelled nanoparticles are stable over a period of 48h as can be seen in Figure V-27. This evaluation at *in-vitro* stage is very important to assess the ability of the nanoparticles to retain the radioisotope incorporated into it. Moreover, it is also reflective of the stability of radiolabelled nanoparticles at physiological conditions before proceeding to *in-vivo* experiments.

V-12 Animal imaging in breast cancer model:

Imaging studies were performed in TSA xenograft tumor model in NOD-SCID mice (n=3). The ^{64}Cu radiolabelled nanoparticles/AGuIX-NODAGA-IR783 (^{64}Cu)(10MBq) were injected intravenously and the optical imaging and PET-MRI scans were recorded.

Optical imaging was done with 760/845 nm filters at 1h and 24h, whereas PET/MRI scan was done using PET/MRI machine as described earlier. At the end of 24h animals were sacrificed and the organs were retrieved to see the probe distribution in the organs.

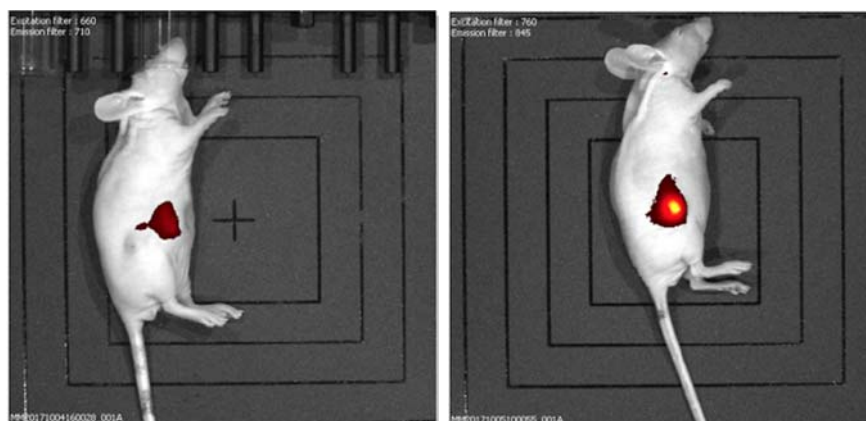


Figure V-28: Optical animal imaging TSA tumor models at 1h and 24h after injection of AGuIX-NODAGA-IR783(^{64}Cu).

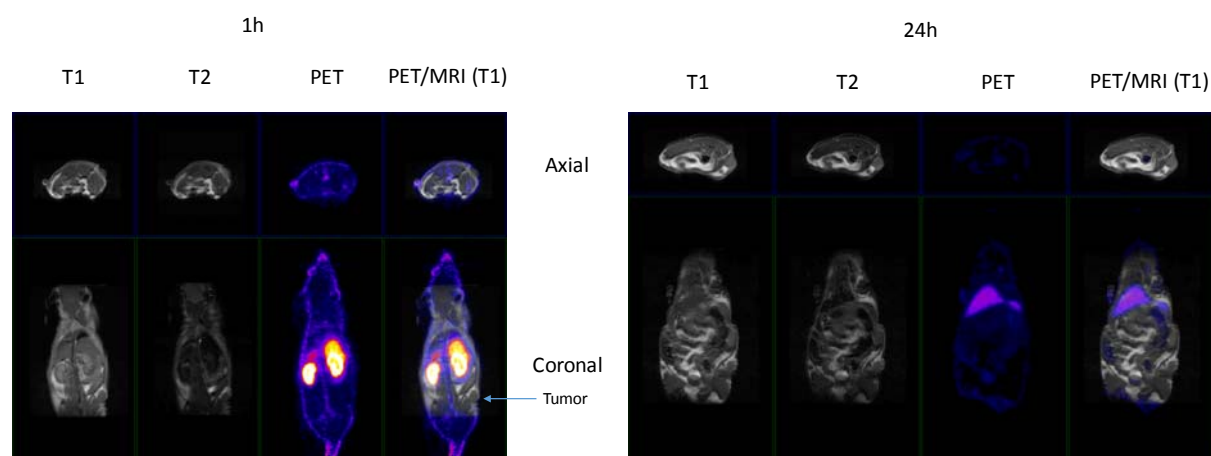


Figure V-29: PET-MRI imaging in TSA tumor models at 1h and 24h after injection of AGuIX-NODAGA-IR783(^{64}Cu).

As can be seen from the images, AGuIX-NODAGA-IR-783 can be used for PET-MRI-Optical trimodal imaging. Owing to the sensitivity of the fluorescent probes and limited depth penetration of the NIR light, the localization of the AGuIX-NODAGA-IR-783 into tumors could be easily traced (Figure V-28). This can be of a high value for the intra-operative surgical guidance. On the other hand, PET-MRI images could provide information about the

global distribution of these nanoparticles as can be seen from the improved MRI contrast and bright PET signals. The substantial decrease of the bright signals from the kidneys from 1h to 24h, signifies renal excretion of these probes. Moreover, these observations were in line with the biodistribution data (Figure V-30).

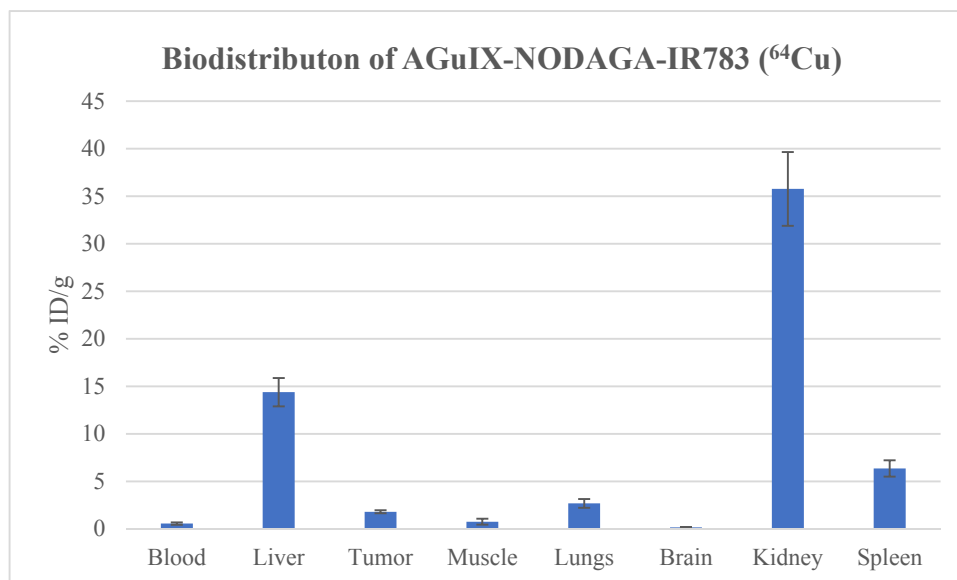


Figure V-30: Biodistribution of AGuIX-NODAGA-IR783 (⁶⁴Cu) at the end of 24h.

At the end of 24h the nanoparticles were observed to be mainly distributed into kidneys (35.76±3.87 % ID/g) indicating the renal clearance as major means of clearance like the pristine AGuIX nanoparticles. In addition, the nanoparticles also accumulated into liver (14.38±1.48 % ID/g) and spleen. This behaviour was slightly different from the AGuIX nanoparticles reported in Chapter II. This could be possibly due to the presence of relatively bulky ICG like macromolecule; IR783 on the nanoparticle, where the hepatic/biliary clearance could be another means of clearance [254]. The accumulation in the tumor was quite modest (1.8±0.15 % ID/g) owing to a relatively small tumor size. Nonetheless, this information gives a valuable insight into the pharmacokinetic behaviour of these complex multifunctional probes and their potential for multimodal imaging.

V-13 Conclusions:

The objective of this chapter was to develop new trifunctional imaging probe that could be used for bioconjugation of antibody Fab' fragments and functionalization of nanoparticles. This has been achieved through a multistep chemical synthesis encompassing appropriate selection of chelator for PET imaging and NIR fluorophore leveraging on the expertise of Chematech and ICMUB in Dijon. Following aspects represent the conclusive remarks towards accomplishing this objective:

- The novel trifunctional imaging probe has been successfully developed through strategic synthetic schemes, chromatographic purifications with moderate yields and excellent purity and spectroscopic characterization.
- The trifunctional probe has been evaluated for its photo-physical characteristics that demonstrate its equivalence with ICG dye which has been the only FDA approved NIR dye for imaging in humans.
- The trifunctional imaging probe has been demonstrated to be site specifically bioconjugated to Fab' fragments of trastuzumab and used in functionalization of the AGuIX nanoparticles towards development of multifunctional theranostics.
- The PET-Optical bimodal conjugate of Fab' fragment of trastuzumab has been evaluated in BT-474 xenograft tumor model to ascertain the tumor targeting potential of this probe using optical imaging.
- The functionalized nanoparticles were radiolabelled with ^{64}Cu and were found to be stable under physiological conditions. Moreover, these multifunctional nanoparticles were evaluated in TSA tumor model using PET-MRI-Optical imaging.

Above achievements clearly demonstrate the versatility of the application of the complex multimodal probes to bioconjugation and functionalization towards development of multifunctional systems.

Chapter VI. Experimental Section

Nuclear Magnetic Resonance Spectroscopy

The ^1H and ^{13}C NMR spectra were recorded at 298 K, 300 K or 330 K on 300 MHz Bruker Avance, 500 MHz Bruker Avance DRX, 600 MHz Bruker Avance II spectrometers using perdeuterated solvents as internal standard. Measurements were carried out at the “Welience, Pôle Chimie Moléculaire de l’Université de Bourgogne (WPCM)”.

Mass Spectrometry

Matrix-Assisted Laser Desorption Ionization - Time of Flight (MALDI-TOF) mass spectrometry was carried out using a Bruker Ultraflex II LRF 2000 spectrometer. High Resolution Mass Spectrometry – ElectroSpray Ionisation (HRMS-ESI) was carried out using a Thermo LTQ Orbitrap XL. Liquid Chromatography – Mass Spectrometry (LC-MS) was carried out using a Bruker Amazon SL coupled to a Dionex HPLC Ultimate 3000 RSLC equipped with a column C_{18} Inertsil ODS-3, 5 μm , 1 \times 15 mm. Measurements were carried out at the “Welience, Pôle Chimie Moléculaire de l’Université de Bourgogne (WPCM)”.

Elemental Analysis

Elemental analysis was performed with a Thermo CHNS/O Electron Flash EA 1112 Series. Measurements were carried out at the “Welience, Pôle Chimie Moléculaire de l’Université de Bourgogne (WPCM)”.

UV-Visible Spectroscopy

UV-visible spectra were recorded on a Jasco V630Bio spectrophotometer (with an automatic thermostated 6-position Peltier cell changer), at 20°C using quartz cuvette (1 cm, 3 mL). Measurement were performed in a solution of Phosphate Buffer Saline (PBS) + 0.05 % NaN_3 or PBS. The sample concentrations were chosen to obtain an absorbance included between 0.08 and 1.

Photophysical Characterization

Phosphate buffered saline (PBS, 100 mM phosphate + 150 mM NaCl, pH 7.4) was prepared using water purified with a PURELAB Ultra system from ELGA (purified to 18.2 $\text{M}\Omega\cdot\text{cm}$). Indocyanine Green (ICG, IR-125, laser grade) and DMSO (+99.9%, for spectroscopy) were purchased from ACROS Organics.

UV-visible spectra were obtained on a Varian Cary 50 scan (single-beam) spectrophotometer by using a rectangular quartz cell (Hellma, 100-QS, 45 \times 12.5 \times 12.5 mm, pathlength 10 mm, chamber volume: 3.5 mL), at 25 °C (using a temperature control system combined with water circulation). Fluorescence spectra (emission/excitation spectra) were recorded with an

HORIBA Jobin Yvon Fluorolog spectrophotometer (software FluorEssence) at 25 °C (using a temperature control system combined with water circulation), using a standard fluorometer cell (Labbox, LB Q, 10 mm). Emission spectra were recorded in the range 755-900 nm after excitation at 740 nm (shutter: Auto Open, excitation slit = 5 nm and emission slit = 5 nm). Excitation spectra were recorded in the range 400-825 nm after emission at 825 nm (shutter: Auto Open, excitation slit = 5 nm and emission slit = 12 nm). All fluorescence spectra were corrected until 850 nm. Fluorescence quantum yields were measured at 25 °C by a relative method using ICG ($\Phi_F = 10.6\%$ in DMSO) as a standard (dilution by a factor of 3 between absorption and fluorescence measurements). The following equation was used to determine the relative fluorescence quantum yield:

$$\Phi_F(x) = (A_s/A_x)(F_x/F_s)(n_x/n_s)^2\Phi_F(s)$$

where A is the absorbance (in the range of 0.01-0.1 A.U.), F is the area under the emission curve, n is the refractive index of the solvents (at 25 °C) used in measurements, and the subscripts s and x represent standard and unknown, respectively. The following refractive index values were used: 1.479 for DMSO and 1.337 for PBS. Stock solution (1.0 mg/mL) of **24** was prepared in DMSO whereas for **36** and **41** was prepared in ultrapure water and subsequently diluted with PBS for UV-vis absorption and fluorescence measurements. Stock solutions of AGuIX-NODAGA-IR-783 were prepared directly in PBS.

Compound Purifications

Flash Chromatography was performed using the Grace Automatic Reveleris\ Flash Chromatography System equipped with a multiple channel detection: UV (214 nm and/or 254 nm) and Evaporative Light Scattering Detection (ELSD). Reveleris C18 12/25/40/80/120 g cartridges were used reversed phase liquid chromatography.

Semi-preparative RP-HPLC were performed on a Thermo Scientific Dionex Ultimate 3000 system equipped with UV-Vis detection using Ultimate 3000 diode array detector at 214, 254, 280, 650 and/or 780 nm. semi-preparative RP-HPLC (Thermo Beta Basic C₁₈ column, 30 x 150 mm) linear gradient from 100 to 0 % (2 min) and 100 % [H₂O/0.1 % TFA (2 min)] at a flow rate of 15.0 mL.min⁻¹.

HPLC Analysis

The purity of the chemical compounds was determined by RP-HPLC on a Thermo Scientific Dionex Ultimate 3000 system with a photodiode detector according to the following methods: RP-HPLC: (Phenomenex Kinetex C₁₈ column, 50-2.1 mm) with CH₃CN and H₂O + 0.1 % TFA as eluents. 5 % CH₃CN (2 min), followed by linear gradient from 5 to 100 % (5 min) of

CH₃CN, 100 % CH₃CN (1.5 min), a return to initial conditions by linear gradient from 100 to 5 % (0.1 min) and 5 % CH₃CN (1.4 min) at a flow rate of 0.5 mL.min⁻¹. UV-vis detection with an Ultimate 3000 diode array detector at 201, 214, 220, 254, 650 and/or 780nm.

AGuIX nanoparticles: For UV-vis detector, the detecting wavelength was set at 295 nm where organic chelators can highly absorb for characterizing empty NP and at 700 nm where copper (Cu) complex of DOTAGA specifically absorb for characterizing Cu incorporated NP. Fluorescence detector ($\lambda_{\text{ex}} = 274 \text{ nm}$, $\lambda_{\text{em}} = 312 \text{ nm}$) was used to when characterizing Gd incorporated NP. The column temperature was maintained at 30 °C. Linear gradient LC elution was carried out with two mobile phases: (A) Milli-Q water/TFA 99.9:0.1 v/v and (B) acetonitrile (CH₃CN)/TFA 99.9:0.1 v/v. Each time, an amount of 20 μL of sample was loaded to an injection valve and injected into a Jupiter C4 column (150 mm \times 4.60 mm, 5 μm , 300 Å, Phenomenex) at a flow rate of 1 mL/min. Then the elution was programmed as follows: 1% of solvent B in 7 min to elute the reactive and fragments, then a gradient from 1% to 90% in 15 min to elute the nanoparticle. The concentration of B was maintained over 7 min. Then, the concentration of solvent B was decreased to 1% over 1 min and maintained during 8 min to re-equilibrate the system for a new analysis. Before the measurement of each sample, a baseline was obtained under the same conditions by injecting Milli-Q water. The purity is calculated by dividing the area under the peak of the particle to the total area under the peaks of the particle and the impurities.

Relaxivity Measurements:

Relaxivity measurements were performed on a Bruker® minispec mq60NMR analyzer (Bruker, USA) at 37 °C at 1.4 T (60 MHz). 300 μL of samples were measured at a specific Gd³⁺ concentration (mM), measured from ICP-OES. The longitudinal relaxation time T1 and the transverse relaxation time T2 (s) were measured.

FTIR Spectroscopy:

Infrared spectra were performed with 'IRAffinity-1 Shimadzu'. Transmittance mode was used with Happ-Genzel apodization function, 30 scans, 4 cm⁻¹ resolution in a range between 400 and 4000 cm⁻¹. pHs of the solutions were adjusted to 2 before being lyophilized. The spectra were recorded on the obtained powders.

Dynamic light scattering (DLS) and zeta potential (for AGuIX nanoparticles)

Measurement was taken on 1 mL or 0.5 mL of the solution with a single use PMMA cuvette (Carl Roth GmbH, Germany) at 20 °C. Attenuator and position were optimized by the device.

Fast mode was enabled to enhance the precision for the measurement of particles with hydrodynamic diameter less than 10 nm. For most of samples, lyophilized powder was redispersed in water to achieve 100 mg/mL solution and diluted to 10 mg/mL in an aqueous solution just before each measurement.

Zeta potential measurements were recorded at 20 °C within a DTS 1061 folded capillary cell (Malvern Instruments Ltd, USA). The zeta potential (ζ) was automatically calculated from electrophoretic mobility based on the Smoluchowski equation, $v = (\epsilon\epsilon_0\zeta / \eta)\zeta$, where v is the measured electrophoretic mobility, η is the viscosity, ϵ is the dielectric constant of the electrolytic solution, $\epsilon_0 \approx 8.854 \times 10^{-12} \text{ C}^2\text{N}^{-1}\text{m}^{-2}$ is the vacuum permittivity. Lyophilized powder was redispersed in water to achieve 100 mg/mL solution and diluted to 10 mg/mL in an aqueous solution containing 5 mM NaCl and adjusted to the desired pH (7.4) just before each measurement.

Materials:

All the macrocyclic compounds used as starting materials for synthesis were provided by CheMatech. All chemicals were purchased from Acros and Aldrich unless otherwise mentioned and were used without further purification. Peptide-grade DMF and all the Fmoc-amino acids were purchased from Iris Biotech or Novabiochem. Organic solvents were removed under reduced pressure using rotary evaporator (Buchi, Switzerland). Water was removed by lyophilisation using freeze dryer (Labconco, USA).

Radiochemistry:

^{64}Cu was obtained as Copper (^{64}Cu) chloride in 0.1N Hydrochloric acid (Cuprymina 925 MBq/mL) from SPARKLE S.r.l, Italy. Radiochromatograms were carried out with a Raytest miniGITA-Star γ radiochromatograph (Raytest, Straubenhardt, Germany) or with a Bioscan AR-2000 radio-TLC Imaging Scanner (Bioscan Inc., Washington, DC).

Animal Imaging:

All animal studies were conducted in accordance with the legislation on the use of laboratory animals (directive 2010/63/EU) and were approved by accredited Ethical committee (C2ea Grand Campus n°105). Female NMRI Nude mice (6-8 weeks, Janvier Labs, France) were subcutaneously injected with 2×10^7 TSA cells (murine mammary adenocarcinoma). Mice were maintained in ventilated housing units under controlled conditions of temperature ($22 \pm 2^\circ\text{C}$), photoperiod (12h light/12h dark) with free access to food and drink. Three to five weeks after tumor cells injection, TSA tumor bearing-mice (n=3) were administered radiolabelled nanoparticles in PBS corresponding to radioactivity of ~ 10 MBq by intravenous injection.

For the HER-2 tumor model, balb/c nude mice (n = 3; 6–8 weeks old, purchased from Charles River, France) were subcutaneously injected the flank with 2×10^7 BT-474 human breast carcinoma cells. After tumor growth, the bimodal bioconjugate was injected intravenously in the lateral tail vein as a ~ 1 mg/mL solution in PBS (100 μ L). For all imaging procedures, mice were anesthetized under isoflurane. Imaging experiments were performed using the imaging instruments available at the imaging platform of CGFL, Dijon.

PET-MRI Imaging:

Simultaneous MRI-PET imaging was performed at 1 and 24 hours after the injection of the radiolabelled nanoparticles on a fully integrated system (MR Solutions, Guilford, UK) consisting of a 7T dry magnet (Powerscan MRS-7024-PW) coupled with a SiPM dual-ring PET-I-802 insert. Mice were anaesthetized with isoflurane (2 % in oxygen) and positioned in a dedicated heating cradle. MRI and PET acquisitions were performed simultaneously. Animal respiration was monitored with abdominal pressure sensor and dedicated software (PC Sam, SAIL, Stony Brook, US). List-mode data were collected in the PET system during 30-60 minutes. Images were reconstructed with the 3D ordered subset expectation maximization (OSEM) algorithm implemented in the system using 2 iterations, 32 subsets and an isotropic voxel size of 0.28 mm. An energy window of 250-750 keV and a coincidence time window of 8 ns were applied to the list-mode data. The algorithm takes into account normalization, random and decay corrections. No attenuation correction was applied. T1 and T2 weighted fast spin echo MR images were acquired with respiratory gating and sequences in axial and coronal plans. T1 sequences were acquired with time of repetition (TR) of 1000 ms, time of echo (TE) of 11 ms. T2 sequences were acquired with TR of 4000 ms, TE of 45 ms. Following parameters were used for both T1 and T2: flip angle of 90° , 4 signal averages, 1 mm slice thickness, 0.15×0.15 mm² transaxial pixel size and 256×256 pixels matrix. The PET-MR fusion image was obtained using VivoQuant (Invicro, Boston, US). Each scan was then visually interpreted. For the gamma counting of the organs, the counter was cross-calibrated to the dose calibrator used to measure the injected dose and the linearity range was determined for all the geometries used in ex-vivo counting. Data were then converted to percentage of injected dose and to percentage of injected dose per gram of tissue.

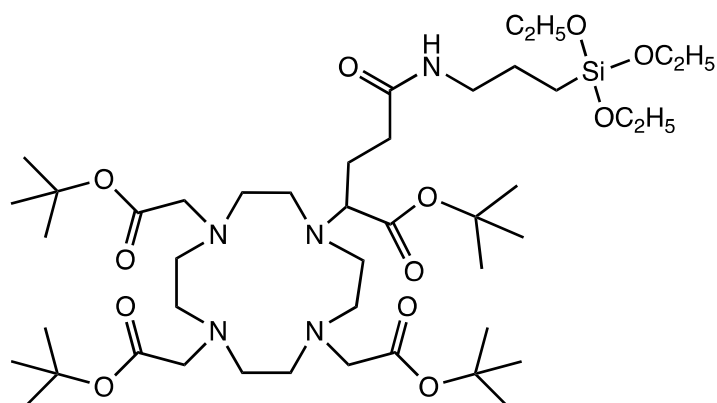
Optical Imaging:

The optical imaging/fluorescence signal was monitored using the Perkin Elmer Ivis Lumina III system. Whole body imaging was acquired at 1 h, 4h and 24 h time points using appropriate excitation/emission settings. All imaging data were analysed with the Living

Image® software. Values are reported as radiant efficiency, allowing direct comparison of images from each experiment. After the last imaging, the mice were euthanized and organs collected for *ex-vivo* imaging at 24 h post-injection. Fluorescence intensities were measured and normalized to photon per second per cm² using the region of interest (ROI) function of the Living Image® software. The ROI cover the entire tissue.

Chemistry

DOTAGA(tBu)₄-APTES (**1**)



Chemical Formula: C₄₄H₈₅N₅O₁₂Si

Molecular Weight: 904.27

DOTA-GA(tBu)₄ (0.9g, 1.284 mmol) was weighed in 100mL round bottom flask and was dissolved in 20mL of DCM under the hood with stirring. DIPEA (1.14mL, 6.55mmol) was added into above solution followed by coupling agents viz. HBTU (0.52g, 1.37 mmol) and HOBt (0.18g, 1.37 mmol) and the solution was left for stirring at room temperature for 15min. APTES (0.3g 1.37mmol) was added to the above solution directly using the 1mL syringe and solution was stirred further at room temperature for 60min after which the product formation was confirmed through MS. The above solution was mixed with 50mL of citric acid solution (pH: 2.5-3) in a separating funnel and the organic layer was recovered. The organic layer was further mixed with 50mL of 5% NaHCO₃ in a separating funnel and the organic layer was recovered. The DCM solution was stirred with 5g of MgSO₄ for 10min and filtered using sintered funnel to receive the dry and clear DCM solution. Organic phase was evaporated under vacuum at 30°C to get a viscous brownish residue, as an intermediate product (Yield: 1.05g, 78%).

HRMS: Calculated for C₄₄H₈₅N₅O₁₂Si:926.585 [M+Na]⁺; Obtained: m/z = 926.584 [M+Na]⁺

¹H NMR (500 MHz, CDCl₃-d) δ 0.4 – 0.7 (m, 2H), 0.7 – 0.8 (m, 1H), 1.0 (dd, *J* = 9.0, 6.7 Hz, 1H), 1.1 – 1.2 (m, 9H), 1.3 – 1.5 (m, 32H), 1.5 (p, *J* = 7.8 Hz, 2H), 1.7 (d, 1H), 1.9 – 2.1 (m, 1H), 2.1 – 2.3 (m, 1H), 2.4 – 3.4 (m, 29H), 3.5 – 3.7 (m, 1H), 3.7 – 3.8 (m, 4H).

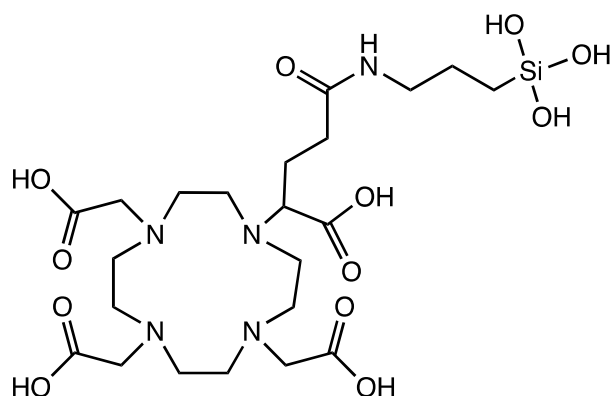
¹³C NMR (126 MHz, CDCl₃) δ 7.5, 7.8, 18.3, 20.4, 23.5, 25.9, 26.8, 27.8, 27.8, 27.9, 27.9, 27.9, 28.2, 28.3, 29.7, 33.0, 38.6, 42.1, 47.6, 49.8, 58.4, 63.6, 80.8, 82.3, 171.1, 173.2.

Elemental Analysis:

Calculated for C₄₄H₈₅N₅O₁₂Si. 0.9HPF₆ (%): C: 51.03, H: 8.36, N:6.76.

Observed (%): C: 51.86, H: 8.91, N: 8.38.

DOTAGA-Silane (**2**)



Chemical Formula: C₂₂H₄₁N₅O₁₂Si

Molecular Weight: 595.68

DOTAGA(tBu)₄-APTES (1g) was weighed into a 100mL round bottom flask and was mixed with 5mL of concentrated hydrochloric acid and stirred for 10min. Later, the acid was evaporated under vacuum at 35°C in 5-15min to get a dried residue. The above dried residue was dissolved in 10mL of water and lyophilized to get a light brown coloured powder (Yield: 850mg, 81%).

¹H NMR (500 MHz, D₂O) δ 0.5 – 0.8 (m, 2H), 1.2 – 1.3 (m, 1H), 1.4 – 1.6 (m, 1H), 1.6 – 1.8 (m, 1H), 1.8 – 2.2 (m, 1H), 2.3 – 4.5 (m, 26H).

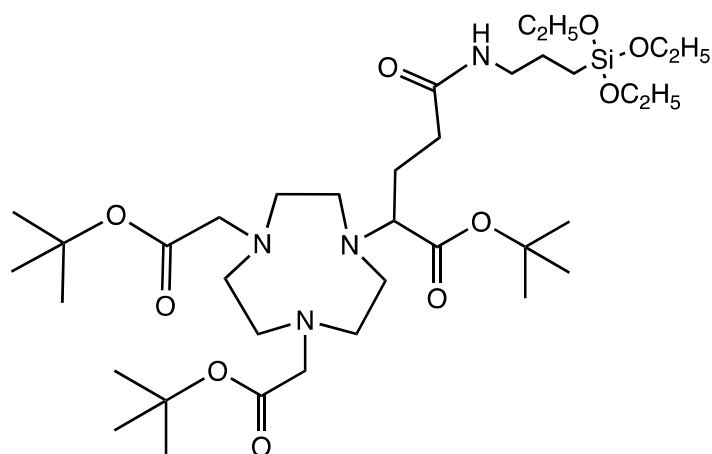
HRMS: Calculated for C₂₂H₄₁N₅O₁₂Si: 596.259 [M+H]⁺; Obtained: m/z = 596.261 [M+H]⁺; 618.242 [M+Na]⁺

Elemental Analysis:

Calculated for C₂₂H₄₁N₅O₁₂Si. HPF₆. 2HCl (%): C: 32.44, H: 5.44, N: 8.60.

Observed (%): C: 32.17, H: 6.54, N: 9.39.

NODAGA(tBu)₃-APTES (**3**)



Chemical Formula: C₃₆H₇₀N₄O₁₀Si

Molecular Weight: 747.06

NODA-GA(tBu)₃ (1.0g, 1.84mmol) was weighed in the 100mL round bottom flask and was dissolved in 20mL of DCM under the hood with stirring. DIPEA (1.3 mL, 7.5mmol) was added into above solution followed by coupling agents viz. HBTU (1.0g, 1.95mmol) and HOBT (1.0g, 1.95mmol) and the solution was left for stirring at room temperature for 15min. APTES (0.43g, 1.95mmol) was added to the above solution directly using the 1mL syringe and solution was stirred further at room temperature for 60min after which the product formation was confirmed through MS. The above solution was mixed with 50mL of citric acid solution (pH: 2.5-3) in a separating funnel and the organic layer was recovered. The organic layer was further mixed with 50mL of 5% NaHCO₃ in a separating funnel and the organic layer was recovered. The DCM solution was stirred with 5g of MgSO₄ for 10min and filtered using sintered funnel to receive the dry and clear DCM solution. Organic phase was evaporated under vacuum at 30°C to get a viscous brownish residue, as an intermediate product (Yield: 1.5g, 99%).

HRMS: Calculated for C₃₆H₇₀N₄O₁₀Si:926.585 [M+Na]⁺; Obtained: m/z = 926.584 [M+Na]⁺

¹H NMR (500 MHz, CDCl₃-d) δ 0.5 – 0.6 (m, 2H), 1.0 – 1.1 (m, 1H), 1.1 – 1.2 (m, 7H), 1.4 (d, 25H), 1.5 – 1.6 (m, 2H), 1.8 (d, *J* = 8.8 Hz, 1H), 1.9 – 2.1 (m, 1H), 2.2 – 2.5 (m, 2H), 2.6 – 3.3 (m, 22H), 3.7 – 3.8 (m, 4H), 6.2 (d, 1H).

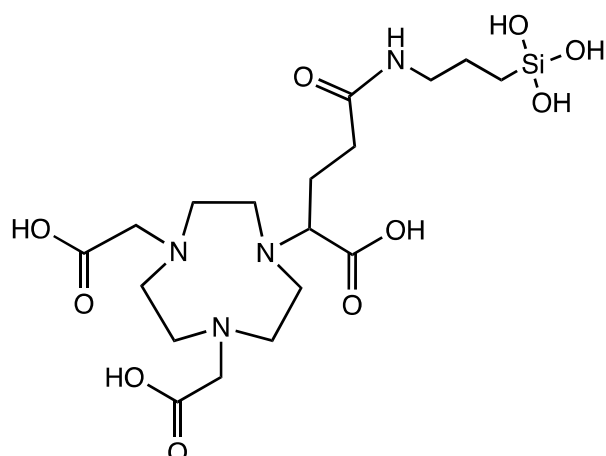
¹³C NMR (126 MHz, CDCl₃) δ 7.8, 18.3, 18.4, 23.1, 26.2, 28.1, 28.2, 28.3, 29.7, 33.4, 38.6, 42.0, 53.7, 55.9, 58.4, 80.8, 165.7, 171.7, 172.8.

Elemental Analysis:

Calculated for C₃₆H₇₀N₄O₁₀Si. 0.6HPF₆ (%): C: 51.81, H: 8.53, N: 6.71.

Observed (%): C: 52.58, H: 9.13, N: 8.85.

NODAGA-Silane (**4**)



Chemical Formula: $C_{18}H_{34}N_4O_{10}Si$

Molecular Weight: 494.57

NODAGA(tBu)₃-APTES was weighed into a 100mL round bottom flask and was mixed with 5mL of concentrated hydrochloric acid and stirred for 10min. Later, the acid was evaporated under vacuum at 35°C in 5-15min to get a dried residue. The above dried residue was dissolved in 10mL of water and lyophilized to get a light brown coloured powder (Yield: 1.2g, 96%).

¹H NMR (500 MHz, D₂O) δ 0.41 – 0.80 (m, 2H), 0.93 – 1.28 (m, 2H), 1.39 – 1.59 (m, 2H), 1.84 – 2.18 (m, 2H), 2.27 – 2.46 (m, 2H), 2.73 (s, 5H), 2.97 – 3.18 (m, 5H), 3.19 – 3.45 (m, 7H), 3.48 – 3.75 (m, 1H), 3.79 – 4.10 (m, 4H).

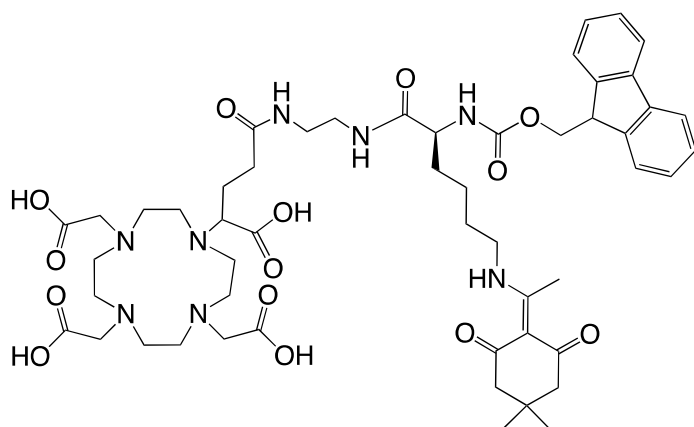
HRMS: Calculated for $C_{18}H_{34}N_4O_{10}Si$:495.211 [M+H]⁺; Obtained: m/z = 495.212 [M+H]⁺ ; 517.191 [M+Na]⁺

Elemental Analysis:

Calculated for $C_{18}H_{34}N_4O_{10}Si \cdot HPF_6 \cdot HCl$ (%): C: 31.93, H: 5.36, N: 8.28.

Observed (%): C: 31.74, H: 6.64, N: 8.81.

DOTAGA-Lys-Fmoc-Dde (**5**)



Chemical Formula: $C_{52}H_{72}N_8O_{14}$

Molecular Weight: 1033.19

Lysine-Fmoc-dde (500mg, 0.938mmol) was weighed into a 50mL RBF to which 2mL of DMF was added, solubilized followed by addition of DIPEA (0.34 mL, 1.92mmol) and stirring for 5min. TSTU (303mg, 1mmol) was added to the above reaction mixture and the reaction was stirred for 30min. The activated lysine formation was verified by LC-MS. DOTAGA-NH₂ was weighed into glass tube and dissolved in DMF: Water - 3mL: 1mL followed by addition of DIPEA to it. The above solution was added to the activated lysine solution and the reaction was left stirred at room temperature for 1h. The solvents were evaporated at 40°C to get a pale yellow viscous solution. The residue was purified by flash chromatography (C18) using water (0.1%TFA) and acetonitrile (0.1%TFA). Appropriate fractions were identified, collected, evaporated, frozen and lyophilized to get the creamish white powder (Yield: 700mg, 73%).

HRMS: Calculated for $C_{52}H_{72}N_8O_{14}$:1033.524 [M+H]⁺; Obtained: m/z = 1033.527 [M+H]⁺, 1055.505 [M+Na]⁺

HPLC: t_R= 3.93min, Purity= 97.93%

¹H NMR (500 MHz, D₂O) δ 1.0 (d, 6H), 1.2 – 1.9 (m, 5H), 1.9 – 2.1 (m, 1H), 2.3 (m, 9H), 2.8 (s, 2H), 3.0 – 4.7 (m, 33H), 5.0 (s, 1H), 7.3 (s, 4H), 7.5 – 8.0 (m, 4H).

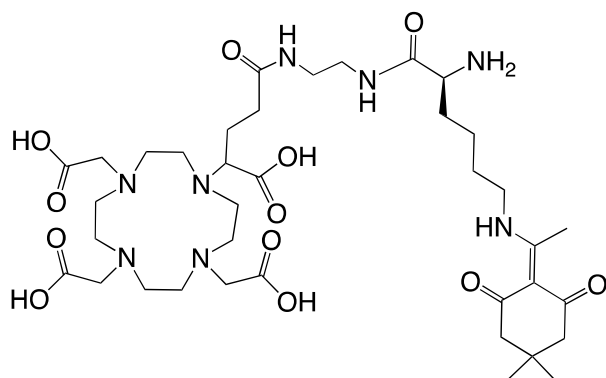
¹³C NMR (126 MHz, D₂O) δ 17.7, 22.7, 27.3, 29.4, 31.3, 33.0, 38.0, 38.6, 43.1, 46.7, 51.6, 53.5, 54.8, 55.3, 66.6, 107.4, 112.8, 115.2, 117.5, 119.8, 125.1, 127.2, 127.7, 140.7, 143.5, 143.8, 157.0, 162.4, 162.7, 162.9, 163.2, 173.9, 174.1, 174.8, 178.7, 199.1

Elemental Analysis:

Calculated for $C_{52}H_{72}N_8O_{14}$. 2.2 TFA (%): C: 52.76, H: 5.82, N: 8.73.

Observed (%): C: 52.53, H: 6.11, N: 8.96.

DOTAGA-Lys-Dde-NH₂ (**6**)



Chemical Formula: C₃₇H₆₂N₈O₁₂

Molecular Weight: 810.95

DOTAGA-Lys-Fmoc-Dde (600mg) was weighed into a 50mL round bottom flask and dissolved in 5mL each of DMF and DEA and the reaction was stirred for 30 min. The solvent was evaporated at 35°C to obtain a yellow viscous residue. The residue was purified by flash chromatography (C18) using water and acetonitrile as eluents. The appropriate fractions were identified, pooled, frozen and lyophilised to give a white powder (Yield: 300mg, 77%).

HRMS: Calculated for C₃₇H₆₂N₈O₁₂:811.456 [M+H]⁺; Obtained: m/z = 811.456 [M+H]⁺, 833.433 [M+Na]⁺

HPLC: t_R = 2.63min, Purity = 99.63%

¹H NMR (500 MHz, D₂O) δ 1.0 (s, 6H), 1.4 (p, *J* = 8.1 Hz, 2H), 1.6 – 2.0 (m, 6H), 2.1 – 2.3 (m, 1H), 2.4 (d, 8H), 2.8 (t, 1H), 2.9 – 3.6 (m, 22H), 3.6 – 3.8 (m, 4H), 3.8 – 4.1 (m, 3H).

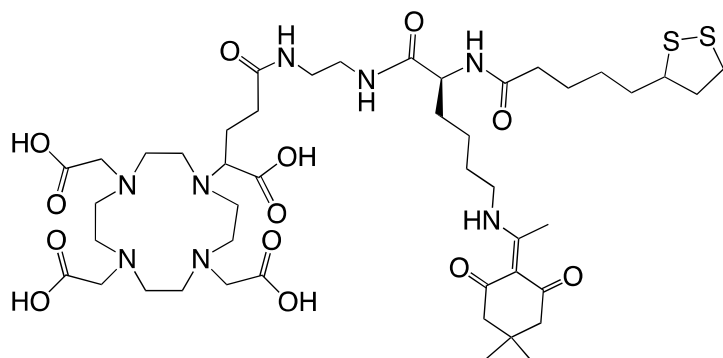
¹³C NMR (126 MHz, D₂O) δ 17.9, 21.5, 21.5, 27.0, 27.6, 27.6, 29.7, 30.2, 30.2, 33.2, 33.5, 38.3, 38.6, 38.8, 38.9, 43.0, 43.0, 44.3, 45.8, 49.6, 50.7, 51.6, 53.0, 53.1, 54.0, 56.2, 56.7, 61.8, 108.2, 169.9, 170.0, 174.9, 174.9, 175.6, 175.7, 200.8.

Elemental Analysis:

Calculated for C₃₇H₆₂N₈O₁₂ · 4H₂O (%): C: 50.33, H: 7.99, N: 12.69.

Observed (%): C: 49.96, H: 8.18, N: 12.91.

DOTAGA-Lys-TA-Dde (7)



Chemical Formula: $C_{45}H_{74}N_8O_{13}S_2$

Molecular Weight: 999.25

DOTAGA-Lys-Dde-NH₂ (350 mg) was weighed in a 50 mL round bottom flask and dissolved in ACN:Water (3.5 mL:1.5 mL). DIPEA (0.6 mL, 3.46 mmol) was added to the above solution and the solution was stirred for 5 min. TA-NHS (262 mg, 0.86 mmol) was weighed in a glass tube and added to the above solution and the reaction was stirred at room temperature for 1 h. The product formation was confirmed by LC-MS. The reaction mixture was evaporated to get a yellow waxy residue. The above residue was purified by flash chromatography (C18) using water and acetonitrile as eluents. Appropriate fractions were identified, pooled, frozen and lyophilized to give a yellowish white powder (420 mg, 95%).

HRMS: Calculated for $C_{45}H_{74}N_8O_{13}S_2$: 1021.470 [M+Na]⁺; Obtained: m/z = 1021.472 [M+Na]⁺

HPLC: t_R = 3.62 min, Purity = 97.62%

¹H NMR (500 MHz, Deuterium Oxide) δ 1.0 (s, 6H), 1.4 – 2.0 (m, 13H), 2.1 – 2.6 (m, 12H), 2.6 – 2.8 (m, 1H), 2.9 (m, 1H), 3.0 – 3.8 (m, 34H), 3.8 – 4.0 (m, 2H), 4.2 (m, 1H).

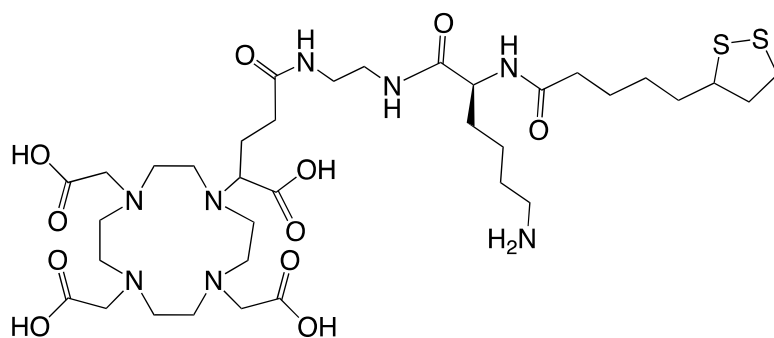
¹³C NMR (126 MHz, D₂O) δ 12.1, 16.3, 17.7, 18.1, 22.9, 25.0, 25.1, 25.2, 27.2, 27.4, 27.9, 28.1, 28.3, 29.7, 30.8, 33.4, 33.8, 33.9, 35.3, 35.4, 36.4, 38.2, 38.6, 38.9, 40.3, 42.5, 43.4, 51.7, 53.6, 53.6, 54.3, 55.2, 56.6, 56.6, 56.7, 63.0, 108.2, 174.3, 174.8, 175.6, 175.6, 176.8, 176.9, 200.6.

Elemental Analysis:

Calculated for $C_{45}H_{74}N_8O_{13}S_2$ (%): C: 54.09, H: 7.46, N: 11.21, S: 6.42.

Observed (%): C: 54.87, H: 9.16, N: 10.53, S: 4.87

DOTAGA-Lys-TA-NH₂ (**8**)



Chemical Formula: C₃₅H₆₂N₈O₁₁S₂

Molecular Weight: 835.05

DOTAGA-Lys-TA-Dde (450mg, 0.42mmol) was weighed in a 50mL round bottom flask and was dissolved in 5 mL of DMF. Imidazole (868mg, 12.6mmol) and hydroxylamine hydrochloride (877mg, 12.6mmol) was weighed in a glass tube and added to the above solution. The reaction mixture was stirred at room temperature for 3h. The reaction was completed as confirmed by LC-MS. The DMF was evaporated at 40°C and the residue was purified by flash chromatographic (C18) using water and acetonitrile as eluents. The appropriate fractions were identified, pooled, evaporated, frozen and lyophilized to get a white powder (Yield: 180mg, 48%).

HRMS: Calculated for C₅₂H₇₂N₈O₁₄:857.387[M+Na]⁺, 858.394 [M+H+Na]⁺; Obtained: m/z = 857.385[M+Na]⁺, 858.390 [M+H+Na]⁺

HPLC: t_R=2.77 min, Purity= 93.28 %

¹H NMR (500 MHz, D₂O) δ 1.1 – 1.4 (m, 4H), 1.5 – 1.8 (m, 9H), 1.8 – 2.0 (m, 2H), 2.1 (m, 1H), 2.2 – 2.4 (m, 3H), 2.4 – 2.5 (m, 1H), 2.7 – 3.5 (m, 26H), 3.6 (m, 4H), 3.9 (m, 2H), 4.1 – 4.2 (m, 1H).

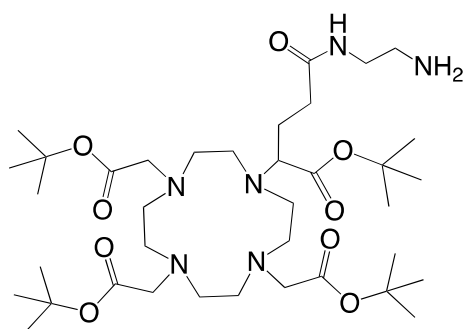
¹³C NMR (126 MHz, D₂O) δ 22.1, 24.9, 24.9, 26.3, 27.9, 30.6, 30.7, 33.4, 33.7, 34.5, 35.1, 35.2, 38.1, 38.5, 38.6, 38.9, 39.1, 40.3, 49.2, 50.3, 50.6, 51.7, 53.8, 53.9, 53.9, 55.6, 56.5, 63.2, 174.2, 174.3, 175.5, 177.0.

Elemental Analysis:

Calculated for C₃₅H₆₂N₈O₁₁S₂ · 5H₂O (%): C: 45.44, H: 7.85, N: 12.11, S: 6.93.

Observed (%): C: 45.39, H: 8.37, N: 13.33, S: 5.77.

DOTAGA(tBu)₄-NH₂ (**9**)



Chemical Formula: C₃₇H₇₀N₆O₉

Molecular Weight: 743.00

DOTA-GA(tBu)₄ (4.3g, 6.13mmol) was weighed in the round bottom flask 100mL and was dissolved in 60mL of ACN under the hood with stirring. DIPEA (6.6mL, 36.8mmol) was added first to the above solution followed by coupling agents viz. HBTU (2.44g, 6.43mmol) and HOBT (0.87g, 6.43mmol), and the solution was left for stirring at room temperature for 10min. Ethylenediamine (20.7mL, 306.7mmol) was dissolved in about 60mL of ACN and added to the DOTA-GA(tBu)₄ solution and was stirred further at room temperature for 30min after which the product formation was confirmed through LC-MS. The solution was evaporated at 35°C to remove ACN to get a viscous residue. The residue was dissolved in 100mL of DCM and successively extracted with 100mL of citric acid (pH-3), 5%NaHCO₃ and water. The organic phase was dried by passing over MgSO₄ and subsequently evaporated to get a viscous residue. The residue was purified by flash chromatography (C18) using Water (0.1%TFA) and ACN (0.1%TFA) as eluent to get a white powder as a TFA salt (Yield: 3.68g, 48%).

HRMS: Calculated for C₃₇H₇₀N₆O₉:743.527 [M+H]⁺; Obtained: m/z = 743.530 [M+H]⁺, 765.509 [M+Na]⁺

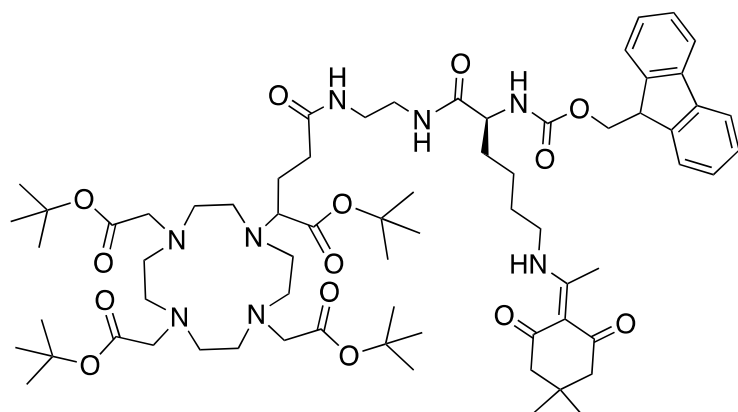
HPLC: t_R= 3.73min, Purity= 99.62%.

Elemental Analysis:

Calculated for C₄₈H₆₅N₇O₁₂. 4.5TFA (%): C: 43.52, H: 5.88, N: 6.77.

Observed (%): C: 43.00, H: 6.89, N: 6.96.

DOTAGA(tBu)₄-Lys-Fmoc-Dde (**10**)



Chemical Formula: C₆₈H₁₀₄N₈O₁₄

Molecular Weight: 1257.62

Fmoc-Lysine-Dde-OH (2.5g, 4.7mmol) was weighed into a 500mL round bottom flask and dissolved in 20mL of ACN and DIPEA (1.7mL, 9.38mmol) and the solution stirred at room temperature for 10 min. TSTU (1.46g, 4.74mmol) was added into lysine solution and reaction stirred at room temperature for 30min for the Lysine-NHS ester formation which was verified by LC-MS. DOTAGA(tBu)₄-NH₂ (3.5g) was weighed into 250mL round bottom flask and dissolved in 30mL ACN and DIPEA (4.17mL, 23.5mmol) and pipetted slowly into the lysine solution. The reaction was stirred for 1h and the peptide coupling was verified by LC-MS. The solvent was evaporated off to get a viscous residue that was purified by flash chromatography (C18) using water (0.1%TFA) and ACN (0.1%TFA) as eluent to get a white powder as a TFA salt (Yield 3.88g, 45%).

HRMS: Calculated for C₆₈H₁₀₄N₈O₁₄:1257.774[M+H]⁺; Obtained: m/z = 1257.775 [M+H]⁺.

HPLC: t_R = 4.94min, Purity = 98.52%

¹H NMR (500 MHz, CDCl₃-d) δ 1.0 (s, 6H), 1.3 – 1.6 (m, 41H), 1.7 (m, 4H), 1.8 – 2.2 (m, 3H), 2.3 (s, 4H), 2.5 (s, 6H), 2.7 – 4.6 (m, 33H), 6.8 (d, 1H), 7.3 (dd, *J* = 7.4, 2.7 Hz, 2H), 7.4 (td, *J* = 7.5, 2.5 Hz, 2H), 7.6 (dd, *J* = 7.5, 2.5 Hz, 2H), 7.7 (d, *J* = 7.6 Hz, 2H), 8.0 (s, 1H), 8.2 – 8.3 (m, 1H), 10.5 (s, 2H).

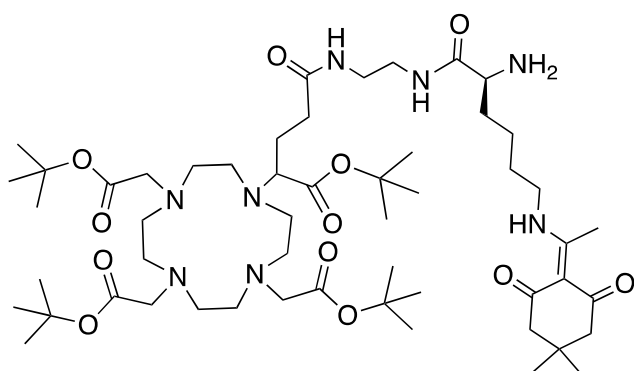
¹³C NMR (126 MHz, CDCl₃) δ 17.2, 17.3, 17.9, 23.0, 27.7, 27.9, 27.9, 28.2, 28.5, 30.1, 32.3, 37.0, 39.3, 43.3, 47.1, 52.7, 53.8, 55.3, 67.0, 105.0, 107.7, 112.8, 115.1, 117.5, 119.8, 119.9, 125.4, 125.5, 127.1, 127.7, 141.1, 141.2, 144.0, 144.0, 156.5, 160.4, 160.7, 161.0, 161.3, 173.1, 173.7, 197.8.

Elemental Analysis:

Calculated for C₆₈H₁₀₄N₈O₁₄. 5.TFA (%): C: 51.26, H: 6.01, N: 6.13.

Observed (%): C: 49.50, H: 6.91, N: 7.72.

DOTAGA(tBu)₄-Lys-Dde-NH₂ (**11**)



Chemical Formula: C₅₃H₉₄N₈O₁₂

Molecular Weight: 1035.38

DOTAGA(tBu)₄-Lys-Fmoc-Dde (3.5 g) was dissolved in 27mL of ACN and 13mL of diethylamine and reaction was stirred at room temperature for 1h. The reaction mixture was stirred for 0.5h and the product was confirmed through LC-MS. The solvents were evaporated at 35°C to get a viscous residue that was purified by flash chromatography (C18) using water (0.1%TFA) and ACN (0.1%TFA) as eluents to obtain a white powder as a TFA salt (Yield: 2.8g, 94%).

HRMS: Calculated for C₅₃H₉₄N₈O₁₂:1035.706 [M+H]⁺; Obtained: m/z = 1035.709 [M+H]⁺, 1057.685 [M+Na]⁺

HPLC: t_R= 4.08min, Purity= 98.86%

¹H NMR (500 MHz, CDCl₃-d) δ 1.0 (s, 6H), 1.2 – 1.6 (m, 38H), 1.7 (h, *J* = 7.3 Hz, 2H), 1.9 (m, 3H), 2.3 (s, 4H), 2.5 (s, 5H), 2.6 – 4.6 (m, 27H), 8.1 (s, 1H), 8.7 (d, 4H).

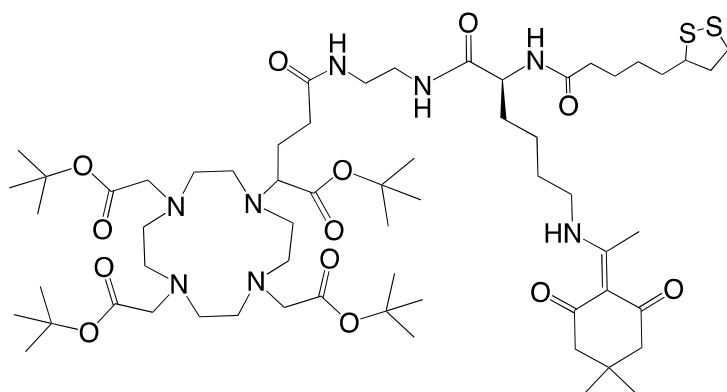
¹³C NMR (126 MHz, CDCl₃) δ 11.0, 17.8, 22.0, 27.9, 28.2, 28.4, 30.1, 30.7, 30.9, 43.0, 52.7, 107.7, 113.0, 115.3, 117.6, 120.0, 160.7, 161.0, 161.2, 161.5, 169.4, 173.8, 197.8.

Elemental Analysis:

Calculated for C₅₃H₉₄N₈O₁₂. 4.5TFA (%): C: 48.09, H: 6.41, N: 7.24.

Observed (%): C: 48.02, H: 6.05, N: 7.72.

DOTAGA(tBu)₄-Lys-TA-Dde (**12**)



Chemical Formula: C₆₁H₁₀₆N₈O₁₃S₂

Molecular Weight: 1223.68

DOTAGA(tBu)₄-Lys-Dde-NH₂ (2.7g) was dissolved in 30mL of ACN in a 500mL round bottom flask, to which DIPEA (2.31mL, 13mmol) was added dropwise and stirred for 10min. Thioctic acid-NHS (832mg, 2.74mmol) was weighed into a glass tube and added directly into the above reaction mixture. The reaction mixture was stirred at room temperature for around 3 h till the product formation was confirmed using LC-MS. The solvent was evaporated using rotavapor at 35°C and the oily residue was purified by flash chromatography (C18) using water (0.1%TFA) and ACN (0.1%TFA) as eluent to get a white powder as a TFA salt (Yield: 2.6g, 95%).

HRMS: Calculated for C₆₁H₁₀₆N₈O₁₃S₂:1245.721 [M+Na]⁺; Obtained: m/z = 1245.720 [M+Na]⁺

HPLC: t_R= 4.73min, Purity= 93.42%

¹H NMR (500 MHz, CDCl₃-d) δ 1.0 (s, 6H), 1.5 (q, *J* = 7.9 Hz, 40H), 1.6 – 1.8 (m, 8H), 1.8 – 2.1 (m, 4H), 2.1 – 2.3 (m, 3H), 2.4 (s, 4H), 2.4 – 2.7 (m, 7H), 2.7 – 4.5 (m, 32H), 7.5 – 8.4 (m, 5H).

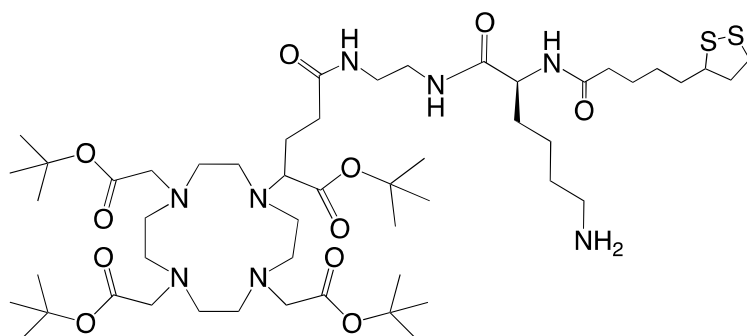
¹³C NMR (126 MHz, CDCl₃) δ 18.1, 23.4, 24.6, 25.6, 25.8, 28.2, 28.5, 28.7, 29.0, 29.1, 30.3, 31.0, 32.1, 32.7, 34.6, 34.7, 36.1, 38.6, 39.6, 40.4, 40.5, 43.4, 53.0, 54.0, 56.3, 56.8, 108.0, 113.1, 115.4, 117.8, 120.1, 160.7, 161.0, 161.3, 161.6, 169.3, 172.9, 173.4, 173.8, 174.1, 198.0.

Elemental Analysis:

Calculated for C₄₈H₆₅N₇O₁₂. 3.TFA (%): C: 51.40, H: 7.02, N:7.16, S:4.10.

Observed (%): C: 50.17, H: 7.79, N: 7.24, S: 3.16.

DOTAGA(tBu)₄-Lys-TA-NH₂ (**13**)



Chemical Formula: C₅₁H₉₄N₈O₁₁S₂

Molecular Weight: 1059.48

DOTAGA(tBu)₄-Lys-TA-Dde (2.5g) was dissolved in 20mL of ACN in 500mL round bottom flask and imidazole (4.22g, 61.3mmol) and hydroxylamine.HCl (4.26g, 61.3mmol) were dissolved in 10mL water. The aqueous base solution was added to the DOTAGA(tBu)₄-Lys-TA-Dde solution and the reaction was stirred at room temperature for 30min following which the product formation was confirmed by LC-MS. The solvents were evaporated off and residue which was purified by flash chromatography (C18) using water (0.1%TFA) and ACN (0.1%TFA) as eluent to get a white powder (Yield: 1.8g, 72%).

HRMS: Calculated for C₅₁H₉₄N₈O₁₁S₂:1081.637 [M+Na]⁺; Obtained: m/z = 1061.636 [M+Na]⁺.

HPLC: t_R= 4.17min, Purity= 99.72%

¹H NMR (500 MHz, CDCl₃-d) δ 1.0 – 1.6 (m, 38H), 1.6 – 1.8 (m, 7H), 1.8 – 2.1 (m, 1H), 2.2 (d, 2H), 2.4 – 4.5 (m, 28H), 7.5 – 8.8 (m, 8H).

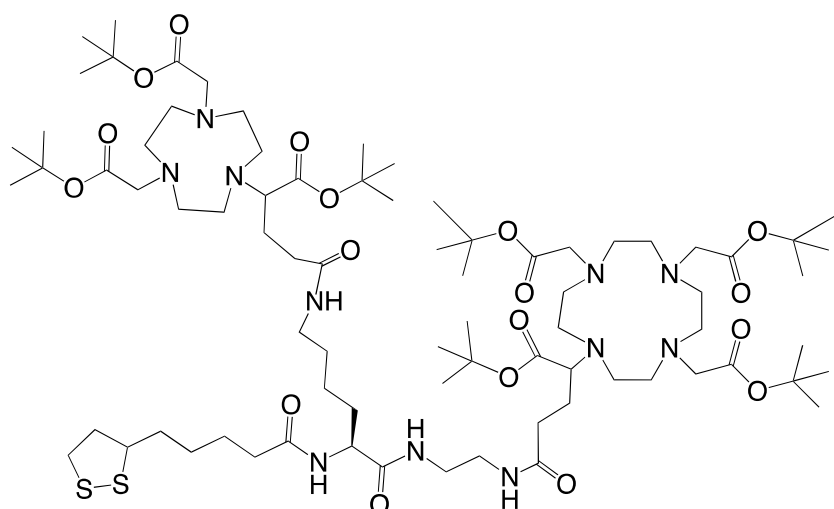
¹³C NMR (126 MHz, CDCl₃) δ 22.6, 25.5, 26.9, 28.1, 28.1, 29.0, 34.7, 35.9, 38.6, 39.6, 40.5, 56.8, 113.1, 115.5, 117.8, 120.1, 160.8, 161.1, 161.4, 161.7, 173.6, 174.3.

Elemental Analysis:

Calculated for C₄₈H₆₅N₇O₁₂. 4.5TFA (%): C: 45.83, H: 6.31, N: 7.13, S: 4.08.

Observed (%): C: 45.69, H: 7.52, N: 8.05, S: 3.16.

DOTAGA(tBu)₄-Lys-TA-NODAGA(tBu)₃ (**14**)



Chemical Formula: C₇₈H₁₄₁N₁₁O₁₈S₂

Molecular Weight: 1585.17

NODAGA(tBu)₃ (400mg, 0.736mmol) was weighed into a 100mL round bottom flask and dissolved in 10mL of ACN and DIPEA (0.39mL, 2.2mmol) and the solution was stirred at room temperature for 10 min. HBTU (285mg, 0.74mmol) and HOBT (100mg, 0.74mmol) was added into the above solution and the reaction stirred at room temperature for 30min following which the reaction was verified by LC-MS. DOTAGA(tBu)₄-Lys-TA-NH₂ (780mg) was weighed into a 100mL round bottom flask and dissolved in 10mL of acetonitrile and DIPEA (0.65mL, 3.67mmol) and pipetted slowly into the activated NODAGA(tBu)₃ solution. The reaction was stirred for 1h and the peptide coupling was verified by LC-MS. The solvent was evaporated off to get a viscous residue that was purified by flash chromatography (C18) using water (0.1%TFA) and acetonitrile (0.1%TFA) as eluent to get a white powder as a TFA salt (Yield: 1.1g, 69%).

HRMS: Calculated for C₇₈H₁₄₁N₁₁O₁₈S₂:1606.978 [M+Na]⁺; Obtained: m/z = 1606.976 [M+Na]⁺

HPLC: t_R= 4.83min, Purity= 91.12%

¹H NMR (500 MHz, CDCl₃-d) δ 1.3 – 1.6 (m, 51H), 1.6 – 1.8 (m, 6H), 1.9 (m, 1H), 2.0 (m, 1H), 2.0 – 2.2 (m, 2H), 2.3 (t, *J* = 7.5 Hz, 2H), 2.3 – 2.7 (m, 5H), 2.7 – 3.5 (m, 24H), 3.5 – 4.4 (m, 10H), 7.3 – 8.3 (m, 4H).

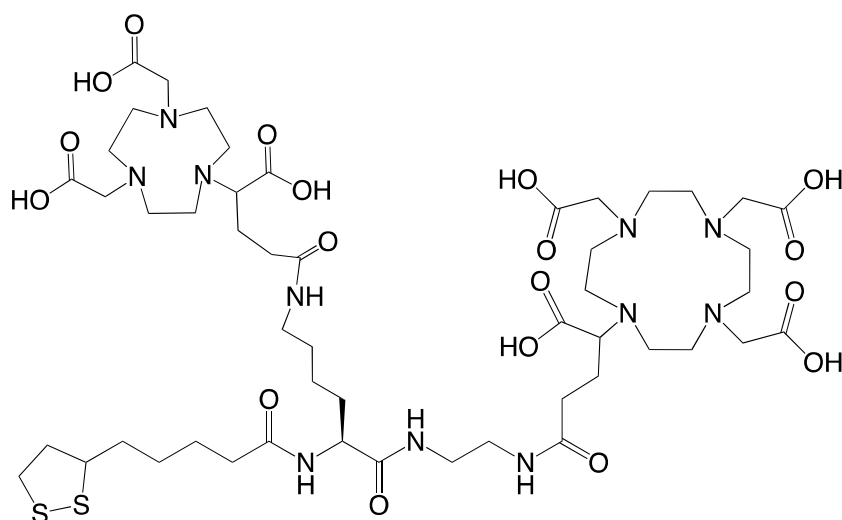
¹³C NMR (126 MHz, CDCl₃) δ 22.7, 25.4, 25.5, 28.0, 28.0, 28.3, 28.8, 32.5, 34.5, 35.8, 38.4, 38.6, 40.2, 50.7, 54.1, 55.9, 56.5, 63.5, 82.7, 115.2, 117.5, 119.8, 160.4, 160.7, 161.0, 161.3, 171.1, 172.6, 172.7, 173.5, 174.0.

Elemental Analysis:

Calculated for C₇₈H₁₄₁N₁₁O₁₈S₂. 5.3TFA (%): C: 48.60, H: 6.74, N: 7.04, S:2.93.

Observed (%): C: 48.53, H: 7.53, N: 8.23, S: 2.06.

DOTAGA-Lys-TA-NODAGA (15)



Chemical Formula: $C_{50}H_{85}N_{11}O_{18}S_2$

Molecular Weight: 1192.41

DOTAGA(tBu)₄-Lys-TA-NODAGA(tBu)₃ (1g) was weighed into a 50mL round bottom flask and was dissolved in 12.5mL of TFA and 12.5mL of dichloromethane. The solution was stirred at room temperature for 24h and the reaction was deemed complete as verified by LC-MS. The solvents were evaporated to get a viscous residue which was purified by flash chromatography (C18) using water (0.1%TFA) and ACN (0.1%TFA) as eluents to get a white powder (Yield: 450mg, 60%).

HRMS: Calculated for $C_{50}H_{85}N_{11}O_{18}S_2$:1192.558 $[M+H]^+$; Obtained: $m/z = 1192.559$ $[M+H]^+$, 1214.540 $[M+Na]^+$

HPLC: $t_R = 2.93$ min, Purity= 91.42%.

1H NMR (500 MHz, D_2O) δ 1.1 – 1.3 (m, 3H), 1.3 (h, $J = 7.6$ Hz, 3H), 1.4 – 1.5 (m, 2H), 1.5 (m, 4H), 1.6 (d, $J = 7.1$ Hz, 1H), 1.7 (m, 2H), 1.8 – 2.0 (m, 4H), 2.0 – 2.2 (m, 1H), 2.2 – 2.3 (m, 2H), 2.3 (m, 2H), 2.4 – 2.6 (m, 3H), 2.7 – 3.7 (m, 35H), 3.7 – 4.1 (m, 8H), 4.1 (m, 1H).

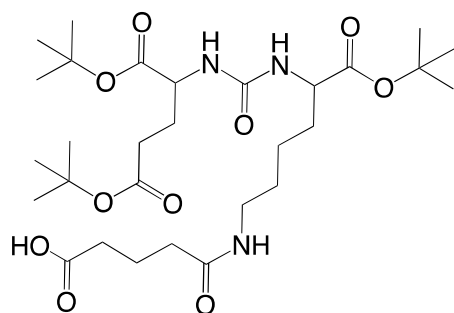
^{13}C NMR (126 MHz, D_2O) δ 16.3, 22.6, 24.5, 24.9, 25.0, 27.6, 27.7, 27.7, 27.8, 27.8, 27.9, 30.6, 32.1, 32.7, 33.6, 33.7, 33.7, 35.1, 35.2, 37.1, 38.0, 38.1, 38.5, 38.6, 39.0, 40.2, 40.3, 40.3, 50.8, 53.9, 55.5, 56.4, 56.6, 63.8, 112.8, 115.1, 117.4, 162.7, 163.0, 174.5, 174.9, 175.2, 177.0.

Elemental Analysis:

Calculated for $C_{50}H_{85}N_{11}O_{18}S_2 \cdot 4.TFA$ (%): C: 42.26, H: 5.44, N:9.35, S:3.89.

Observed (%): C: 42.49, H: 6.50, N: 9.95, S: 3.95.

PSMA(tBu)₃-Glutarate (**16**)



Chemical Formula: C₂₉H₅₁N₃O₁₀

Molecular Weight: 601.74

PSMA(tBu)₃ (600mg, 1.23mmol) was weighed into a 250mL round bottom flask and was dissolved in 6mL of anhydrous acetonitrile, to which was added DIPEA (0.43mL, 2.46mmol) and the reaction was stirred for 5min. Glutaric anhydride (215mg, 1.85 mmol) was weighed into glass tube and added directly into the PSMA solution and the reaction mixture was stirred for 1h at room temperature, the product formation was verified by LC-MS. The reaction mixture was evaporated at 35°C to get a brownish residue which was purified by flash chromatography (C18) using water and acetonitrile as eluents to get a translucent product (Yield: 560 mg, 76%).

HRMS: Calculated for C₂₉H₅₁N₃O₁₀:602.364 [M+H]⁺; Obtained: m/z = 602.364 [M+H]⁺, 624.345 [M+Na]⁺

HPLC: t_R= 4.52min, Purity= 90.12%

¹H NMR (500 MHz, CDCl₃-d) δ 1.1 – 1.6 (m, 31H), 1.6 – 1.8 (m, 1H), 1.9 (hd, *J* = 6.9, 4.2 Hz, 2H), 1.9 – 2.0 (m, 1H), 2.1 – 2.5 (m, 5H), 2.9 – 3.1 (m, 1H), 3.3 (m, 1H), 3.6 (hept, *J* = 6.7 Hz, 1H), 4.0 – 4.5 (m, 2H), 5.8 (d, *J* = 8.3 Hz, 1H), 6.0 (d, *J* = 8.0 Hz, 1H), 6.7 – 7.0 (m, 1H), 7.9 – 9.0 (m, 1H).

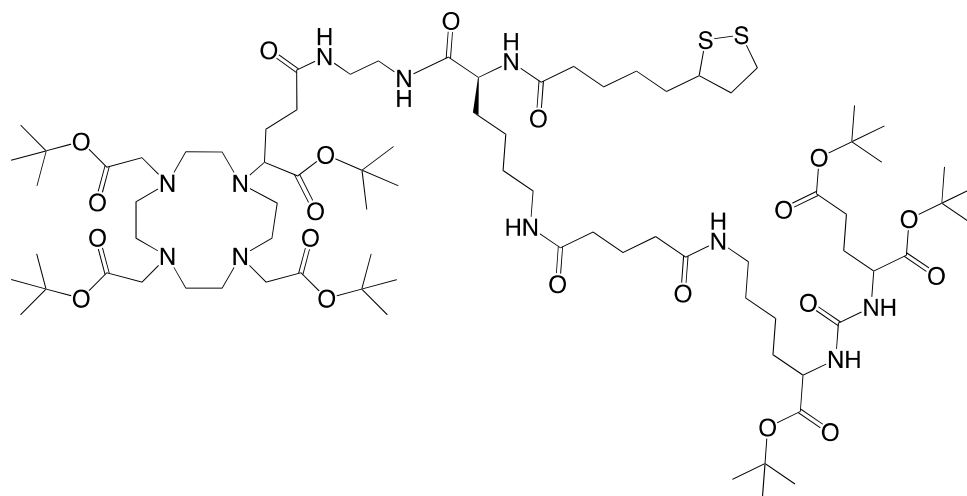
¹³C NMR (126 MHz, CDCl₃) δ 11.8, 18.4, 22.0, 22.2, 28.1, 28.2, 28.7, 31.8, 32.0, 32.4, 34.8, 35.8, 38.9, 41.4, 52.4, 52.9, 53.3, 80.8, 81.4, 82.0, 158.0, 172.7, 172.8, 173.2, 173.5, 177.7.

Elemental Analysis:

Calculated for C₂₉H₅₁N₃O₁₀ (%): C: 57.89, H: 8.54, N: 6.98.

Observed (%): C: 56.83, H: 9.28, N: 7.35.

DOTAGA(tBu)₄-Lys-TA-Glu-PSMA(tBu)₃ (**17**)



Chemical Formula: C₈₀H₁₄₃N₁₁O₂₀S₂
Molecular Weight: 1643.20

PSMA(tBu)₃-Glutarate (400mg, 0.66mmol) was weighed into a 100mL round bottom flask and dissolved in 10mL of ACN and DIPEA (0.12mL, 0.66mmol) and the solution was stirred at room temperature for 10 min. TSTU (205mg, 0.66mmol) was added into above solution and reaction stirred at room temperature for 30min following which the reaction was verified by LC-MS. DOTAGA(tBu)₄-Lys-TA-NH₂ (705mg) was weighed into a 100mL round bottom flask and dissolved in 10mL of acetonitrile and DIPEA (0.59mL, 3.33mmol) and pipetted slowly into activated PSMA(tBu)₃-Glutarate solution. The reaction was stirred for 1h and the peptide coupling was verified by LC-MS. The solvent was evaporated off to get a viscous residue that was purified by flash chromatography (C18) using water (0.1%TFA) and acetonitrile (0.1%TFA) as eluent to get a white powder as a TFA salt (Yield: 1.05g, 75%).

HRMS: Calculated for C₈₀H₁₄₃N₁₁O₂₀S₂:1643.002 [M+H]⁺; Obtained: m/z = 1643.008 [M+H]⁺, 1664.985 [M+Na]⁺.

HPLC: t_R= 5.08min, Purity= 95.85%

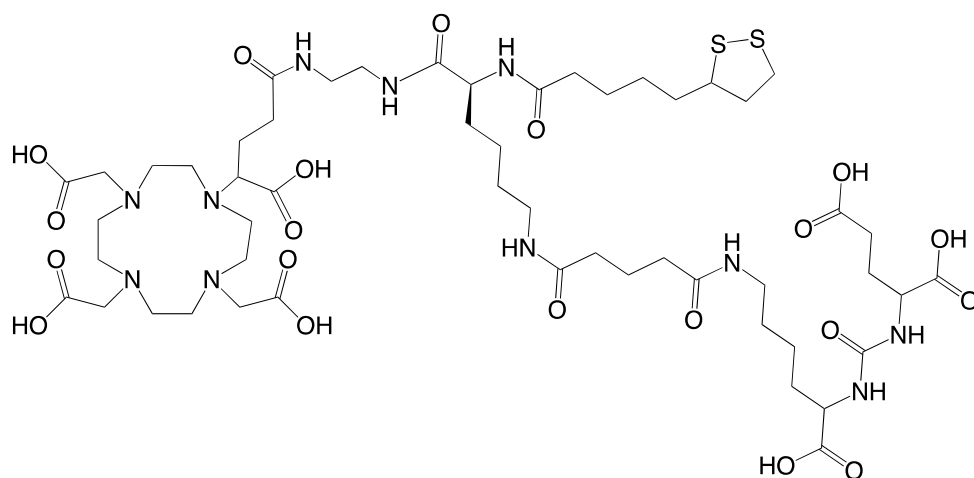
¹H NMR (500 MHz, CDCl₃-d) δ 1.1 – 1.6 (m, 72H), 1.6 (m, 5H), 1.7 – 1.8 (m, 4H), 1.8 – 1.9 (m, 2H), 1.9 (m, 3H), 2.1 (m,2H), 2.2 (s, 1H), 2.2 – 2.3 (m, 5H), 2.3 (m, 3H), 2.4 – 2.7 (m, 5H), 2.7 – 4.5 (m, 39H).

¹³C NMR (126 MHz, CDCl₃) δ 17.8, 22.2, 22.7, 25.6, 28.2, 28.2, 28.3, 28.4, 28.9, 29.1, 31.9, 34.8, 35.4, 36.0, 38.6, 38.9, 40.5, 53.2, 53.6, 53.9, 56.7, 80.7, 81.5, 82.0, 113.1, 115.4, 117.8, 120.1, 158.1, 161.1, 161.3, 161.6, 172.6, 172.9, 173.1, 173.7.

Elemental Analysis:

Calculated for C₄₈H₆₅N₇O₁₂. 4.TFA (%): C: 50.35, H: 7.06, N:7.34, S:3.05.
Observed (%): C: 49.48, H: 7.69, N: 7.92, S: 2.47.

DOTAGA-Lys-TA-Glu-PSMA (18)



Chemical Formula: $C_{52}H_{87}N_{11}O_{20}S_2$

Molecular Weight: 1250.45

DOTAGA(tBu)₄-Lys-TA-Glu-PSMA(tBu)₃ (1g) was weighed into a 50mL round bottom flask and was dissolved in 12.5mL of TFA and 12.5mL of dichloromethane. The solution was stirred at room temperature for 24h, following which the reaction was deemed complete as verified by LC-MS. The solvents were evaporated to get a viscous residue which was purified by flash chromatography (C18) using water (0.1%TFA) and ACN (0.1%TFA) as eluents to get a white powder (Yield: 240mg, 34%).

HRMS: Calculated for $C_{52}H_{87}N_{11}O_{20}S_2$:1250.564 $[M+H]^+$; Obtained: $m/z = 1250.568$ $[M+H]^+$, 1272.542 $[M+Na]^+$

HPLC: $t_R = 3.01$ min, Purity= 99.01%

1H NMR (500 MHz, D₂O) δ 1.2 (t, $J = 7.3$ Hz, 4H), 1.2 – 1.4 (m, 6H), 1.4 – 1.5 (m, 4H), 1.5 – 1.6 (m, 4H), 1.6 – 1.7 (m, 3H), 1.7 – 1.8 (m, 3H), 1.8 – 2.0 (m, 4H), 2.0 – 2.1 (m, 1H), 2.2 (t, $J = 7.5$ Hz, 4H), 2.2 (td, $J = 7.2, 2.5$ Hz, 2H), 2.4 (m, 5H), 2.8 – 4.0 (m, 37H), 4.0 – 4.2 (m, 3H).

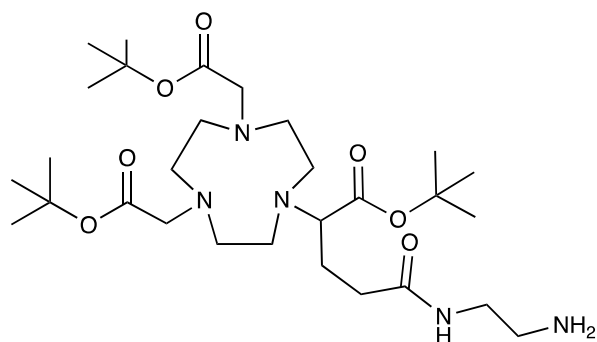
^{13}C NMR (126 MHz, D₂O) δ 22.0, 22.3, 22.6, 24.9, 25.0, 26.3, 27.8, 27.9, 27.9, 30.1, 30.6, 30.7, 33.7, 33.8, 35.0, 35.1, 35.2, 38.1, 38.5, 38.6, 39.0, 40.3, 40.3, 42.2, 52.6, 53.2, 53.9, 56.6, 115.1, 117.5, 159.2, 174.5, 175.5, 175.5, 176.2, 176.9, 177.1, 177.2.

Elemental Analysis:

Calculated for $C_{48}H_{65}N_7O_{12}$. 2.TFA (%): C: 45.49, H: 6.07, N:10.42, S: 4.34.

Observed (%): C: 45.36, H: 7.03, N: 10.87, S: 3.62.

NODAGA(tBu)₃-NH₂ (**19**)



Chemical Formula: C₂₉H₅₅N₅O₇
Molecular Weight: 585.79

NODAGA(tBu)₃ (1g, 1.84 mmol) was weighed into a 100mL round bottom flask and dissolved in 10mL of ACN under the hood with stirring. 1.3mL of DIPEA (0.97g, 7.36 mmol) was added first to the above solution followed by coupling agents viz. HBTU (0.75g, 1.93 mmol) and HOBt (0.26g, 1.93mmol), and the solution was left for stirring at room temperature for 10-15min. Ethylenediamine was dissolved in about 10mL of ACN and added to the NODAGA-GA(tBu)₃ solution and stirred further at room temperature for 1h. The solution was evaporated at 35°C to remove ACN. The residue was dissolved in 50mL of DCM and sequentially extracted with 50mL each of citric acid solution (pH 3), NaHCO₃ (5%) and finally water using a separating funnel to remove water soluble components. The organic phase was dried over MgSO₄, filtered and evaporated to get yellowish residue which was purified by reverse phase (C18) flash chromatography using water (0.1%TFA) and acetonitrile (0.1%TFA) as eluents. The product was recovered as a white solid in form of TFA salt (Yield: 1134 mg, 68%).

ESI-MS: Calculated for C₂₉H₅₅N₅O₇: 585.41; Obtained: m/z = 586.24 [M+H]⁺.

HRMS: Calculated for C₂₉H₅₅N₅O₇: 586.417 [M+H]⁺; Obtained: m/z = 586.419 [M+H]⁺

HPLC: t_R= 3.84min, Purity= 97.55%

¹H NMR (500 MHz, CDCl₃-d) δ 1.5 (m, 27H), 1.9 – 2.2 (m, 2H), 2.4 (t, *J* = 7.3 Hz, 2H), 2.8 – 3.9 (m, 22H).

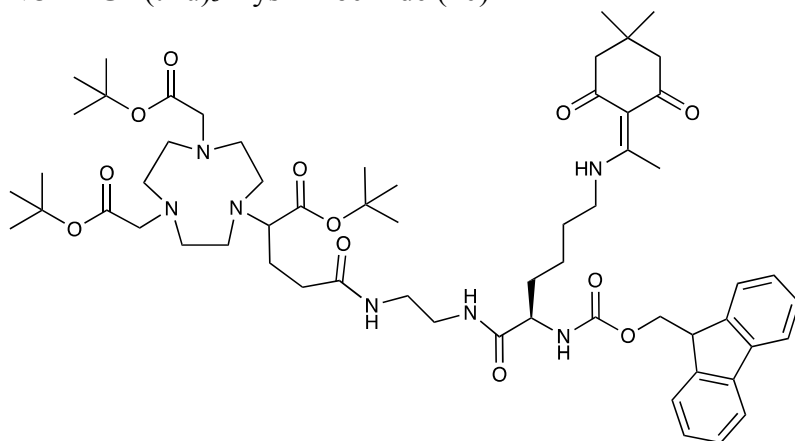
¹³C NMR (126 MHz, CDCl₃-d) δ 17.9, 21.5, 27.0, 27.6, 29.7, 30.2, 33.5, 38.3, 38.6, 38.9, 43.0, 45.8, 49.6, 50.7, 51.6, 53.0, 53.1, 54.0, 56.2, 61.8, 108.2, 169.9, 170.0, 174.9, 175.6, 175.7.

Elemental Analysis:

Calculated for C₂₉H₅₅N₅O₇. 2.8TFA (%): C: 45.92, H: 6.44, N: 7.74.

Observed (%): C: 45.31, H: 6.30, N: 7.55.

NODAGA(tBu)₃-Lys-Fmoc-Dde (**20**)



Chemical Formula: C₆₀H₈₉N₇O₁₂

Molecular Weight: 1099.66

Lysine-Fmoc-Dde-OH (550mg, 1.033 mmol) was dissolved in 10mL of acetonitrile (ACN) in a 50mL round bottom flask to which DIPEA (0.37 mL, 2.065mmol) was added dropwise followed by addition of TSTU (349mg, 1.136mmol). The reaction was left to stir at room temperature for 1h. NODAGA(tBu)₃-NH₂ (805 mg) was dissolved in 10mL of acetonitrile and DIPEA (1.1 mL, 6.193 mmol), stirred for 5min and added into the activated lysine solution. The reaction mixture was left to stir at room temperature for 2h. The reaction mixture was evaporated at 35°C to remove acetonitrile to get a white residue, which was dissolved in 50mL of chloroform. The chloroform solution was mixed with 50mL of water to extract the water-soluble components in a separating funnel. The organic layer was recovered and evaporated off to get a viscous residue which was purified by reverse phase (C18) flash chromatography using water (0.1%TFA) and acetonitrile (0.1%TFA) as eluents. The product was recovered as a white solid in form of TFA salt (Yield: 580 mg, 44%).

ESI-MS (m/z): Calculated for C₆₀H₈₉N₇O₁₂:1099.66; Obtained: m/z = 551.03 [M+H]²⁺.

HRMS: Calculated for C₆₀H₈₉N₇O₁₂:1100.664 [M+H]⁺; Obtained: m/z = 1100.667 [M+H]⁺

HPLC: t_R = 5.24min, Purity = 97.51%

¹H NMR (500 MHz, CDCl₃-d) δ 13.39 (t, *J* = 5.3 Hz, 1H), 8.11 (m, 2H), 7.81 – 7.70 (m, 3H), 7.68 – 7.52 (m, 2H), 7.45 – 7.35 (m, 2H), 7.32 (tt, *J* = 7.4, 1.3 Hz, 2H), 4.81 – 3.90 (m, 7H), 3.87 – 3.54 (m, 2H), 3.54 – 3.28 (m, 12H), 3.27 – 2.78 (m, 9H), 2.55 (s, 3H), 2.45 (t, *J* = 7.2 Hz, 2H), 2.36 (d, *J* = 6.1 Hz, 5H), 2.16 (m, 1H), 2.08 – 1.99 (m, 1H), 1.97 – 1.83 (m, 1H), 1.80 – 1.64 (m, 4H), 1.56 – 1.37 (m, 27H), 1.02 (s, 6H).

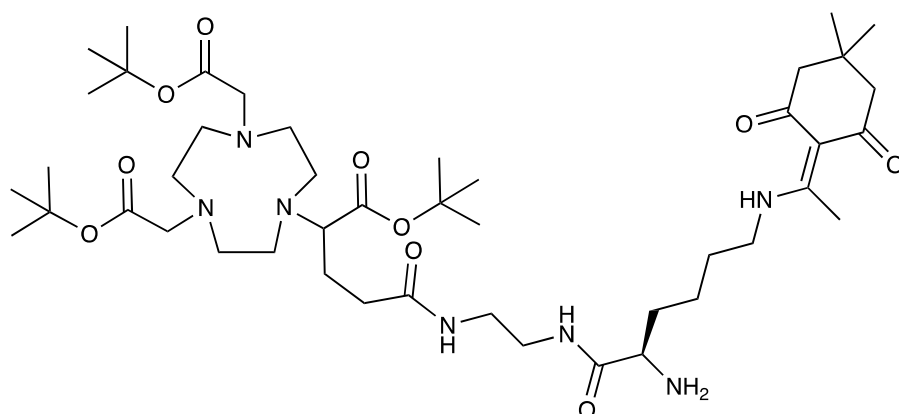
¹³C NMR (126 MHz, CDCl₃) δ 18.0, 22.9, 25.1, 28.0, 28.0, 28.2, 28.5, 30.1, 32.6, 39.3, 43.3, 47.1, 52.6, 54.8, 55.9, 67.1, 76.8, 77.0, 77.3, 83.2, 107.7, 115.1, 117.4, 119.9, 125.3, 127.1, 127.7, 141.2, 143.9, 160.9, 161.2, 170.4, 170.5, 173.8, 180.4, 198.0.

Elemental Analysis:

Calculated for C₂₉H₅₅N₅O₇ · 1.5TFA (%): C: 59.51, H: 7.17, N:7.71.

Observed (%): C: 59.39, H: 7.14, N:7.70.

NODAGA(tBu)₃-Lys-Dde-NH₂ (**21**)



Chemical Formula: C₄₅H₇₉N₇O₁₀

Molecular Weight: 877.59

NODAGA(tBu)₃-Lysine-Fmoc-Dde (172mg) was dissolved in 10mL of diethylamine and 10mL of dichloromethane in 100mL flask and the reaction mixture was stirred for 2h. The solvents were evaporated at 35°C to get the light brownish residue which was purified by reverse phase (C18) flash chromatography using water (0.1%TFA) and acetonitrile (0.1%TFA) as eluents. The product was recovered as a white solid in form of TFA salt (Yield: 90 mg, 48%).

ESI-MS (m/z): Calculated for C₄₅H₇₉N₇O₁₀:877.59; Obtained: 439.75 [M+H]²⁺ and 878.5 [M+H]⁺.

HRMS: Calculated for C₄₅H₇₉N₇O₁₀:878.596 [M+H]⁺; Obtained: m/z = 878.598 [M+H]⁺

HPLC: t_R = 4.13min, Purity = 97.86%

¹H NMR (500 MHz, CDCl₃-d) δ 0.9 (s, 6H), 1.4 (m, 27H), 1.6 (p, *J* = 7.1 Hz, 2H), 1.9 (t, 2H), 2.3 (s, 3H), 2.4 (t, *J* = 7.2 Hz, 1H), 2.5 (s, 2H), 2.7 – 2.9 (m, 1H), 3.0 (d, 7H), 3.1 – 3.2 (m, 3H), 3.2 – 3.5 (m, 4H), 3.5 – 3.6 (m, 1H), 3.9 (t, *J* = 6.9 Hz, 1H), 8.6 (d, *J* = 6.8 Hz, 1H), 9.7 (s, 1H).

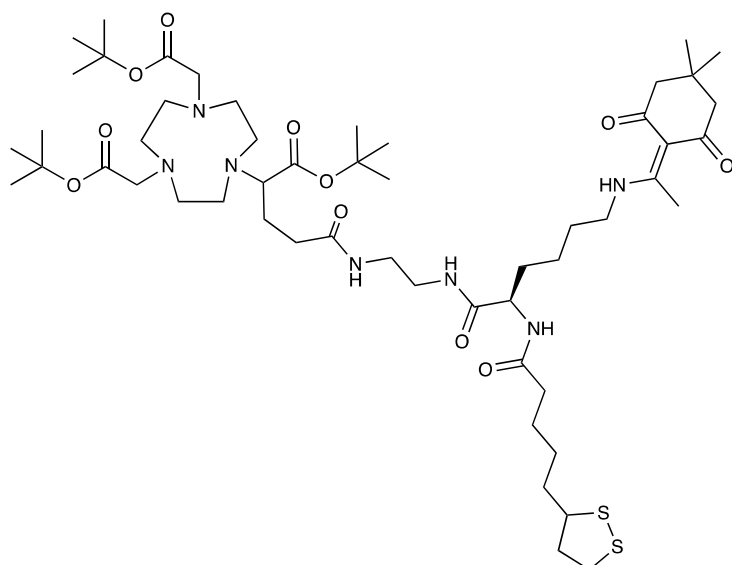
¹³C NMR (126 MHz, CDCl₃) δ 17.9, 22.2, 24.6, 28.0, 28.1, 28.2, 30.1, 30.6, 32.4, 39.3, 43.0, 52.8, 53.8, 55.9, 63.5, 77.6, 83.3, 107.8, 115.5, 117.8, 161.7, 161.9, 169.3, 173.0, 173.8, 189.8, 197.8.

Elemental Analysis:

Calculated for C₂₉H₅₅N₅O₇ · 2.8TFA (%): C: 50.76, H: 6.89, N:8.19.

Observed (%): C: 50.79, H: 7.42, N:8.32.

NODAGA(tBu)₃-Lys-TA-Dde (**22**)



Chemical Formula: C₅₃H₉₁N₇O₁₁S₂

Molecular Weight: 1065.62

NODAGA(tBu)₃-Lys-Dde-NH₂ (90mg) was taken into a 100mL round bottom flask. 3 mL of acetonitrile and DIPEA (0.071mL, 0.398 mmol) was added to the above solution which was stirred for 5min. Thioctic acid-NHS ester (31mg, 0.1 mmol) was weighed into glass tube and added into above solution which was stirred at room temperature for 1h. The reaction mixture was evaporated to remove the excess solvents to get the yellowish residue/concentrate. This residue was purified by reverse phase (C18) flash chromatography using water (0.1%TFA) and acetonitrile (0.1%TFA) as eluents. The product was recovered as a yellowish white solid in form of of TFA salt (Yield: 80 mg, 81%).

ESI-MS (m/z): Calculated for C₅₃H₉₁N₇O₁₁S₂:1065.62; Obtained: 534.04 [M+H]²⁺.

HRMS: Calculated for C₅₃H₉₁N₇O₁₁S₂:1066.629 [M+H]⁺; Obtained: m/z = 1066.629 [M+H]⁺

HPLC: t_R = 5.05min, Purity = 93.29%

¹H NMR (500 MHz, CDCl₃-d) δ 0.9 – 1.0 (s, 6H), 1.1 – 1.2 (m, 2H), 1.3 – 1.5 (m, 32H), 1.5 – 1.7 (m, 5H), 1.7 – 1.9 (m, 2H), 2.0 – 2.1 (m, 1H), 2.2 – 2.2 (t, *J* = 7.6 Hz, 2H), 2.3 – 2.3 (s, 4H), 2.3 – 2.4 (m, 2H), 2.5 – 2.5 (s, 3H), 3.0 – 3.0 (s, 19H), 3.0 – 3.1 (m, 2H), 3.2 – 3.3 (m, 2H), 3.3 – 3.4 (m, 2H), 3.4 – 3.5 (m, 1H), 3.6 – 3.8 (m, 4H), 7.9 – 8.0 (t, *J* = 5.3 Hz, 2H).

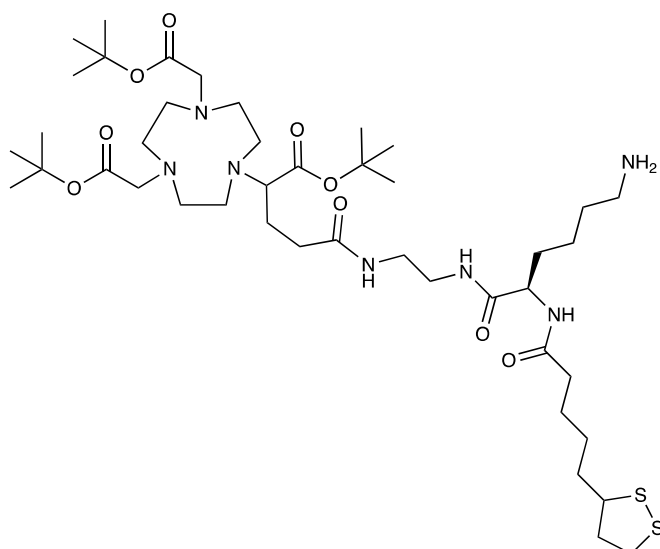
¹³C NMR (126 MHz, CDCl₃) δ 18.0, 18.4, 23.1, 24.9, 25.4, 28.1, 28.1, 28.3, 28.5, 28.9, 30.1, 31.9, 32.4, 34.6, 35.9, 38.4, 39.1, 39.4, 40.2, 43.3, 52.7, 55.9, 56.5, 58.5, 63.7, 83.4, 84.4, 107.7, 170.2, 172.9, 173.8, 197.9, 200.1.

Elemental Analysis:

Calculated for C₂₉H₅₅N₅O₇. 2.1TFA (%): C: 52.61, H: 7.19, N:7.51, S:4.91.

Observed (%): C: 51.21, H:7.36, N:7.89, S:3.92.

NODAGA(tBu)₃-Lys-TA-NH₂ (**23**)



Chemical Formula: C₄₃H₇₉N₇O₉S₂

Molecular Weight: 901.54

NODAGA(tBu)₃-Lys-TA-Dde (400mg) was weighed into 100mL round bottom flask and dissolved in 5mL of DMF. Imidazole (774mg, 11.26 mmol) and hydroxylamine hydrochloride (782mg, 11.26 mmol) were added into the above solution. The reaction was stirred at room temperature for 30min and the solvent was evaporated partially to remove DMF at 35°C to a brownish concentrate. This concentrate was purified by reverse phase (C18) flash chromatography using water (0.1%TFA) and acetonitrile (0.1%TFA) as eluents. The product was recovered as a yellowish white solid (Yield: 200 mg, 52%).

ESI-MS (m/z): Calculated for C₄₃H₇₉N₇O₉S₂: 901.54; Obtained: 451.75 [M+H]²⁺.

HRMS: Calculated for C₄₃H₇₉N₇O₉S₂:902.545 [M+H]⁺; Obtained: m/z = 902.547 [M+H]⁺

HPLC: t_R= 4.17min, Purity= 96.76%

¹H NMR (500 MHz, CDCl₃-d) δ 1.1 – 1.3 (m, 1H), 1.4 (d, *J* = 5.2 Hz, 32H), 1.5 – 1.8 (m, 9H), 1.8 (m, 1H), 2.0 (m, 2H), 2.2 (t, *J* = 7.6 Hz, 2H), 2.2 – 2.5 (m, 4H), 2.7 – 3.8 (m, 34H), 4.3 (q, *J* = 7.2 Hz, 1H), 7.4 (m, 1H), 7.8 (d, *J* = 5.5 Hz, 1H), 8.0 (d, *J* = 5.8 Hz, 1H).

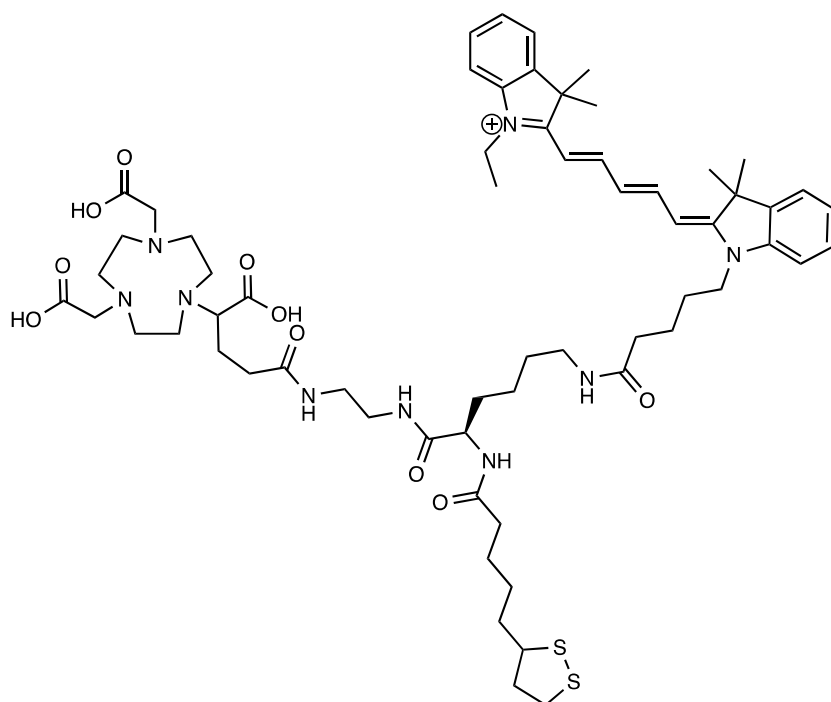
¹³C NMR (126 MHz, CDCl₃) δ 22.0, 24.6, 25.1, 25.3, 26.5, 28.0, 28.1, 28.8, 31.8, 32.6, 33.5, 34.5, 34.6, 35.9, 38.4, 38.5, 39.0, 39.2, 39.3, 40.2, 53.3, 56.4, 56.5, 56.5, 63.4, 83.0, 115.4, 117.8, 161.4, 161.7, 170.9, 172.9, 173.0, 173.8. CDCl₃

Elemental Analysis:

Calculated for C₂₉H₅₅N₅O₇. 3.2TFA (%): C: 46.83, H: 6.54, N:7.74, S:5.06.

Observed (%): C: 46.83, H:7.31, N:7.89, S:4.82.

NODAGA-Lys-TA-Cy5 (**24**)



Chemical Formula: $C_{43}H_{79}N_7O_9S_2$

Molecular Weight: 901.54

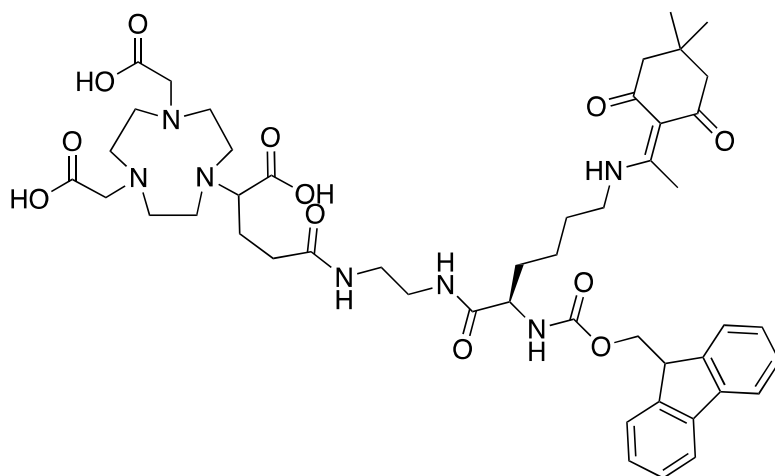
Cy5 (18.06mg, 33 μ mol) was weighed into a 50mL round bottom flask and dissolved in 1mL of acetonitrile containing DIPEA (12 μ L, 67 μ mol). The solution was stirred for 5min followed by addition of TSTU (10.2 mg, 33 μ mol). The reaction was left stirring at room temperature for 30min. NODAGA(tBu)₃-Lys-TA-NH₂(43mg) was weighed in a glass tube and was dissolved in 1mL of ACN and of DIPEA (24 μ L, 133 μ mol). This solution was added into the dye solution and the reaction was stirred at room temperature for 4h. The solution was evaporated to remove the solvents at room temperature. The residue was dissolved in 1mL of DCM and 1mL of TFA and the reaction was stirred at room temperature for 6h to effect deprotection of NODAGA moiety. The solvents were evaporated and the residue was purified by semi-prep HPLC using water (0.1%TFA) and ACN (0.1%TFA) as eluents. The product was recovered as a dark blue powder (10 mg, 20%).

ESI-MS (m/z): Calculated for $C_{64}H_{94}N_9O_{10}S_2$: 1212.66 ; Obtained: 606.89 [M+H]²⁺.

HRMS: Calculated for $C_{64}H_{94}N_9O_{10}S_2$:1212.655 [M+H]⁺; Obtained: m/z = 1212.658 [M+H]⁺

HPLC: t_R = 4.67min, Purity= 94.63%

NODAGA-Lys-Fmoc-Dde (**25**)



Chemical Formula: C₄₈H₆₅N₇O₁₂

Molecular Weight: 932.09

Lysine-Fmoc-Dde (2.68g, 5.03mmol) was weighed into a 100mL round bottom flask and solubilized in 16mL of DMF, this was followed by addition of DIPEA (0.9mL, 5.03mmol) and stirring for 5min. TSTU (1.55g, 5.03mmol) was added to the above reaction mixture and reaction stirred for 30min. the NHS ester formation was confirmed by LC-MS. NODAGA-NH₂ (2g, 4.8mmol) was weighed into glass tube and dissolved into DMF: Water - 12mL:4mL and DIPEA (3.4mL, 19.2mmol). The above solution was pipetted into the activated lysine solution and the reaction was left stirred at room temperature for 1h. The solvents were evaporated at 40°C for 30min to get a pale yellow viscous solution that was purified by flash chromatography (C18) using water (0.1%TFA) and acetonitrile (0.1%TFA) as eluents to get a white powder (Yield:3.6 g, 68%).

HRMS: Calculated for C₄₈H₆₅N₇O₁₂:932.476 [M+H]⁺; Obtained: m/z = 932.475 [M+H]⁺

HPLC: t_R= 4.12min, Purity= 99.45%

¹H NMR (300 MHz, MeOD-d₄) δ 1.0 (s, 6H), 1.3 – 2.2 (m, 8H), 2.3 (d, 6H), 2.5 (s, 3H), 2.7 – 3.3 (m, 12H), 3.4 – 4.1 (m, 8H), 4.2 (d, *J* = 6.7 Hz, 1H), 4.3 (dd, *J* = 10.5, 6.7 Hz, 1H), 4.5 (m, 1H), 7.2 – 7.5 (m, 4H), 7.7 (dd, *J* = 7.4, 3.9 Hz, 2H), 7.8 (d, *J* = 7.4 Hz, 2H).

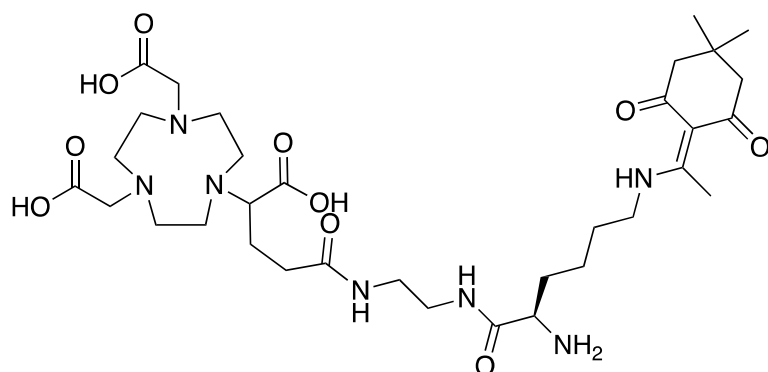
¹³C NMR (75 MHz, MeOD-d₄) δ 18.5, 24.2, 26.4, 28.4, 29.4, 31.0, 32.6, 33.7, 44.3, 53.3, 56.4, 64.5, 67.9, 108.6, 116.1, 119.9, 121.0, 126.3, 128.2, 128.9, 142.6, 145.2, 145.3, 158.6, 162.4, 162.8, 175.1, 175.2, 175.5, 175.5, 199.9.

Elemental Analysis:

Calculated for C₄₈H₆₅N₇O₁₂. 1.5TFA (%): C, 55.53; H, 6.08; N, 8.89.

Observed (%): C: 55.48, H: 6.85, N: 8.89.

NODAGA-Lys-Dde-NH₂ (**26**)



Chemical Formula: C₃₃H₅₅N₇O₁₀

Molecular Weight: 709.84

500mg of NODAGA-Lys-Fmoc-Dde was weighed into a 100mL round bottom flask and dissolved in 5mL of methanol. Diethylamine (5mL) was added into the above solution and the solution was stirred at room temperature for 5-10min, the reaction was deemed complete as verified by LC-MS. The solution was evaporated at 30°C to remove methanol/DEA to get a viscous brownish residue. This residue was purified by flash chromatography (C18) using water (0.1%TFA) and acetonitrile (0.1%TFA) as eluents to get a white powder as a TFA salt (Yield: 480 mg, 95%).

HRMS: Calculated for C₃₃H₅₅N₇O₁₀:710.408 [M+H]⁺; Obtained: m/z = 710.409 [M+H]⁺

HPLC: t_R= 2.76min, Purity= 98.72%

¹H NMR (500 MHz, MeOD) δ 1.0 (s, 6H), 1.5 (dq, *J* = 9.7, 7.7, 7.2 Hz, 2H), 1.7 (p, *J* = 7.0 Hz, 2H), 1.7 – 1.9 (m, 2H), 1.9 – 2.0 (m, 1H), 2.0 – 2.1 (m, 1H), 2.3 (s, 4H), 2.3 – 2.4 (m, 2H), 2.5 (s, 3H), 2.7 – 3.3 (m, 12H), 3.3 – 3.4 (m, 3H), 3.5 (t, *J* = 6.9 Hz, 2H), 3.6 (t, *J* = 7.2 Hz, 1H), 3.6 – 4.1 (m, 5H).

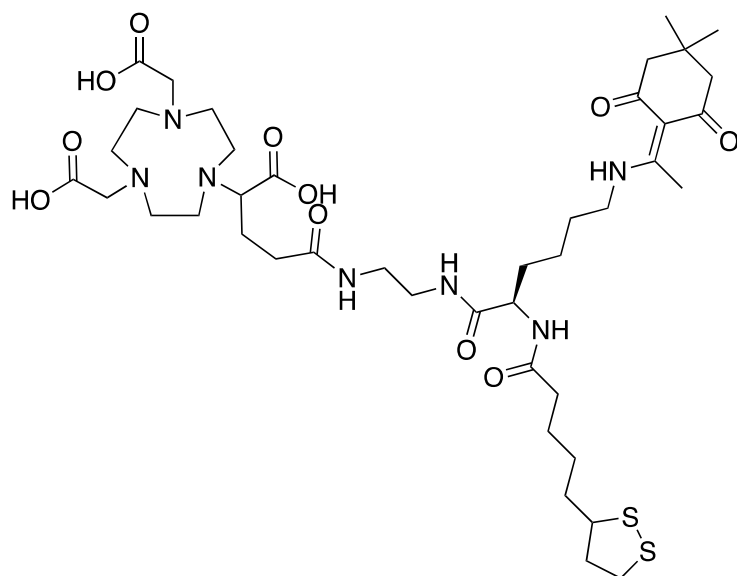
¹³C NMR (126 MHz, MeOD) δ 18.4, 23.3, 26.5, 28.4, 29.5, 31.1, 32.1, 33.7, 39.9, 40.3, 44.0, 53.4, 54.4, 64.5, 108.7, 116.4, 118.7, 161.7, 162.0, 170.3, 175.1, 175.5, 175.6, 199.9.

Elemental Analysis:

Calculated for C₂₉H₅₅N₅O₇ · 3.5TFA (%): C: 43.32; H: 5.32; N: 8.84.

Observed (%): C: 43.34; H: 6.27; N: 9.45.

NODAGA-Lys-TA-Dde (27)



Chemical Formula: $C_{41}H_{67}N_7O_{11}S_2$

Molecular Weight: 898.15

NODAGA-Lys-Dde-NH₂ (1.2g) was taken into a 100mL round bottom flask, to which was added 10 mL of MeOH and DIPEA (1.2mL, 6.8mmol) followed by stirring for 5min. Thioctic acid-NHS (514mg, 1.7mmol) was weighed into glass tube, dissolved in 5mL of ACN and added into above solution which was stirred at room temperature for 3h. The reaction mixture was evaporated to remove the excess of solvents to get the yellowish residue. This residue was further purified by flash chromatography (C18) using water (0.1%TFA) and acetonitrile (0.1%TFA) as eluents to get a white powder after lyophilization (Yield: 980 mg, 80%).

HRMS: Calculated for $C_{41}H_{67}N_7O_{11}S_2$: 898.441 [M+H]⁺; Obtained: m/z = 898.442 [M+H]⁺

HPLC: t_R = 3.76min, Purity = 99.32%

¹H NMR (500 MHz, MeOD-*d*₄) δ 1.2 – 1.5 (m, 4H), 1.5 – 1.7 (m, 7H), 1.7 – 1.8 (m, 2H), 1.9 – 2.0 (m, 1H), 2.0 – 2.1 (m, 2H), 2.2 (td, *J* = 7.3, 1.6 Hz, 2H), 2.3 – 2.4 (m, 3H), 2.6 – 3.2 (m, 16H), 3.4 – 3.6 (m, 2H), 3.6 – 4.0 (m, 4H), 4.2 (m, 1H).

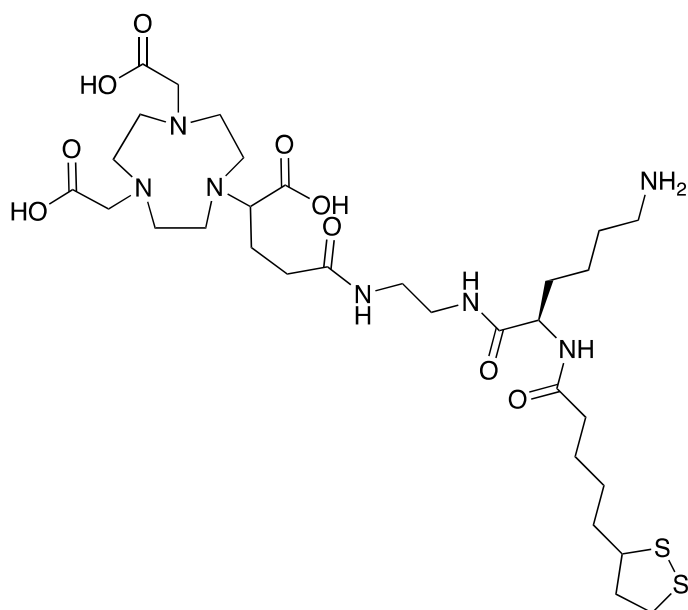
¹³C NMR (126 MHz, MeOD-*d*₄) δ 23.9, 24.2, 26.4, 26.5, 26.5, 28.1, 29.8, 29.9, 30.6, 32.3, 33.7, 35.7, 35.7, 36.5, 36.6, 39.3, 39.9, 40.2, 40.4, 41.3, 41.3, 54.8, 57.6, 64.4, 116.7, 119.0, 120.4, 162.2, 162.5, 162.8, 174.6, 175.1, 175.5, 176.3, 176.3.

Elemental Analysis:

Calculated for $C_{41}H_{67}N_7O_{11}S_2 \cdot 2TFA$ (%): C: 47.99, H: 6.18, N: 8.71, S: 5.69.

Observed (%): C: 47.52, H: 6.64, N: 8.63, S: 5.0.

NODAGA-Lys-TA-NH₂ (**28**)



Chemical Formula: C₃₁H₅₅N₇O₉S₂

Molecular Weight: 733.94

NODAGA-Lys-TA-Dde (800mg) was weighed into a 100mL round bottom flask and dissolved in 10mL of methanol. Imidazole (1.22g, 17.8mmol) and hydroxylamine hydrochloride (1.22g, 17.8mmol) was added into the above solution and few drops of water were added to dissolve them in methanolic solution. The solution was stirred at room temperature for 30min and reaction was deemed complete as verified by LC-MS. The solution was evaporated at 30°C to remove methanol to obtain a viscous whitish residue. This residue was purified by flash chromatography (C18) using water (0.1%TFA) and acetonitrile (0.1%TFA) as eluents to get a white powder after lyophilization (550mg, 72%).

HRMS: Calculated for C₃₁H₅₅N₇O₉S₂:734.357 [M+H]⁺; Obtained: m/z = 734.358 [M+H]⁺

HPLC: t_R= 2.91min, Purity= 93.62%

¹H NMR (500 MHz, MeOD-*d*₄) δ 1.2 – 1.5 (m, 4H), 1.5 – 1.7 (m, 7H), 1.7 – 1.8 (m, 2H), 1.9 – 2.0 (m, 1H), 2.0 – 2.1 (m, 2H), 2.2 (td, *J* = 7.3, 1.6 Hz, 2H), 2.3 – 2.4 (m, 3H), 2.6 – 3.2 (m, 16H), 3.4 – 3.6 (m, 2H), 3.6 – 4.0 (m, 4H), 4.2 (m, 1H).

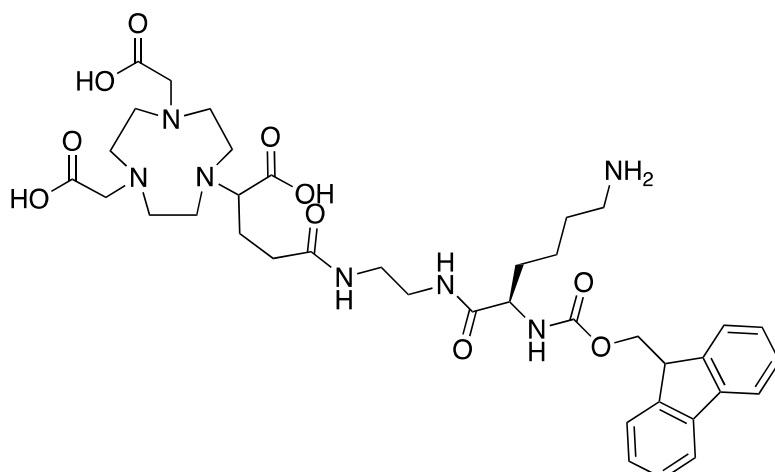
¹³C NMR (126 MHz, MeOD-*d*₄) δ 23.9, 24.2, 26.4, 26.5, 26.5, 28.1, 29.8, 29.9, 30.6, 32.3, 33.7, 35.7, 35.7, 36.5, 36.6, 39.3, 39.9, 40.2, 40.4, 41.3, 41.3, 54.8, 57.6, 64.4, 116.7, 119.0, 120.4, 162.2, 162.5, 162.8, 174.6, 175.1, 175.5, 176.3, 176.3.

Elemental Analysis:

Calculated for C₂₉H₅₅N₅O₇. 3TFA (%): C, 41.30; H, 5.43; N, 9.11; S: 5.96

Observed (%): C: 40.81, H: 6.34, N: 9.21, S: 5.19.

NODAGA-Lys-Fmoc-NH₂ (**29**)



Chemical Formula: C₃₈H₅₃N₇O₁₀

Molecular Weight: 767.88

500mg of NODAGA-Lys-Fmoc-dde was weighed into a 100mL round bottom flask and dissolved in 10mL of methanol. Imidazole (1.1g, 16.1mmol) and hydroxylamine.HCl (1.1g, 16.1mmol) was added into the above solution and few drops of water were added to dissolve them in methanolic solution. The solution was stirred at room temperature for 15min and the reaction was deemed complete as verified by LC-MS. The solution was evaporated at 30°C to remove methanol to get a viscous whitish residue. This residue was purified by flash chromatography (C18) using Water (0.1%TFA) and acetonitrile (0.1%TFA) as eluents to get a white powder as a TFA salt (Yield: 465mg, 94%).

HRMS: Calculated for C₃₈H₅₃N₇O₃:768.392 [M+H]⁺; Obtained: m/z = 768.392 [M+H]⁺

HPLC: t_R= 3.32min, Purity= 100%

¹H NMR (500 MHz, MeOD -d₄) δ 1.1 – 1.4 (m, 2H), 1.6 (m, 3H), 1.7 (m, 1H), 1.9 (m, 1H), 2.0 (m, 1H), 2.3 (m, 2H), 2.6 – 3.2 (m, 15H), 3.4 (t, *J* = 7.2 Hz, 1H), 3.5 – 4.0 (m, 5H), 4.1 (t, *J* = 6.6 Hz, 1H), 4.2 – 4.4 (m, 2H), 7.2 (t, *J* = 7.4 Hz, 2H), 7.3 (t, *J* = 7.4 Hz, 2H), 7.6 (t, *J* = 7.1 Hz, 2H), 7.7 (d, *J* = 7.5 Hz, 2H).

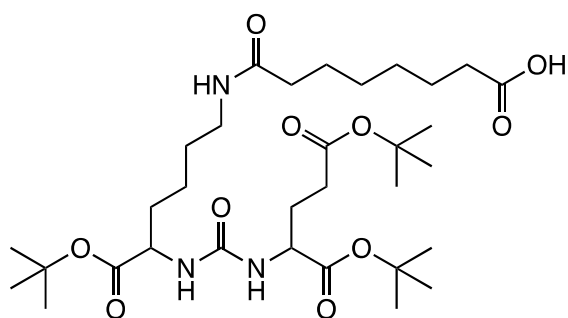
¹³C NMR (126 MHz, MeOD) δ 23.8, 26.4, 28.1, 32.4, 33.7, 39.9, 40.1, 40.5, 56.5, 64.4, 67.9, 114.3, 116.7, 119.0, 121.0, 121.3, 126.2, 128.2, 128.9, 142.6, 142.6, 145.1, 145.3, 158.6, 161.8, 162.1, 162.4, 175.1, 175.5.

Elemental Analysis:

Calculated for C₃₈H₅₃N₇O₃. 3TFA (%): C: 47.61, H: 5.09, N: 8.83

Observed (%): C: 47.63, H: 5.82, N: 9.19.

PSMA(tBu)₃-Suberate (**30**)



Chemical Formula: C₃₂H₅₇N₃O₁₀

Molecular Weight: 643.82

Suberic acid (103mg, 0.69mmol) was weighed into a 50mL round bottom flask to which was added 1mL of ACN, the suberic acid remained undissolved. DIPEA (0.102mL, 0.57mmol) was added into the above solution, which effected the dissolution of suberic acid in ACN. TSTU (176mg, 0.57mmol) was weighed into a glass tube and added directly into the suberic acid solution which was stirred for 30min. The monoester formation was confirmed by LC-MS. PSMA(tBu)₃ (280mg, 0.57mmol) was weighed into a glass tube and was dissolved into 1mL of ACN followed by addition of DIPEA (0.2mL, 1.148mmol). The PSMA solution was pipetted into the activated suberic acid solution. The reaction was stirred for 1h at room temperature and the reaction completion was verified by LC-MS. The solvent was evaporated to obtain a viscous translucent residue that was further purified by flash chromatography (C18) using water and acetonitrile as eluents to get a translucent product (Yield: 200mg, 53%).

HRMS: Calculated for C₃₂H₅₇N₃O₁₀:644.411 [M+H]⁺; Obtained: m/z = 644.414 [M+H]⁺, 666.393 [M+Na]⁺.

HPLC: t_R= 4.77min, Purity= 90.80%

¹³C NMR (126 MHz, CDCl₃) δ 18.4, 22.5, 25.2, 25.6, 28.0, 28.1, 28.5, 28.6, 28.8, 31.7, 32.4, 35.4, 36.3, 38.9, 40.9, 52.3, 53.1, 53.3, 53.4, 80.5, 80.6, 81.5, 81.5, 81.9, 157.6, 172.4, 172.4, 172.7, 172.7, 173.8, 178.2.

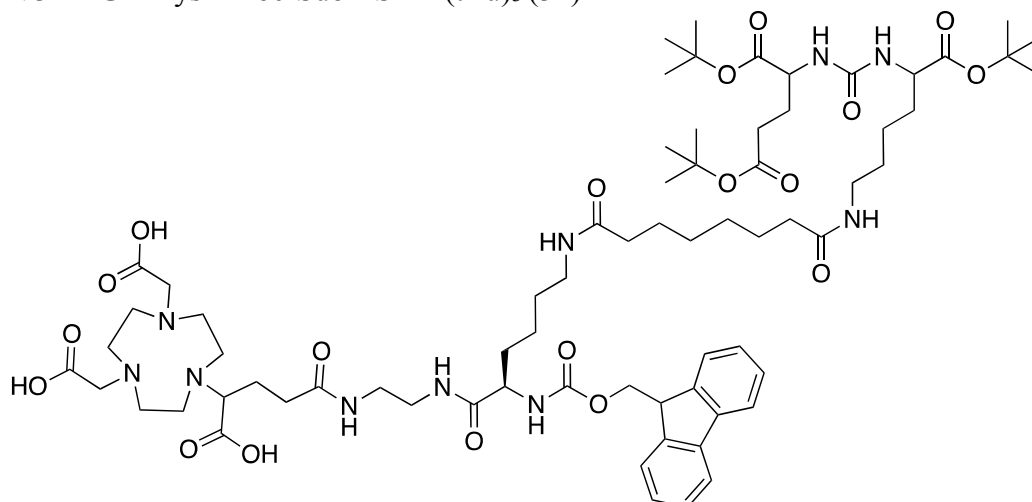
¹H NMR (500 MHz, CDCl₃) δ 1.1 – 1.5 (m, 27H), 1.5 – 1.7 (m, 4H), 1.7 – 1.9 (m, 1H), 2.1 (m, 1H), 2.1 – 2.4 (m, 4H), 3.1 (m, 1H), 3.3 (m, 1H), 4.3 (td, *J* = 8.2, 4.6 Hz, 1H), 5.9 (m, 1H), 6.5 (dq, *J* = 11.3, 5.5 Hz, 1H).

Elemental Analysis:

Calculated for C₃₂H₅₇N₃O₁₀ (%): C: 59.70, H: 8.92, N: 6.53.

Observed (%): C: 59.07, H: 9.35, N: 8.12.

NODAGA-Lys-Fmoc-Sub-PSMA(tBu)₃ (**31**)



Chemical Formula: C₇₀H₁₀₈N₁₀O₁₉

Molecular Weight: 1393.69

PSMA(tBu)₃-Suberate (80mg) was weighed into a glass tube and dissolved in 2mL of ACN and this solution was added into a 50mL round bottom flask. To the above solution was added DIPEA (0.022mL, 0.124mmol) by pipette followed by direct addition of TSTU (38mg, 0.124mmol) weighed previously into a glass tube. The reaction was stirred at room temperature for 30min and the NHS ester formation was verified by LC-MS. NODAGA-Lys-Fmoc-NH₂ (96mg) was weighed into a glass tube and dissolved in 2mL each of acetonitrile and MeOH followed by base treatment with DIPEA (0.044mL, 0.249mmol). This solution was added into activated PSMA(tBu)₃-Suberate solution and the reaction was stirred at room temperature for 2.5h after which the reaction was deemed complete as verified by LC-MS. The residue obtained upon solvent evaporation was purified by flash chromatography (C18) using water (0.1%TFA) and acetonitrile (0.1%TFA) as eluents to get a white product after lyophilization (Yield: 162mg, 87%).

HRMS: Calculated for C₇₀H₁₀₈N₁₀O₁₉:1393.786 [M+H]⁺; Obtained: m/z = 1393.786 [M+H]⁺

HPLC: t_R= 4.77min, Purity= 99.55%

¹H NMR (500 MHz, MeOD-*d*₄) δ 1.3 – 1.3 (m, 2H), 1.3 – 1.5 (m, 27H), 1.5 – 1.6 (m, 2H), 1.6 – 1.7 (m, 3H), 1.7 – 1.9 (m, 2H), 2.0 – 2.1 (m, 1H), 2.2 (s, 8H), 2.3 – 2.4 (m, 2H), 2.8 – 2.9 (m, 1H), 2.9 – 3.1 (m, 2H), 3.1 – 3.3 (m, 8H), 3.4 (m, 1H), 3.5 – 3.7 (m, 2H), 3.7 – 3.8 (m, 2H), 4.0 – 4.3 (m, 2H), 4.4 (m, 1H), 7.2 – 7.9 (m, 4H).

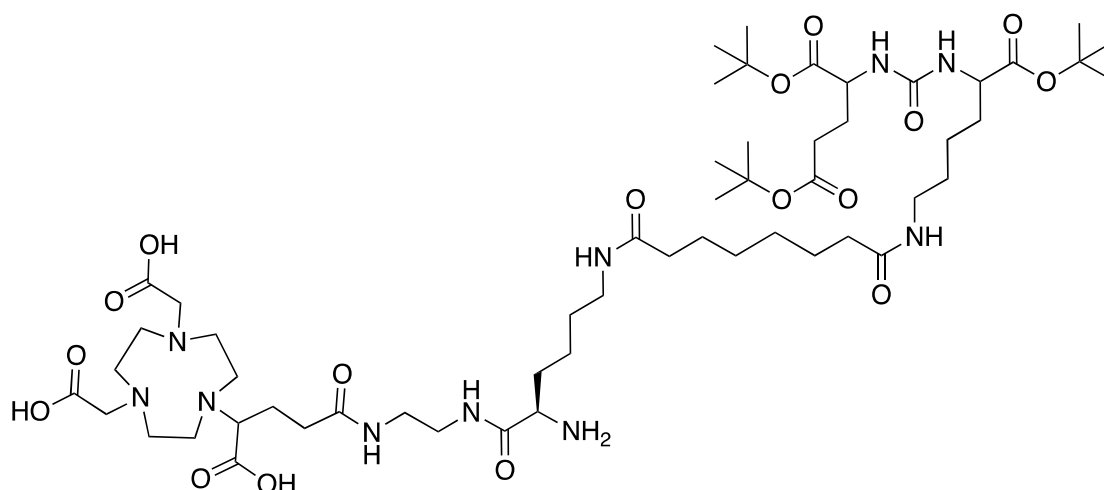
¹³C NMR (126 MHz, MeOD-*d*₄) δ 13.1, 23.9, 24.4, 26.9, 27.2, 28.3, 28.3, 28.3, 29.0, 29.9, 29.9, 30.0, 30.7, 32.5, 33.1, 37.0, 40.0, 40.1, 40.2, 43.6, 48.5, 48.6, 48.8, 49.0, 49.1, 49.3, 49.5, 54.1, 54.8, 55.7, 56.6, 67.8, 68.1, 81.7, 82.5, 82.7, 120.9, 126.3, 128.2, 128.8, 142.5, 158.4, 159.9, 173.4, 173.7, 173.9, 175.2, 175.9, 176.1, 176.1.

Elemental Analysis:

Calculated for C₇₂H₁₀₉N₁₀O₂₁. 0.7TFA (%): C: 58.20, H: 7.44, N: 9.51

Observed (%): C: 58.02, H: 8.44, N: 9.52.

NODAGA-Lys-Sub-PSMA(tBu)₃-NH₂(**32**)



Chemical Formula: C₅₅H₉₈N₁₀O₁₇

Molecular Weight: 1171.44

NODAGA-Lys-Fmoc-Sub-PSMA(tBu)₃ (140mg) was weighed into a glass tube and dissolved in 5mL methanol and added into a 25mL round bottom flask. To the above solution was added 5 mL of diethylamine followed by stirring at room temperature for 30min. The Fmoc deprotection was deemed complete as verified by LC-MS. The residue obtained upon solvent evaporation was purified by flash chromatography (C18) using water (0.1%TFA) and acetonitrile (0.1%TFA) as eluents to get a white product recovered after lyophilization (Yield: 102mg, 67%).

HRMS: Calculated for C₅₅H₉₈N₁₀O₁₇:1193.700 [M+H]⁺; Obtained: m/z = 1193.701 [M+H]⁺

HPLC: t_R = 4.05min, Purity = 98.31%

¹H NMR (500 MHz, MeODI-*d*₄) δ 1.3 – 1.4 (m, 5H), 1.4 – 1.5 (m, 30H), 1.5 – 1.6 (m, 4H), 1.6 – 1.7 (m, 5H), 1.7 – 2.0 (m, 4H), 2.0 – 2.1 (m, 2H), 2.1 – 2.2 (m, 1H), 2.2 (td, *J* = 7.5, 3.4 Hz, 4H), 2.3 – 2.4 (m, 2H), 2.4 – 2.5 (m, 2H), 2.8 – 3.3 (m, 16H), 3.3 – 3.5 (m, 3H), 3.6 (t, *J* = 7.3 Hz, 1H), 3.8 (t, *J* = 6.6 Hz, 1H), 4.1 (dd, *J* = 8.2, 5.2 Hz, 1H), 4.2 (dd, *J* = 8.7, 5.1 Hz, 1H).

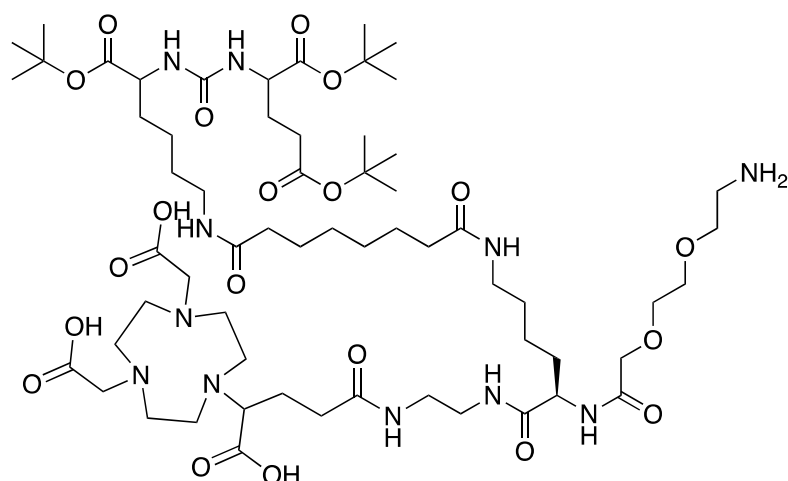
¹³C NMR (126 MHz, MeODI-*d*₄) δ 23.5, 24.2, 26.8, 27.1, 28.5, 28.6, 29.3, 30.2, 30.4, 32.4, 32.7, 33.4, 34.0, 37.3, 40.0, 40.1, 40.3, 40.5, 49.9, 54.4, 54.7, 55.1, 64.8, 82.0, 82.8, 83.1, 116.9, 119.2, 160.2, 162.3, 162.6, 170.7, 173.7, 174.0, 174.2, 175.4, 175.8, 176.4, 176.6.

Elemental Analysis:

Calculated for C₅₅H₉₈N₁₀O₁₇. 3.8TFA (%): C: 46.85; H: 6.39; N: 8.73.

Observed (%): C: 46.89, H: 6.33, N: 8.98.

NODAGA-Lys-Sub-PSMA(tBu)₃-PEG₂-NH₂(**33**)



Chemical Formula: C₆₁H₁₀₉N₁₁O₂₀

Molecular Weight: 1316.60

The Fmoc-PEG₂-COOH (18mg, 0.047mmol) was weighed into a 25mL round bottom flask and was dissolved in 1mL of ACN. DIPEA (0.009mL, 0.051mmol) was added into the above solution and the solution was stirred for 5min followed by addition of TSTU (15mg, 0.049). The reaction was further stirred for 30min and ester formation was verified by LC-MS. NODAGA-Lys-Sub-PSMA(tBu)₃-NH₂ (55mg) was dissolved in 2mL of MeOH and DIPEA (0.033mL, 0.187mmol) and was pipetted into PEG solution. The reaction was stirred for 30min and amide coupling was verified by LC-MS. 1mL of diethylamine was added into above reaction mixture and the reaction was stirred at room temperature for 30min. The deprotection was verified by LC-MS. The solvents were evaporated off and the residue was purified by flash chromatography (C18) using water (0.1%TFA) and acetonitrile (0.1%TFA) as eluents to get a white product after lyophilization (Yield: 48mg, 56%)

HRMS: Calculated for C₆₁H₁₀₉N₁₁O₂₀:1316.792 [M+H]⁺; Obtained: m/z = 1316.793 [M+H]⁺, 1338.773 [M+Na]⁺.

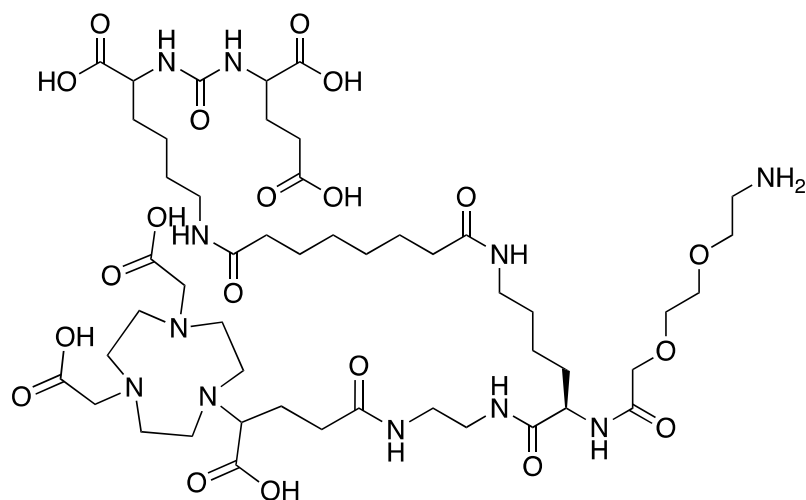
HPLC: t_R= 4.03min, Purity= 92.11%

Elemental Analysis:

Calculated for C₆₁H₁₀₉N₁₁O₂₀. 3.5 TFA(%): C: 47.6; H: 6.61; N: 8.98.

Observed (%): C: 47.26, H: 6.62, N: 8.72.

NODAGA-Lys-Sub-PSMA-PEG₂-NH₂ (**34**)



Chemical Formula: C₄₉H₈₅N₁₁O₂₀

Molecular Weight: 1148.28

NODAGA-Lys-Sub-PSMA(tBu)₃-PEG₂-NH₂ (30mg) was taken in a 25mL round bottom flask to which was added 1mL each of DCM and TFA. The reaction was stirred for 60min at room temperature after which deprotection was confirmed by LC-MS. The solvents were evaporated off at 35°C and 2 times flushed-evaporated with DCM to get a translucent residue which was purified by semi preparative HPLC (C18) using water (0.1%TFA) and acetonitrile (0.1%TFA) as eluents to get a white product. Yield: 20mg, 60%.

HRMS: Calculated for C₄₉H₈₅N₁₁O₂₀: 1148.604 [M+H]⁺; Obtained: m/z = 1148.605 [M+H]⁺.

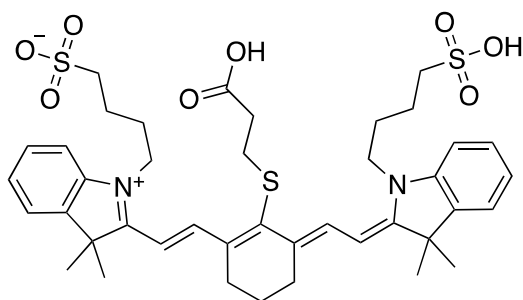
HPLC: t_R = 2.60min, Purity = 96.17%

Elemental Analysis:

Calculated for C₄₉H₈₅N₁₁O₂₀. 3.5TFA. 6H₂O (%): C: 40.63; H: 6.12; N: 9.31.

Observed (%): C: 40.12, H: 6.11, N: 9.51.

IR-783-Propionic Acid (**35**)



Chemical Formula: C₄₁H₅₃N₂O₈S₃

Molecular Weight: 797.05

IR-783 (56mg, 0.067mmol) was weighed into a 25mL round bottom flask to which was added 3mL of MeOH. Triethylamine (0.038mL, 0.267mmol) and 3-Mercaptopropionic acid (0.012mL, 0.133mmol) was pipetted into the dye solution and the reaction was stirred overnight (15h) protected from light in dark. The solvents were evaporated to get a dark green residue which was purified by semi-prep HPLC (C18) using water (0.1%TFA) and acetonitrile (0.1%TFA) as eluents to get a green powder (Yield: 45 mg, 66%).

HRMS: Calculated for C₄₁H₅₃N₂O₈S₃:797.295 [M]⁺; Obtained: m/z = 797.295 [M]⁺, 819.277 [M-H+Na]⁺.

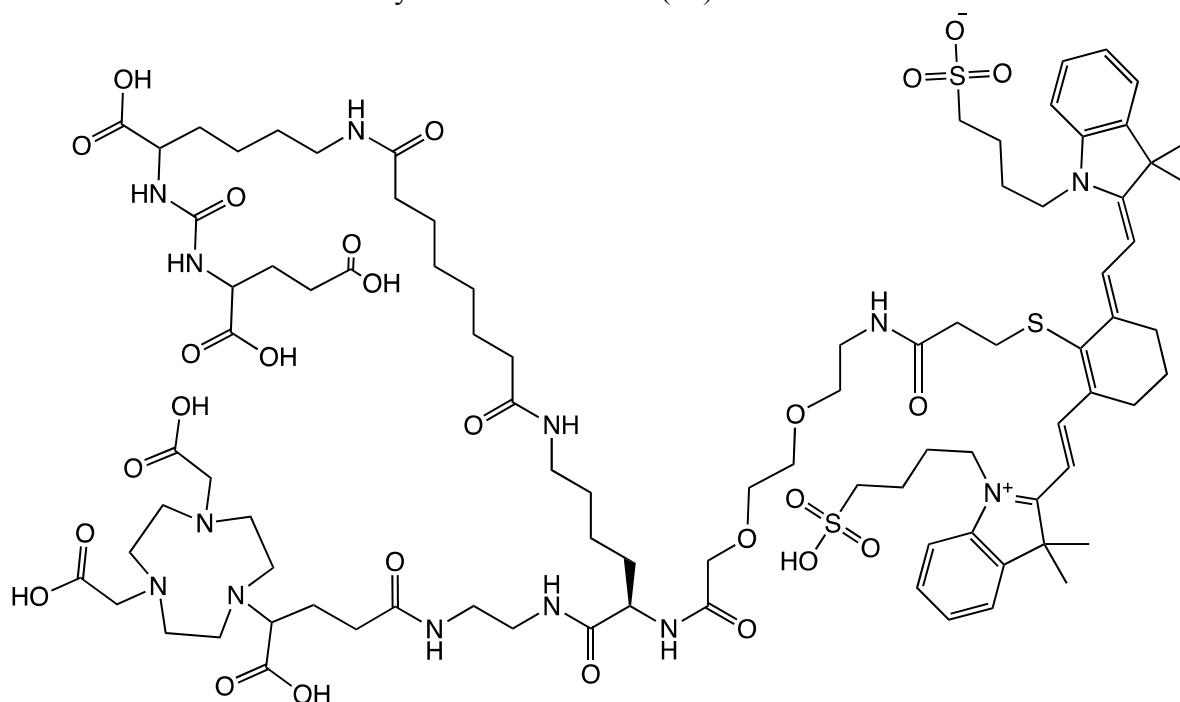
HPLC: t_R= 3.86min, Purity= 99.15%

Elemental Analysis:

Calculated for C₄₁H₅₃N₂O₈S₃. 1TFA (%): C: 56.63, H: 5.97, N, 3.07, S:10.55.

Observed (%): C: 56.35, H: 6.30, N: 2.95, S: 9.32.

PSMA-Suberate-NODAGA-Lys-PEG2-PA-IR783 (36)



Chemical Formula: $C_{90}H_{136}N_{13}O_{27}S_3$

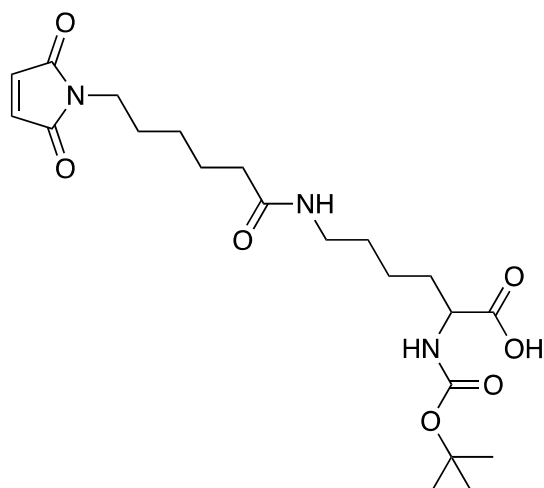
Molecular Weight: 1928.32

IR783-Propionic acid (8mg) was weighed into eppendorf tube and dissolved in anhydrous 0.4mL of DMF, followed by addition of Triethylamine (0.004mL, 0.028mmol) and TSTU (3mg, 0.01mmol). The reaction mixture was stirred for 15min and the NHS ester was verified by LC-MS. NODAGA-Lys-Sub-PSMA-PEG₂-NH₂ was weighed into eppendorf tube (12mg) and was dissolved in 0.4mL of 0.5M Borate buffer (pH was measured and adjusted to between 7-8, if needed with 2M NaOH). The aqueous solution was added into DMF solution and the reaction mixture was stirred for 15min after which the product formation was verified by LC-MS. The solution was directly purified by Semiprep HPLC (C18) using water (0.1%TFA) and acetonitrile (0.1%TFA) as eluents to get a green powder after lyophilization (6mg, 32%).

HRMS: Calculated for $C_{90}H_{136}N_{13}O_{27}S_3$:1970.846 $[M-2H+2Na]^+$; Obtained: $m/z = 1970.853$ $[M-2H+2Na]^+$.

HPLC: $t_R = 3.93$ min, Purity= 97.93%

6-Maleimidohexanoic-Lysine-Boc (37)



Chemical Formula: $C_{21}H_{33}N_3O_7$

Molecular Weight: 439.51

6-Mercaptohexanoic acid (204mg, 0.947 mmol) was weighed into a 50mL round bottom flask and dissolved in 4mL of ACN, to which was added DIPEA (0.18mL, 0.99mmol) followed by TSTU (305mg, 0.99mmol). The reaction was stirred for 30min and the NHS ester formation was verified by LC-MS. Boc-Lys-OH (236mg, 0.95mmol) was dissolved in 4mL of MeOH and DIPEA (0.34mL, 1.9mmol) and was pipetted into the maleimide solution. The reaction was stirred at room temperature for 1h and the product formation was verified by LC-MS. The solvents were evaporated to get a residue that was purified by flash chromatography (C18) using water (0.1%TFA) and acetonitrile (0.1%TFA) as eluents to get a cream colored powder after lyophilisation (Yield: 451 mg, 96%).

HRMS: Calculated for $C_{21}H_{33}N_3O_7$:462.221 $[M+Na]^+$; Obtained: $m/z = 462.222 [M+Na]^+$.

HPLC: $t_R = 3.55$ min, Purity= 96.80%

1H NMR (500 MHz, $CDCl_3-d$) δ 1.2 – 1.3 (m, 2H), 1.4 (d, $J = 3.0$ Hz, 10H), 1.5 – 1.7 (m, 4H), 1.8 (m, 1H), 2.1 (m, 2H), 3.1 – 3.2 (m, 2H), 3.5 (t, $J = 7.2$ Hz, 2H), 6.6 – 6.9 (m, 1H).

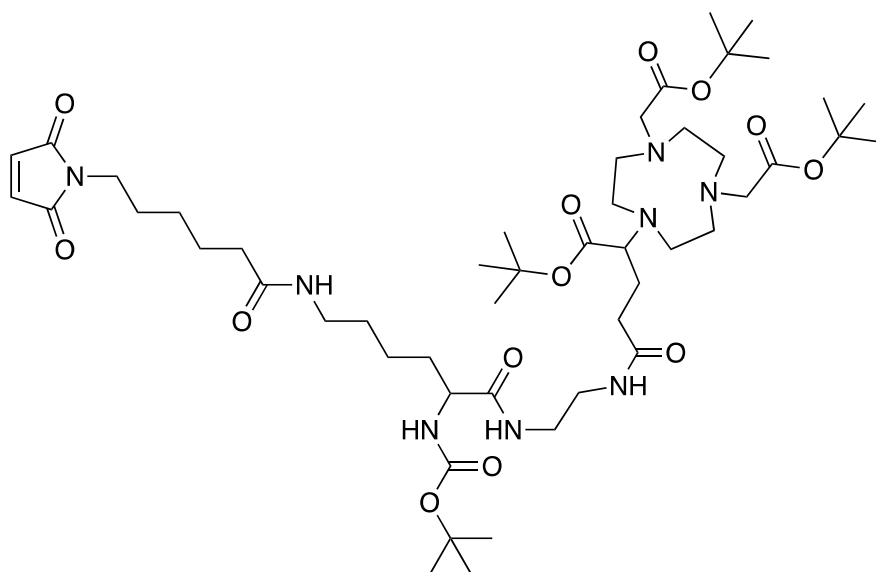
^{13}C NMR (126 MHz, $CDCl_3-d$) δ 26.6, 29.1, 30.1, 32.0, 32.6, 35.8, 39.9, 41.5, 42.9, 57.1, 83.8, 138.0, 160.1, 175.1, 178.1, 178.7.

Elemental Analysis:

Calculated for $C_{21}H_{33}N_3O_7 \cdot 2.5H_2O$ (%): C: 52.06, H: 7.91, N: 8.67.

Observed (%): C: 51.83, H: 7.49, N: 9.74.

6-Maleimidohexanoic-Lysine-Boc-NODAGA(tBu)₃ (**38**)



Chemical Formula: C₅₀H₈₆N₈O₁₃

Molecular Weight: 1007.28

6-Maleimidohexanoic-Lysine-Boc (180mg) was dissolved in 5mL of acetonitrile (ACN) in 50mL round bottom flask to which DIPEA (0.073 mL, 0.41mmol) was added dropwise followed by addition of TSTU (126mg, 0.410mmol). The reaction was left to stir at room temperature for 1h. NODAGA(tBu)₃-NH₂(240 mg) was dissolved in 10mL of acetonitrile and DIPEA (0.29 mL, 1.64 mmol), stirred for 5min and added into the activated lysine solution. The reaction mixture was left to stir at room temperature for 2h. The reaction mixture was evaporated at 35°C to remove acetonitrile to get a translucent residue, which was purified by reverse phase (C18) flash chromatography using water (0.1%TFA) and acetonitrile (0.1%TFA) as eluents. The product was recovered as a white solid after lyophilization. (Yield: 280 mg, 55%).

HRMS: Calculated for C₅₀H₈₆N₈O₁₃:1007.638 [M+H]⁺; Obtained: m/z = 1007.639 [M+H]⁺.

¹H NMR (500 MHz, CDCl₃-d) δ 1.2 – 1.4 (m, 4H), 1.4 (s, 38H), 1.6 (m, 5H), 1.7 – 1.8 (m, 2H), 2.0 – 2.1 (m, 1H), 2.1 (dq, 1H), 2.2 (q, 2H), 2.4 (t, *J* = 7.2 Hz, 2H), 2.5 – 3.6 (m, 21H), 3.6 – 3.9 (m, 5H), 4.0 – 4.2 (m, 1H), 4.3 – 4.6 (m, 1H), 6.7 (s, 2H).

¹³C NMR (126 MHz, CDCl₃-d) δ 17.5, 22.6, 25.2, 26.2, 28.0, 28.0, 28.2, 28.3, 28.5, 32.2, 32.5, 36.1, 37.2, 37.6, 38.9, 39.1, 39.5, 50.4, 53.9, 54.7, 55.9, 63.5, 79.8, 83.1, 114.8, 117.1, 134.1, 160.6, 160.9, 170.7, 170.9, 173.1, 173.6, 174.2.

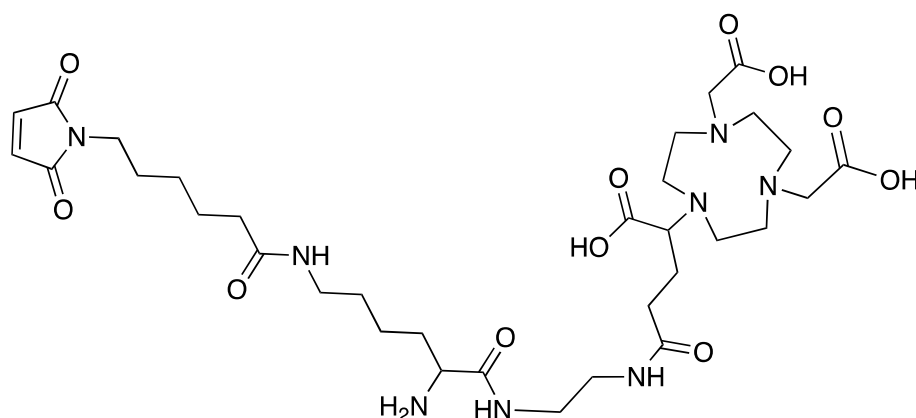
HPLC: t_R = 4.68min, Purity = 98.02%

Elemental Analysis:

Calculated for C₂₁H₃₃N₃O₇ · 2TFA · 4H₂O (%): C: 49.61, H: 7.40, N: 8.57.

Observed (%): C: 49.61, H: 7.56, N: 9.38.

6-Maleimidohexanoic-Lysine-NODAGA-NH₂ (**39**)



Chemical Formula: C₃₃H₅₄N₈O₁₁

Molecular Weight: 738.84

6-Maleimidohexanoic-Lysine-Boc-NODAGA(tBu)₃ (180mg) was weighed into a 50mL round bottom flask and was dissolved in 3mL of TFA. The solution was stirred at room temperature for 3h, after which the reaction was deemed complete as verified by LC-MS. The TFA was evaporated to get a viscous residue which was dissolved in 5mL of DCM and re-evaporated to remove residual TFA. The residue was purified by flash chromatography (C18) using water (0.1%TFA) and acetonitrile (0.1%TFA). The product was obtained as a cream white powder after lyophilization of the appropriately identified and collected fractions (Yield: 110mg, 76%).

HRMS: Calculated for C₃₃H₅₄N₈O₁₁: 739.398 [M+H]⁺; Obtained: m/z = 739.400 [M+H]⁺.

HPLC: t_R = 2.6min, Purity = 90.20%

¹H NMR (500 MHz, D₂O) δ 1.3 (m, 3H), 1.4 – 1.6 (m, 7H), 1.7 – 1.8 (m, 2H), 1.9 (m, 1H), 2.0 – 2.1 (m, 1H), 2.1 (t, *J* = 7.4 Hz, 2H), 2.3 – 2.4 (m, 2H), 3.0 (m, 9H), 3.1 – 3.3 (m, 15H), 3.3 – 3.5 (m, 4H), 3.5 (dd, *J* = 7.8, 6.5 Hz, 1H), 3.8 (s, 4H), 3.9 (t, *J* = 6.7 Hz, 1H), 6.8 (s, 2H).

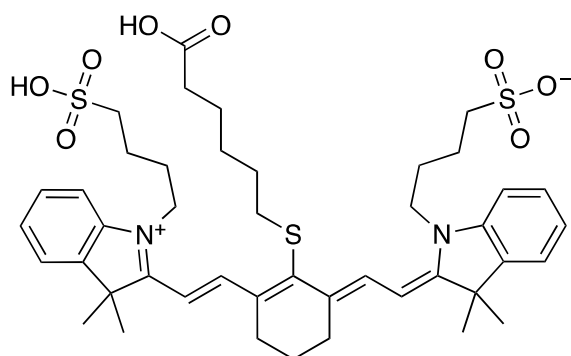
¹³C NMR (126 MHz, D₂O) δ 21.5, 24.3, 24.9, 25.4, 27.3, 28.0, 30.4, 32.6, 35.6, 37.4, 38.5, 38.7, 38.7, 42.2, 50.8, 53.2, 55.8, 64.1, 115.1, 117.5, 134.3, 162.8, 163.0, 169.9, 173.3, 175.4, 175.4, 176.7.

Elemental Analysis:

Calculated for C₂₁H₃₃N₃O₇ · 2TFA · 2H₂O (%): C: 44.31, H: 6.03, N: 11.17.

Observed (%): C: 43.85, H: 6.47, N: 11.29.

IR-783-Hexanoic Acid (**40**)



Chemical Formula: $C_{44}H_{59}N_2O_8S_3$

Molecular Weight: 840.14

IR-783 (56mg, 0.07mmol) was weighed into a 25mL round bottom flask to which was added 3mL of MeOH (dye was soluble with clear green solution). Triethylamine (0.036mL, 0.267mmol) and 6-mercaptohexanoic acid (22mg, 0.133mmol) was pipetted into the dye solution and reaction was stirred overnight (15h) protected from light in dark. The solvents were evaporated to get a dark green residue which was purified by semi-prep HPLC (C18) using water (0.1%TFA) and acetonitrile (0.1%TFA). The fractions were identified, evaporated and lyophilized to get a green powder (Yield: 45 mg, 68%).

HRMS: Calculated for $C_{44}H_{57}N_2O_8S_3$:837.328 [M-2H]⁻; Obtained: m/z = 837.331 [M-2H]⁻

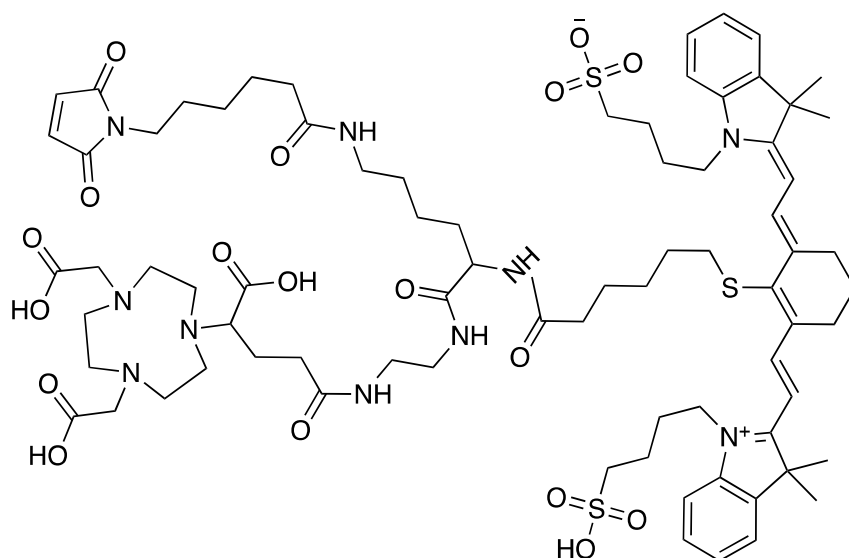
HPLC: t_R = 4.29min, Purity = 97.96%

Elemental Analysis:

Calculated for $C_{44}H_{59}N_2O_8S_3 \cdot 3H_2O$ (%): C: 59.10, H: 7.33, N: 3.13, S: 10.08.

Observed (%): C: 58.89, H: 7.07, N: 2.72, S: 10.53.

6-Maleimidohexanoic-Lysine-NODAGA-HA-IR783 (41)



Chemical Formula: $C_{77}H_{111}N_{10}O_{18}S_3$

Molecular Weight: 1560.97

IR-783-Hexanoic Acid (24mg) was weighed into an eppendorf tube and dissolved in anhydrous 0.5mL of DMF, followed by addition of triethylamine (0.015mL, 0.108mmol) and TSTU (8.5mg, 0.027mmol). The reaction mixture was stirred for 15min and the NHS ester was verified by LC-MS. 6-Maleimidohexanoic-Lysine-NODAGA-NH₂ was weighed into an eppendorf tube (20mg) and was dissolved in 0.5mL of 0.5M Borate buffer (pH was measured and adjusted to between 7-8, if needed with 2M NaOH). The aqueous solution was added into the DMF solution and the reaction mixture was stirred for 15min. The solution was directly purified by semi-prep HPLC to get a green powder after lyophilization (Yield: 15mg, 32%).

HRMS: Calculated for $C_{77}H_{111}N_{10}O_{18}S_3$:1559.723 [M]⁺; Obtained: m/z = 1559.727 [M]⁺

HPLC: t_R= 4.17min, Purity= 99.11%

Chapter VII. References

References:

1. Kelkar SS, Reineke TM: **Theranostics: combining imaging and therapy**. *Bioconjugate chemistry* 2011, **22**(10):1879-1903.
2. Shi J, Kantoff PW, Wooster R, Farokhzad OC: **Cancer nanomedicine: progress, challenges and opportunities**. *Nature Reviews Cancer* 2017, **17**(1):20.
3. Weiner GJ: **Monoclonal antibody mechanisms of action in cancer**. *Immunologic research* 2007, **39**(1-3):271-278.
4. Shepard HM, Phillips GL, Thanos CD, Feldmann M: **Developments in therapy with monoclonal antibodies and related proteins**. *Clinical Medicine* 2017, **17**(3):220-232.
5. Wicki A, Witzigmann D, Balasubramanian V, Huwylar J: **Nanomedicine in cancer therapy: challenges, opportunities, and clinical applications**. *Journal of controlled release* 2015, **200**:138-157.
6. Bertrand N, Wu J, Xu X, Kamaly N, Farokhzad OC: **Cancer nanotechnology: the impact of passive and active targeting in the era of modern cancer biology**. *Advanced drug delivery reviews* 2014, **66**:2-25.
7. Sharma RA, Plummer R, Stock JK, Greenhalgh TA, Ataman O, Kelly S, Clay R, Adams RA, Baird RD, Billingham L: **Clinical development of new drug-radiotherapy combinations**. *Nature Reviews Clinical Oncology* 2016, **13**(10):627-642.
8. Taupin F, Flaender M, Delorme R, Brochard T, Mayol J-F, Arnaud J, Perriat P, Sancey L, Lux F, Barth RF: **Gadolinium nanoparticles and contrast agent as radiation sensitizers**. *Physics in medicine and biology* 2015, **60**(11):4449.
9. Hainfeld JF, Slatkin DN, Smilowitz HM: **The use of gold nanoparticles to enhance radiotherapy in mice**. *Physics in medicine and biology* 2004, **49**(18):N309.
10. Cui L, Her S, Borst GR, Bristow RG, Jaffray DA, Allen C: **Radiosensitization by gold nanoparticles: Will they ever make it to the clinic?** *Radiotherapy and Oncology* 2017.
11. James ML, Gambhir SS: **A molecular imaging primer: modalities, imaging agents, and applications**. *Physiological reviews* 2012, **92**(2):897-965.
12. Weissleder R, Pittet MJ: **Imaging in the era of molecular oncology**. *Nature* 2008, **452**(7187):580.
13. Azhdarinia A, Ghosh P, Ghosh S, Wilganowski N, Sevic-Muraca EM: **Dual-labelling strategies for nuclear and fluorescence molecular imaging: a review and analysis**. *Molecular imaging and biology* 2012, **14**(3):261-276.
14. Price EW, Orvig C: **Matching chelators to radiometals for radiopharmaceuticals**. *Chemical Society Reviews* 2014, **43**(1):260-290.
15. Lee Y-S: **Radiopharmaceuticals for molecular imaging**. *Open Nucl Med J* 2010, **2**:178-185.
16. Berry E, Bulpitt AJ: **Fundamentals of MRI: an interactive learning approach**: CRC Press; 2008.
17. Merbach AS, Helm L, Toth E: **The chemistry of contrast agents in medical magnetic resonance imaging**: John Wiley & Sons; 2013.
18. Mahmoudi M, Hosseinkhani H, Hosseinkhani M, Boutry S, Simchi A, Journeay WS, Subramani K, Laurent S: **Magnetic resonance imaging tracking of stem cells in vivo using iron oxide nanoparticles as a tool for the advancement of clinical regenerative medicine**. *Chemical Reviews* 2010, **111**(2):253-280.
19. Huang W-Y, Davis JJ: **Multimodality and nanoparticles in medical imaging**. *Dalton Transactions* 2011, **40**(23):6087-6103.
20. Stephen ZR, Kievit FM, Zhang M: **Magnetite nanoparticles for medical MR imaging**. *Materials today* 2011, **14**(7-8):330-338.
21. Tóth É, Helm L, Merbach AE: **Relaxivity of MRI contrast agents**. In: *Contrast Agents I*. edn.: Springer; 2002: 61-101.
22. Reynolds CH, Annan N, Beshah K, Huber JH, Shaber SH, Lenkinski RE, Wortman JA: **Gadolinium-loaded nanoparticles: new contrast agents for magnetic resonance imaging**. *Journal of the American Chemical Society* 2000, **122**(37):8940-8945.
23. Bonnet CS, Tóth É: **MRI probes for sensing biologically relevant metal ions**. *Future medicinal chemistry* 2010, **2**(3):367-384.
24. Thakor AS, Jokerst JV, Ghanouni P, Campbell JL, Mittra E, Gambhir SS: **Clinically approved nanoparticle imaging agents**. *Journal of Nuclear Medicine* 2016, **57**(12):1833-1837.

25. Kim D, Lee N, Park YI, Hyeon T: **Recent Advances in Inorganic Nanoparticle-Based NIR Luminescence Imaging: Semiconductor Nanoparticles and Lanthanide Nanoparticles.** *Bioconjugate chemistry* 2016, **28**(1):115-123.
26. Kim J, Lee N, Hyeon T: **Recent development of nanoparticles for molecular imaging.** *Phil Trans R Soc A* 2017, **375**(2107):20170022.
27. Pichler BJ, Judenhofer MS, Pfannenbergs C: **Multimodal Imaging Approaches: PET/CT and PET/MRI.** In: *Molecular Imaging I.* edn.: Springer; 2008: 109-132.
28. Lee S, Chen X: **Dual-modality probes for in vivo molecular imaging.** *Molecular imaging* 2009, **8**(2):7290.2009. 00013.
29. Zaidi H, Mawlawi O, Orton CG: **Simultaneous PET/MR will replace PET/CT as the molecular multimodality imaging platform of choice.** *Medical Physics* 2007, **34**(5):1525-1528.
30. Ghosh S, Azhdarinia A: **Advances in the development of multimodal imaging agents for nuclear/near-infrared fluorescence imaging.** *Current medicinal chemistry* 2015, **22**(29):3390-3404.
31. Vandenberghe S, Marsden PK: **PET-MRI: a review of challenges and solutions in the development of integrated multimodality imaging.** *Physics in Medicine & Biology* 2015, **60**(4):R115.
32. Li X, Zhang X-N, Li X-D, Chang J: **Multimodality imaging in nanomedicine and nanotheranostics.** *Cancer biology & medicine* 2016, **13**(3):339.
33. Sancey L, Lux F, Kotb S, Roux S, Dufort S, Bianchi A, Cremillieux Y, Fries P, Coll J-L, Rodriguez-Lafrasse C: **The use of theranostic gadolinium-based nanoprobe to improve radiotherapy efficacy.** *The British journal of radiology* 2014, **87**(1041):20140134.
34. Sherry AD, Caravan P, Lenkinski RE: **Primer on gadolinium chemistry.** *Journal of Magnetic Resonance Imaging* 2009, **30**(6):1240-1248.
35. Morlieras J, Dufort S, Sancey L, Truillet C, Mignot A, Rossetti F, Dentamaro M, Laurent S, Vander Elst L, Muller RN: **Functionalization of small rigid platforms with cyclic RGD peptides for targeting tumors overexpressing $\alpha\beta3$ -integrins.** *Bioconjugate chemistry* 2013, **24**(9):1584-1597.
36. Kretschy D, Koellensperger G, Hann S: **Stability assessment of different chelating moieties used for elemental labelling of bio-molecules.** *Metallomics* 2011, **3**(12):1304-1309.
37. Duijzentkunst DAS, Kwekkeboom DJ, Bodei L: **Somatostatin Receptor 2-Targeting Compounds.** *Journal of Nuclear Medicine* 2017, **58**(Supplement 2):54S-60S.
38. Caravan P, Ellison JJ, McMurry TJ, Lauffer RB: **Gadolinium (III) chelates as MRI contrast agents: structure, dynamics, and applications.** *Chemical reviews* 1999, **99**(9):2293-2352.
39. Wu N, Kang CS, Sin I, Ren S, Liu D, Ruthengael VC, Lewis MR, Chong H-S: **Promising bifunctional chelators for copper 64-PET imaging: practical 64 Cu radiolabelling and high in vitro and in vivo complex stability.** *JBIC Journal of Biological Inorganic Chemistry* 2016, **21**(2):177-184.
40. Velikyan I, Maecke H, Langstrom B: **Convenient preparation of 68Ga-based PET-radiopharmaceuticals at room temperature.** *Bioconjugate chemistry* 2008, **19**(2):569-573.
41. Notni J, Pohle K, Wester H-J: **Comparative gallium-68 labelling of TRAP-, NOTA-, and DOTA-peptides: practical consequences for the future of gallium-68-PET.** *EJNMMI research* 2012, **2**(1):28.
42. Fani M, Del Pozzo L, Abiraj K, Mansi R, Tamma ML, Cescato R, Waser B, Weber WA, Reubi JC, Maecke HR: **PET of somatostatin receptor-positive tumors using 64Cu-and 68Ga-somatostatin antagonists: the chelate makes the difference.** *Journal of nuclear medicine* 2011, **52**(7):1110-1118.
43. Moreau M, Poty S, Vrigneaud J-M, Walker P, Guillemin M, Raguin O, Oudot A, Bernhard C, Goze C, Boschetti F: **MANOTA: a promising bifunctional chelating agent for copper-64 immunoPET.** *Dalton Transactions* 2017, **46**(42):14659-14668.
44. Bernhard C, Moreau M, Lhenry D, Goze C, Boschetti F, Rousselin Y, Brunotte F, Denat F: **DOTAGA-Anhydride: A Valuable Building Block for the Preparation of DOTA-Like Chelating Agents.** *Chemistry-A European Journal* 2012, **18**(25):7834-7841.
45. Pansare VJ, Hejazi S, Faenza WJ, Prud'homme RK: **Review of long-wavelength optical and NIR imaging materials: contrast agents, fluorophores, and multifunctional nano carriers.** *Chemistry of materials* 2012, **24**(5):812-827.
46. Martinić I, Eliseeva SV, Petoud S: **Near-infrared emitting probes for biological imaging: Organic fluorophores, quantum dots, fluorescent proteins, lanthanide (III) complexes and nanomaterials.** *Journal of Luminescence* 2017, **189**:19-43.

47. Ulrich G, Zissel R, Harriman A: **The chemistry of fluorescent bodipy dyes: versatility unsurpassed.** *Angewandte Chemie International Edition* 2008, **47**(7):1184-1201.
48. Hilderbrand SA, Kelly KA, Weissleder R, Tung C-H: **Monofunctional near-infrared fluorochromes for imaging applications.** *Bioconjugate chemistry* 2005, **16**(5):1275-1281.
49. Luo S, Zhang E, Su Y, Cheng T, Shi C: **A review of NIR dyes in cancer targeting and imaging.** *Biomaterials* 2011, **32**(29):7127-7138.
50. Lavis LD, Raines RT: **Bright ideas for chemical biology.** *ACS chemical biology* 2008, **3**(3):142-155.
51. Bunschoten A, van Willigen DM, Buckle T, van den Berg NS, Welling MM, Spa SJ, Wester H-Jr, van Leeuwen FW: **Tailoring fluorescent dyes to optimize a hybrid RGD-tracer.** *Bioconjugate chemistry* 2016, **27**(5):1253-1258.
52. Zhang J, Liu Z, Lian P, Qian J, Li X, Wang L, Fu W, Chen L, Wei X, Li C: **Selective imaging and cancer cell death via pH switchable near-infrared fluorescence and photothermal effects.** *Chemical Science* 2016, **7**(9):5995-6005.
53. Yuan A, Wu J, Tang X, Zhao L, Xu F, Hu Y: **Application of near-infrared dyes for tumor imaging, photothermal, and photodynamic therapies.** *Journal of pharmaceutical sciences* 2013, **102**(1):6-28.
54. Yang X, Shi C, Tong R, Qian W, Zhau HE, Wang R, Zhu G, Cheng J, Yang VW, Cheng T: **Near IR heptamethine cyanine dye-mediated cancer imaging.** *Clinical cancer research* 2010:1078-0432. CCR-1010-0059.
55. Shi C, Wu JB, Chu GC, Li Q, Wang R, Zhang C, Zhang Y, Kim HL, Wang J, Zhau HE: **Heptamethine carbocyanine dye-mediated near-infrared imaging of canine and human cancers through the HIF-1 α /OATPs signaling axis.** *Oncotarget* 2014, **5**(20):10114.
56. Poty S, Désogère P, Šimeček J, Bernhard C, Goncalves V, Goze C, Boschetti F, Notni J, Wester HJ, Denat F: **MA-NOTMP: A Triazacyclononane Trimethylphosphinate Based Bifunctional Chelator for Gallium Radiolabelling of Biomolecules.** *ChemMedChem* 2015, **10**(9):1475-1479.
57. Poty S, Gourni E, Désogère P, Boschetti Fdr, Goze C, Maecke HR, Denat F: **AMD3100: A Versatile Platform for CXCR4 Targeting 68Ga-Based Radiopharmaceuticals.** *Bioconjugate chemistry* 2016, **27**(3):752-761.
58. Vlahov IR, Leamon CP: **Engineering folate-drug conjugates to target cancer: from chemistry to clinic.** *Bioconjugate chemistry* 2012, **23**(7):1357-1369.
59. Lu Y, Low PS: **Folate-mediated delivery of macromolecular anticancer therapeutic agents.** *Advanced drug delivery reviews* 2012, **64**:342-352.
60. Gruner BA, Weitman SD: **The folate receptor as a potential therapeutic anticancer target.** *Investigational new drugs* 1998, **16**(3):205-219.
61. Ledermann J, Canevari S, Thigpen T: **Targeting the folate receptor: diagnostic and therapeutic approaches to personalize cancer treatments.** *Annals of Oncology* 2015, **26**(10):2034-2043.
62. Gaertner F, Kessler H, Wester H-J, Schwaiger M, Beer A: **Radiolabelled RGD peptides for imaging and therapy.** *European journal of nuclear medicine and molecular imaging* 2012, **39**(1):126-138.
63. Folkman J: **Tumor angiogenesis: therapeutic implications.** *New england journal of medicine* 1971, **285**(21):1182-1186.
64. Gurrath M, Müller G, Kessler H, Aumailley M, Timpl R: **Conformation/activity studies of rationally designed potent anti-adhesive RGD peptides.** *The FEBS Journal* 1992, **210**(3):911-921.
65. Gottschalk KE, Kessler H: **The structures of integrins and integrin-ligand complexes: implications for drug design and signal transduction.** *Angewandte Chemie International Edition* 2002, **41**(20):3767-3774.
66. Liu S: **Radiolabelled cyclic RGD peptide bioconjugates as radiotracers targeting multiple integrins.** *Bioconjugate chemistry* 2015, **26**(8):1413-1438.
67. Israeli RS, Powell CT, Fair WR, Heston WD: **Molecular cloning of a complementary DNA encoding a prostate-specific membrane antigen.** *Cancer research* 1993, **53**(2):227-230.
68. Mohammed AA, Shergill IS, Vandal MT, Gujral SS: **ProstaScint™ and its role in the diagnosis of prostate cancer.** *Expert review of molecular diagnostics* 2007, **7**(4):345-349.
69. Lütje S, Boerman OC, van Rij CM, Sedelaar M, Helfrich W, Oyen WJ, Mulders PF: **Prospects in radionuclide imaging of prostate cancer.** *The Prostate* 2012, **72**(11):1262-1272.
70. Machulkin AE, Ivanenkov YA, Aladinskaya AV, Veselov MS, Aladinskiy VA, Beloglazkina EK, Koteliansky VE, Shakhbazyan AG, Sandulenko YB, Majouga AG: **Small-molecule PSMA ligands.**

- Current state, SAR and perspectives.** *Journal of drug targeting* 2016, **24**(8):679-693.
71. Benešová M, Bauder-Wüst U, Schäfer M, Klika KD, Mier W, Haberkorn U, Kopka K, Eder M: **Linker Modification Strategies To Control the Prostate-Specific Membrane Antigen (PSMA)-Targeting and Pharmacokinetic Properties of DOTA-Conjugated PSMA Inhibitors.** *Journal of Medicinal Chemistry* 2016, **59**(5):1761-1775.
72. Eckelmann D, Kusari S, Spiteller M: **Occurrence and spatial distribution of maytansinoids in Putterlickia pyracantha, an unexplored resource of anticancer compounds.** *Fitoterapia* 2016, **113**:175-181.
73. Yook S, Cai Z, Lu Y, Winnik MA, Pignol J-P, Reilly RM: **Intratumorally injected ¹⁷⁷Lu-labelled gold nanoparticles: gold nanoseed brachytherapy with application for neoadjuvant treatment of locally advanced breast cancer.** *Journal of Nuclear Medicine* 2016, **57**(6):936-942.
74. Moreau M, Raguin O, Vrigneaud J-M, Collin B, Bernhard C, Tizon X, Boschetti Fdr, Duchamp O, Brunotte Fo, Denat F: **DOTAGA-trastuzumab. A new antibody conjugate targeting HER2/Neu antigen for diagnostic purposes.** *Bioconjugate chemistry* 2012, **23**(6):1181-1188.
75. Scott AM, Allison JP, Wolchok JD: **Monoclonal antibodies in cancer therapy.** *Cancer Immunity Archive* 2012, **12**(1):14.
76. Cazzamalli S, Dal Corso A, Widmayer F, Neri D: **Chemically-defined antibody-and small molecule-drug conjugates for in vivo tumor targeting applications: a comparative analysis.** *Journal of the American Chemical Society* 2018.
77. Sivaram AJ, Wardiana A, Howard CB, Mahler SM, Thurecht KJ: **Recent Advances in the Generation of Antibody–nanomaterial Conjugates.** *Advanced healthcare materials* 2017.
78. Pensa E, Cortés E, Corthey G, Carro P, Vericat C, Fonticelli MH, Benitez G, Rubert AA, Salvarezza RC: **The chemistry of the sulfur–gold interface: in search of a unified model.** *Accounts of chemical research* 2012, **45**(8):1183-1192.
79. Beck A, Goetsch L, Dumontet C, Corvaia N: **Strategies and challenges for the next generation of antibody-drug conjugates.** *Nature Reviews Drug Discovery* 2017, **16**(5):315-337.
80. Cal PM, Bernardes GJ, Gois PM: **Cysteine-Selective Reactions for Antibody Conjugation.** *Angewandte Chemie International Edition* 2014, **53**(40):10585-10587.
81. Koniev O, Wagner A: **Developments and recent advancements in the field of endogenous amino acid selective bond forming reactions for bioconjugation.** *Chemical Society Reviews* 2015, **44**(15):5495-5551.
82. Ishii Y, Lehrer SS: **Effects of the state of the succinimido-ring on the fluorescence and structural properties of pyrene maleimide-labelled alpha alpha-tropomyosin.** *Biophysical journal* 1986, **50**(1):75-80.
83. Nair DP, Podgórski M, Chatani S, Gong T, Xi W, Fenoli CR, Bowman CN: **The thiol-Michael addition click reaction: a powerful and widely used tool in materials chemistry.** *Chemistry of Materials* 2013, **26**(1):724-744.
84. Meyer J-P, Adumeau P, Lewis JS, Zeglis BM: **Click chemistry and radiochemistry: the first 10 years.** *Bioconjugate chemistry* 2016, **27**(12):2791-2807.
85. Hausner SH, Carpenter RD, Bauer N, Sutcliffe JL: **Evaluation of an integrin $\alpha\beta 6$ -specific peptide labelled with [¹⁸F] fluorine by copper-free, strain-promoted click chemistry.** *Nuclear medicine and biology* 2013, **40**(2):233-239.
86. Kolb HC, Finn M, Sharpless KB: **Click chemistry: diverse chemical function from a few good reactions.** *Angewandte Chemie International Edition* 2001, **40**(11):2004-2021.
87. Simon M, Zangemeister-Wittke U, Plückthun A: **Facile double-functionalization of designed ankyrin repeat proteins using click and thiol chemistries.** *Bioconjugate chemistry* 2012, **23**(2):279-286.
88. Chaudhuri S, Korten T, Diez S: **Tetrazine–trans-cyclooctene Mediated Conjugation of Antibodies to Microtubules Facilitates Subpicomolar Protein Detection.** *Bioconjugate Chemistry* 2017, **28**(4):918-922.
89. Maggi A, Ruivo E, Fissers J, Vangestel C, Chatterjee S, Joossens J, Sobott F, Staelens S, Stroobants S, Van Der Veken P: **Development of a novel antibody–tetrazine conjugate for bioorthogonal pretargeting.** *Organic & biomolecular chemistry* 2016, **14**(31):7544-7551.
90. Majoul N, Aouida S, Bessaïs B: **Progress of porous silicon APTES-functionalization by FTIR**

- investigations. *Applied Surface Science* 2015, **331**:388-391.
91. Bruce IJ, Sen T: **Surface modification of magnetic nanoparticles with alkoxysilanes and their application in magnetic bioseparations.** *Langmuir* 2005, **21**(15):7029-7035.
 92. Bini RA, Marques RFC, Santos FJ, Chaker JA, Jafelicci Jr M: **Synthesis and functionalization of magnetite nanoparticles with different amino-functional alkoxysilanes.** *Journal of magnetism and magnetic materials* 2012, **324**(4):534-539.
 93. Chen S, Hayakawa S, Shirotsaki Y, Fujii E, Kawabata K, Tsuru K, Osaka A: **Sol-Gel Synthesis and Microstructure Analysis of Amino-Modified Hybrid Silica Nanoparticles from Aminopropyltriethoxysilane and Tetraethoxysilane.** *Journal of the American Ceramic Society* 2009, **92**(9):2074-2082.
 94. Beganskienė A, Sirutkaitis V, Kurtinaitienė M, Juškėnas R, Kareiva A: **FTIR, TEM and NMR investigations of Stöber silica nanoparticles.** *Mater Sci (Medžiagotyra)* 2004, **10**:287-290.
 95. Rossi LM, Shi L, Quina FH, Rosenzweig Z: **Stöber synthesis of monodispersed luminescent silica nanoparticles for bioanalytical assays.** *Langmuir* 2005, **21**(10):4277-4280.
 96. Mehrotra R, Singh A: **Recent trends in metal alkoxide chemistry.** *Progress in Inorganic Chemistry* 1997, **46**:239-454.
 97. Rofsky NM, Sherry AD, Lenkinski RE: **Nephrogenic systemic fibrosis: a chemical perspective.** *Radiology* 2008, **247**(3):608-612.
 98. Mignot A, Truillet C, Lux F, Sancey L, Louis C, Denat F, Boschetti F, Bocher L, Gloter A, Stéphan O: **A Top-Down synthesis route to ultrasmall multifunctional Gd-Based silica nanoparticles for theranostic applications.** *Chemistry-A European Journal* 2013, **19**(19):6122-6136.
 99. Morlieras J, Chezal J-M, Miot-Noirault E, Vidal A, Besse S, Kryza D, Truillet C, Mignot A, Antoine R, Dugourd P: **In vivo evidence of the targeting of cartilaginous tissue by pyridinium functionalized nanoparticles.** *Chemical Communications* 2013, **49**(29):3046-3048.
 100. Truillet C, Bouziotis P, Tsoukalas C, Brugière J, Martini M, Sancey L, Brichart T, Denat F, Boschetti F, Darbost U: **Ultrasmall particles for Gd-MRI and 68Ga-PET dual imaging.** *Contrast media & molecular imaging* 2015, **10**(4):309-319.
 101. Trivedi ER, Ma Z, Waters EA, Macrenaris KW, Subramanian R, Barrett AG, Meade TJ, Hoffman BM: **Synthesis and characterization of a porphyrazine-Gd (III) MRI contrast agent and in vivo imaging of a breast cancer xenograft model.** *Contrast media & molecular imaging* 2014, **9**(4):313-322.
 102. Debouttière PJ, Roux S, Vocanson F, Billotey C, Beuf O, Favre-Réguillon A, Lin Y, Pellet-Rostaing S, Lamartine R, Perriat P: **Design of gold nanoparticles for magnetic resonance imaging.** *Advanced Functional Materials* 2006, **16**(18):2330-2339.
 103. Kryza D, Taleb J, Janier M, Marmuse L, Miladi I, Bonazza P, Louis C, Perriat P, Roux S, Tillement O: **Biodistribution study of nanometric hybrid gadolinium oxide particles as a multimodal SPECT/MR/optical imaging and theragnostic agent.** *Bioconjugate chemistry* 2011, **22**(6):1145-1152.
 104. Bouziotis P, Stellas D, Thomas E, Truillet C, Tsoukalas C, Lux F, Tsotakos T, Xanthopoulos S, Paravatou-Petsotas M, Gaitanis A: **68Ga-radiolabelled AGuIX nanoparticles as dual-modality imaging agents for PET/MRI-guided radiation therapy.** *Nanomedicine* 2017.
 105. Vrigneaud J-M, Walker P, Barbier B, Camacho A, Oudot A, Collin B, Brunotte F: **Performance evaluation of the PET component of a sequential APD-based micro-PET/MR imaging system.** *Biomedical Physics & Engineering Express* 2017, **3**(3):035006.
 106. Alric C, Miladi I, Kryza D, Taleb J, Lux F, Bazzi R, Billotey C, Janier M, Perriat P, Roux S: **The biodistribution of gold nanoparticles designed for renal clearance.** *Nanoscale* 2013, **5**(13):5930-5939.
 107. Alric C, Taleb J, Duc GL, Mandon C, Billotey C, Meur-Herland AL, Brochard T, Vocanson F, Janier M, Perriat P: **Gadolinium chelate coated gold nanoparticles as contrast agents for both X-ray computed tomography and magnetic resonance imaging.** *Journal of the American Chemical Society* 2008, **130**(18):5908-5915.
 108. Miladi I, Alric C, Dufort S, Mowat P, Dutour A, Mandon C, Laurent G, Bräuer-Krisch E, Herath N, Coll JL: **The in vivo radiosensitizing effect of gold nanoparticles based MRI contrast agents.** *Small*

- 2014, **10**(6):1116-1124.
109. Butterworth KT, Nicol JR, Ghita M, Rosa S, Chaudhary P, McGarry CK, McCarthy HO, Jimenez-Sanchez G, Bazzi R, Roux S: **Preclinical evaluation of gold-DTDTPA nanoparticles as theranostic agents in prostate cancer radiotherapy.** *Nanomedicine* 2016, **11**(16):2035-2047.
 110. Laurent G, Bernhard C, Dufort S, Sánchez GJ, Bazzi R, Boschetti F, Moreau M, Vu T, Collin B, Oudot A: **Minor changes in the macrocyclic ligands but major consequences on the efficiency of gold nanoparticles designed for radiosensitization.** *Nanoscale* 2016, **8**(23):12054-12065.
 111. Díaz-Mochón JJ, Bialy L, Bradley M: **Full Orthogonality between Dde and Fmoc: The Direct Synthesis of PNA–Peptide Conjugates.** *Organic Letters* 2004, **6**(7):1127-1129.
 112. Amendola V, Meneghetti M: **Size evaluation of gold nanoparticles by UV– vis spectroscopy.** *The Journal of Physical Chemistry C* 2009, **113**(11):4277-4285.
 113. Haiss W, Thanh NT, Aveyard J, Fernig DG: **Determination of size and concentration of gold nanoparticles from UV– Vis spectra.** *Analytical chemistry* 2007, **79**(11):4215-4221.
 114. Hrkach J, Von Hoff D, Ali MM, Andrianova E, Auer J, Campbell T, De Witt D, Figa M, Figueiredo M, Horhota A: **Preclinical development and clinical translation of a PSMA-targeted docetaxel nanoparticle with a differentiated pharmacological profile.** *Science translational medicine* 2012, **4**(128):128ra139-128ra139.
 115. Nagesh PK, Johnson NR, Boya VK, Chowdhury P, Othman SF, Khalilzad-Sharghi V, Hafeez BB, Ganju A, Khan S, Behrman SW: **PSMA targeted docetaxel-loaded superparamagnetic iron oxide nanoparticles for prostate cancer.** *Colloids and Surfaces B: Biointerfaces* 2016, **144**:8-20.
 116. Huang B, Otis J, Joice M, Kotlyar A, Thomas TP: **PSMA-targeted stably linked “dendrimer-glutamate urea-methotrexate” as a prostate cancer therapeutic.** *Biomacromolecules* 2014, **15**(3):915-923.
 117. Banerjee SR, Foss CA, Horhota A, Pullambhatla M, McDonnell K, Zale S, Pomper MG: **111In-and IRDye800CW-Labelled PLA–PEG Nanoparticle for Imaging Prostate-Specific Membrane Antigen-Expressing Tissues.** *Biomacromolecules* 2016, **18**(1):201-209.
 118. Zhu C, Bandekar A, Sempkowski M, Banerjee SR, Pomper MG, Bruchertseifer F, Morgenstern A, Sofou S: **Nanoconjugation of PSMA-targeting ligands enhances perinuclear localization and improves efficacy of delivered alpha-particle emitters against tumor endothelial analogues.** *Molecular cancer therapeutics* 2016, **15**(1):106-113.
 119. Azad BB, Banerjee SR, Pullambhatla M, Lacerda S, Foss CA, Wang Y, Ivkov R, Pomper MG: **Evaluation of a PSMA-targeted BNF nanoparticle construct.** *Nanoscale* 2015, **7**(10):4432-4442.
 120. Kasten BB, Liu T, Nedrow-Byers JR, Benny PD, Berkman CE: **Targeting prostate cancer cells with PSMA inhibitor-guided gold nanoparticles.** *Bioorganic & medicinal chemistry letters* 2013, **23**(2):565-568.
 121. Abad JM, Mertens SF, Pita M, Fernández VM, Schiffrin DJ: **Functionalization of thioctic acid-capped gold nanoparticles for specific immobilization of histidine-tagged proteins.** *Journal of the American Chemical Society* 2005, **127**(15):5689-5694.
 122. Philip R, Penzkofer A, Bäumler W, Szeimies R, Abels C: **Absorption and fluorescence spectroscopic investigation of indocyanine green.** *Journal of Photochemistry and Photobiology A: Chemistry* 1996, **96**(1-3):137-148.
 123. Dy GW, Gore JL, Forouzanfar MH, Naghavi M, Fitzmaurice C: **Global Burden of Urologic Cancers, 1990-2013.** *European Urology* 2017, **71**(3):437-446.
 124. Stamey TA, Johnstone IM, McNeal JE, Lu AY, Yemoto CM: **Preoperative serum prostate specific antigen levels between 2 and 22 ng./mL. correlate poorly with post-radical prostatectomy cancer morphology: prostate specific antigen cure rates appear constant between 2 and 9 ng./mL.** *The Journal of Urology* 2002, **167**(1):103-111.
 125. Hillier SM, Maresca KP, Femia FJ, Marquis JC, Foss CA, Nguyen N, Zimmerman CN, Barrett JA, Eckelman WC, Pomper MG *et al*: **Preclinical Evaluation of Novel Glutamate-Urea-Lysine Analogues That Target Prostate-Specific Membrane Antigen as Molecular Imaging Pharmaceuticals for Prostate Cancer.** *Cancer Research* 2009, **69**(17):6932.
 126. Gorin MA, Rowe SP, Denmeade SR: **Clinical Applications of Molecular Imaging in the Management of Prostate Cancer.** *PET Clin* 2017, **12**(2):185-192.
 127. Rajasekaran AK, Anilkumar G, Christiansen JJ: **Is prostate-specific membrane antigen a**

- multifunctional protein?** *American Journal of Physiology - Cell Physiology* 2005, **288**(5):C975-C981.
128. Israeli RS, Powell CT, Corr JG, Fair WR, Heston WDW: **Expression of the Prostate-specific Membrane Antigen.** *Cancer Research* 1994, **54**(7):1807.
129. Ghosh A, Heston WDW: **Tumor target prostate specific membrane antigen (PSMA) and its regulation in prostate cancer.** *Journal of Cellular Biochemistry* 2004, **91**(3):528-539.
130. Chang SS: **Overview of Prostate-Specific Membrane Antigen.** *Reviews in Urology* 2004, **6**(Suppl 10):S13-S18.
131. Navrátil M, Ptáček J, Šácha P, Starková J, Lubkowski J, Bařinka C, Konvalinka J: **Structural and biochemical characterization of the folyl-poly- γ -l-glutamate hydrolyzing activity of human glutamate carboxypeptidase II.** *FEBS Journal* 2014, **281**(14):3228-3242.
132. Barinka C, Rojas C, Slusher B, Pomper M: **Glutamate carboxypeptidase II in diagnosis and treatment of neurologic disorders and prostate cancer.** *Current medicinal chemistry* 2012, **19**(6):856-870.
133. Liu H, Rajasekaran AK, Moy P, Xia Y, Kim S, Navarro V, Rahmati R, Bander NH: **Constitutive and antibody-induced internalization of prostate-specific membrane antigen.** *Cancer research* 1998, **58**(18):4055-4060.
134. Israeli RS, Powell CT, Corr JG, Fair WR, Heston WD: **Expression of the prostate-specific membrane antigen.** *Cancer research* 1994, **54**(7):1807-1811.
135. Maurer T, Eiber M, Schwaiger M, Gschwend JE: **Current use of PSMA-PET in prostate cancer management.** *Nature reviews Urology* 2016, **13**(4):226.
136. Pillai MRA, Nanabala R, Joy A, Sasikumar A, Knapp FFR: **Radiolabelled enzyme inhibitors and binding agents targeting PSMA: effective theranostic tools for imaging and therapy of prostate cancer.** *Nuclear medicine and biology* 2016, **43**(11):692-720.
137. Hillier SM, Maresca KP, Femia FJ, Marquis JC, Foss CA, Nguyen N, Zimmerman CN, Barrett JA, Eckelman WC, Pomper MG: **Preclinical evaluation of novel glutamate-urea-lysine analogues that target prostate-specific membrane antigen as molecular imaging pharmaceuticals for prostate cancer.** *Cancer research* 2009, **69**(17):6932-6940.
138. Taneja SS: **ProstaScint® Scan: Contemporary use in clinical practice.** *Reviews in urology* 2004, **6**(Suppl 10):S19.
139. Kahn D, Williams RD, Haseman MK, Reed NL, Miller SJ, Gerstbrein J: **Radioimmunoscintigraphy with In-111-labelled capromab pendetide predicts prostate cancer response to salvage radiotherapy after failed radical prostatectomy.** *Journal of Clinical Oncology* 1998, **16**(1):284-289.
140. Nargund V, Al Hashmi D, Kumar P, Gordon S, Otitie U, Ellison D, Carroll M, Baithun S, Britton KE: **Imaging with radiolabelled monoclonal antibody (MUJ591) to prostate-specific membrane antigen in staging of clinically localized prostatic carcinoma: comparison with clinical, surgical and histological staging.** *BJU international* 2005, **95**(9):1232-1236.
141. Vallabhajosula S, Kuji I, Hamacher KA, Konishi S, Kostakoglu L, Kothari PA, Milowski MI, Nanus DM, Bander NH, Goldsmith SJ: **Pharmacokinetics and biodistribution of 111In- and 177Lu-labelled J591 antibody specific for prostate-specific membrane antigen: prediction of 90Y-J591 radiation dosimetry based on 111In or 177Lu?** *Journal of Nuclear Medicine* 2005, **46**(4):634-641.
142. Bander NH, Milowsky MI, Nanus DM, Kostakoglu L, Vallabhajosula S, Goldsmith SJ: **Phase I trial of 177lutetium-labelled J591, a monoclonal antibody to prostate-specific membrane antigen, in patients with androgen-independent prostate cancer.** *Journal of Clinical Oncology* 2005, **23**(21):4591-4601.
143. Zhou J, Neale JH, Pomper MG, Kozikowski AP: **NAAG peptidase inhibitors and their potential for diagnosis and therapy.** *Nature reviews Drug discovery* 2005, **4**(12):1015.
144. Wu AM, Senter PD: **Arming antibodies: prospects and challenges for immunoconjugates.** *Nature biotechnology* 2005, **23**(9):1137.
145. Leyton JV, Olafsen T, Lepin EJ, Hahm S, Bauer KB, Reiter RE, Wu AM: **Humanized radioiodinated minibody for imaging of prostate stem cell antigen-expressing tumors.** *Clinical Cancer Research* 2008, **14**(22):7488-7496.
146. Pandit-Taskar N, O'Donoghue JA, Ruan S, Lyashchenko SK, Carrasquillo JA, Heller G, Martinez DF, Cheal SM, Lewis JS, Fleisher M: **First-in-human imaging with 89Zr-Df-IAB2M Anti-PSMA minibody in patients with metastatic prostate cancer: Pharmacokinetics, biodistribution,**

- dosimetry, and lesion uptake.** *Journal of Nuclear Medicine* 2016, **57**(12):1858-1864.
147. Smith-Jones PM, Vallabhajosula S, Navarro V, Bastidas D, Goldsmith SJ, Bander NH: **Radiolabelled monoclonal antibodies specific to the extracellular domain of prostate-specific membrane antigen: preclinical studies in nude mice bearing LNCaP human prostate tumor.** *Journal of Nuclear Medicine* 2003, **44**(4):610-617.
148. Vallabhajosula S, Goldsmith SJ, Hamacher KA, Kostakoglu L, Konishi S, Milowski MI, Nanus DM, Bander NH: **Prediction of myelotoxicity based on bone marrow radiation-absorbed dose: radioimmunotherapy studies using ⁹⁰Y- and ¹⁷⁷Lu-labelled J591 antibodies specific for prostate-specific membrane antigen.** *Journal of Nuclear Medicine* 2005, **46**(5):850-858.
149. Holland JP, Divilov V, Bander NH, Smith-Jones PM, Larson SM, Lewis JS: **⁸⁹Zr-DFO-J591 for immunoPET of prostate-specific membrane antigen expression in vivo.** *Journal of Nuclear Medicine* 2010, **51**(8):1293-1300.
150. Alt K, Wiehr S, Ehrlichmann W, Reischl G, Wolf P, Pichler BJ, Elsässer-Beile U, Bühler P: **High-resolution animal PET imaging of prostate cancer xenografts with three different ⁶⁴Cu-labelled antibodies against native cell-adherent PSMA.** *The Prostate* 2010, **70**(13):1413-1421.
151. Chatalic KL, Veldhoven-Zweistra J, Bolkestein M, Hoeben S, Koning GA, Boerman OC, de Jong M, van Weerden WM: **A Novel ¹¹¹In-Labelled Anti-Prostate-Specific Membrane Antigen Nanobody for Targeted SPECT/CT Imaging of Prostate Cancer.** *Journal of Nuclear Medicine* 2015, **56**(7):1094-1099.
152. Banerjee SR, Pullambhatla M, Byun Y, Nimmagadda S, Green G, Fox JJ, Horti A, Mease RC, Pomper MG: **⁶⁸Ga-Labelled Inhibitors of Prostate-Specific Membrane Antigen (PSMA) for Imaging Prostate Cancer.** *Journal of Medicinal Chemistry* 2010, **53**(14):5333-5341.
153. Kularatne SA, Wang K, Santhapuram H-KR, Low PS: **Prostate-Specific Membrane Antigen Targeted Imaging and Therapy of Prostate Cancer Using a PSMA Inhibitor as a Homing Ligand.** *Molecular Pharmaceutics* 2009, **6**(3):780-789.
154. Barinka C, Hlouchova K, Rovenska M, Majer P, Dauter M, Hin N, Ko Y-S, Tsukamoto T, Slusher BS, Konvalinka J *et al*: **Structural Basis of Interactions between Human Glutamate Carboxypeptidase II and Its Substrate Analogs.** *Journal of Molecular Biology* 2008, **376**(5):1438-1450.
155. Banerjee SR, Pullambhatla M, Shallal H, Lisok A, Mease RC, Pomper MG: **A modular strategy to prepare multivalent inhibitors of prostate-specific membrane antigen (PSMA).** *Oncotarget* 2011, **2**(12):1244.
156. Mesters JR, Barinka C, Li W, Tsukamoto T, Majer P, Slusher BS, Konvalinka J, Hilgenfeld R: **Structure of glutamate carboxypeptidase II, a drug target in neuronal damage and prostate cancer.** *The EMBO journal* 2006, **25**(6):1375-1384.
157. Anderson MO, Wu LY, Santiago NM, Moser JM, Rowley JA, Bolstad ES, Berkman CE: **Substrate specificity of prostate-specific membrane antigen.** *Bioorganic & medicinal chemistry* 2007, **15**(21):6678-6686.
158. Kozikowski AP, Nan F, Conti P, Zhang J, Ramadan E, Bzdega T, Wroblewska B, Neale JH, Pshenichkin S, Wroblewski JT: **Design of remarkably simple, yet potent urea-based inhibitors of glutamate carboxypeptidase II (NAALADase).** *Journal of medicinal chemistry* 2001, **44**(3):298-301.
159. Pomper MG, Musachio JL, Zhang J, Scheffel U, Zhou Y, Hilton J, Maini A, Dannals RF, Wong DF, Kozikowski AP: **¹¹C-MCG: synthesis, uptake selectivity, and primate PET of a probe for glutamate carboxypeptidase II (NAALADase).** *Molecular imaging* 2002, **1**(2):15353500200202109.
160. Uprimny C, Kroiss AS, Decristoforo C, Fritz J, von Guggenberg E, Kendler D, Scarpa L, di Santo G, Roig LG, Maffey-Steffan J: **⁶⁸Ga-PSMA-11 PET/CT in primary staging of prostate cancer: PSA and Gleason score predict the intensity of tracer accumulation in the primary tumour.** *European journal of nuclear medicine and molecular imaging* 2017, **44**(6):941-949.
161. Prasad V, Steffen IG, Diederichs G, Makowski MR, Wust P, Brenner W: **Biodistribution of [⁶⁸Ga] PSMA-HBED-CC in patients with prostate cancer: Characterization of uptake in normal organs and tumour lesions.** *Molecular Imaging and Biology* 2016, **18**(3):428-436.
162. Uprimny C, Kroiss AS, Fritz J, Decristoforo C, Kendler D, von Guggenberg E, Nilica B, Maffey-Steffan J, di Santo G, Bektic J: **Early PET imaging with [⁶⁸] Ga-PSMA-11 increases the detection rate of local recurrence in prostate cancer patients with biochemical recurrence.** *European*

- Journal of Nuclear Medicine and Molecular Imaging* 2017:1-9.
163. Eder M, Schäfer M, Bauder-Wüst U, Hull W-E, Wängler C, Mier W, Haberkorn U, Eisenhut M: **68Ga-complex lipophilicity and the targeting property of a urea-based PSMA inhibitor for PET imaging.** *Bioconjugate chemistry* 2012, **23**(4):688-697.
 164. Kularatne SA, Zhou Z, Yang J, Post CB, Low PS: **Design, Synthesis, and Preclinical Evaluation of Prostate-Specific Membrane Antigen Targeted 99mTc-Radioimaging Agents.** *Molecular Pharmaceutics* 2009, **6**(3):790-800.
 165. Hillier SM, Maresca KP, Lu G, Merkin RD, Marquis JC, Zimmerman CN, Eckelman WC, Joyal JL, Babich JW: **99mTc-labelled small-molecule inhibitors of prostate-specific membrane antigen for molecular imaging of prostate cancer.** *Journal of Nuclear Medicine* 2013, **54**(8):1369-1376.
 166. Vallabhajosula S, Nikolopoulou A, Babich JW, Osborne JR, Tagawa ST, Lipai I, Solnes L, Maresca KP, Armor T, Joyal JL: **99mTc-labelled small-molecule inhibitors of prostate-specific membrane antigen: pharmacokinetics and biodistribution studies in healthy subjects and patients with metastatic prostate cancer.** *Journal of Nuclear Medicine* 2014, **55**(11):1791-1798.
 167. Gourni E, Henriksen G: **Metal-Based PSMA Radioligands.** *Molecules* 2017, **22**(4):523.
 168. Kratochwil C, Giesel FL, Stefanova M, Benešová M, Bronzel M, Afshar-Oromieh A, Mier W, Eder M, Kopka K, Haberkorn U: **PSMA-targeted radionuclide therapy of metastatic castration-resistant prostate cancer with 177Lu-labelled PSMA-617.** *Journal of Nuclear Medicine* 2016, **57**(8):1170-1176.
 169. Eder M, Schäfer M, Bauder-Wüst U, Hull W-E, Wängler C, Mier W, Haberkorn U, Eisenhut M: **68Ga-Complex Lipophilicity and the Targeting Property of a Urea-Based PSMA Inhibitor for PET Imaging.** *Bioconjugate Chemistry* 2012, **23**(4):688-697.
 170. Ceci F, Uprimny C, Nilica B, Geraldo L, Kendler D, Kroiss A, Bektic J, Horninger W, Lukas P, Decristoforo C: **68Ga-PSMA PET/CT for restaging recurrent prostate cancer: which factors are associated with PET/CT detection rate?** *European journal of nuclear medicine and molecular imaging* 2015, **42**(8):1284-1294.
 171. Eiber M, Maurer T, Souvatzoglou M, Beer AJ, Ruffani A, Haller B, Graner F-P, Kübler H, Haberkorn U, Eisenhut M: **Evaluation of hybrid 68Ga-PSMA ligand PET/CT in 248 patients with biochemical recurrence after radical prostatectomy.** *Journal of Nuclear Medicine* 2015, **56**(5):668-674.
 172. Rauscher I, Maurer T, Beer AJ, Graner F-P, Haller B, Weirich G, Doherty A, Gschwend JE, Schwaiger M, Eiber M: **Value of 68Ga-PSMA HBED-CC PET for the assessment of lymph node metastases in prostate cancer patients with biochemical recurrence: comparison with histopathology after salvage lymphadenectomy.** *Journal of Nuclear Medicine* 2016, **57**(11):1713-1719.
 173. Perera M, Papa N, Christidis D, Wetherell D, Hofman MS, Murphy DG, Bolton D, Lawrentschuk N: **Sensitivity, Specificity, and Predictors of Positive 68Ga-Prostate-specific Membrane Antigen Positron Emission Tomography in Advanced Prostate Cancer: A Systematic Review and Meta-analysis.** *European Urology* 2016, **70**(6):926-937.
 174. Uprimny C: **68Ga-PSMA-11 PET/CT: the rising star of nuclear medicine in prostate cancer imaging?** *Wiener Medizinische Wochenschrift* 2017:1-9.
 175. Benešová M, Schäfer M, Bauder-Wüst U, Afshar-Oromieh A, Kratochwil C, Mier W, Haberkorn U, Kopka K, Eder M: **Preclinical evaluation of a tailor-made DOTA-conjugated PSMA inhibitor with optimized linker moiety for imaging and endoradiotherapy of prostate cancer.** *Journal of Nuclear Medicine* 2015, **56**(6):914-920.
 176. Scarpa L, Buxbaum S, Kendler D, Fink K, Bektic J, Gruber L, Decristoforo C, Uprimny C, Lukas P, Horninger W *et al*: **The 68Ga/177Lu theragnostic concept in PSMA targeting of castration-resistant prostate cancer: correlation of SUVmax values and absorbed dose estimates.** *European Journal of Nuclear Medicine and Molecular Imaging* 2017, **44**(5):788-800.
 177. Yadav M, Ballal S, Tripathi M, DamLe N, Sahoo R, Roesch F, Bal C: **Post-therapeutic dosimetry of 177Lu-DKFZ-PSMA-617 in treatment of patients with castration resistant prostate cancer.** *Journal of Nuclear Medicine* 2016, **57**(supplement 2):1017.
 178. Heck MM, Retz M, Tauber R, Knorr K, Kratochwil C, Eiber M: **[PSMA-targeted radioligand therapy in prostate cancer].** *Urologe A* 2017, **56**(1):32-39.
 179. Wustemann T, Bauder-Wust U, Schafer M, Eder M, Benesova M, Leotta K, Kratochwil C, Haberkorn

- U, Kopka K, Mier W: **Design of Internalizing PSMA-specific Glu-ureido-based Radiotherapeutics**. *Theranostics* 2016, **6**(8):1085-1095.
180. Gourni E, Canovas C, Goncalves V, Denat F, Meyer PT, Maecke HR: **(R)-NODAGA-PSMA: A Versatile Precursor for Radiometal Labelling and Nuclear Imaging of PSMA-Positive Tumors**. *PLOS ONE* 2015, **10**(12):e0145755.
181. Nakajima T, Mitsunaga M, Bander NH, Heston WD, Choyke PL, Kobayashi H: **Targeted, Activatable, In Vivo Fluorescence Imaging of Prostate-Specific Membrane Antigen (PSMA) Positive Tumors Using the Quenched Humanized J591 Antibody-Indocyanine Green (ICG) Conjugate**. *Bioconjugate Chemistry* 2011, **22**(8):1700-1705.
182. Watanabe R, Sato K, Hanaoka H, Harada T, Nakajima T, Kim I, Paik CH, Wu AM, Choyke PL, Kobayashi H: **Minibody-Indocyanine Green Based Activatable Optical Imaging Probes: The Role of Short Polyethylene Glycol Linkers**. *ACS Medicinal Chemistry Letters* 2014, **5**(4):411-415.
183. Mazzocco C, Fracasso G, Germain-Genevois C, Dugot-Senant N, Figini M, Colombatti M, Grenier N, Couillaud F: **In vivo imaging of prostate cancer using an anti-PSMA scFv fragment as a probe**. *Scientific reports* 2016, **6**:23314.
184. Chen Y, Dhara S, Banerjee SR, Byun Y, Pullambhatla M, Mease RC, Pomper MG: **A low molecular weight PSMA-based fluorescent imaging agent for cancer**. *Biochemical and Biophysical Research Communications* 2009, **390**(3):624-629.
185. Kovar JL, Cheung LL, Simpson MA, Olive DM: **Pharmacokinetic and Biodistribution Assessment of a Near Infrared-Labelled PSMA-Specific Small Molecule in Tumor-Bearing Mice**. *Prostate Cancer* 2014, **2014**:10.
186. Bao K, Lee JH, Kang H, Park GK, El Fakhri G, Choi HS: **PSMA-targeted contrast agents for intraoperative imaging of prostate cancer**. *Chemical Communications* 2017, **53**(10):1611-1614.
187. Lütje S, Rijpkema M, Franssen G, Fracasso G, Helfrich W, Eek A, Oyen W, Colombatti M, Boerman O: **Dual-modality image-guided surgery of prostate cancer with a radiolabelled fluorescent anti-PSMA monoclonal antibody**. *Journal of Nuclear Medicine* 2014, **55**(supplement 1):162.
188. Banerjee SR, Pullambhatla M, Byun Y, Nimmagadda S, Foss CA, Green G, Fox JJ, Lupold SE, Mease RC, Pomper MG: **Sequential SPECT and Optical Imaging of Experimental Models of Prostate Cancer with a Dual Modality Inhibitor of the Prostate-Specific Membrane Antigen**. *Angew Chem Int Ed* 2011, **50**(39):9167-9170.
189. Lee H, Mason JC, Achilefu S: **Synthesis and Spectral Properties of Near-Infrared Aminophenyl-, Hydroxyphenyl-, and Phenyl-Substituted Heptamethine Cyanines**. *The Journal of Organic Chemistry* 2008, **73**(2):723-725.
190. Zhegalova NG, Gonzales G, Berezin MY: **Synthesis of nitric oxide probes with fluorescence lifetime sensitivity**. *Organic & Biomolecular Chemistry* 2013, **11**(47):8228-8234.
191. Flanagan JH, Khan SH, Menchen S, Soper SA, Hammer RP: **Functionalized Tricarbocyanine Dyes as Near-Infrared Fluorescent Probes for Biomolecules**. *Bioconjugate Chemistry* 1997, **8**(5):751-756.
192. Zaheer A, Wheat TE, Frangioni JV: **IRDye78 Conjugates for Near-Infrared Fluorescence Imaging**. *Molecular Imaging* 2002, **1**(4):15353500200221302.
193. Sowell J, Mason JC, Streckowski L, Patonay G: **Binding constant determination of drugs toward subdomain IIIA of human serum albumin by near-infrared dye-displacement capillary electrophoresis**. *Electrophoresis* 2001, **22**(12):2512-2517.
194. Pichler BJ, Judenhofer Ms Fau - Pfannenbergs C, Pfannenbergs C: **Multimodal imaging approaches: PET/CT and PET/MRI**. (0171-2004 (Print)).
195. Lhenry D, Larrouy M, Bernhard C, Goncalves V, Raguin O, Provent P, Moreau M, Collin B, Oudot A, Vrigneaud JM: **BODIPY: A highly versatile platform for the design of bimodal imaging probes**. *Chemistry-A European Journal* 2015, **21**(37):13091-13099.
196. Duheron V, Moreau M, Collin B, Sali W, Bernhard C, Goze C, Gautier T, Pais de Barros J-P, Deckert V, Brunotte F: **Dual labelling of lipopolysaccharides for SPECT-CT imaging and fluorescence microscopy**. *ACS chemical biology* 2013, **9**(3):656-662.
197. Maindron N, Ipuy M, Bernhard C, Lhenry D, Moreau M, Carme S, Oudot A, Collin B, Vrigneaud JM, Provent P: **Near-Infrared-Emitting BODIPY-trisDOTA¹¹¹In as a Monomolecular Multifunctional Imaging Probe: From Synthesis to In Vivo Investigations**. *Chemistry-A European Journal* 2016,

- 22(36):12670-12674.
198. Berezin MY, Lee H, Akers W, Guo K, Goiffon RJ, Almutairi A, Fréchet JM, Achilefu S: **Engineering NIR dyes for fluorescent lifetime contrast**. In: *Engineering in Medicine and Biology Society, 2009 EMBC 2009 Annual International Conference of the IEEE: 2009*: IEEE; 2009: 114-117.
 199. Afshar-Oromieh A, Avtzi E, Giesel FL, Holland-Letz T, Linhart HG, Eder M, Eisenhut M, Boxler S, Hadaschik BA, Kratochwil C *et al*: **The diagnostic value of PET/CT imaging with the 68Ga-labelled PSMA ligand HBED-CC in the diagnosis of recurrent prostate cancer**. *European Journal of Nuclear Medicine and Molecular Imaging* 2015, **42**(2):197-209.
 200. Merten H, Brandl F, Plückthun A, Zangemeister-Wittke U: **Antibody–Drug Conjugates for Tumor Targeting** □ **Novel Conjugation Chemistries and the Promise of non-IgG Binding Proteins**. *Bioconjugate chemistry* 2015, **26**(11):2176-2185.
 201. Perez HL, Cardarelli PM, Deshpande S, Gangwar S, Schroeder GM, Vite GD, Borzilleri RM: **Antibody–drug conjugates: current status and future directions**. *Drug discovery today* 2014, **19**(7):869-881.
 202. Chari RV: **Targeted cancer therapy: conferring specificity to cytotoxic drugs**. *Acc Chem Res* 2008, **41**(1):98-107.
 203. Sun MM, Beam KS, Cervený CG, Hamblett KJ, Blackmore RS, Torgov MY, Handley FG, Senter PD, Alley SC: **Reduction-alkylation strategies for the modification of specific monoclonal antibody disulfides**. *Bioconjugate chemistry* 2005, **16**(5):1282.
 204. Acchione M, Kwon H, Jochheim CM, Atkins WM: **Impact of linker and conjugation chemistry on antigen binding, Fc receptor binding and thermal stability of model antibody–drug conjugates**. In: *MABs: 2012*: Taylor & Francis; 2012: 362-372.
 205. Boylan NJ, Zhou W, Proos RJ, Tolbert TJ, Wolfe JL, Laurence JS: **Conjugation site heterogeneity causes variable electrostatic properties in Fc conjugates**. *Bioconjugate chemistry* 2013, **24**(6):1008.
 206. Wakankar AA, Feeney MB, Rivera J, Chen Y, Kim M, Sharma VK, Wang YJ: **Physicochemical stability of the antibody– drug conjugate trastuzumab-DM1: changes due to modification and conjugation processes**. *Bioconjugate chemistry* 2010, **21**(9):1588-1595.
 207. Hamblett KJ, Senter PD, Chace DF, Sun MM, Lenox J, Cervený CG, Kissler KM, Bernhardt SX, Kopcha AK, Zabinski RF: **Effects of drug loading on the antitumor activity of a monoclonal antibody drug conjugate**. *Clinical cancer research* 2004, **10**(20):7063-7070.
 208. Jackson D, Atkinson J, Guevara CI, Zhang C, Kery V, Moon S-J, Virata C, Yang P, Lowe C, Pinkstaff J: **In vitro and in vivo evaluation of cysteine and site specific conjugated herceptin antibody–drug conjugates**. *PLoS One* 2014, **9**(1):e83865.
 209. Boswell CA, Mundo EE, Zhang C, Bumbaca D, Valle NR, Kozak KR, Fourie A, Chuh J, Koppada N, Saad O: **Impact of drug conjugation on pharmacokinetics and tissue distribution of anti-STEAP1 antibody–drug conjugates in rats**. *Bioconjugate chemistry* 2011, **22**(10):1994-2004.
 210. Lyons A, King DJ, Owens RJ, Yarranton GT, Millican A, Whittle NR, Adair JR: **Site-specific attachment to recombinant antibodies via introduced surface cysteine residues**. *Protein Engineering, Design and Selection* 1990, **3**(8):703-708.
 211. Agarwal P, Bertozzi CR: **Site-specific antibody–drug conjugates: the nexus of bioorthogonal chemistry, protein engineering, and drug development**. *Bioconjugate chemistry* 2015, **26**(2):176.
 212. Jeffrey SC, Burke PJ, Lyon RP, Meyer DW, Sussman D, Anderson M, Hunter JH, Leiske CI, Miyamoto JB, Nicholas ND: **A potent anti-CD70 antibody–drug conjugate combining a dimeric pyrrolobenzodiazepine drug with site-specific conjugation technology**. *Bioconjugate chemistry* 2013, **24**(7):1256-1263.
 213. Dennler P, Chiotellis A, Fischer E, Brégeon D, Belmont C, Gauthier L, Lhospice F, Romagne Fo, Schibli R: **Transglutaminase-based chemo-enzymatic conjugation approach yields homogeneous antibody–drug conjugates**. *Bioconjugate chemistry* 2014, **25**(3):569-578.
 214. Lhospice F, Bregeon D, Belmont C, Dennler P, Chiotellis A, Fischer E, Gauthier L, Boedec A, Rispaud H, Savard-Chambard S: **Site-specific conjugation of monomethyl auristatin E to anti-CD30 antibodies improves their pharmacokinetics and therapeutic index in rodent models**. *Molecular pharmaceutics* 2015, **12**(6):1863-1871.
 215. Dennler P, Bailey LK, Spycher PR, Schibli R, Fischer E: **Microbial Transglutaminase and c-myc-Tag: A Strong Couple for the Functionalization of Antibody-Like Protein Scaffolds from**

- Discovery Platforms.** *ChemBioChem* 2015, **16**(5):861-867.
216. Grünberg J, Jeger S, Sarko D, Dennler P, Zimmermann K, Mier W, Schibli R: **DOTA-functionalized polylysine: a high number of DOTA chelates positively influences the biodistribution of enzymatic conjugated anti-tumor antibody chCE7agl.** *PLoS one* 2013, **8**(4):e60350.
217. Zuberbühler K, Casi G, Bernardes GJ, Neri D: **Fucose-specific conjugation of hydrazide derivatives to a vascular-targeting monoclonal antibody in IgG format.** *Chemical Communications* 2012, **48**(56):7100-7102.
218. Zhou Q, Stefano JE, Manning C, Kyazike J, Chen B, Gianolio DA, Park A, Busch M, Bird J, Zheng X: **Site-specific antibody–drug conjugation through glycoengineering.** *Bioconjugate chemistry* 2014, **25**(3):510-520.
219. Boeggeman E, Ramakrishnan B, Pasek M, Manzoni M, Puri A, Loomis KH, Waybright TJ, Qasba PK: **Site specific conjugation of fluoroprobes to the remodeled Fc N-glycans of monoclonal antibodies using mutant glycosyltransferases: application for cell surface antigen detection.** *Bioconjugate chemistry* 2009, **20**(6):1228-1236.
220. Qasba PK: **Glycans of antibodies as a specific site for drug conjugation using glycosyltransferases.** *Bioconjugate chemistry* 2015, **26**(11):2170-2175.
221. Rabuka D: **Chemoenzymatic methods for site-specific protein modification.** *Current opinion in chemical biology* 2010, **14**(6):790-796.
222. Ponte JF, Sun X, Yoder NC, Fishkin N, Laleau R, Coccia J, Lanieri L, Bogalhas M, Wang L, Wilhelm S *et al.*: **Understanding How the Stability of the Thiol-Maleimide Linkage Impacts the Pharmacokinetics of Lysine-Linked Antibody–Maytansinoid Conjugates.** *Bioconjugate Chemistry* 2016, **27**(7):1588-1598.
223. Behrens CR, Ha EH, Chinn LL, Bowers S, Probst G, Fitch-Bruhns M, Monteon J, Valdiosera A, Bermudez A, Liao-Chan S: **Antibody–drug conjugates (ADCs) derived from interchain cysteine cross-linking demonstrate improved homogeneity and other pharmacological properties over conventional heterogeneous ADCs.** *Molecular pharmaceutics* 2015, **12**(11):3986-3998.
224. Hull EA, Livanos M, Miranda E, Smith MEB, Chester KA, Baker JR: **Homogeneous Bispecifics by Disulfide Bridging.** *Bioconjugate Chemistry* 2014, **25**(8):1395-1401.
225. Schumacher FF, Nunes JP, Maruani A, Chudasama V, Smith ME, Chester KA, Baker JR, Caddick S: **Next generation maleimides enable the controlled assembly of antibody–drug conjugates via native disulfide bond bridging.** *Organic & biomolecular chemistry* 2014, **12**(37):7261-7269.
226. Nelson AL: **Antibody fragments: hope and hype.** In: *MABs: 2010*: Taylor & Francis; 2010: 77-83.
227. Freise AC, Wu AM: **In vivo imaging with antibodies and engineered fragments.** *Molecular immunology* 2015, **67**(2):142-152.
228. Xenaki KT, Oliveira S, van Bergen en Henegouwen PM: **Antibody or Antibody Fragments: Implications for Molecular Imaging and Targeted Therapy of Solid Tumors.** *Frontiers in Immunology* 2017, **8**:1287.
229. Nelson AL, Reichert JM: **Development trends for therapeutic antibody fragments.** *Nature biotechnology* 2009, **27**(4):331.
230. Waldmann TA, Strober W, Mogielnicki RP: **The renal handling of low molecular weight proteins: II. Disorders of serum protein catabolism in patients with tubular proteinuria, the nephrotic syndrome, or uremia.** *Journal of Clinical Investigation* 1972, **51**(8):2162.
231. Ogawa M, Kosaka N, Choyke PL, Kobayashi H: **H-Type Dimer Formation of Fluorophores: A Mechanism for Activatable, in Vivo Optical Molecular Imaging.** *ACS Chemical Biology* 2009, **4**(7):535-546.
232. Nakajima T, Mitsunaga M, Bander NH, Heston WD, Choyke PL, Kobayashi H: **Targeted, activatable, in vivo fluorescence imaging of Prostate-specific Membrane Antigen (PSMA)-positive tumors using the quenched humanized J591 antibody-ICG conjugate.** *Bioconjugate chemistry* 2011, **22**(8):1700.
233. Watanabe R, Sato K, Hanaoka H, Harada T, Nakajima T, Kim I, Paik CH, Wu AM, Choyke PL, Kobayashi H: **Minibody-indocyanine green based activatable optical imaging probes: the role of short polyethylene glycol linkers.** *ACS medicinal chemistry letters* 2014, **5**(4):411.
234. Gajria D, Chandarlapaty S: **HER2-amplified breast cancer: mechanisms of trastuzumab resistance and novel targeted therapies.** *Expert review of anticancer therapy* 2011, **11**(2):263-275.

235. Sampath L, Kwon S, Ke S, Wang W, Schiff R, Mawad ME, Sevick-Muraca EM: **Dual-labelled trastuzumab-based imaging agent for the detection of human epidermal growth factor receptor 2 overexpression in breast cancer.** *Journal of Nuclear Medicine* 2007, **48**(9):1501-1510.
236. Wang X, Aldrich MB, Yang Z, Zhou N, Xie Q, Liu C, Sevick-Muraca E: **Influence of chelator and near-infrared dye labelling on biocharacteristics of dual-labelled trastuzumab-based imaging agents.** *Chinese Journal of Cancer Research* 2016, **28**(3):362.
237. Kikuchi Y, Uno S, Nanami M, Yoshimura Y, Iida S-i, Fukushima N, Tsuchiya M: **Determination of concentration and binding affinity of antibody fragments by use of surface plasmon resonance.** *Journal of bioscience and bioengineering* 2005, **100**(3):311-317.
238. Hermanson GT: **Bioconjugate techniques:** Academic press; 2013.
239. Zhou Z, Zhang J, Zhang Y, Ma G, Su Z: **Specific Conjugation of the Hinge Region for Homogeneous Preparation of Antibody Fragment-Drug Conjugate: A Case Study for Doxorubicin-PEG-anti-CD20 Fab' Synthesis.** *Bioconjugate chemistry* 2016, **27**(1):238-246.
240. Tang Y, Wang J, Scollard DA, Mondal H, Holloway C, Kahn HJ, Reilly RM: **Imaging of HER2/neu-positive BT-474 human breast cancer xenografts in athymic mice using 111 In-trastuzumab (Herceptin) Fab fragments.** *Nuclear medicine and biology* 2005, **32**(1):51-58.
241. Behr TM, Goldenberg DM, Becker W: **Reducing the renal uptake of radiolabelled antibody fragments and peptides for diagnosis and therapy: present status, future prospects and limitations.** *European journal of nuclear medicine* 1998, **25**(2):201-212.
242. Anselmo AC, Mitragotri S: **Nanoparticles in the clinic.** *Bioengineering & Translational Medicine* 2016, **1**(1):10-29.
243. Kim JS, Rieter WJ, Taylor KM, An H, Lin W, Lin W: **Self-assembled hybrid nanoparticles for cancer-specific multimodal imaging.** *Journal of the American Chemical Society* 2007, **129**(29):8962.
244. Rieter WJ, Kim JS, Taylor KM, An H, Lin W, Tarrant T, Lin W: **Hybrid silica nanoparticles for multimodal imaging.** *Angewandte Chemie* 2007, **119**(20):3754-3756.
245. Santra S, Bagwe RP, Dutta D, Stanley JT, Walter GA, Tan W, Moudgil BM, Mericle RA: **Synthesis and characterization of fluorescent, radio-opaque, and paramagnetic silica nanoparticles for multimodal bioimaging applications.** *Advanced Materials* 2005, **17**(18):2165-2169.
246. Park J-H, Gu L, Von Maltzahn G, Ruoslahti E, Bhatia SN, Sailor MJ: **Biodegradable luminescent porous silicon nanoparticles for in vivo applications.** *Nature materials* 2009, **8**(4):331-336.
247. He X, Wu X, Wang K, Shi B, Hai L: **Methylene blue-encapsulated phosphonate-terminated silica nanoparticles for simultaneous in vivo imaging and photodynamic therapy.** *Biomaterials* 2009, **30**(29):5601-5609.
248. Bhakta G, Sharma RK, Gupta N, Cool S, Nurcombe V, Maitra A: **Multifunctional silica nanoparticles with potentials of imaging and gene delivery.** *Nanomedicine: Nanotechnology, Biology and Medicine* 2011, **7**(4):472-479.
249. Miot-Noirault E, Vidal A, Morlieras J, Bonazza P, Auzeloux P, Besse S, Dauplat M-M, Peyrode C, Degoul F, Billotey C: **Small rigid platforms functionalization with quaternary ammonium: Targeting extracellular matrix of chondrosarcoma.** *Nanomedicine: Nanotechnology, Biology and Medicine* 2014, **10**(8):1887-1895.
250. Truillet C, Lux F, Moreau J, Four M, Sancey L, Chevreux S, Boeuf G, Perriat P, Frochot C, Antoine R: **Bifunctional polypyridyl-Ru (II) complex grafted onto gadolinium-based nanoparticles for MR-imaging and photodynamic therapy.** *Dalton Transactions* 2013, **42**(34):12410-12420.
251. Truillet C, Thomas E, Lux F, Huynh LT, Tillement O, Evans MJ: **Synthesis and characterization of 89Zr-labelled ultrasmall nanoparticles.** *Molecular pharmaceuticals* 2016, **13**(7):2596-2601.
252. Morlieras J, Chezal J-M, Miot-Noirault E, Roux A, Heinrich-Balard L, Cohen R, Tarrit S, Truillet C, Mignot A, Hachani R *et al*: **Development of gadolinium based nanoparticles having an affinity towards melanin.** *Nanoscale* 2013, **5**(4):1603-1615.
253. Anderson CJ, Ferdani R: **Copper-64 radiopharmaceuticals for PET imaging of cancer: advances in preclinical and clinical research.** *Cancer Biotherapy and Radiopharmaceuticals* 2009, **24**(4):379-393.
254. Halle B, Poulsen T, Pedersen H: **Indocyanine green plasma disappearance rate as dynamic liver function test in critically ill patients.** *Acta Anaesthesiologica Scandinavica* 2014, **58**(10):1214-1219.

Chapter VIII. Publications

Peer reviewed journals:

1. *One-Pot Direct Synthesis for Multifunctional Ultrasmall Hybrid Silica Nanoparticles*. Tran, Vu-Long; **Thakare, Vivek**; Rossetti, Fabien; Baudouin, Anne; Ramniceanu, Gregory; Doan, Bich-Thuy; Mignet, Nathalie; Comby-Zerbino, Clothilde; Antoine, Rodolphe; Dugourd, Philippe; Boschetti, Frédéric; Denat, Franck; Louis, Cédric; Roux, Stéphane; Doussinneau, Tristan; Tillement, Olivier; Lux, François. DOI: 10.1039/C8TB00195B (Paper) *J. Mater. Chem. B*, 2018, 6, 4821-4834.
2. *Functionalization of gadolinium chelates silica nanoparticle through silane chemistry for bimodal MRI/PET imaging*. Vu-Long Tran*, **Vivek Thakare***, Marco Natuzzi, Mathieu Moreau, Alexandra Oudot, Alan Courteau, Jean-Marc Vrigneaud, Cédric Louis, Stéphane Roux, Frédéric Boschetti, Franck Denat, Olivier Tillement and François Lux. Manuscript accepted in *Contrast Media and Molecular Imaging*. (*-Equal contribution)
3. *Covalent functionalization of theranostic silica nanoparticles based on multimodal platform for PET/MRI/Optical imaging*. **Vivek Thakare**, Vu-Long Tran, Marco Natuzzi, Mathieu Moreau, Alexandra Oudot, Alan Courteau, Jean-Marc Vrigneaud, Cédric Louis, Stéphane Roux, Frédéric Boschetti, Franck Denat, Olivier Tillement and François Lux. Manuscript under preparation.
4. *An easy and versatile approach for the design of Monomolecular Multimodal Imaging Probes for hybrid optical/SPECT or PET imaging*. Adrien Dubois[§], **Vivek Thakare[§]**, Claire Bernhard, Martin Ipuay, Mathieu Moreau, Anthony Romieu, Frédéric Boschetti, Christine Goze and Franck Denat. Manuscript under preparation. (§-Equal contribution)
5. *Characterization and biodistribution of Au nanoparticles loaded in PLGA nanocarriers using an original encapsulation process*. Gautier Laurent, Claudia Flores, Yann Pellequer, Rana Bazzi, **Vivek Sudam Thakare**, Franck Denat, Stéphane Roux, and Arnaud Béduneau. Manuscript submitted.

Patents:

1. V.L. Tran, F. Lux, O. Tillement, F. Rosetti, **V. Thakare**. *Method for synthesizing silica nanoparticles*. **European Patent EP17305701**, 2017. Submitted.

Book Chapter:

1. M. B. Ferruz, V. Ivosev, K. Haume, E.G. Lilian, A. Traore, **V. Thakare**, S. Rosa, P. de Vera, V.L. Tran, A. Mika, D. Boscolo, S. Grellet, A. Verkhovtsev, B.A. Huber, K. T. Butterworth, K. M. Prise, F. J. Currell, N. J. Mason, J. Golding, E. Scifoni, G. Garcia, F. Boschetti, F. Lux, O. Tillement, C. Louis, K. Stokbro, A. V. Solov'yov, S. Lacombe. *New Research in Ionizing Radiation and Nanoparticles: The ARGENT Project*. In: Andrey Solov'yov (Ed.), **Nanoscale Insights into Ion-Beam Cancer Therapy**, Springer 2017.

Oral Talks:

1. *Developing building blocks for cancer theranostics*; **Vivek Thakare**, Frederic Boschetti, Franck Denat. ARGENT International Conference, 22-24 January, 2018, Paris, France.
2. *Lysine as a versatile platform for the design of multimodal(optical/SPECT or PET) imaging probes*; C. Goze, C. Bernhard, N. Maindron, M. Ipuay, D. Lhenry, M. Moreau, **V. Thakare**, A. Dubois, F. Boschetti, F. Denat. 30th Annual Congress of the European Association of Nuclear Medicine – EANM'17, 21– 25 October, 2017, Vienna, Austria.
3. *Multifunctional systems for cancer therapy and diagnosis*; **Vivek Thakare**, Frederic Boschetti, Franck Denat. Journée Ecole Doctorale - 2016, 18-19 May 2017, Dijon, France.
4. *Development and characterization of targeted nanoparticles for cancer*; **Vivek Thakare**, Frederic Boschetti, Franck Denat. ARGENT Annual Project Meeting, 22-24, February 2017 Belfast, UK.
5. *Development and characterization of AGuIX and gold nanoparticle conjugates for cancer targeting*; **Vivek Thakare**, Frederic Boschetti, Franck Denat. ARGENT Annual Project Meeting, 29 Nov-3 Dec 2015, Obergurgl, Austria.

Poster Presentations:

1. *Development of Monomolecular Multimodal Imaging Probes for Optical/Nuclear Imaging*; I. E. Valverde, C. Bernhard, N. Maindron, M. Ipuay, D. Lhenry, M. Moreau, **V. Thakare**, A. Dubois, F. Boschetti, F. Denat, C. Goze. The Studium Conference: Is Multimodal Imaging an Invention with a Future? The Input of Chemistry, 11-13 December 2017, Orléans, France.
2. *Cetuximab-gold nanoconjugates for cancer therapy and diagnosis: Synthesis and characterization*; **Vivek Thakare**, Frederic Boschetti, Mathieu Moreau, Franck Denat, Gloria Jimenez Sanchez, Stephane Roux. Journée Ecole Doctorale - 2016, 19-20 May 2016, Besançon, France.
3. *Design and characterization of macromolecular conjugates of monoclonal antibody for cancer therapy and diagnosis*; **Vivek Thakare**, Frederic Boschetti, Mathieu Moreau, Franck Denat, Elöse Thomas, Lux Francoise, Olivier Tillement. Nanohybrides 13, 9-12 May 2016, Pourquerolles, France.
4. *Design and characterization of macromolecular conjugates of monoclonal antibody for cancer therapy and diagnosis*; **Vivek Thakare**, Frederic Boschetti, Mathieu Moreau, Franck Denat, Elöse Thomas, Lux Francoise, Olivier Tillement. Young Research Fellow Meeting 2016, 15-17 February 2016, Lille, France.
5. *Cetuximab-gold nanoconjugates for cancer therapy and diagnosis: Synthesis and characterization*; **Vivek Thakare**, Frederic Boschetti, Mathieu Moreau, Franck Denat, Gloria Jimenez Sanchez, Stephane Roux. 2nd Biologics and Biosimilars Congress, 1-2 February 2016, Berlin, Germany.

Abstract:

The objective of this thesis was to develop multifunctional tools for cancer theranosis, particularly based on nanotechnology. The work is based on the premise of monomolecular multimodal platform that aims to create the building blocks that can be used for the synthesis of functionalized nanoparticles, bioconjugates or targeted small molecular imaging probes.

The initial work focused on the synthesis of the chelator based silane precursors. These novel precursors were employed for the functionalization of AGuIX nanoparticles and have also been implicated in a one pot AGuIX synthesis. Radiolabelling of these nanoparticles was performed with the aim to evaluate the stability of these nanoparticles under physiological conditions. Furthermore, these nanoparticles were investigated in TSA tumor model in order to evaluate their pharmacokinetics, biodistribution behaviour and value in PET-MRI imaging. In the second part of the work, building blocks/ligands have been developed and successfully deployed for the functionalization of gold nanoparticles. Multimodal ligands containing different combinations of chelators, targeting moieties, functional groups and dyes were synthesized. Gold nanoparticles for PET-MRI and PSMA targeting SPECT imaging were further radiolabelled ($^{64}\text{Cu}/^{111}\text{In}$) and showed excellent stability. PSMA targeting ligand exhibited good affinity towards PSMA, whereas the in vivo studies of the gold nanoparticles for PET-MRI in TSA tumor model demonstrated good pharmacokinetics properties, underscoring their potential in cancer imaging and radiotherapy.

The latter half of the thesis work focusses on the development of PET-Optical probes for PSMA positive cancer targeting imaging using small molecular probes, and for bioconjugation to antibody fragments and nanoparticles. A PSMA targeting probe based on NODAGA and IR-783 dye has been developed and characterized for its affinity, photophysical and radiolabelling properties. Likewise, a similar probe bearing a maleimide handle has been successfully used for the site-specific labelling of trastuzumab Fab' fragments and functionalization of AGuIX nanoparticles. These bioconjugates and the nanoparticles have been thoroughly characterized and evaluated in relevant biological models to highlight their value in cancer theranosis.

Keywords: Nanoparticles, functionalization, AGuIX, NODAGA, DOTAGA, bioconjugation, multimodality, theranosis, PET-MRI, PET-Optical, PSMA.

Résumé:

L'objectif de cette thèse était de développer des outils multifonctionnels pour l'élaboration d'agents théranostiques en oncologie, notamment à base de nanotechnologies. Le projet est basé sur l'utilisation de plateformes multimodales monomoléculaires comme précurseurs pour la synthèse de nanoparticules, de bioconjugués ou encore de sondes imageantes à base de petites molécules.

Les premiers travaux ont concerné la synthèse de précurseurs silanes comportant un agent chélatant. Ces nouveaux précurseurs ont été mis en oeuvre pour la fonctionnalisation de nanoparticules AGuIX et ont également été utilisés dans un nouveau procédé de synthèse « one-pot » d'AGuIX. Le radiomarquage de ces nanoparticules a été réalisé dans le but d'évaluer la stabilité de ces nanoparticules dans des conditions physiologiques. Par ailleurs, ces nanoparticules ont été étudiées dans un modèle de tumeur TSA afin de déterminer leur comportement pharmacocinétique, leur biodistribution et leur potentiel en imagerie bimodale TEP-IRM.

Dans une deuxième partie, des blocs de construction / ligands ont été développés et utilisés avec succès pour la fonctionnalisation de nanoparticules d'or. Des ligands multimodaux contenant différentes combinaisons de chélateurs, de fonctions de ciblage, de groupes fonctionnels et de chromophores, ont été synthétisés. Les nanoparticules d'or pour l'imagerie TEP-IRM et SPECT (ciblant le PSMA) ont été ensuite radiomarquées ($^{64}\text{Cu}/^{111}\text{In}$) et ont montré une excellente stabilité. Le ligand à base de PSMA présente une bonne affinité vis-à-vis du PSMA, tandis que les études *in vivo* dans un modèle tumoral TSA des nanoparticules d'or pour l'IRM-TEP ont démontré les bonnes propriétés pharmacocinétiques de ces nanoparticules fonctionnalisées, et donc leur potentiel en imagerie et en radiothérapie.

La dernière partie du travail de thèse concerne le développement de sondes TEP-Optique pour l'imagerie ciblée de tumeurs surexprimant le PSMA en utilisant de petites sondes moléculaires, ainsi que pour leur bioconjugaison sur des fragments d'anticorps et des nanoparticules. Une sonde ciblant le PSMA, à base de NODAGA et du fluorophore IR-783, a été développée et caractérisée afin de déterminer ses propriétés photophysiques, son affinité pour le PSMA, et les conditions de radiomarquage. Enfin, un analogue comportant une fonction maléimide a été utilisée avec succès pour le marquage site spécifique de fragments Fab' du trastuzumab, ainsi que pour la fonctionnalisation de nanoparticules AGuIX. Ces bioconjugués et ces nanoparticules ont été soigneusement caractérisés et évalués dans des modèles biologiques pertinents afin de mettre en évidence leur intérêt comme agents théranostiques.

Mots clés: Nanoparticules, fonctionnalisation, AGuIX, NODAGA, DOTAGA, bioconjugaison, multimodalité, théranostique, TEP-IRM, TEP-Optique, PSMA.